**University of Alberta**

# Some Aspects of Production Data Integration in Reservoir Modeling

by

**Zulfiquar Ali Reza**

A thesis submitted to the Faculty of Graduate Studies and Research in partial fulfillment of the requirements for the degree of **Doctor of Philosophy**.

in

Petroleum Engineering

Department of Civil and Environmental Engineering

Edmonton, Alberta
Spring 2003

National Library
of Canada

Acquisitions and
Bibliographic Services

395 Wellington Street
Ottawa ON K1A 0N4
Canada

Bibliothèque nationale
du Canada

Acquisisitons et
services bibliographiques

395, rue Wellington
Ottawa ON K1A 0N4
Canada

*Your file Votre référence*
*ISBN: 0-612-82161-7*
*Our file Notre référence*
*ISBN: 0-612-82161-7*

The author has granted a non-exclusive licence allowing the National Library of Canada to reproduce, loan, distribute or sell copies of this thesis in microform, paper or electronic formats.

The author retains ownership of the copyright in this thesis. Neither the thesis nor substantial extracts from it may be printed or otherwise reproduced without the author's permission.

L'auteur a accordé une licence non exclusive permettant à la Bibliothèque nationale du Canada de reproduire, prêter, distribuer ou vendre des copies de cette thèse sous la forme de microfiche/film, de reproduction sur papier ou sur format électronique.

L'auteur conserve la propriété du droit d'auteur qui protège cette thèse. Ni la thèse ni des extraits substantiels de celle-ci ne doivent être imprimés ou aturement reproduits sans son autorisation.

**Canada**

**University of Alberta**

**Library Release Form**

**Name of Author**: Zulfiquar Ali Reza

**Title of Thesis**: Some Aspects of Production Data Integration in Reservoir Modeling

**Degree**: Doctor of Philosophy

**Year this Degree Granted**: 2003

Permission is hereby granted to the University of Alberta Library to reproduce single copies of this thesis and to lend or sell such copies for private, scholarly or scientific research purposes only.

The author reserves all other publication and other rights in association with the copyright in the thesis, and except as herein before provided, neither the thesis nor any substantial portion thereof may be printed or otherwise reproduced in any material form whatever without the author's prior written permission.

Zulfiquar Ali Reza

Zulfiquar Ali Reza
C/O Dr K. K. H. Siddiqui
11 BaluHakkak Lane
P.O. Circus Avenue
Kolkata 700017, India

**Date**: Feb 28, 2003

**University of Alberta**

**Faculty of Graduate Studies and Research**

The undersigned certify that they have read, and recommend to the Faculty of Graduate Studies and Research for acceptance, a thesis entitled **Some Aspects of Production Data Integration in Reservoir Modeling** submitted by Zulfiquar Ali Reza in partial fulfillment of the requirements for the degree of **Doctor of Philosophy** in *Petroleum Engineering.*

Dr. C. V. Deutsch (Supervisor)

fc Dr. A. C. Reynolds (External)

Dr. M. Polikar

Dr. D. R. Schmitt

Dr. L. B. Cunha

Dr. S. Lele

**Date:** Feb 27, 2003

# Abstract

The realistic description of reservoirs for the purpose of flow simulation is a longstanding problem. The true reservoir description will never be known. The integration of dynamic production data reduces uncertainty; the reduction in uncertainty is proportional to the amount of historical data and the interference between the wells. This thesis develops methods to incorporate historical production data into numerical reservoir models.

The first problem tackled is the simultaneous inversion of porosity and permeability using a geostatistics-based integration algorithm. The algorithm is developed and a numerical code is implemented. Some illustrative examples are presented and sensitivity issues are analysed.

Production data informs the nature of heterogeneity in the reservoir. The inversion algorithm is modified to permit inversion of variograms. The predictive capability of the reservoir models is improved with the updating of the variogram through inversion. The algorithm was also extended to invert for fault zone properties. The fault locations are assumed known through seismic and the properties are inferred with the available production data. The advantages and the limitations are identified.

# Acknowledgements

I am grateful to my supervisor Professor Clayton Deutsch for his support, guidance and supervision. Working with Dr Deutsch has been a treasure of experience for me. I greatly gained from his astute reasonableness, analytical sense at every stage of this research.

I gratefully acknowledge the assistance that I received from Dr Xian-Huan Wen. I must also thank all the students of Centre for Computational Geostatistics for their camaradarie.

This PhD work was in most part supported by Canadian International Development Agency to which I am gratefully indebted. I would like to express my gratitude to Ms Lori Constantine of International Programs, University of Alberta International, for her assistance, encouragement ever since the commencement of my study at University of Alberta. Gratitude also goes to Ms Bonnie Motyka, Ms Renee Vaugeois, and Ms Margo Nelson of University of Alberta International for their support in numerous occasions.

Lastly, I acknowledge my family's patience, encouragement and love at all times. Their presence in my life means more than anything.

# Table of Contents


**1 Introduction** 1

1.1 Data Used in Reservoir Characterization . . . . . 2

1.2 Dynamic Data and Spatial Information . . . . . 2

1.3 Outline of the Thesis . . . . . 4

**2 Literature Review** 6

2.1 Classical Inversion Techniques . . . . . 6

2.2 Regularization Based Techniques . . . . . 7

2.3 Bayesian Estimation . . . . . 8

2.4 Zonation Methods . . . . . 9

2.5 Cokriging Based Methods . . . . . 10

2.6 Simulated Annealing Based Techniques . . . . . 12

2.7 Two-Step Approaches and Indirect Methods . . . . . 12

2.8 Recent Developments . . . . . 17

**3 Mathematics of Production Data Integration** 18

3.1 Inverse Problem . . . . . 18

3.2 Ill-posedness of Inverse Problems . . . . . 19

3.3 Forward Problem Formulation . . . . . 20

3.4 Objective Function . . . . . 21

3.5 Parameter Estimation Algorithms . . . . . 22

3.6 Gradient Based Methods . . . . . 24

3.7 Nongradient Optimization Techniques . . . . . 31

3.8 Search Methods . . . . . 31

3.9 Bound Constrained Optimization . . . . . 33

3.10 Regularization . . . . . 35

3.11 Sequential Self-Calibration Technique . . . . . 36

**4 Simultaneous Inversion of $\phi/\ln(k)$ Using Multiple Well Production Data 46**

4.1 Simultaneous Inversion Problem . . . . . 46

4.2 Example 1: A Deterministic Example . . . . . 49

4.3 Some Sensitivity Studies . . . . . 61

4.4 An Implementation Issue: Propagation of Optimal Corrections . . . . . 76

4.5 Example 2: A Stochastic Example . . . . . 76

4.6 Discussion . . . . . 88

**5 Simultaneous Inversion of Unique $\phi/\ln(k)$ Features From Production Data 89**

5.1 A Synthetic Reservoir Model with Unique $\phi/\ln(k)$ Features . . . . . 89

5.2 Effect of Production Data . . . . . 98

5.3 Influence of Local Data . . . . . 107

**6 Simultaneouos Inversion with Variogram Updating 113**

6.1 Variogram Inversion Algorithm . . . . . 113

6.2 A Synthetic Application . . . . . 114

6.3 High Nugget Effect Inversion Using Production Data . . . . . 133

6.4 Effect of Production Data . . . . . 140

6.5 Some Remarks on Variogram Modeling Module . . . . . 154

**7 Fault Property Inversion Using Production Data 159**

7.1 Algorithm Description . . . . . 159

7.2 Sealing Fault Example . . . . . 160

7.3 High Permeability Fault Example . . . . . 173

7.4 Sensitivity Studies . . . . . 179

7.5 Effect of Production Data . . . . . 187

**8 Discussion and Future Developments 202**

8.1 Discussion . . . . . 202

8.2 Limitations . . . . . 204

8.3 Recommended Future Developments . . . . . 204

**Bibliography 207**

**A Parameter Files in Computer Codes 222**

A.1 Program: **ssckphi** . . . . . 222

A.2 Program: **ssckphiv** . . . . . 224
A.3 Program: **ssckphif** . . . . . 226

**B Sensitivity Analysis and Derived Information** **229**
B.1 Introduction . . . . . 229
B.2 Sensitivity Computation . . . . . 229
B.3 Base Case Reservoir Description . . . . . 230
B.4 Region Specification for Sensitivity Computation . . . . . 233
B.5 Typical Sensitivity Coefficient Behavior . . . . . 233
B.6 Factors Affecting Sensitivity Coefficients . . . . . 238
B.7 Discussion . . . . . 246

**C Inversion with Pressure Derivative Mismatch** **252**
C.1 Mathematics of Inversion with Pressure Derivative Mismatch . . . . . 252

# List of Figures


3.1 Flowchart of the Sequential Self-Calibration method . . . . . 39

3.2 Analytical one dimensional solution of tracer flow and its approximation using a Gaussian cumulative function and immiscible two-phase displacement 40

3.3 Schematic illustration of tracking streamline through discretized numerical model . . . . . 42

4.1 Reference $\phi$ and $\ln(k)$ fields: Deterministic Example . . . . . 49

4.2 Production data obtained from the reference field: Deterministic Example . 50

4.3 Static well data for $\phi$ and $\ln(k)$: Deterministic Example Run 1 . . . . . 52

4.4 Updated $\phi$ and $\ln(k)$ fields: Deterministic Example Run 1 . . . . . 52

4.5 Pressure responses computed from initial and updated $\phi$ and $\ln(k)$ fields with the true data: Deterministic Example Run 1 . . . . . 53

4.6 Objective function values of the inversion process: Deterministic Example Run 1 . . . . . 53

4.7 Updated $\phi$ fields at each iteration of the inversion process: Deterministic Example Run 1 . . . . . 54

4.8 Updated $\ln(k)$ fields at each iteration of the inversion process: Deterministic Example Run 1 . . . . . 55

4.9 Conditional simulation of $\phi$ and $\ln(k)$ fields honoring only static information (local data, global distribution and prior variography) . . . . . 56

4.10 Pressure responses computed from conditionally simulated $\phi$ and $\ln(k)$ fields with the true data . . . . . 56

4.11 Conditional simulation of $\phi$ and $\ln(k)$ fields honoring only static local data, and prior variography information . . . . . 57

4.12 Pressure responses computed from conditionally simulated $\phi$ and $\ln(k)$ fields with the true data . . . . . 58

4.13 Updated $\phi$ and $\ln(k)$ fields: Deterministic Example Run 2 . . . . . 58

4.14 Pressure responses computed from initial and updated $\phi$ and $\ln(k)$ fields with the true data: Deterministic Example Run 2 . . . . . 59
4.15 Objective function values of the inversion process: Deterministic Example Run 2 . . . . . 59
4.16 Updated $\phi$ fields at each iteration of the inversion process: Deterministic Example Run 2 . . . . . 60
4.17 Updated $\ln(k)$ fields at each iteration of the inversion process: Deterministic Example Run 2 . . . . . 60
4.18 Updated $\phi$ and $\ln(k)$ fields: Deterministic Example Run 3 . . . . . 61
4.19 Pressure responses computed from initial and updated $\phi$ and $\ln(k)$ fields with the true data: Deterministic Example Run 3 . . . . . 62
4.20 Objective function values of the inversion process: Deterministic Example Run 3 . . . . . 62
4.21 Updated $\phi$ fields at each iteration of the inversion process: Deterministic Example Run 3 . . . . . 63
4.22 Updated $\ln(k)$ fields at each iteration of the inversion process: Deterministic Example Run 3 . . . . . 63
4.23 Updated $\phi$ and $\ln(k)$ fields: Deterministic Example Run 4 . . . . . 64
4.24 Pressure responses computed from initial and updated $\phi$ and $\ln(k)$ fields with the true data: Deterministic Example Run 4 . . . . . 64
4.25 Objective function values of the inversion process: Deterministic Example Run 4 . . . . . 65
4.26 Updated $\phi$ fields at each iteration of the inversion process: Deterministic Example Run 4 . . . . . 65
4.27 Updated $\ln(k)$ fields at each iteration of the inversion process: Deterministic Example Run 4 . . . . . 66
4.28 Updated $\phi$ and $\ln(k)$ fields: Initial Field $\phi = 0.2$ and $\ln(k) = 1.0$ . . . . . 67
4.29 Updated $\phi$ and $\ln(k)$ fields: Initial Field $\phi = 0.2$ and $\ln(k) = 3.15$ . . . . . 67
4.30 Updated $\phi$ and $\ln(k)$ fields: Initial Field $\phi = 0.2$ and $\ln(k) = 6.0$ . . . . . 67
4.31 Updated $\phi$ and $\ln(k)$ fields: $2 \times 2$ Master Points Case . . . . . 68
4.32 Updated $\phi$ and $\ln(k)$ fields: $3 \times 3$ Master Points Case . . . . . 69
4.33 Updated $\phi$ and $\ln(k)$ fields: $4 \times 4$ Master Points Case . . . . . 69
4.34 Updated $\phi$ and $\ln(k)$ fields: $6 \times 6$ Master Points Case . . . . . 69
4.35 Updated $\phi$ and $\ln(k)$ fields: $7 \times 7$ Master Points Case . . . . . 70

4.36 Updated $\phi$ and $\ln(k)$ fields: Updating frequency - every 1 iteration . . . . . 71
4.37 Updated $\phi$ and $\ln(k)$ fields: Updating frequency - every 2 iterations . . . . 71
4.38 Updated $\phi$ and $\ln(k)$ fields: Updating frequency - every 3 iterations . . . . 71
4.39 Updated $\phi$ and $\ln(k)$ fields: Updating frequency - every 4 iterations . . . . 72
4.40 Updated $\phi$ and $\ln(k)$ fields: Updating frequency - every 8 iterations . . . . 72
4.41 Updated $\phi$ and $\ln(k)$ fields: Updating frequency - every 10 iterations . . . . 72
4.42 Updated $\phi$ and $\ln(k)$ fields: Prior Variogram Set 1 in Table 4.6 . . . . . 74
4.43 Updated $\phi$ and $\ln(k)$ fields: Prior Variogram Set 2 in Table 4.6 . . . . . 74
4.44 Updated $\phi$ and $\ln(k)$ fields: Prior Variogram Set 3 in Table 4.6 . . . . . 74
4.45 Updated $\phi$ and $\ln(k)$ fields: Prior Variogram Set 4 in Table 4.6 . . . . . 75
4.46 Updated $\phi$ and $\ln(k)$ fields: Base Case . . . . . 77
4.47 Pressure responses computed from initial and updated $\phi$ and $\ln(k)$ fields with the true data: Base Case . . . . . 77
4.48 Objective function values of the inversion process: Base Case . . . . . 78
4.49 Reference $\phi$ and $\ln(k)$ fields: Stochastic Example . . . . . 78
4.50 Production data obtained from the reference field: Stochastic Example . . . 79
4.51 Histograms of reference $\phi$ and $\ln(k)$ fields: Stochastic Example . . . . . 80
4.52 Scatterplot of reference $\phi$ and $\ln(k)$ distributions: Stochastic Example . . . 80
4.53 Static well data for $\phi$ and $\ln(k)$: Stochastic Example Run 1 . . . . . 81
4.54 Updated $\phi$ and $\ln(k)$ fields: Stochastic Example Run 1 . . . . . 81
4.55 Pressure responses computed from initial and updated $\phi$ and $\ln(k)$ fields with the true data: Stochastic Example Run 1 . . . . . 82
4.56 Objective function values of the inversion process: Stochastic Example Run 1 82
4.57 Updated $\phi$ fields at each iteration of the inversion process: Stochastic Example Run 1 . . . . . 83
4.58 Updated $\ln(k)$ fields at each iteration of the inversion process: Stochastic Example Run 1 . . . . . 83
4.59 Static well data for $\phi$ and $\ln(k)$: Stochastic Example Run 2 . . . . . 84
4.60 Updated $\phi$ and $\ln(k)$ fields: Stochastic Example Run 2 . . . . . 84
4.61 Pressure responses computed from initial and updated $\phi$ and $\ln(k)$ fields with the true data: Stochastic Example Run 2 . . . . . 85
4.62 Objective function values of the inversion process: Stochastic Example Run 2 85
4.63 Updated $\phi$ fields at each iteration of the inversion process: Stochastic Example Run 2 . . . . . 86

4.64 Updated $\ln(k)$ fields at each iteration of the inversion process: Stochastic Example Run 2 . . . . . 87

5.1 Reference $\phi$ and $\ln(k)$ fields . . . . . 90
5.2 Production data obtained for 8 wells from the reference field . . . . . 90
5.3 Histograms of reference $\phi$ and $\ln(k)$ fields . . . . . 91
5.4 Scatterplot of reference $\phi$ and $\ln(k)$ values . . . . . 91
5.5 Variograms of reference $\phi$ and $\ln(k)$ . . . . . 91
5.6 Static well data for $\phi$ and $\ln(k)$ . . . . . 92
5.7 Updated $\phi$ and $\ln(k)$ fields: Run 1 . . . . . 93
5.8 Pressure responses computed from initial and updated $\phi$ and $\ln(k)$ fields with the true data: Run 1 . . . . . 93
5.9 Objective function values of the inversion process: Run 1 . . . . . 94
5.10 Updated $\phi$ fields at each iteration of the inversion process: Run 1 . . . . . 95
5.11 Updated $\ln(k)$ fields at each iteration of the inversion process: Run 1 . . . . 96
5.12 Updated $\phi$ and $\ln(k)$ fields: Run 2 . . . . . 97
5.13 Pressure responses computed from initial and updated $\phi$ and $\ln(k)$ fields with the true data: Run 2 . . . . . 97
5.14 Objective function values of the inversion process: Run 2 . . . . . 98
5.15 Updated $\phi$ fields at each iteration of the inversion process: Run 2 . . . . . 99
5.16 Updated $\ln(k)$ fields at each iteration of the inversion process: Run 2 . . . . 100
5.17 Production data obtained from the reference field: 6 Well Case . . . . . 101
5.18 Updated $\phi$ and $\ln(k)$ fields: 6 Well Case . . . . . 102
5.19 Pressure responses computed from initial and updated $\phi$ and $\ln(k)$ fields with the true data: 6 Well Case . . . . . 102
5.20 Objective function values of the inversion process: 6 Well Case . . . . . 102
5.21 Updated $\phi$ fields at each iteration of the inversion process: 6 Well Case . . 103
5.22 Updated $\ln(k)$ fields at each iteration of the inversion process: 6 Well Case 103
5.23 Production data obtained from the reference field: 4 Well Case . . . . . 104
5.24 Updated $\phi$ and $\ln(k)$ fields: 4 Well Case . . . . . 104
5.25 Pressure responses computed from initial and updated $\phi$ and $\ln(k)$ fields with the true data: 4 Well Case . . . . . 105
5.26 Objective function values of the inversion process: 4 Well Case . . . . . 105
5.27 Updated $\phi$ fields at each iteration of the inversion process: 4 Well Case . . 106

5.28 Updated $\ln(k)$ fields at each iteration of the inversion process: 4 Well Case 106
5.29 Static well data for $\phi$ and $\ln(k)$: 15 Local Data Case . . . . . 107
5.30 Updated $\phi$ and $\ln(k)$ fields: 15 Local Data Case . . . . . 108
5.31 Pressure responses computed from initial and updated $\phi$ and $\ln(k)$ fields with the true data: 15 Local Data Case . . . . . 108
5.32 Objective function values of the inversion process: 15 Local Data Case . . . 108
5.33 Updated $\phi$ fields at each iteration of the inversion process: 15 Local Data Case 109
5.34 Updated $\ln(k)$ fields at each iteration of the inversion process: 15 Local Data Case . . . . . 109
5.35 Updated $\phi$ and $\ln(k)$ fields: No Local Data Case . . . . . 110
5.36 Pressure responses computed from initial and updated $\phi$ and $\ln(k)$ fields with the true data: No Local Data Case . . . . . 111
5.37 Objective function values of the inversion process: No Local Data Case . . 111
5.38 Updated $\phi$ fields at each iteration of the inversion process: No Local Data Case . . . . . 112
5.39 Updated $\ln(k)$ fields at each iteration of the inversion process: No Local Data Case . . . . . 112

6.1 Reference $\phi$ and $\ln(k)$ fields: Example 1 . . . . . 115
6.2 Production data obtained from the reference field: Example 1 . . . . . 116
6.3 Histograms of reference $\phi$ and $\ln(k)$ fields: Example 1 . . . . . 117
6.4 Scatterplot between reference $\phi$ and $\ln(k)$ values: Example 1 . . . . . 117
6.5 Variograms of reference $\phi$ and $\ln(k)$ distributions: Example 1 . . . . . 117
6.6 Variograms estimated from well data for $\phi$ and $\ln(k)$: Example 1 . . . . . 118
6.7 Static well data for $\phi$ and $\ln(k)$: Example 1 . . . . . 118
6.8 Reference, prior and updated variograms for $\phi$ at each outer iteration: Example 1 Run 1. (Direction with azimuth 0) . . . . . 119
6.9 Reference, prior and updated variograms for $\phi$ at each outer iteration: Example 1 Run 1. (Direction with azimuth 90) . . . . . 120
6.10 Reference, prior and updated variograms for $\ln(k)$ at each outer iteration: Example 1 Run 1. (Direction with azimuth 0) . . . . . 121
6.11 Reference, prior and updated variograms for $\ln(k)$ at each outer iteration: Example 1 Run 1. (Direction with azimuth 90) . . . . . 122
6.12 Mismatch norm of data integration at each outer iteration: Example 1 Run 1 123

6.13 Reference, prior and updated variograms for $\phi$ at each outer iteration: Example 1 Run 2. (Direction with azimuth 0) . . . . . 124
6.14 Reference, prior and updated variograms for $\phi$ at each outer iteration: Example 1 Run 2. (Direction with azimuth 90) . . . . . 125
6.15 Reference, prior and updated variograms for $\ln(k)$ at each outer iteration: Example 1 Run 2. (Direction with azimuth 0) . . . . . 126
6.16 Reference, prior and updated variograms for $\ln(k)$ at each outer iteration: Example 1 Run 2. (Direction with azimuth 90) . . . . . 127
6.17 Mismatch norm of data integration at each outer iteration: Example 1 Run 2 128
6.18 Reference, prior and updated variograms for $\phi$ at each outer iteration: Example 1 Run 3. (Direction with azimuth 0) . . . . . 129
6.19 Reference, prior and updated variograms for $\phi$ at each outer iteration: Example 1 Run 3. (Direction with azimuth 90) . . . . . 130
6.20 Reference, prior and updated variograms for $\ln(k)$ at each outer iteration: Example 1 Run 3. (Direction with azimuth 0) . . . . . 131
6.21 Reference, prior and updated variograms for $\ln(k)$ at each outer iteration: Example 1 Run 3. (Direction with azimuth 90) . . . . . 132
6.22 Mismatch norm of data integration at each outer iteration: Example 1 Run 3 133
6.23 Reference $\phi$ and $\ln(k)$ fields: High Nugget Effect Example . . . . . 134
6.24 Production data obtained from the reference field: High Nugget Effect Example 135
6.25 Histograms of reference $\phi$ and $\ln(k)$ fields: High Nugget Effect Example . . 136
6.26 Scatterplot between reference $\phi$ and $\ln(k)$ values: High Nugget Effect Example 136
6.27 Variograms of reference $\phi$ and $\ln(k)$ distributions: High Nugget Effect Example 136
6.28 Static well data for $\phi$ and $\ln(k)$: High Nugget Effect Example . . . . . 137
6.29 Reference, prior and updated variograms for $\phi$ at each outer iteration: High Nugget Effect Example. (Direction with azimuth 0) . . . . . 137
6.30 Reference, prior and updated variograms for $\phi$ at each outer iteration: High Nugget Effect Example. (Direction with azimuth 90) . . . . . 138
6.31 Reference, prior and updated variograms for $\ln(k)$ at each outer iteration: High Nugget Effect Example. (Direction with azimuth 0) . . . . . 138
6.32 Reference, prior and updated variograms for $\ln(k)$ at each outer iteration: High Nugget Effect Example. (Direction with azimuth 90) . . . . . 139
6.33 Mismatch norm of data integration at each outer iteration: High Nugget Effect Example . . . . . 139

6.34 Reference $\phi$ and $\ln(k)$ fields: Production Data Sensitivity Example . . . . . 140
6.35 Histograms of reference $\phi$ and $\ln(k)$ fields: Production Data Sensitivity Example . . . . . 141
6.36 Scatterplot between reference $\phi$ and $\ln(k)$ values: Production Data Sensitivity Example . . . . . 141
6.37 Variograms of reference $\phi$ and $\ln(k)$ distributions: Production Data Sensitivity Example . . . . . 141
6.38 Well locations for the 3 cases: 4, 6 and 8 well case . . . . . 142
6.39 Production data obtained from the reference field: 4 well case . . . . . 142
6.40 Production data obtained from the reference field: 6 well case . . . . . 143
6.41 Production data obtained from the reference field: 8 well case . . . . . 144
6.42 Reference, prior and updated variograms for $\phi$ at each outer iteration: 4 Well case. (Direction with azimuth 45) . . . . . 145
6.43 Reference, prior and updated variograms for $\phi$ at each outer iteration: 4 Well case. (Direction with azimuth 135) . . . . . 146
6.44 Reference, prior and updated variograms for $\ln(k)$ at each outer iteration: 4 Well case. (Direction with azimuth 45) . . . . . 147
6.45 Reference, prior and updated variograms for $\ln(k)$ at each outer iteration: 4 Well case. (Direction with azimuth 135) . . . . . 148
6.46 Mismatch norm of data integration at each outer iteration: 4 Well case . . . 149
6.47 Reference, prior and updated variograms for $\phi$ at each outer iteration: 6 Well case. (Direction with azimuth 45) . . . . . 150
6.48 Reference, prior and updated variograms for $\phi$ at each outer iteration: 6 Well case. (Direction with azimuth 135) . . . . . 151
6.49 Reference, prior and updated variograms for $\ln(k)$ at each outer iteration: 6 Well case. (Direction with azimuth 45) . . . . . 152
6.50 Reference, prior and updated variograms for $\ln(k)$ at each outer iteration: 6 Well case. (Direction with azimuth 135) . . . . . 153
6.51 Mismatch norm of data integration at each outer iteration: 6 Well case . . . 154
6.52 Reference, prior and updated variograms for $\phi$ at each outer iteration: 8 Well case. (Direction with azimuth 45) . . . . . 155
6.53 Reference, prior and updated variograms for $\phi$ at each outer iteration: 8 Well case. (Direction with azimuth 135) . . . . . 156

6.54 Reference, prior and updated variograms for $\ln(k)$ at each outer iteration: 8 Well case. (Direction with azimuth 45) . . . . . 157
6.55 Reference, prior and updated variograms for $\ln(k)$ at each outer iteration: 8 Well case. (Direction with azimuth 135) . . . . . 158
6.56 Mismatch norm of data integration at each outer iteration: 8 Well case . . . 158

7.1 Reference faulted $\phi$ and $\ln(k)$ fields: Sealing Fault Example (Case A) . . . . 161
7.2 Production data obtained for 10 wells from the reference field: Sealing Fault Example (Case A) . . . . . 161
7.3 Histograms of reference $\phi$ and $\ln(k)$ fields: Sealing Fault Example (Case A) 162
7.4 Scatterplot of reference $\phi$ and $\ln(k)$ distributions: Sealing Fault Example (Case A) . . . . . 162
7.5 Static well data for $\phi$ and $\ln(k)$: Fault Property Inversion . . . . . 163
7.6 Updated $\phi$ and $\ln(k)$ fields: Sealing Fault Example (Case A) . . . . . 163
7.7 Pressure responses computed from initial and updated $\phi$ and $\ln(k)$ fields with the true data: Sealing Fault Example (Case A) . . . . . 164
7.8 Objective function values of the inversion process: Sealing Fault Example (Case A) . . . . . 164
7.9 Fault zone $\phi$ values at each outer iteration: Sealing Fault Example (Case A) 164
7.10 Fault zone $\ln(k)$ values at each outer iteration: Sealing Fault Example (Case A) . . . . . 165
7.11 Updated $\phi$ fields at some iterations of the inversion process: Sealing Fault Example (Case A) . . . . . 166
7.12 Updated $\ln(k)$ fields at some iterations of the inversion process: Sealing Fault Example (Case A) . . . . . 167
7.13 Reference faulted $\phi$ and $\ln(k)$ fields: Sealing Fault Example (Case B) . . . . 168
7.14 Production data obtained for 10 wells from the reference field: Sealing Fault Example (Case B) . . . . . 168
7.15 Updated $\phi$ and $\ln(k)$ fields: Sealing Fault Example (Case B) . . . . . 169
7.16 Pressure responses computed from initial and updated $\phi$ and $\ln(k)$ fields with the true data: Sealing Fault Example (Case B) . . . . . 169
7.17 Objective function values of the inversion process: Sealing Fault Example (Case B) . . . . . 169
7.18 Fault zone $\phi$ values for each outer iteration: Sealing Fault Example (Case B) 170

7.19 Fault zone $\ln(k)$ values for each outer iteration: Sealing Fault Example (Case B) . . . . . 170
7.20 Updated $\phi$ fields at some iterations of the inversion process: Sealing Fault Example (Case B) . . . . . 171
7.21 Updated $\ln(k)$ fields at some iterations of the inversion process: Sealing Fault Example (Case B) . . . . . 172
7.22 Reference faulted $\phi$ and $\ln(k)$ fields: High Permeability Fault Example (Case A) . . . . . 173
7.23 Production data obtained for 10 wells from the reference field: High Permeability Fault Example (Case A) . . . . . 174
7.24 Histograms of reference $\phi$ and $\ln(k)$ fields: High Permeability Fault Example (Case A) . . . . . 174
7.25 Scatterplot of reference $\phi$ and $\ln(k)$ distributions: High Permeability Fault Example (Case A) . . . . . 175
7.26 Updated $\phi$ and $\ln(k)$ fields: High Permeability Fault Example (Case A) . . 175
7.27 Pressure responses computed from initial and updated $\phi$ and $\ln(k)$ fields with the true data: High Permeability Fault Example (Case A) . . . . . 175
7.28 Objective function values of the inversion process: High Permeability Fault Example (Case A) . . . . . 176
7.29 Fault zone $\phi$ values at each outer iteration: High Permeability Fault Example (Case A) . . . . . 176
7.30 Fault zone $\ln(k)$ values at each outer iteration: High Permeability Fault Example (Case A) . . . . . 176
7.31 Updated $\phi$ fields at some iterations of the inversion process: High Permeability Fault Example (Case A) . . . . . 177
7.32 Updated $\ln(k)$ fields at some iterations of the inversion process: High Permeability Fault Example (Case A) . . . . . 178
7.33 Reference faulted $\phi$ and $\ln(k)$ fields: High Permeability Fault Example (Case B) . . . . . 179
7.34 Production data obtained for 10 wells from the reference field: High Permeability Fault Example (Case B) . . . . . 180
7.35 Updated $\phi$ and $\ln(k)$ fields: High Permeability Fault Example (Case B) . . 180
7.36 Pressure responses computed from initial and updated $\phi$ and $\ln(k)$ fields with the true data: High Permeability Fault Example (Case B) . . . . . 181

7.37 Objective function values of the inversion process: High Permeability Fault Example (Case B) . . . . . 181
7.38 Fault zone $\phi$ values for each outer iteration: High Permeability Fault Example (Case B) . . . . . 181
7.39 Fault zone $\ln(k)$ values for each outer iteration: High Permeability Fault Example (Case B) . . . . . 182
7.40 Updated $\phi$ fields at some iterations of the inversion process: High Permeability Fault Example (Case B) . . . . . 183
7.41 Updated $\ln(k)$ fields at some iterations of the inversion process: High Permeability Fault Example (Case B) . . . . . 184
7.42 Updated $\phi$ and $\ln(k)$ fields: A Priori Fault Zone $\ln(k)$ of 1.0 and $\phi$ of 0.01 . 185
7.43 Updated $\phi$ and $\ln(k)$ fields: A Priori Fault Zone $\ln(k)$ of 1.0 and $\phi$ of 0.1 . . 185
7.44 Objective function values at each outer iteration for different a priori values 186
7.45 Fault zone $\ln(k)$ values at each outer iteration for different a priori values . 186
7.46 Fault zone $\phi$ values at each outer iteration for different a priori values . . . 187
7.47 Updated $\phi$ and $\ln(k)$ fields: 6 Master Point Case . . . . . 188
7.48 Updated $\phi$ and $\ln(k)$ fields: 10 Master Point Case . . . . . 188
7.49 Objective function values at each outer iteration for varying number of master points . . . . . 189
7.50 Fault zone $\ln(k)$ values at each outer iteration for varying number of master points . . . . . 189
7.51 Fault zone $\phi$ values at each outer iteration for varying number of master points 190
7.52 Well locations for 3, and 4 well cases . . . . . 190
7.53 Production data obtained from the reference field: 3 Well Case . . . . . 191
7.54 Updated $\phi$ and $\ln(k)$ fields: 3 Well Case . . . . . 192
7.55 Pressure responses computed from initial and updated $\phi$ and $\ln(k)$ fields with the true data: 3 Well Case . . . . . 192
7.56 Objective function values of the inversion process: 3 Well Case . . . . . 193
7.57 Fault zone $\phi$ values for each outer iteration: 3 Well Case . . . . . 193
7.58 Fault zone $\ln(k)$ values for each outer iteration: 3 Well Case . . . . . 193
7.59 Updated $\phi$ fields at some outer iterations: 3 Well Case . . . . . 194
7.60 Updated $\ln(k)$ fields at some outer iterations: 3 Well Case . . . . . 195
7.61 Production data obtained from the reference field: 4 Well Case . . . . . 197
7.62 Updated $\phi$ and $\ln(k)$ fields: 4 Well Case . . . . . 198

7.63 Pressure responses computed from initial and updated $\phi$ and $\ln(k)$ fields with the true data: 4 Well Case . . . . . 198
7.64 Objective function values of the inversion process: 4 Well Case . . . . . 199
7.65 Fault zone $\phi$ values for each outer iteration: 4 Well Case . . . . . 199
7.66 Fault zone $\ln(k)$ values for each outer iteration: 4 Well Case . . . . . 199
7.67 Updated $\phi$ fields at some outer iterations: 4 Well Case . . . . . 200
7.68 Updated $\ln(k)$ fields at some outer iterations: 4 Well Case . . . . . 201

A.1 Discretization and numbering of numerical reservoir model used in the **ssck-phi** code . . . . . 223

B.1 Porosity model for the 'base case' . . . . . 231
B.2 Relative permeability and capillary pressure curves used for the 'base case' 231
B.3 Flow responses for the 'base case' . . . . . 232
B.4 Parameter regions definition for the 'base case' . . . . . 234
B.5 Sensitivity coefficients for the 'base case' . . . . . 235
B.6 Sensitivity coefficients for the 'base case': 1 Well Case . . . . . 236
B.7 Sensitivity coefficients for different regions . . . . . 237
B.8 Effect of reporting specification on sensitivity coefficients . . . . . 238
B.9 Effect of aquifer strength on pressure sensitivity coefficients . . . . . 239
B.10 Effect of well control on pressure sensitivity coefficients . . . . . 240
B.11 Effect of temporal discretization on pressure sensitivity coefficients . . . . . 242
B.12 Effect of heterogeneity on sensitivity coefficients . . . . . 243
B.13 Effect of degree of heterogeneity on sensitivity coefficients . . . . . 244
B.14 Effect of region volume on sensitivity coefficients . . . . . 245
B.15 Effect of well location on sensitivity coefficients . . . . . 247
B.16 Parameter regions specification to study the effect of grid orientation . . . . 248
B.17 Effect of grid orientation on pressure sensitivity coefficient . . . . . 249
B.18 Sensitivity coefficients for regular parameter regions . . . . . 250
B.19 Effect of grid coarsening on sensitivity coefficients . . . . . 251

# List of Tables


1.1 Typical dynamic data and their information content . . . . . 3

4.1 Prior variogram information used for $\phi$: Example 1 . . . . . 51
4.2 Prior variogram information used for $\ln(k)$ in Example 1 . . . . . 51
4.3 Summarized responses of sensitivity exercise to initial $\phi$ and $\ln(k)$ fields . . 66
4.4 Summarized responses of sensitivity exercise to number of master points . . 68
4.5 Summarized responses of sensitivity exercise to master point locations . . . 70
4.6 Prior variogram information used in sensitivity exercise . . . . . 73
4.7 Summarized responses of sensitivity exercise to prior variography information 73
4.8 Inner optimization parameters used in sensitivity exercise . . . . . 75
4.9 Summarized responses of sensitivity exercise to inner optimization parameters 75
4.10 Variogram information used for both $\phi$ and $\ln(k)$: Stochastic Example Run 1 80

5.1 Prior variogram information used for $\phi$: Run 1 . . . . . 92
5.2 Prior variogram information used for both $\ln(k)$: Run 1 . . . . . 92
5.3 Prior variogram information used for $\phi$: Run 2 . . . . . 94
5.4 Prior variogram information used for $\ln(k)$: Run 2 . . . . . 94

6.1 Final variogram model obtained for $\phi$ after 15 iterations: Example 1 Run 1 118
6.2 Final variogram model obtained for $\ln(k)$ after 15 iterations: Example 1 Run 1 118
6.3 Final variogram model obtained for $\phi$ after 15 iterations: Example 1 Run 2 124
6.4 Final variogram model obtained for $\ln(k)$ after 15 iterations: Example 1 Run 2 125
6.5 Final variogram model obtained for $\phi$ after 16 iterations: Example 1 Run 3 128
6.6 Final variogram model obtained for $\ln(k)$ after 16 iterations: Example 1 Run 3 129
6.7 Prior variogram information used for $\phi$: High Nugget Effect Example . . . . 135
6.8 Prior variogram information used for $\ln(k)$: High Nugget Effect Example . . 137
6.9 Final variogram model obtained for $\phi$ after 7 iterations: High Nugget Effect Example . . . . . 139

6.10 Final variogram model obtained for $\ln(k)$ after 7 iterations: High Nugget Effect Example . . . . . 140
6.11 Prior variogram information used for $\phi$: Production Data Sensitivity Example 142
6.12 Prior variogram information used for $\ln(k)$: Production Data Sensitivity Example . . . . . 142
6.13 Final variogram model obtained for $\phi$ after 11 iterations: 4 Well case . . . . 143
6.14 Final variogram model obtained for $\ln(k)$ after 11 iterations: 4 Well case . . 144
6.15 Final variogram model obtained for $\phi$ after 13 iterations: 6 Well case . . . . 144
6.16 Final variogram model obtained for $\ln(k)$ after 13 iterations: 6 Well case . . 145
6.17 Final variogram model obtained for $\phi$ after 10 iterations: 8 Well case . . . . 149
6.18 Final variogram model obtained for $\ln(k)$ after 10 iterations: 8 Well case . . 149

B.1 Porosity and permeability variogram models for the 'base case' reservoir model 230
B.2 Well control history for the 'base case' simulation with four wells . . . . . 233
B.3 Well control history for the 'base case' simulation with only Well 1 . . . . . 236
B.4 Well control and event history for simulations for aquifer strength study with artificial well control . . . . . 241
B.5 Event history in study of temporal discretization on sensitivity . . . . . 241

# List of Symbols

## Common Notation

$a_s^{sl}$: flow rate associated with the streamline, $s$

$\alpha$: parameter vector involved in a forward model

$\hat{\alpha}$: parameter vector to be estimated in the inverse problem

**A**: transmissibility matrix (which accounts for spatial and time discretizations, as well as boundary conditions)

$B$: formation volume factor (res vol/std vol)

**B**: right hand side matrix in the flow equation (accounts for time discretization and flow boundary conditions)

$C_D$: covariance matrix of observed data

$C_\alpha$: covariance matrix of inversion parameters

$c_t$: total compressibility (1/psi)

**d**: a measurement of model response (nonlinear function of the parameter vector, **a**)

$d_i^{sim}$: simulated flow responses

$d_i^{obs}$: observed production data

$D^{sim}$: vector of simulated flow responses

$D^{obs}$: vector of observed production data

$\epsilon$: a very small positive number

$f$: fractional flow rate

$\mathbf{f^n}$: source/sink term in the flow equation

$\mathbf{F}$: any mathematical model used in a forward problem

$\{f\}^t$: fractional flow rate matrix at time $t$

$f_j(t)$: fractional flow rate at location $j$ and time $t$

$f'_j(t)$: induced fractional flow rate at location $j$ and time $t$ due to permeability perturbation

$f_j^{cal}(t)$: numerically calculated fractional flow rate value at well $j$ and time $t$

$f_j^{obs}(t)$: measured fractional flow rate data at well $j$ and time $t$

$f_s^{sl}(t)$: fractional flow of streamline $s$ at time $t$

**ft**: feet

$g(\mathbf{a})$: a nonlinear function of vector $\mathbf{a}$

$\Gamma(k)$: Gamma function of argument $k$

$_{GLS}$: subscript for generalized least square

$h$: thickness of the reservoir (ft)

$\mathbf{H}$: Hessian matrix

$k$: absolute permeability (md)

$\overline{k}$: average permeability

$k'$: perturbed permeability field

$\Delta k_m$: permeability perturbation due to master point location $m$

$k_e$: effective permeability

$K(r_D, t_D)$: weighting function

$L$: half domain size

$L_D$: dimensionless half domain size

$L^2$: squared norm

$\lambda$: scalar step size in minimization algorithm

$\lambda_j^0$ **and** $\lambda_j^g$: kriging weights attributed to master point $j$, cells 0 and $g$

$\lambda_1$: correlation length of maximum continuity

$\lambda_2$: correlation length of minimum continuity

$\frac{\lambda_1}{\lambda_2}$: anisotropy ratio of permeability field

$\ln(k)$: natural logarithm of absolute permeability ln(md)

$_{LS}$: subscript for least square

$m$: slope of the semilog plot

$\mu$: viscosity (cp)

$_{\max}$: maximum

$_{\min}$: minimum

$N$: number of values

$N_t$: number of time levels for simulation

$n_m$: total number of master points

$n_{mp}$: number of master points

$n_{s,c}$: number of cells crossed by a streamline $s$ from injector to producer

$n_{tf}$: number of time steps for fractional flow measurements

$n_{tp}$: number of time steps for pressure measurements

$n_{wf}$: number of wells that have fractional flow data

$n_{wf}^{sl}$: total number of streamlines arriving to well $w_f$

$n_{wp}$: number of wells that have pressure data

$\nabla$: Nabla operator

$O$: objective function

$\omega_i$: weight given to individual observation $d_i^{sim}$

$p$: pressure (psi)

$\mathbf{p^n}$: discretized pressure vector at time step $n$

$\{p\}^t$: pressure matrix at time $t$

$\Delta p$: pressure drawdown

$p_i$: initial reservoir pressure (psi)

$p_i(t)$: pressure at location $i$ at time $t$

$p_i^{cal}(t)$: numerically calculated pressure value at well $i$ and time $t$

$p_D$: dimensionless pressure

$p_i^{obs}(t)$: measured pressure data at well $i$ and time $t$

$p_{wf}$: well flowing pressure

$p(r,t)$: pressure at radial distance $r$ (ft) and time $t$ (hours)

$p(t)$: observed well pressure at time $t$

$p(\mathbf{u},t)$: observed pressure at well location $\mathbf{u}$ and time $t$

$p(\mathbf{u}',t)$: observed pressure at well location $\mathbf{u}'$ and time $t$

$p_{wf}$: well bore flowing pressure

$P_i^j, j = 1,\ldots,N_i$: calibrated relationship of facies proportion

$\frac{\partial p_i}{\partial \phi_j}$: partial derivative of $p_i$ with respect to $\phi_j$

$\frac{\partial p_i}{\partial y_j}$: partial derivative of $p_i$ with respect to $y_j$

$\phi$: porosity

$\phi_i$: porosity at location $i$

$\Delta\phi_i$: porosity perturbation due to master point at location $i$

$\overline{\Delta\phi}$: average porosity perturbation

$\Psi(k)$: Euler's Psi function of argument $k$

$q$: flow rate (STB/d)

$q(\mathbf{u}, t)$: observed well flow rate at location $\mathbf{u}$ and time $t$

$q(\mathbf{u}', t)$: observed well flow rate at location $\mathbf{u}'$ and time $t$

$q_o$: oil flow rate (STB/d)

$q_g$: gas flow rate (STB/d)

$q_w$: water flow rate (STB/d)

$q_s^{sl}$: flow rate associated with streamline $s$

$r$: radial distance from the well bore (ft)

$r_D$: dimensionless radius

$r_w$: well bore radius (ft)

$\mathbb{R}^n$: Euclidean space of $n$-tuple

$\rho$: correlation coefficient

$\rho$: correlation coefficient between porosity and log permeability

$S$: sensitivity coefficient matrix, also saturation

$s_{k,f,m,t}(j)$: sensitivity coefficient of fractional flow rate at point $j$ due to permeability perturbation at master point location $m$

$s_{k,p,m,t}(i)$: sensitivity coefficient of pressure at point $i$ due to permeability perturbation at master point location $m$

$\sigma^2$: variance

$t$: time (hours)

$t_i$: time level for simulation

$t_D$: dimensionless time

$T$: transmissibility

$\mathbf{T_{1,2}}$: transmissibility term at the face of two adjacent grid blocks 1 and 2

$^T$: superscript for transposition

$\tau_{i,j}^{\phi}$: porosity kriging weights at location $i$ for porosity data at location $j$

$\tau_{i,j}^{y}$: log permeability kriging weights at location $i$ for log permeability data at location $j$

$\tau_s$: time-of-flight of streamline $s$

$\Delta\tau_{s,c}$: associated time-of-flight for streamline $s$ to pass through cell $c$

$\mathbf{u}, \mathbf{u} \in A$: a location within the entire space, $A$

$V$: annular region

$w$: number of well locations ($w = 1, \ldots, n_w$)

$W_{1/2,1/2}(z)$: Whittaker's function of arguments $z$, 1/ 2 and 1/2

$W_f(j,t)$: weight assigned to fractional flow rate data at well $j$ and time $t$

$W_p(i,t)$: weight assigned to pressure data at well $i$ and time $t$

$_{WLS}$: subscript for weighted least square

$x, y, z$: dimensions of cell (Cartesian coordinate system)

$\xi_i$: log permeability collocated kriging weights at location $i$ for porosity data at location $i$

$\Delta x, \Delta y, \Delta z$: set out changes in cell dimensions

$y$: $y = \ln(k)$

$y_i$: $y$ variable at location $i$

$\Delta y_i$: log permeability perturbation due to master point at location $i$

$\overline{\Delta y}$: average log permeability perturbation

$\frac{\partial y_i}{\partial \phi_j}$: partial derivative of $y_i$ with respect to $\phi_j$

$\frac{\partial y_i}{\partial y_j}$: partial derivative of $y_i$ with respect to $y_j$

## Acronyms

**CPU:** central processing unit

**GPST:** generalized pulse spectrum technique

**mNAD:** mean normalized absolute deviation

**mNE:** mean normalized error

**pdf:** probability density function

**SGI:** Silicon Graphics, Inc.

**SSC:** sequential self-calibration

**STB:** stock tank barrel

# Chapter 1

# Introduction

An essential element for successful reservoir management is the ability to reliably forecast the reservoir performance with as little uncertainty as possible. Predicting reservoir performance depends mainly on two aspects among myriad of factors. First, one must be able to identify the physics of the subsurface flow and adequately engineer a mathematical model to simulate such phenomena. Second, one must have 'appropriate' characterization of the reservoir through some discretized numerical reservoir models. This thesis focuses primarily on the latter aspect. Incomplete data and inability to model the physics of fluid flow at a suitably small scale lead to uncertainty. Subsurface reservoir models that "by construction" honor the historical production data should yield significantly more accurate predictions of reservoir performance with reduced uncertainty than those that do not. This research aims to develop new techniques that link available production data and static information on the distribution of permeability and porosity in reservoir models.

The motivation for this research was the recognition that there is strong need for improvement in the available techniques of dynamic data integration to construct realistic reservoir models. Current modeling techniques suffer from the limitation of not accommodating realistically complex heterogeneities of the subsurface reservoir system. Incorporation of simplistic physics and homogenization of critical reservoir features are still the only way to resolve this reservoir characterization problem. The reason for adapting such naive approaches is not the lack of motivation, but the problem is an inverse problem and highly underdetermined.

This research does not search for a panacea of this long-standing issue in reservoir characterization; this attempts to incrementally improve upon the current techniques. Undertaking of this research evolved through a "roller-coaster" learning experience corroborating the presence of enormous difficulties associated with the inverse problem. Ideas had to be modified at different stages and the scope of the work had to be narrowed to accomodate practical problems.

## Problem Description

Reservoir development plan using detailed 3D reservoir models requires models of structure, stratigraphy, and properties. Interpretive, deterministic and geostatistical techniques for constructing models of lithofacies and properties are used that constrain the models to static data from core, logs, seismic, and geologic interpretation. However, honoring all data including the dynamic pressure or historical production data is quite difficult. In

practice, trial-and-error history matching is still the most common approach at the final stage of modeling. The problem of fully integrating production and pressure data in the construction of reservoir models lends itself to a variety of approaches. Property models within the volume of influence of a well are generated through a one-step mathematical inversion of the pressure response. The problems with these techniques are the intense computations needed to generate a solution that is not unique and may be inconsistent with some of the static data. In other approaches, the property models are generated in several steps with a first-step coding of the well-derived data into a spatial property representation. A detailed classification of the techniques available for dynamic data integration is discussed in Chapter 2.

## 1.1 Data Used in Reservoir Characterization

In the broader sense, available data [179] for reservoir characterization can be classified into geological data, geophysical data, and engineering data. Geological data arises from a variety of sources including core description, thin sections, microscopes, image analysis, X-ray tomography, stable isotope analysis, sedimentological models, diagenetic models, markers, interval definitions, maps, cross-sections, and remote sensing. Geophysical data available for reservoir characterization can be from 2D and 3D seismic profile, cross-hole tomography, multi-component seismic, vertical seismic profile, shear wave logging, and isochrons for structure tops. Sources of engineering data include well log analysis, conventional and special core analysis, pressure transient tests, production history, tracer test, CT scan, NMR data, and drilling and completion information.

The primary objective of this research is integration of dynamic data in reservoir modelling. The subsequent section describes dynamic data available for reservoir description.

## 1.2 Dynamic Data and Spatial Information

Different sources of data have varying type and amount of information about the reservoir heterogeneity. Each data type has the potential to inform us about some subset of spatial characteristics. Scale and the support volume of the different data sources also vary. The spatial representations from some important data types and some issues concerning our ability to extract these spatial data are listed below. Table 1.1 gives the information content of some important data sources.

Mathematical inversion methods for single well test pressure data and interpretive tools are largely in place [70, 101, 163, 177]. This is perhaps the subject of most well test analyses research. Well test interpretation is a standard reservoir engineering practice. Some of the typical single-well test data are RFT data, drawdown/buildup test data, variable rate test data, production logs and permanent pressure gauges. For instance, interpretation of RFT data is quite useful particularly for decisions like production strategy, change in well configurations, well workovers or perforation jobs.

Compared to single-well test data, multiple-wells test data are more extensive in terms of areal coverage and provide specific connectivity information between wells. Data sufficiency, i.e., whether sufficient data are available to establish significant contributions, is an important issue. Suitable method to quantify connectivity between two locations is imperative. The approach of geo-objects, collections of locations/blocks connected to each other,

| **Data Available** | **Information Content** |
|---|---|
| Pressure as function of depth (e.g., Repeat Formation Tester ) | - Communication between strata<br>- Communication across faults<br>- Location of fluid contacts |
| Buildup/drawdown test $p(t)$ | - Distance to boundaries<br>- Effective $kh$<br>- Flow regime (e.g., fractures)<br>- Aquifer influx/fluid extent |
| Multirate test data | - More details |
| Production logging ($q$(depth)) | - Permeability of different layers/strata (ratio or "relative" $k$ between layers) |
| Permanent pressure gauges ($p(t)$, $t$ from 0 to present) | - $kh$ for coarse grid or information between wells<br>- "Map" interwell region<br>- Boundaries and interwell communication |
| Interference tests $p(\mathbf{u},t)$, $q(\mathbf{u},t)$ and $p(\mathbf{u}',t)$, $q(\mathbf{u}',t)$ | - Presence of sealing faults<br>- Fault transmissibility<br>- Qualitative measure of connectivity<br>- Effective $k$<br>- Flow/pressure pathways |
| Tracer data | - More unique model<br>- Tell how a well is isolated or connected with other wells |
| $P$, $q_o$, $q_g$ as functions of dimensionless time at each well | - $kh$ at each well (relatively larger areas)<br>- Drainage volume for each well<br>- Local facies information indirectly through $k_{ro}/k_{rg}$ ratios<br>- $\overline{k}_{coarse\ scale}$ effective permeability<br>- Interwell communication from fractional flow/pressure data |

Table 1.1: Typical dynamic data and their information content.

is used for this purpose.

According to existing dominant production mechanisms, historical production data may also be classified into different categories. The classification can be with respect to reservoir depletion with or without water drive, with gas-cap drive, water injection or gas injection. Dynamic data integration technique in each of these reservoir cases has unique implementation issues.

Expansion drive and gravity segregation drive are the main sources of reservoir potential for many reservoirs. Estimation procedure of drainage volume for each well should be properly devised. Relative permeability ratios (gas to oil), $\frac{k_{ro}}{k_{rg}}$, may also explain something about the lithofacies proportions within drainage area, since different facies usually have different $\frac{k_{ro}}{k_{rg}}$ ratios. One can have GOR data that provide useful information on reservoir heterogeneities.

Before breakthrough of water, no new information on the spatial distribution of heterogeneities than that from single- or multiple-well test data is available. The data reveal almost the same information as in the case of depletion without water drive. After water breakthrough fractional recovery data ($q_w$, $q_o$) are available. Original water contact data (e.g. surface-point connectivity), $\overline{k}_{coarse\ scale}$ effective permeability distribution may be obtained from the available data. Also, $\frac{\overline{k}_{ro}}{\overline{k}_{rw}}$ may indicate facies proportions in the "contacted region".

These data are similar to those available from water-drive depletion, except between production wells and original gas-cap, instead of aquifer. Interwell connectivity data and the stratigraphic surface correlation can be established. Fractional recovery data ($\frac{k_{ro}}{k_{rg}}$) may indicate facies proportion.

More definitive determination of $\overline{k}_e$ between wells, particularly after breakthrough, is possible. Flow capacity ($kh$) around injection wells, connected volume between injector/producer pairs can be estimated. Breakthrough times may explain anisotropic variogram, interwell facies connectivity, and permeability distribution. Measurement of heterogeneities, calibration and calculation of connected volume from the 3D reservoir model are crucial issues.

## 1.3 Outline of the Thesis

In this thesis, the topics are presented in the following sequence. Chapter 1 introduces the problem and describes various sources of information. Chapter 2 discusses the available literature. Chapter 3 briefly relates the inverse problem formulation, the mathematics of the inverse problem, some elements of production data integration. The material covered in this chapter is generic in nature, and not an original contribution of this research. Chapter 4 relates the algorithm developed for the simultaneous inversion of porosity and permeability. Some illustrative examples as well as sensitivity issues are discussed. Chapter 5 describes the inversion of a reservoir with unique features. Discussion on some influential parameters on inversion is also given. Chapter 6 discusses the implementation of the data integration algorithm with variogram updating. Variogram uncertainty analysis with this piece of code is discussed here. Chapter 7 relates the inversion algorithm for fault properties. Finally, Chapter 8 gives an overall discussion on the scope of this research. Future recommendations are also laid out in this chapter. There are also three appendices. Appendix A briefly describes the parameter files for codes implemented. Appendix B is an independent study

on the information that can be obtained from sensitivity coefficients. Appendix C describes the mathematics of incorporating pressure derivative mismatch in the inversion algorithm.

# Chapter 2

# Literature Review

Production data integration is an inverse problem, that is, a parameter estimation problem. The dynamic production data contain important information about petrophysical properties such as permeability, porosity. Any reliable reservoir characterization study should account for these dynamic data. The objective here is to generate reservoir models that reproduce these dynamic together with static data and measures of spatial continuity.

The classification of the techniques presented in this review is subjective. The chronology of the methods, their distinctness and salient aspects were the criteria for the classification. The methods overlap, which would be true of any classification scheme. A common aspect of almost all the approaches is the formulation of a misfit or mismatch function and the application of a minimization algorithm. Furthermore, in many formulations, the problem is ill-posed. The solution space (model space) is not unique. There are many solutions, an infinite number for most inverse problems of interest, within the solution space. A natural consequence in many of these techniques is an effort to make the problem well-posed, or in mathematical parlance, regularized.

A thorough review of the subject of parameter identification in reservoir simulations is also given by, for instance, Jacquard and Jain [108], Gavalas et al. [78], Watson et al. [200], Feitosa et al. [75, 76], or Oliver [149]; and by Yeh [216] and Carrera and Neuman [27] in groundwater hydrology.

## 2.1 Classical Inversion Techniques

Early approaches to the integration of pressure transient data used inverse techniques for parameter identification or history matching. The most elementary approach to tackle this kind of problem is the trial and error method. Because of its simplicity in formulation, trial and error methods are still widely used for history matching. Such methods require significant professional and computation time.

Automatic history matching addresses this inverse problem. The objective of history matching is to estimate reservoir petrophysical parameters from pressure and/ or flow rate data [45, 72, 84, 109, 157, 186]. Most methods are based on the premise that the best spatial distribution of reservoir parameters minimizes the difference between observed and calculated pressure data at well locations. These techniques seek direct spatial distributions of reservoir parameters that honor the pressure measurements through pressure response simulation.

Most automatic history matching techniques are based on gradient method or streamline based methods [71]. One of the important aspects of gradient based history matching techniques is computation of the gradients or sensitivity coefficients. Schemes like perturbation methods, rigorous finite differencing of the physical flow equations [5, 18, 19], convolution integral method [30, 108], optimal control theory [33, 34, 199, 200], have been utilized. The method of Anterion et al. [5] is now commonly referred to as the gradient simulator method. Up to 1972, most of the work done was based on perturbation methods. In perturbation-based methods, the gradients are calculated by first making an initial simulator base run and then repeating the simulator run after perturbing each parameter to be estimated. In the finite difference based approaches, the sensitivity coefficients are derived by setting up new equations from the original partial differential equations describing the physical flow system; the new set of equations are then finite differenced. A close alternative approach to this is to derive the gradients directly from the finite-difference form of the physical flow equations. The convolution integral method is applicable only for linear problems, in which case, it is actually equivalent to the adjoint (optimal control) method. Optimal control theory based methods use the system of equations as equality constraints for the minimization problem of the misfit function with the unknown parameters serving as control variables.

## 2.2 Regularization Based Techniques

The inverse problem is often ill-posed partly due to the lack of continuous dependence, that is, small variation in data may result in unbounded changes in the model estimates, and also to the non-uniqueness of the solution space, which means more than one estimate can satisfy the same set of observed data [181, 214, 216]. To tackle the stability and efficiency problem, a versatile technique was devised by Tsien and Chen [194]. Since its inception in 1974, the technique has been subsequently modified and improved further by Chen and his colleagues [37, 38, 39, 89, 132, 133]. Essentially the Generalized Pulse-Spectrum Technique (GPST) is a combination of a Newton-like iterative algorithm and the Tikhonov regularization method. The capability of GPST has been demonstrated in performing history matching for one-dimensional single-phase reservoir simulators in [36], for two-dimensional single-phase simulators in [131] and for two-dimensional two-phase models in [187]. Hierarchical multigrid approach, in which the estimation is performed on successively finer grids until convergence is reached, is applied to improve the efficiency of GPST further [35, 40]. Landa et al. [123] used a similar technique to integrate well test, production, shut-in pressure, log, core, and geological data.

Another promising numerical method based on regularization techniques proposed by Kravaris and Seinfeld [117, 118, 119] appears particularly suitable for two-dimensional single-phase simulator models [126] and for two-phase models [127]. These methods apply Tikhonov regularization method first and then the well-posed problem is solved by the partial conjugate gradient method of Nazareth [143]. Cubic spline function is used in these methods to approximate the unknown parameters. Makhlouf et al. [135] extended this numerical algorithm to estimate absolute permeability in multiphase, multi-layered petroleum reservoirs based on noisy observed data, such as pressure, water cut, gas-oil ratio and rates of liquid and gas production from individual layers.

Both these groups of techniques do not require any *a priori* information on the parameters to be estimated.

## 2.3 Bayesian Estimation

A Bayesian estimation framework was proposed by Gavalas et al. in 1976 [78] for reservoir modeling using dynamic production data. The underlying theory behind this technique is to reduce the statistical uncertainty by using additional prior information, for instance autocorrelation and mean values of permeability and porosity. Shah et al. [181] showed that if reliable prior information about permeability or porosity is available, Bayesian estimation will improve the variance of the estimation error. Similar Bayesian approach was used much later by the workers at the Norwegian University of Science and Technology to integrate historical production data [95, 193]. The problem of integrating production data is formulated in a lower dimensional parameter space where, for the sake of mathematical tractability, the parameters are often assumed multivariate Gaussian.

Neuman and Yakowitz [145] used an extended Bayesian approach to estimate actual values of transmissivity in two dimensional study and covariance functions. Clifton and Neuman [44] demonstrated the importance of jointly inverting permeability and pressure data through conditional simulation. They found that the conditioning effect of the pressure data in a full inversion is much greater than that of kriging.

Cooley proposed a method to incorporate prior information having unknown reliability into the nonlinear regression model by adding a penalty function [46]. The resulting composite objective function consists of two terms: the weighted sum of squared errors in the pressure and the sum of weighted errors in the parameters. Dagan [49] used an *a priori* selected analytical technique and Gaussian conditional mean for the inverse problem.

Maximum likelihood methods [26, 27, 28, 29, 74] have long been used for parameter estimation with dynamic data. This is a general non-linear technique that estimates reservoir parameters using prior estimates along with transient or steady state pressure data. Early development of this method is presented in Carrera and Neuman [27, 28] and Feinerman et al. [74]. Parameter estimation is performed using the maximum likelihood theory, incorporating the prior information into the likelihood function. The nonlinear flow equation is solved by a numerical method. Both steady-state and transient pressure data can be integrated into the model; however, this method is computationally intensive.

Oliver [149] used Gauss-Newton method to obtain the maximum *a posteriori* estimate (mean and covariance) that minimizes the objective function derived directly from the *a posteriori* probability density function. Multi-well pressure data and prior information are honored in this technique, however, at each iteration of Gauss-Newton method, the forward problem is solved using a reservoir simulator. Chu et al. [42] presented an efficient method of computing sensitivity coefficients required in the approach. This method yields a smoothed version of the true distribution. Conditional realizations with given variability are constructed using Cholesky decomposition of the covariance matrix estimated by assuming that permeability distribution is Gaussian and pressure data is a linear function of permeability. Reparameterization based on spectral decomposition reduces the number of the parameters to be estimated by the Gauss-Newton procedure [149]. More recently, a reparameterization technique based on subspace method was presented to further improve the computational efficiency in the Gauss-Newton procedure by Reynolds et al. [170]. He et al. [93] extended this method for a three dimensional reservoir model. In another effort, the same authors [92] developed a multistep procedure to generate reservoir models conditioned to well test data. The ensemble realizations by this method provides a good empirical approximation to the posteriori probability density function for the reservoir model, which

can be used for Monte Carlo inference. Oliver et al. [152] presented a procedure to approximately sample the pdf of a model conditional to production data. They pointed out that it is important to generate a suite of realizations which reflect a proper sampling in order to characterize uncertainty in reservoir description and reservoir performance predictions. Abacioglu et al. [1] applied a similar technique to a field example in estimation of heterogeneous anisotropic permeability fields from multiwell interference.

He and Chambers [91] implemented a method based on Bayesian estimation technique with restricted-step Gauss-Newton method and an extension of Carter's method for sensitivity coefficients. The approach updates permeability, porosity and skin factor based on individual simulation cells, geological features, or on constant multipliers applied in well-test radius of investigation.

Wu et al. [208, 209] developed a discrete adjoint method for generating sensitivity coefficients related to two-phase flow production data. The method directly generates the sensitivity of the calculated data to the model parameters. Using these sensitivity coefficients, an efficient Gauss-Newton algorithm is applied to generate maximum a posteriori estimates and realizations of the rock property fields. Wu [206] presented another new iterative algorithm for building reservoir models conditioned to multiphase production data and geostatistical data. This approach avoids computation of sensitivities relying on solving the inversion equations through functional extremum.

Oliver et al. [151] presented Markov Chain Monte-Carlo methods to condition a permeability field to pressure data. Cunha et al. [47, 48] used a hybrid Markov Chain Monte-Carlo algorithm to generate realizations of permeability conditioned to prior mean, variance and multiwell pressure data. These realizations represent samples from the correct a posteriori probability distribution.

Srinivasan and Caers [182] implemented a Markov Chain Monte-Carlo algorithm to integrate permeability connectivity information caontained in the flow response data. Prior to integrating the response data, a neural-network based procedure is used on these data to filter out the connectivity information.

Rogerro [171] used a Bayesian inversion technique and an efficient optimization algorithm to integrate multiple well historical data and prior geostatistical information. The procedure permits direct selection of constrained realization.

## 2.4 Zonation Methods

All numerical reservoir characterization models, irrespective of static or dynamic nature, should fall into this category inasmuch as the original problem is infinite-dimensional but is modeled by a finite number of parameters. Notwithstanding this fact, the subsequent methods have been grouped in this category because of emphasis of the zonation approach.

Some of the early methods [27, 44, 71, 108, 145] have already been grouped as the classical techniques for a historical perspective. While the zonation method is effective in reducing the number of unknowns, sufficient *a priori* information is not usually available to enable specification of the zones on any physical basis. Zonation methods are active research area. Amongst the newer methods are pilot point method, sequential self-calibrated method, and others.

Pilot point method [55, 125, 168] is a zonation method that starts by simulating a conditional transmissivity field. The generated field is then modified by adding additional or fictional transmissivity data at some selected locations, termed pilot points, to improve

the calibration of the pressure data. Adjoint sensitivity analysis is used to determine the locations where additional transmissivity data should be included [124]. The additional transmissivity data at the pilot points are treated as local data, a new conditional realization of transmissivity is then generated, and, the flow model is run again. The iteration of adding pilot points is continued until least-squared error criterion is met or the addition of more pilot points does not improve the calibration. This method is, however, computationally expensive and cannot efficiently handle pressure data from multiple hydraulic tests at different times. Fasanino et al. [73] applied this model in inverse modeling of a gas reservoir. Bissell et al. [17] evaluated pilot point method to an alternative gradzone method, where groups of grid cells in the model are modified.

Sequential self-calibrated method [25, 81] combines geostatistical and optimization techniques. A geostatistical technique is used to generate a reservoir parameter model conditioned to local measurements of parameters. The initial model is modified to minimize the misfit function through an optimization procedure. In order to reduce the parameter dimension, the optimization is parameterized as a function of the perturbations of permeability at a few selected locations, called master points. The perturbation values at the master locations are determined from the optimization procedure by minimizing the squared difference of the simulated and observed pressures. The resulting perturbations are propagated throughout the entire reservoir domain by kriging to obtain the perturbation field that is subsequently added to the initial field. The flow equation is linearized to obtain fast solution in the optimization process. An iterative process is used in order to avoid the errors in the linear approximation of the flow equation, that is, the modified reservoir model is input again into the reservoir simulator and new perturbation values calculated until the actual solution of pressure from the numerical reservoir simulator is close to the observed data. This approach accounts for measurement errors in the data and the uncertainty in flow boundary conditions. It is computationally efficient. Promising results were obtained by using this approach in groundwater hydrology [201, 203, 204, 219].

Blanc et al. [20] presented a solution to the problem of constraining geostatistical models by well test pressure data similar to the pilot point method or sequential self-calibrated method. In this method, a well test simulator is coupled with a nonlinear constrained optimization program for an inversion loop so that a set of optimal facies or rock-type properties and well-skin that give best fit between the simulated and measured pressure data are obtained. Sensitivity coefficients are computed numerically, and in each iteration, full numerical solution of well test pressures are computed by a well test simulator. The method is thus computationally inefficient.

Xue and Datta-Gupta [211] developed a two stage approach similar to pilot-point technique but incorporated the prior information in a different way. The covariance matrix is embedded in the parameterization of the permeability field.

## 2.5 Cokriging Based Methods

Kitanidis and his colleagues [99, 116] applied cokriging to simulate transmissivity and pressure fields using covariance or cross-covariance models based on field measurements of transmissivity and pressure. The cross-covariance between transmissivity and pressure is developed through linearization of the single phase steady state flow equation. Parameters in the covariance and cross-variance are estimated from the measured data and the linearized flow equation using a maximum likelihood method. Realizations are then con-

structed using Cholesky decomposition of the covariance matrix. Cholesky decomposition is computationally efficient only for small problems. However, the steady-state pressure data are reproduced only under the assumptions that the relationship between transmissivity and pressure is linear which is valid only for small variance of transmissivity, the permeability distribution is Gaussian, and flow is uniform.

In linearized semi-analytical cokriging method [175, 176], a linearized form of the single phase steady-state flow equation is used to develop analytical expressions of cross-covariances of permeability and pressure assuming uniform flow and infinite domain. Transient pressure is accounted for with the linearity assumption between change of pressure and time.

Harvey and Gorelick [88] presented a cokriging method, combining numerical simulation of flow and tracer transport with a linear estimation, to construct permeability field that sequentially accounts for permeability, pressure and tracer arrival times. Integrating tracer arrival time data improves the accuracy of the permeability estimation. Tracer arrival time quantiles are found to be robust indicators of flow paths and flow barriers.

Yeh et al. [215] applied a similar but iterative technique to account for the nonlinear relationship between permeability and pressure in the estimation through successive linear approximation. It first estimates a permeability field by cokriging from the available permeability and steady-state pressure data. The flow equation is then solved numerically to obtain a pressure field, which is computationally intensive. The covariance and cross-covariance of permeability and pressure are then updated and a new permeability field can be obtained by again cokriging using the updated covariance and cross-covariance. This process is continued until the variance of estimated permeability stabilizes.

In another cokriging based method, fast Fourier transform method [85, 86] is applied to the linearized steady-state flow equation. Transmissivity and pressure perturbations are represented in the spectral domain as Fourier integrals in two dimension. The covariance and cross-covariance are represented as functions of the spectral and cross-spectral density. Transmissivity realizations conditioned to the pressure data are constructed by adding the difference between the unconditional simulation and kriged values of the unconditional simulation to the kriged values using the field data [56, 113]. This method is computationally fast when there are a large number of pressure data.

Huang et al. [106, 107] integrated time-lapse seismic and production data in reservoir characterization. The uncertainty was quantified by the statistics on reservoir-scale 3D acoustic impedance blocks. Using collocated cokriging the impedances were transformed into reservoir parameter through a petrophysical relationship while respecting the well information. The results are finally transferred from the time domain to a spatial one for flow simulation.

Hu et al. [102] proposed a new kriging algorithm to estimate lithofacies proportions in well test areas of investigation. Method consists in kriging jointly the proportions of all lithofacies in the area through a weighted power averaging of lithofacies permeabilities. For multiple well tests, an iterative process is used to account for their interaction.

Srinivasan and Journel [183] interpreted well test derived effective permeability as linear average of small scale permeability values indexed with a power. A kriging on the power transformed permeability fields followed by an inverse power transform allows generating estimated permeability fields over the drainage area.

## 2.6 Simulated Annealing Based Techniques

Deutsch [59, 60, 64] was among the first to present an approach, based on simulated annealing, that integrates well test-derived effective permeabilities in stochastic reservoir models. Some practical considerations are discussed by him and his colleagues [61, 62]. Ouenes and his colleagues [155, 156, 184] employed simulating annealing for automatic history matching. Petrophysical and reservoir engineering parameters are estimated through an automatic and multiwell history matching using simulated annealing method. A least-square error objective function defined by the oil, gas, and water productions at each well is minimized by the simulated annealing method. At each iteration in the simulated annealing method, a limited number of reservoir parameters are adjusted. The impact of these new parameters on the objective function is evaluated by forward reservoir simulation, which is too costly for routine application for large number of parameters and iteration steps used in this approach.

In another simulated annealing approach proposed by Tauzin [189], the objective function is evaluated analytically which improves the computational time. An analytical influence function is defined to approximate the perturbation on the pressure transient due to a local heterogeneity. This influence function is derived from the analytical solution of transient pressure in an infinite homogeneous reservoir containing a single circular discontinuity from Rosa and Horne [174]. This approximation is usually sufficiently accurate to predict the direction and the order of magnitude of the pressure perturbation caused by the permeability perturbation.

Tracer data reveal important information on the interwell connectivity. Datta-Gupta et al. [53, 54] sequentially applied the simulated annealing method to account for both pressure and tracer data in the construction of reservoir permeability model. A semi-analytical transient time algorithm was used for fast calculation of tracer travel time in the simulated annealing [51]. Vasco et al. [196] attempted to integrate multiphase production history data using 3D multiphase semi-analytical streamline model based on simulated annealing technique. Kulkarni and Datta-Gupta [120] employed a streamline based approach to estimate relative permeability information from production data. Application of streamline based production data integrating approaches can be found in the literature [121, 195, 198]. Yoon et al. [217] developed a streamlined-based multiscale approach to data integration accounting for varying resolution of different data types.

Maroongroge et al. [137] investigated the effectiveness of vertical tracer profiling for determining reservoir zonation. Tracer history is used to condition the permeability model using a simulating annealing method and a least square history matching method. Conditioning to tracer history substantially constrains the model and it is particularly important when the horizontal variogram is unknown. The use of vertical tracer profiling can substantially improve the results compared to the case when the integrated breakthrough curve is used. However, this would be quite difficult and costly to implement in the field.

## 2.7 Two-Step Approaches and Indirect Methods

Production data can be used to estimate statistical parameters, such as the mean, covariance, or the fractal dimension that describe the spatial distribution of reservoir properties. These parameters are subsequently used to characterize the reservoir.

These indirect techniques seek to construct geological models that honor critical features

interpreted from the production data. Some relationship is first established between the production data and some reservoir parameters or their spatial variation. This relationship then serves as a constraint in the construction of the geological model so that the production data are indirectly integrated into the reservoir model. The first step is to analyze transient production data and infer spatial heterogeneity features of the underlying reservoir model. These heterogeneity features may be in the forms of general information on the degree of heterogeneity, anisotropy and zonation of the reservoir properties; the presence of internal or external reservoir boundaries such as faults, lithofacies changes, water-oil contacts, stratigraphic pinchouts; the presence of high flow channels or low permeable zones in an area and the distance to these zones; in multiple well systems, water breakthrough time and recovery efficiencies inform connectivity between wells; effective transmissivity and facies proportions in the well bore vicinity, etc.

Chang et al. [32] give an example of the connection between different engineering data including well test data, production data, production performance data, hydrogeochemical data and the geological model. Lord and Collins [134] implemented an approach to detect compartmentalization in gas reservoirs using production data. Vashist et al. [197] and Bard et al [9] implemented integrated approaches for carbonate reservoir charcterization. Bandiziol and Massonnat [8] integrated pressure transient test and geological data for horizontal permeability anisotropy characterization. Head et al. [94] used multiple probe pressure data for reservoir anisotropy determination. Other references on integrated approaches include [24, 90, 128].

Yadavalli et al [212, 213] used pressure transient data from single or multiple sets of well tests to estimate permeability variograms, and they were able to obtain reliable horizontal variogram models in cases where no information is available on the short scale structure of the variogram. Chang and Yortsos [31] and Beier [12, 158] showed that pressure transient field data could indicate fractal reservoir structure and the parameters of the fractal model. Grindrod and Impey [82, 83] also estimated fractal geometry parameters from permeability and pressure data using a maximum likelihood method.

Once the statistical parameters are estimated, they are used in geostatistical techniques to construct reservoir models. The contribution of production data lies in the improvement in the estimation of statistical parameters describing the reservoir heterogeneity. In some cases, such as when the reservoir parameters are Gaussian, and the relationship between the reservoir parameter and pressure data are linear, the constructed geostatistical reservoir model may also directly honor the pressure data.

Effective permeability within the drainage area of the well obtained from well test data [101, 177] does not resolve local details of the spatial distribution of permeability. However, welltest-derived effective permeability can be regarded as the average value of the heterogeneous permeability values in the vicinity of the test well [2, 146]. Deutsch [59, 64, 65, 66, 67] presented an approach, based on simulated annealing, that integrates well test-derived effective permeabilities in stochastic reservoir models. The volume and type of averaging formed by the well test are first calibrated by forward simulating the well test on a number of stochastic reservoir models that are consistent with the geological interpretation, core, well log, and seismic data. Ranking of the inverted models are considered in some studies [68]. Scale and precision of seismic data in the reservoir models are considered by Deutsch et al. [69]. The effective permeability from the well-test is assumed to be the power average of the heterogeneous permeability within the influence volume of the well test [2]. The optimal volume and power parameter for the averaging process are obtained from the calibration as

suggested by Alabert [2]. Stochastic reservoir models are then constructed with simulated annealing to honor the well-derived average permeabilities. Results showed the improvement in characterizing permeability heterogeneity and waterflooding predictions when the effective permeabilities are constrained in the model.

A similar approach was presented by Sagar et al. [178] but using a geometric average of permeability values within the influence region. The approach of Deutsch was extended by Tauzin [189] to directly integrate the pressure transient data using a simple analytical algorithm based on Rosa and Horne [173, 174] to quickly evaluate the objective function due to the single perturbation of permeability.

Hird et al. [97, 98] used reservoir connectivity parameters as indirect well-performance constraints in the conditional simulation of a stochastic reservoir model. Reservoir connectivity parameter was defined by a functional relationship between fractional area connected and permeability percentile cutoffs. This connectivity parameter is found to be strongly correlated to the well performance, such as secondary recovery efficiency, drainable hydrocarbon pore volume, floodable hydrocarbon pore volume and also water breakthrough time. Based on a strong correlation between the spatial reservoir properties and the reservoir performance, they suggested use of the connectivity parameter to constrain the reservoir model using simulated annealing. Alabert and Modot [4] also defined connectivity of a permeability field in terms of the connected pore volume.

Holden et al. [100] presented an approach to indirectly account for well test data to improve the simulation of lithofacies and petrophysics under the framework of two-stage stochastic simulation as suggested by Haldorsen [50, 87]. Using an analytical tool, the pressure data is used to estimate pressure support and then the shortest distance from the well to a possible channel boundary, connection between two wells by a high permeable zone and channel geometry. The channel structure is then simulated using these interpretations with a marked point process model. Average permeability in the part of the channel intersected by the well is estimated from the well test data. The permeability field was then generated together with the core/ log data using stochastic Gaussian model. Alabert and Massonnat [3] used well test data to infer information on channels and lobe dimensions in addition to average permeability.

Britto and Grader [23] applied transient pressure data to identify local impermeable regions or high-flow channels. Vashist et al. [197] presented a technique for defining reservoir facies that incorporates the geological features of deposition and diagenesis with the dynamic flow capacity (kh) of the reservoir. The ranges of permeability for different reservoir facies are determined through multiple regression analysis based on their dynamic flow capacity (kh) data in tested wells.

Benkendorfer et al. [13] presented a different approach to indirectly integrate production data using a two-step approach. That is, the permeability values estimated from well-test data are regarded as the sum of a core-based permeability and a large-scale permeability due to fractures and leached zones. The core-based permeability and the large scale permeability are constructed separately. The final model is the sum of the two models. This two-step approach is applicable when a significant difference exists between core-based permeability and production-scale permeability.

Feitosa et al. [75, 76] presented a new inversion solution, called Inverse Solution Algorithm (ISA) based on Oliver's perturbation solution [146]. The algorithm generates a smoothed approximation to the true permeability field as a function of distance from the well. Based on the pressure data from draw down and buildup tests, the absolute perme-

ability is estimated as a function of distance from the well [76, 147], or a function of both distance and angle from the well.

Huang and Kelkar [105] presented a procedure for integrating three dimensional seismic data and production data to develop a detailed reservoir description. Impedance distribution is constructed by the inversion of the seismic data, then porosity field, consistent with the impedance data, is simulated, and finally permeability field, consistent with porosity and dynamic well test data, is constructed. The initial permeability field is then perturbed randomly until the simulated well test data match the measured data. Forward simulator is used to calculate the pressure or flow rate response after each perturbation of permeability, thus it is computationally inefficient. To improve the efficiency, for a highly correlated porosity and permeability, the bounds of perturbations can be narrowed. The same authors, in another paper [104], discussed dynamic data integration in frequency domain. The spatial relationship-variogram is represented by power spectra and self-correlation in the frequency domain. Huang et al. [103] also explore the impact of dynamic data integration in the uncertainty of prediction of the multiphase systems.

Deng [57] and Deng and Horne [58] presented an analytical approach to interpret pressure and tracer data from multiple wells simultaneously to characterize the two dimensional permeability distribution in heterogeneous reservoir. The correlation between permeability and dispersivity is sought, and the convection-dispersion equation and diffusion equation to a system of first-order equations in permeability are reformulated. The system of equations is then solved to yield the permeability distribution for appropriate boundary conditions.

Several other authors have examined the sensitivity of transient pressure response to the spatial distribution of permeabilities, such as McElwee [139] and Sykes et al. [185]. The pressure response for a multirate test was found more sensitive to reservoir heterogeneities than a single flow rate test [173]. The effectiveness of the data in estimating local-scale permeability can be measured by its spatial resolution [51, 148, 150]. The higher the resolution of a data to a given parameter, the more information this data carries on the spatial variation of the parameter. Datta-Gupta et al. [51] used the concept of a resolution matrix to give information on the spatial averaging involved in the parameter estimation due to limited sampling, as well as quantitatively evaluate the relative worth of additional data. The resolution of pressure data in constraining local permeability variations in heterogeneous media is limited. Oliver [150] showed that interference tests are generally more effective than single-well tests at improving the resolution. On the other hand, interwell tracer data can be very sensitive to local heterogeneities [52, 58]. Also, both transient pressure data and tracer data appear to resolve flow barriers better than flow channels [51].

Wu and Datta-Gupta [207] proposed a travel time inversion method for production data integration based on seismic waveform imaging. The method minimizes a 'travel time shift' at each well derived by maximizing the cross-correlation between the observed and calculated production response. An optimal control method via a Gauss-Newton method is employed to compute the sensitivity of the travel time with respect to reservoir parameters.

Rahon et al. [165, 166, 167] developed geological shape inversion technique with improved gradient computation. The devised method is capable of identifying the limits of the reservoir, position of the faults, thickness and dimensions of channels. Geological shapes are modeled by triangulation as a 2D or 3D surface. A finite element structure is associated to each object and the Cartesian coordinates of the nodes in this triangulation are matched in the inversion process.

Jensen and Kelkar [111, 112] employed cross-correlation between pairs of production

wells to determine the inter-well relationships, preferential flow directions and flow barriers. They incorporated Wavelet transformation tools in reservoir characterization technique in the form of a better search neighborhood definition. In an earlier paper [110] by the same authors, exploratory data analysis of production data was performed. A local and global analysis along both the temporal and spatial axis were considered.

Rogerro and Hu [172] used gradual deformation method to continuously modify a geostatistical realization while respecting its global mean and variogram. This method was coupled with an efficient optimization algorithm. Efficiency is obtained by selecting the number of deformation parameters in the model and optimization sequences. Reis et al. [169] applied gradual deformation technique for history matching to a real oil field located in Offshore Brazil. Lepine et al. [129] demonstrated an uncertainty analysis technique in predictive reservoir simulation through gradient information.

Landa and Horne [122] devised a procedure to integrate well test data, reservoir performance history and 4D seismic information into reservoir characterization. Both cell-based and object-based modeling were formulated. They used the gradient simulator method to compute sensitivities. 4D seismic information was considered to be in the form of maps of change of saturation in the reservoir. The value of data integration was evaluated with the variance analysis.

Gomez et al. [80] investigated an application of Tunneling Method, a global optimization technique in history matching of petroleum reservoir. This method could be used as an alternative to reformulation of the problem if the previously obtained reservoir parameters are not in the feasible region.

Phan and Horne [159] implemented a method to integrate dynamic data from multiple sources to infer reservoir properties. They emphasized depth-averaged data has poor resolution, and implemented a method to combine layer by layer seismic information and production data.

Bi et al. [16] developed a procedure to condition a stochastic channel to well-test pressure data and well observations of the channel thickness and the depth of the top of the channel. Zhang et al. [218] implements a procedure to condition a stochastic channel to well-test pressure, as well as static observations of the channel thickness and depth of the channel top data.

Wen et al. [205] extended sequential self-calibration method and another inverse technique named geo-morphing to invert for lithofacies distribution using multiphase production data. Both of these techniques attempt to modify the field of Gaussian deviates while maintaining fixed truncation threshold through an optimization procedure. Maintaining fixed threshold field, which has been previously computed on the basis of prior information of lithofacies production data, well data, and other static data, guarantees preservation of the initial geostatistical structure.

Chu et al. [41] implemented a two-loop iteration method based on inverse solution theory to construct the objection function and the gradient method to generate the maximum a posteriori estimates. The technique uses a Krylov space-based method to solve the linear part involved in the minimization thus avoiding explicit construction of the sensitivity coefficient matrix.

Ates and Kelkar [6, 7] also developed a dual-loop procedure for optimizing both relative permeability and heterogeneity characteristics. The method combines Gauss-Newton and conjugate gradient algorithms avoiding construction of the sensitivity coefficient matrix.

Indirect methods provide flexibility to account for production data in the construction

of reservoir models with less computational effort than full inversion. However, the success of these techniques in constraining reservoir models essentially relies on the quality of the interpretation of production data to represent reservoir heterogeneities. Some more recent techniques not presented in the above classification scheme are described below.

## 2.8 Recent Developments

Mantica et al. [136] devised a hybrid optimization technique combining a gradient based technique with a chaotic sampling technique to integrate information from production and seismic data. Their technique is based on a non-linear dynamical system.

Li et al. [130] used adjoint equations for three-dimensional, three-phase flow to calculate dimensionless sensitivity of production data to permeability fields as well as skin factors. This allows one to perform history-matching using the Levenbeg-Marquardt or Gauss-Newton method.

Raghavan et al. [164] integrated geological, geophysical and numerically simulated well test data of a fluvial reservoir. They implemented a 'porosity cube' model using seismic and well-log data. Upscaling of the 'porosity cube' was done preserving pay thickness, pore-volume, and connectivity between high- and low-porosity materials.

Masumoto [138] devised a method for simultaneous matching of pressure and its derivatives for two phase fluid flow in heterogeneous reservoirs. An adjoint method was used for gradient calculation of the objective function having two terms. One term is the pressure mismatch and the other is the mismatch of pressure change rate.

Queipo et al. [162] proposes a "surrogate modeling" technique to generate porosity and permeability models. Their approach named NEGO involves numerical reservoir model based on neural networks, DACE modeling and adaptive sampling. The NEGO algorithm effectively identifies promising areas for reservoir characterization.

# Chapter 3

# Mathematics of Production Data Integration

Characterization of detailed 3-D reservoir models entails working in a high dimensional space with a multitude of parameters to be estimated. There are various reservoir model properties for which inversion techniques, mentioned in the literature review (Chapter 2), are applied. In most cases, these reservoir parameters are transmissibility, distance to boundaries, effective flow capacities in the vicinity of wells, productivity of wells, measures of interwell communication (absolute/relative $kh$), coarse grid representation of $kh$, or $\phi$, facies connectivity between wells, drainage volumes around wells, facies proportions around/between wells, connectivity between wells and connected surfaces, local measures of heterogeneity (e.g., variogram, covariance, mean and variance of permeability and porosity).

Production data integration in reservoir characterization is an *inverse problem*. The intent is to build numerical reservoir models that by construction integrate all types of dynamic data along with all static information about the reservoirs. In order to implement techniques for production data integration, one needs to understand the difficulties and limitations of *inverse problems*. The characteristics of the *inverse problem* of production data integration and the basic framework and elements of most algorithms including the ones developed in later chapters are presented here. The description in this chapter is generic in nature and not a specific contribution of the present work; however, this mathematical background is essential to understand the developments in later chapters.

## 3.1 Inverse Problem

Consider a physical system defined by a set of model parameters. Observable performances of this system are its responses. The *direct* or *forward problem* is to predict the responses once the system and the model parameters are defined, *inverse problem* is to infer the values of the model parameters from some observed values of its responses. An *identification problem* is when the model parameters and the observed values are known but the system is not identified. Mathematically, one can consider the following problem: find $\alpha$ such that

$$F(d, \alpha) = 0 \tag{3.1}$$

where both $\alpha$ and $d$ are sets of data or variables on which the solution depends and $F$ is the functional relation among $d$ and $\alpha$. Typically, (3.1) is referred to as a *direct* or *forward*

problem if $F$ and $\alpha$ are given and $d$ is the unknown, *inverse* problem if $F$ and $d$ are known and $\alpha$ is the unknown, *identification* problem when $d$ and $\alpha$ are known while the functional relation or the mathematical model $F$ is unknown.

The usual approach to the solution of the inverse problem (3.1) entails the following:

1. Construct the *mathematical model* or the *functional relation* $F$.
2. Solve the *forward* formulation of the problem with a guess of the data set $\alpha$.
3. Define a *discrepancy function* or *objective function* between the solution in Step 2 and observed values.
4. Formulate and implement an *optimization algorithm* to minimize the *objective function.*

In production data integration, these steps are briefly explained here.

1. Construction of *subsurface flow equation.* Depending on the rigor of the study, 2-D or 3-D formulation of single or multiphase flow equations are modeled through some discretization technique.
2. Data here are the numerical reservoir models of the petrophysical properties involved. Properties are permeability, porosity, and in some cases fluid saturations. Initial guess of the these properties is often made from static well data. *Direct* problem is solved through some numerical solution technique.
3. *Objective function* is determined from the mismatch of the simulated flow responses and the observed production data.
4. *Minimization* technique is adopted in order to update the numerical model of the reservoirs.

Solution of an *inverse problem* is difficult in most cases. Deferring the discussion on specific solution techniques or approaches, the next section briefly explains the difficulties associated with the solution of an inverse problem.

## 3.2 Ill-posedness of Inverse Problems

In engineering, one often resorts to linearization (or quasilinearization) of a nonlinear problem. A linearized (or quasilinearized) form of Problem 3.1

$$\mathbf{F}\hat{\alpha} = D \tag{3.2}$$

is said to be *well-posed* when

- for each $D \in \mathbb{R}^{n_{obs}}$, there exists a $\hat{\alpha} \in \mathbb{R}^{n_{par}}$, called a *solution*, for which (3.2) holds;
- the solution $\hat{\alpha}$ is unique; and
- the solution is stable with respect to perturbations in $D$. That means that if $\mathbf{F}\hat{\alpha}_0 = D_0$ and $\mathbf{F}\hat{\alpha} = D$, then $\hat{\alpha}_0 \to \hat{\alpha}$ whenever $D \to D_0$.

A problem that is not well-posed is said to be *ill-posed.* Inverse problems are inherently ill-posed.

Essentially, solution of inverse problem means making inference of a physical system from real data. Issues regarding the solution algorithm of an inverse problems may be: dimensionality, non-uniqueness, consistency, robustness and so forth.

Characterizing any physical system such as a petroleum reservoir is an infinite dimensional problem. Properties at an infinite number of points are to be identified. Solution of this infinite dimensional problem is out of the question. The problem is thus redefined in a finite-dimensional setup.

There are many models in the solution space (model space) that can match the system performance. Non-uniqueness may arise because of attempting to derive a large number of essentially continuous parameters from a limited number of responses. Also, identifiability of the physics, mechanisms or even procedures may lead to a loss of uniqueness. For instance, one may often have to correlate some calculated or estimated parameters like acoustic impedance from seismics with other variables such as porosity, permeability, and fluid saturations affecting these measurements. The choice of variables may lead to non-uniqueness.

Reservoir characterization, like most inverse problems, entails numerous data of different types and information content. There is often some inconsistency due to different levels of accuracy within the same data type or different types of data. Also, some data may be in the time domain while some in the space domain.

Moreover, the scales or volumetric supports of various data may lead to inconsistencies. For example, well logs have a different volumetric support than well test data or core plug data. Inconsistency may also arise through application of different methods.

Many of these issues are still to be resolved to a satisfactory level in dynamic data integration. This is one reason that this field is an active area of research. Most methods attempt to reduce the non-uniqueness. However, it is difficult to agree on a suitable measure of such reduction. Consistency is a difficult issue especially in the presence of sparse data and many degrees of freedom. Due to its infinite dimensionality, it is not possible to completely deal with the robustness issue. This motivates the need for exploration of more efficient reservoir characterization techniques with dynamic data.

The next sections describe in some detail the formulation of the *forward* problem and possible *objective functions* in production data integration.

## 3.3 Forward Problem Formulation

This is basically the core subject of reservoir simulation and reservoir dynamics. To formulate the *direct* problem, one needs to consider the following:

- Conservation laws:
  - Mass conservation law
  - Momentum conservation law
  - Energy conservation law
- Macroscopic law of fluid flow through porous media: Darcy's law.
- Constitutive relationships:

- Equation of state
- Relative permeability and capillary pressure relationships.

Combining the above equations, we obtain 2- or 3-dimensional single or multiphase flow equations in the form of a system of partial differential equations. This system of equations are discretized into a set of non-linear algebraic equations. The discretized equations are solved with some nonlinear matrix solution techniques. In most cases, these techniques are iterative methods.

## 3.4 Objective Function

*Objective* or *discrepancy* function is the mismatch between the data obtained by solving the forward problem using the current estimate of the model and the observed dynamic data. In the context of production data integration, the objective function, $O$, can be formulated as:

$$O = \sum_{i=1}^{n_{obs}} w_i (d_i^{obs} - d_i^{sim})^2 \tag{3.3}$$

where $n_{obs}$ is the number of observations (production data), $d_i^{obs}$ are the observed production data, $d_i^{sim}$ are the simulated flow responses from the solution of the forward flow problem, while $w_i$ are the weights given to individual observed data. Typically, the purpose of these weights is to make the objective function dimensionless. The matricial expression of Equation (3.3) is the following:

$$O = (D^{obs} - D^{sim})^T W (D^{obs} - D^{sim}) \tag{3.4}$$

Determination of the weights can be very subjective. Modelers experience and association with the data can provide ideas for 'adhoc' estimation of the weights. Performances of sensors used in obtaining the observed data may affect the choices of the weights. Regular calibration of the sensors or probes can provide one the signal-to-noise ratio curves of the devices. These curves can be used to dissociate noisy components in the data.

Numerical reservoir models are gridded values of the petrophysical properties. In this research, the properties of interest are absolute permeability and porosity. Consider a reservoir model size of $n_x \times n_y \times n_z$, where $n_x$, $n_y$, and $n_z$ are number of grid blocks in $x$, $y$, and $z$ direction. With only two reservoir properties of interest (permeability and porosity), the number of parameters in the minimization algorithm will be $2 \times n_x \times n_y \times n_z$. This can be an enormously large number of parameters. Thus, a smaller set of reservoir properties may be chosen as the parameters for the minimization algorithm. Let these parameters be denoted by $\alpha_j, j = 1, \cdots, n_{par}$, where $n_{par}$ is the number of parameters.

The objective function can be formulated in a number of ways. The difference in these formulations stems from various considerations, namely, the minimization algorithms used, normalization of units, robustifying of the minimization algorithm, and so forth.

In *Least Square Formulation*, the matrix $W$ in 3.4 is an identity matrix. The major limitation of this formulation is that it gives rise to numerical problems when the orders of magnitude of the individual data vary significantly.

In *Weighted Least Square Formulation*, in order to avoid any problem with orders of magnitude, the matrix $W$ is a diagonal matrix that assigns individual weights to each observation. This normalizes individual observation and regularizes the numerical problem

to some extent. The concept of assigning some data a higher weight compared to others based on some engineering heuristics is also possible with this formulation. The rationale of weighting can also be founded on the premise of degree of uncertainty or confidence of the individual data. Thus, Weighted Least Square Formulation gives a space of freedom or flexibility in the inversion algorithm.

*Generalized Least Square Formulation* is based on probabilistic theory, and includes the dispersion characteristics or covariance of the data in the objective formulation [140, 188]. Regularization of the minimization problem can be actuated by incorporating prior information about the parameter involved. The objective function is expressed as:

$$O_{GLS} = \frac{1}{2}(D^{obs} - D^{sim})^T C_D^{-1}(D^{obs} - D^{sim}) + \frac{1}{2}(\alpha - \alpha_{prior})^T C_\alpha^{-1}(\alpha - \alpha_{prior}) \tag{3.5}$$

where $C_D$ is the covariance matrix of the observation. The main idea behind $C_D$ is that this matrix relates the correlation among the observations. In a simplified case, it may be assumed that the observations are independent of each other, and thus the covariance matrix reduces to a diagonal matrix. The diagonal elements are the variance of the observations ($\sigma_D^2$). $C_\alpha$ is the covariance matrix of the parameters of the inversion problem. $\alpha_{prior}$ are the set of parameters obtained before the application of the inversion algorithm. It may be the set of parameters obtained from the previous inversion step. The covariance matrix $C_\alpha$ may be obtained from geostatistical information. This formulation introduces both *a priori and* statistical information about the parameter set $\alpha$. Application of this approach in reservoir characterization was first studied by Oliver [149].

## 3.5 Parameter Estimation Algorithms

The minimization algorithm in the context of dynamic data integration is to estimate $\hat{\alpha} = \hat{\alpha}^*$ such that

$$\hat{\alpha}^* = \arg\min_{\hat{\alpha}} O(D, \hat{\alpha}) \tag{3.6}$$

where objective function ($O$) is considered a function of observed data ($D$) and the reservoir parameters ($\hat{\alpha}$) to be inverted. Minimization algorithms in the context of inverse problems are often referred to as *parameter estimation algorithms*. Parameter estimation is only a subproblem of the vast domain of optimization problems. The intent of all parameter estimation algorithms is to minimize a discrepancy function. There is an extensive literature and many tools are devised in this area of optimization [14, 15, 77, 160].

We say $\hat{\alpha}^*$ is a global minimizer for problem 3.6 if

$$O(D, \hat{\alpha}^*) \leq O(D, \hat{\alpha}), \quad \forall \hat{\alpha} \in \mathbb{R}^{n_{par}}$$

We say $\hat{\alpha}^*$ is a local minimizer for problem 3.6 if

$$O(D, \hat{\alpha}^*) \leq O(D, \hat{\alpha}), \quad \forall \alpha \in B(\hat{\alpha}^*, \rho^*)$$

where

$$B(\hat{\alpha}^*, \rho^*) \triangleq \{\hat{\alpha} \in \mathbb{R}^{n_{par}} \mid \| \hat{\alpha} - \hat{\alpha}^* \| \leq \rho^*\}.$$

The next section is devoted to optimality conditions for solving minimization problems of the form 3.6.

## Optimality Conditions

It is impossible to tell whether a vector is a solution of an optimization problem without checking if it satisfies optimality conditions. *Necessary conditions* are those that must be satisfied by any local minimizer. *Sufficient conditions* are those implying that a point is local minimizer. Optimality conditions can be presented in some forms. The basic form expresses the fact that the objective function value must increase in the vicinity of a local minimizer.

*Necessary conditions* of optimality are those that must be satisfied by any solution to (3.6), under assumptions of differentiability. Suppose that, $O(D,\cdot)$ in (3.6) is continuously differentiable and $\hat{\alpha}$ is a local minimizer for (3.6). Then

$$\nabla O(D,\hat{\alpha}^*) = \frac{\partial O(D,\hat{\alpha}^*)}{\partial \hat{\alpha}} = 0.$$

*Sufficiency conditions* of optimality is presented next. Suppose that $O(D,\hat{\alpha})$ is twice continuously differentiable. If $\hat{\alpha}^* \in \mathbb{R}$ is such that $\nabla O(D,\hat{\alpha}^*) = 0$, and the Hessian of the objective function at $\hat{\alpha}^*$

$$\mathbf{H}^* = \Delta^2_{\alpha\alpha} O(D,\hat{\alpha}^*) = \frac{\partial^2 O(D,\hat{\alpha}^*)}{\partial \hat{\alpha}^2}$$

where

$$H_{i,j} = \frac{\partial^2 O(D,\alpha)}{\partial \alpha_i \partial \alpha_j}$$

satisfies the condition

$$y^T \mathbf{H}^* y > 0 \quad \forall y \neq 0, \quad y \in \mathcal{R}^{n_{par}}.$$

Then $\hat{\alpha}^*$ is a strict local minimizer.

Above equation implies the matrix $\mathbf{H}^*$ is *positive- definite*. It should be noted that $\mathbf{H}$ is symmetric matrix, i.e.

$$H_{i,j} = H_{j,i} \quad \Leftrightarrow \quad \mathbf{H} = \mathbf{H}^T$$

The *positive-definiteness* of the *Hessian* matrix is central to many minimization algorithm. Consider $O(D,\hat{\alpha})$ to be convex. Applying Taylor's expansion in the neighborhood of $\hat{\alpha}$, the function $O(D,\hat{\alpha}+\hat{\Delta}\alpha)$ is approximated:

$$O(D,\hat{\alpha}+\hat{\Delta}\alpha) = O(D,\hat{\alpha}) + \nabla O(D,\hat{\alpha})^T \Delta\hat{\alpha} + \frac{1}{2}\Delta\hat{\alpha}^T \mathbf{H} \Delta\hat{\alpha} + \bigcirc(\hat{\Delta}\alpha^3)$$

where $\mathbf{H}$ is evaluated at $\hat{\alpha}$. At optimal point (i.e. $\hat{\alpha} \to \hat{\alpha}^*$), $\nabla O(D,\hat{\alpha}) \to \nabla O(D,\alpha^*)$ and $\mathbf{H} \to \mathbf{H}^*$. Following section discusses the basic minimization algorithm that can be used in the parameter estimation problems.

## Basic Minimization Algorithm

Minimization problems as in (3.6) are usually "solved" by iterative methods, which construct infinite sequences, $\{\hat{\alpha}^i\}_{i=0}^{\infty}$, of progressively better approximations to a "solution", that is, to a point satisfying an optimality condition. These iterative methods are referred to as *optmization algorithms.*

Literature of optimization algorithms is vast and rich. Taxonomy of optimization techniques can be based on various premises. Problems can be formulated as constrained or unconstrained.

The unconstrained optimization problem is central to the development of optimization algorithms. Constrained optimization algorithms are often extensions of unconstrained algorithms. The discussion below starts with unconstrained problems and moves to constrained problems. Only a few of algorithms that are applicable to reservoir parameter estimation are mentioned here.

## 3.6 Gradient Based Methods

Optimality conditions presented previously apply mainly to gradient based methods. Basic assumptions in most gradient based algorithms are:

- Objective function $O(D, \hat{\alpha})$ is continuous
- $O(D, \hat{\alpha})$ is at least twice differentiable

The basic concept in the gradient approach is that under the assumption of continuous differentiability and $\nabla O(D, \hat{\alpha}) \neq 0$ for a given value $\hat{\alpha} = \hat{\alpha}_0$, it is always possible to reduce the value of $O(D, \cdot)$ from its current value. This reduction is brought about by introducing a change in the parameters, i.e.,

$$O(D, \hat{\alpha}_0 + \lambda h) < O(D, \hat{\alpha}_0)$$

where $h \in \mathbb{R}^{n_{par}}$ is a *descent direction* and $\lambda > 0$ is a scalar *step size*. Proof of the existence of a descent direction, $h$, in the neighborhood of $\hat{\alpha}_0$ can be obtained Using Taylor's Expansion.

$$O(D, \hat{\alpha}_0 + \lambda h) = O(D, \hat{\alpha}_0) + \lambda \nabla O(D, \hat{\alpha}_0)^T + \bigcirc(h^2) \tag{3.7}$$

Examining Equation 3.7, it can be observed that it is always possible to find the scalar $\lambda > 0$ provided $h$ satisfies the condition

$$\nabla O(D, \hat{\alpha}_0)^T h < 0.$$

The direction $h$ satisfying the above condition is called *direction of sufficient descent.* This guarantees the existence of $\lambda$ and $h$, provided $O(D, \hat{\alpha}_0) \neq 0$.

Thus, the gradient algorithms entails

- Finding a *sufficient descent direction* $(h)$.
- Determining an adequate *step size* $(\lambda)$.

The practical stopping criterion of these algorithms is

$$|\nabla O(D, \hat{\alpha}^*)| < \epsilon.$$

where $\epsilon > 0$. This implies the *necessary condition* in a practical sense. The main limitations of the above criterion is that, in the absence of convexity, the solution may become stuck in a local minima.

Common gradient based methods include Steepest Descent Method, Armijo Gradient Method, Newton Method, Gauss-Newton Method, Conjugate Gradient Method, and Quasi-Newton Method. These are briefly described below. Brief discussion of Singular Value Decomposition Algorithms follows subsequently.

### Steepest Descent Method

An algorithm for solving problem (3.6) is called a *descent method* if it constructs sequences $\{\hat{\alpha}^i\}_{i=0}^{\infty}$, such that

$$O(D, \hat{\alpha}^{i+1}) < O(D, \hat{\alpha}^i) \quad \forall i \in \mathbb{N} \quad (\text{and} \quad \hat{\alpha}^i \in \mathbb{R}^{n_{par}} \quad \forall i \in \mathbb{N}).$$

It is the earliest gradient method invented by Cauchy more than 100 years ago. It corresponds to an algorithm with a sufficient descent direction $h_i$ defined by $h_i = -\nabla O(D, \hat{\alpha}_0)$. Algorithm for Steepest Descent Method is the following for $\hat{\alpha}_0 \in \mathbb{R}^{n_{par}}$:

**Step 0.** Set $i = 0$.

**Step 1.** Compute the *search* direction

$$h_i = -\nabla O(D, \hat{\alpha}_i).$$

Stop if $\nabla O(D, \hat{\alpha}_i) = 0$.

**Step 2.** Compute the step size

$$\lambda_i \in \lambda(D, \hat{\alpha}_i) \triangleq \arg\min_{\lambda \geq 0} O(D, \hat{\alpha}_i + \lambda h_i).$$

**Step 3.** Set

$$\hat{\alpha}_{i+1} = \hat{\alpha}_i + \lambda_i h_i,$$

replace $i$ by $i + 1$, and go to Step 1.

Problems with this algorithm are that it is quite inefficient and it contains a nonimplementable step size rule. Moreover, it has only linear rate of convergence; however, it is the simplest approach.

### Armijo Gradient Method

Armijo gradient method accommodates a step size rule that is implementable. This increases the efficiency of the descent algorithm. The algorithm follows for $\hat{\alpha}_0 \in \mathbb{R}^{n_{par}}$ and parameters $a, b \in (0, 1), k^* \in \mathbb{Z}$:

**Step 0.** Set $i = 0$.

**Step 1.** Compute the *search* direction

$$h_i = -\nabla O(D, \hat{\alpha}_i).$$

Stop if $\nabla O(D, \hat{\alpha}_i) = 0$.

**Step 2.** Compute the step size $\lambda_i = b^{k_i}$, where $k_i \in \mathbb{Z}$ is such that

$$O(D, \hat{\alpha}_i + b^{k_i} h_i) - O(D, \hat{\alpha}_i) \leq -b^{k_i} a \parallel \nabla O(D, \hat{\alpha}_i) \parallel^2$$

and

$$O(D, \hat{\alpha}_i + b^{k_i - 1} h_i) - O(D, \hat{\alpha}_i) > -b^{k_i - 1} a \parallel \nabla O(D, \hat{\alpha}_i) \parallel^2 .$$

**Step 3.** Set

$$\hat{\alpha}_{i+1} = \hat{\alpha}_i + \lambda_i h_i,$$

replace $i$ by $i + 1$, and go to Step 1.

### Newton Method

Newton's algorithm is one of the oldest and best methods for solving optimization problems. In its simplest form it converges only if the initial guess is sufficiently close to a solution.

The idea behind Newton's algorithm consists of decomposing the nonlinear equation problem (3.6), for which one is unable to obtain an explicit solution, into an infinite sequence of linear equations constituting *successive approximations*, for which one can obtain an explicit solution. Thus, given the current approximation $\hat{\alpha}_i \in \mathbb{R}^{n_{par}}$ to a solution of (3.6), one linearizes (3.6) about $\hat{\alpha}_i$ using Taylor expansion and constructs the approximating problem

$$O(D, \hat{\alpha}_i) + \nabla O(D, \hat{\alpha}_i)^T (\hat{\alpha} - \hat{\alpha}_i) = 0.$$

whose explicit solution

$$\hat{\alpha}_{i+1} = \hat{\alpha}_i - \nabla O(D, \hat{\alpha}_i)^{-T} O(D, \hat{\alpha}_i). \tag{3.8}$$

is the next, and hopefully better, approximation to a solution of (3.6). This simplest version of Newton method is sometimes known as Local Newton Method.

The logical extension of Local Newton Method, defined by (3.8), to problem (3.6), is as follows. Given a current estimate $\hat{\alpha}_i$ of the local minimizer $\hat{\alpha}^*$ we expand $O(D, \cdot)$ to second-order terms about $\hat{\alpha}_i$

$$O(D, \hat{\alpha}) \approx O(D, \hat{\alpha}_i) + \nabla O(D, \hat{\alpha}_i)^T (\hat{\alpha} - \hat{\alpha}_i) + \frac{1}{2} (\hat{\alpha} - \hat{\alpha}_i)^T \mathbf{H}(D, \hat{\alpha}_i)(\hat{\alpha} - \hat{\alpha}_i). \tag{3.9}$$

Assuming that $\mathbf{H}(D, \hat{\alpha}_i)$ is positive-definite, we can compute the minimizer $\hat{\alpha}_{i+1}$ of the right-hand side of (3.9) explicitly, by setting its gradient equal to zero, i.e., by solving the equation

$$\nabla O(D, \hat{\alpha}_i) + \mathbf{H}(D, \hat{\alpha}_i)(\hat{\alpha}_{i+1} - \hat{\alpha}_i) = 0. \tag{3.10}$$

Since, $\mathbf{H}(D, \hat{\alpha}_i)$ must be non-singular for $\hat{\alpha}_i$ close enough to $\hat{\alpha}^*$, (3.10) defines the iteration process

$$\hat{\alpha}_{i+1} = \hat{\alpha}_i - \mathbf{H}(D, \hat{\alpha}_i)^{-1} \nabla O(D, \hat{\alpha}_i) \qquad i = 0, 1, 2, \ldots$$

There are two problems with this method: first, it converges to a solution of (3.6) only when initialized with a sufficiently good initial guess $\hat{\alpha}_0$; second, it is basically a root-finding, not an optimization algorithm, and hence, when applied to a nonconvex function $O(D, \hat{\alpha})$, it can converge to a local maximizer instead of a minimizer. This can be shown by premultiplying Equation (3.10) by $(\hat{\alpha}_{i+1} - \hat{\alpha}_i)$ and transposing the resulting equation, i.e.,

$$\nabla O(D, \hat{\alpha}_i)^T (\hat{\alpha}_{i+1} - \hat{\alpha}_i) = -(\hat{\alpha}_{i+1} - \hat{\alpha}_i)^T \ \mathbf{H}(D, \hat{\alpha}_i) \ (\hat{\alpha}_{i+1} - \hat{\alpha}_i). \tag{3.11}$$

Equation (3.11) does not guarantee a direction of descent unless $\mathbf{H}(D, \hat{\alpha}_i)$ is positive-definite.

Note that using *any* positive-definite matrix $\tilde{\mathbf{H}}$ instead of the actual $\mathbf{H}(D, \hat{\alpha})$ it is possible to have a method that guarantees a descent direction. Another concern with Newton's method is that it requires not only the first derivative of $O$ but also the second derivatives. This may become computationally expensive.

### Gauss-Newton Method

Another variant of Newton method, known as Gauss-Newton method, is widely used in parameter estimation problem. Consider the least square problem discussed in Section 3.4.

Let $\psi(\hat{\alpha}) = D^{sim}(\hat{\alpha}) - D^{obs}$. The idea in this algorithm is to linearize the function around the current point $\hat{\alpha}_i$

$$\tilde{\psi}(\alpha, \hat{\alpha}_i) = \psi(\hat{\alpha}_i) + \nabla\psi(\hat{\alpha}_i)^T(\alpha - \hat{\alpha}_i).$$

and minimize the norm of the linearized function $\tilde{\psi}$, i.e.,

$$\begin{aligned}\hat{\alpha}_{i+1} &= \arg\min_{\alpha \in \mathbb{R}^{n_{par}}} \frac{1}{2} \parallel \tilde{\psi}(\alpha, \hat{\alpha}_i) \parallel^2 \\ &= \hat{\alpha}_i - \left(\nabla\psi(\hat{\alpha}_i)\nabla\psi(\hat{\alpha}_i)^T\right)^{-1} \nabla\psi(\hat{\alpha}_i)\psi(\hat{\alpha}_i).\end{aligned}$$

The direction $\left(\nabla\psi(\hat{\alpha}_i)\nabla\psi(\hat{\alpha}_i)^T\right)^{-1} \nabla\psi(\hat{\alpha}_i)\psi(\hat{\alpha}_i)$ in the Gauss-Newton method is a descent direction since

$$\nabla\psi(\hat{\alpha}_i)\psi(\hat{\alpha}_i) = \nabla\left((1/2) \parallel \psi(\alpha) \parallel^2\right)$$

and

$$\nabla\psi(\hat{\alpha}_i)\nabla\psi(\hat{\alpha}_i)^T > 0$$

The derivation of the Gauss-Newton method for the case of weighted least square formulation is developed here. In the case of weighted least square formulation, $O$ is defined (Section 3.4) as

$$O(D, \hat{\alpha}) = (D^{obs} - D^{sim}(\hat{\alpha}))^T W (D^{obs} - D^{sim}(\hat{\alpha}))$$

where $\hat{\alpha} \in \mathbb{R}^{n_{par}}$ and $D^{obs}, D^{sim}(\hat{\alpha}) \in \mathbb{R}^{n_{obs}}$.

The derivative of simulated data with respect to the vector of parameters $\hat{\alpha}$ is the sensitivity matrix $G$ given by

$$G \triangleq \frac{\partial D^{sim}}{\partial \hat{\alpha}} = \left[\hat{g}_1, \hat{g}_2, \cdots, \hat{g}_i, \cdots, \hat{g}_{n_{par}}\right]$$

where

$$\hat{g}_i \triangleq \frac{\partial D^{sim}}{\partial \hat{\alpha}_i} = \begin{bmatrix} \frac{\partial d_1^{sim}}{\partial \hat{\alpha}_i} \\ \frac{\partial d_2^{sim}}{\partial \hat{\alpha}_i} \\ \vdots \\ \frac{\partial d_{n_{obs}}^{sim}}{\partial \hat{\alpha}_i} \end{bmatrix}$$

*Sensitivity coefficient*, $s_{i,j}$, the magnitude of which indicates how much $d_i^{sim}$ is affected by a change in $\hat{\alpha}_j$, is defined as

$$s_{i,j} = \frac{\partial d_i^{sim}}{\partial \hat{\alpha}_j}.$$

Assuming matrix $\mathbf{W}$ to be symmetric with constant coefficients and using Equation (3.8), we have $\nabla O(D, \hat{\alpha})$ and $\mathbf{H}(D, \hat{\alpha})$:

$$\nabla O(D, \hat{\alpha}) = -2\mathbf{G}^T\mathbf{W}(D^{obs} - D^{sim})$$

and

$$\mathbf{H}(D, \hat{\alpha}) = 2\mathbf{G}^T\mathbf{W}\mathbf{G} - 2\frac{\partial \mathbf{G}^T}{\partial \hat{\alpha}}\mathbf{W}(D^{obs} - D^{sim}).$$

The Hessian matrix for the Gauss-Newton method $\mathbf{H}_{GN}$ is defined as the first term of Equation 3.11, i.e.,

$$\mathbf{H}_{GN} \triangleq 2\mathbf{G}^T\mathbf{W}\mathbf{G}.$$

Imposing positive definiteness of $\mathbf{W}$, we guarantee that $\mathbf{H}_{GN}$ will be at least semi-positive definite. This is not far from the requirement of positive definiteness. Further modification of matrix $\mathbf{H}_{GN}$ renders stabilization.

This formulation ensures the right descent direction. In the limiting condition, i.e., $\mathbf{H}_{GN} \leftarrow \mathbf{H}$ that has quadratic rate of convergence. Moreover, in the computation of $\mathbf{H}_{GN}$, only the first derivatives are required. This makes the algorithm efficient.

Lack of positive definiteness in $\mathbf{H}_{GN}$ stems directly from the structure of $\mathbf{G}$. Possible reasons are:

- Data insufficiency for parameter resolution.
  - $\frac{\partial D^{sim}}{\partial \hat{\alpha}_i} = 0$ for some $i$ renders $\mathbf{H}_{GN}$ singular.
  - $\| \frac{\partial D^{sim}}{\partial \hat{\alpha}_i} \| \ll \| \frac{\partial D^{sim}}{\partial \hat{\alpha}_j} \| \qquad \forall j \neq i$ for some $i$ render ill-conitioning of $\mathbf{H}_{GN}$.
- Linear combination of parameters.

Understanding the reasons of lack of positive definiteness can be very illuminating in the solution of an inverse problem.

In the case of *generalized least square* formulation discussed in Section 3.4, the computation of objective function, gradient and the Hessian is performed in the following manner:

$$O(D, \hat{\alpha}) = \frac{1}{2}(D^{obs} - D^{sim}(\hat{\alpha}))^T \mathbf{C}_D^{-1}(D^{obs} - D^{sim}(\hat{\alpha})) + \frac{1}{2}(\hat{\alpha} - \alpha_{prior})^T \mathbf{C}_\alpha^{-1}(\hat{\alpha} - \alpha_{prior})$$

$$\nabla O(D, \hat{\alpha}) = -\mathbf{G}^T \mathbf{C}_D^{-1}(D^{obs} - D^{sim}) + \mathbf{C}_\alpha^{-1}(\hat{\alpha} - \alpha_{prior})$$

and

$$\mathbf{H}(D, \hat{\alpha}) = \mathbf{G}^T \mathbf{C}_D^{-1} \mathbf{G} - \frac{\partial \mathbf{G}^T}{\partial \hat{\alpha}} \mathbf{C}_D^{-1}(D^{obs} - D^{sim}) + \mathbf{C}_\alpha^{-1}.$$

The Gauss-Newton Hessian $\mathbf{H}_{GN}$, in this case, is defined as:

$$\mathbf{H}_{GN} \equiv \mathbf{G}^T \mathbf{C}_D^{-1} \mathbf{G} + \mathbf{C}_\alpha^{-1}. \tag{3.12}$$

Imposing positive definiteness of the matrices $\mathbf{C}_D$ and $\mathbf{C}_\alpha$ ensures $\mathbf{H}_{GN}$ to be positive definite. Moreover, addition of $\mathbf{C}_\alpha$ introduces further stabilization in the Gauss-Newton Hessian matrix.

### Conjugate Gradient Methods

Hestenes and Stiefel [96] first proposed methods of conjugate directions as a technique for solving large systems of linear equations. There are many variants available differing in line search, restarting, scaling, preconditioning, and so forth. An algorithm for one of the conjugate gradient variants for $\hat{\alpha}_0 \in \mathbb{R}^{n_{par}}$:

**Step 0.** Set $i = 0$, $g_0 = \nabla O(D, \hat{\alpha}_0)$, and $h_0 = -g_0$.

**Step 1.** Compute the step size

$$\lambda_i = \arg\min_{\lambda \geq 0} O(D, \hat{\alpha}_i + \lambda h_i).$$

**Step 2.** Update: Set

$$\begin{cases} \hat{\alpha}_{i+1} = \hat{\alpha}_i + \lambda_i h_i, \\ g_{i+1} = \nabla O(D, \hat{\alpha}_{i+1}), \\ \gamma_i = \| g_{i+1} \|^2 \, / \, \| g_i \|^2, \\ h_{i+1} = -g_{i+1} + \gamma_i h_i. \end{cases}$$

**Step 3.** Replace $i$ by $i+1$, and go to Step 1.

Conjugate gradient methods aim to improve the convergence rate of steepest descent method without incurring the computational overhead in Newton's method. The algorithm is simple and easy to implement when $\nabla O(D, \cdot)$ is already computed. It requires very little storage; however, numerical error accumulation seriously affects the solution.

### Quasi-Newton Method

Quasi-Newton Methods for unconstrained optimization approximate the Newton search direction, usually without evaluating second order derivatives of the objective function. Variants of this method include secant methods and variable metric methods. Among the widely used algorithms are Davidon-Fletcher-Powell (DFP) and Broyden-Fletcher-Goldfarb-Shanno (BFGS) algorithms and their variations. The basic BFGS algorithm is discussed below. For $\hat{\alpha}_0 \in \mathbb{R}^{n_{par}}$, and $H_0$, a symmetric $n \times n$, positive definite matrix,

**Step 0.** Set $i = 0$.

**Step 1.** If $g_i = \nabla O(D, \hat{\alpha}_i) = 0$, stop. Else compute

$$\lambda_i = \arg\min_{\lambda \geq 0} O(D, \hat{\alpha}_i - \lambda H_i^{-1} g_i).$$

**Step 2.** Compute

$$\hat{\alpha}_{i+1} = \hat{\alpha}_i - \lambda_i H_i^{-1} g_i,$$

$$g_{i+1} = \nabla O(D, \hat{\alpha}_{i+1}),$$

$$\Delta\hat{\alpha}_i = \hat{\alpha}_{i+1} - \hat{\alpha}_i, \qquad \Delta g_i = g_{i+1} - g_i,$$

$$H_{i+1} = H_i + \frac{1}{\Delta g_i^T \Delta\hat{\alpha}_i} \Delta g_i \Delta g_i^T - \frac{1}{\Delta\hat{\alpha}_i^T H_i \Delta\hat{\alpha}_i} (H_i \Delta\hat{\alpha}_i)(H_i \Delta\hat{\alpha}_i)^T. \tag{3.13}$$

**Step 3.** Replace $i$ by $i+1$, and go to Step 1.

The most popular Quasi-Newton Method is the clever way to compute $H_{i+1}$ as one shown in Equation (3.13).

### Singular Value Decomposition Algorithm

Singular Value Decomposition or Spectral Decomposition of a matrix can be used to solve some parameter estimation problems. This technique is, in fact, used to analyze the existence of a solution. The idea is that any matrix $\mathbf{A} \in \mathbb{C}^{n \times n}$ can be reduced to

$$\mathbf{A} = \mathbf{U} \Sigma \mathbf{V}^H \tag{3.14}$$

where $\mathbf{U} \in \mathbb{C}^{m\times m}$ and $\mathbf{V} \in \mathbb{C}^{n\times n}$ are two unitary matrices (orthogonal matrices in case of real-valued), i.e.,

$$\mathbf{U}^H\mathbf{U} = \mathbf{U}\mathbf{U}^H = \mathbf{I}_m$$

$$\mathbf{V}^H\mathbf{V} = \mathbf{V}\mathbf{V}^H = \mathbf{I}_n$$

$$\Sigma = \text{diag}(\sigma_1, \ldots, \sigma_p) \in \mathbb{C}^{m\times n} \qquad \text{with } p = \min(m, n)$$

and $\sigma_1 \geq \ldots \geq \sigma_p \geq 0$. Here, the superscript $H$ denotes the operation of taking the conjugate transpose. Formula 3.14 is called Singular Value Decomposition (SVD) of $\mathbf{A}$ and the numbers $\sigma_i$ (or $\sigma_i(\mathbf{A})$) are called singular values of $\mathbf{A}$. If $\mathbf{A}$ is real-valued matrix, $\mathbf{U}$ and $\mathbf{V}$ will be also be real-valued and in above equations superscript $T$ (Transpose) must be written instead of $H$ (Hermitian).

From (3.14) it follows that (considering real-valued matrices) $\mathbf{A}^T = \mathbf{V}\Sigma\mathbf{U}^T$ so that $\mathbf{U}$ and $\mathbf{V}$ being orthogonal, $\mathbf{A}^T\mathbf{A} = \mathbf{V}\Sigma^2\mathbf{V}^T$ and $\mathbf{A}\mathbf{A}^T = \mathbf{U}\Sigma^2\mathbf{U}^T$. As far as the rank is concerned, if $\sigma_1 \geq \ldots \geq \sigma_r > \sigma_{r+1} = \ldots = \sigma_p = 0$, then the rank of $\mathbf{A}$ is $r$. An interpretation of matrices $\mathbf{U}$ and $\mathbf{V}$ is that the kernel of $\mathbf{A}$ is the span of the column vectors of $\mathbf{V}$, $\{v_{r+1}, \ldots, v_n\}$ and the range of $\mathbf{A}$ is the span of the column vectors of $\mathbf{U}$, $\{u_1, \ldots, u_r\}$.

Suppose that $\mathbf{A} \in \mathbb{R}^{m\times n}$ has rank equal to $r$ and that it admits SVD of the type $\mathbf{U}^T\mathbf{A}\mathbf{V} = \Sigma$. The matrix $\mathbf{A}^\dagger = \mathbf{V}\Sigma^\dagger\mathbf{U}^T$ is called the *Moore-Penrose pseudo-inverse* or *genearalized inverse* matrix of $\mathbf{A}$, where

$$\Sigma^\dagger = \text{diag}\left(\frac{1}{\sigma_1}, \ldots, \frac{1}{\sigma_r}, 0, \ldots, 0\right).$$

In nonlinear parameter estimation, Singular Value Decomposition can be used. Previously, we had from first order approximation of $D^{sim}(\hat{\alpha})$ around a given $\hat{\alpha}_0$

$$D^{sim}(\hat{\alpha}_0 + \Delta\alpha) = D^{sim}(\hat{\alpha}_0) + \frac{\partial D^{sim}}{\partial \hat{\alpha}}\Delta\alpha. \tag{3.15}$$

Now, $\frac{\partial D^{sim}}{\partial \hat{\alpha}} = \mathbf{G}$ and setting

$$D^{sim}(\hat{\alpha}_0 + \Delta\alpha) = D^{obs}$$

and we obtain from (3.15)

$$\mathbf{G}\Delta\alpha = D^{obs} - D^{sim}(\hat{\alpha}_0). \tag{3.16}$$

Equation 3.16 can be solved using Singular Value Decomposition,

$$\mathbf{G} = \mathbf{U}\Sigma\mathbf{V}^T$$

$$\begin{aligned}\Delta\alpha &= \mathbf{G}^\dagger\left(D^{obs} - D^{sim}(\hat{\alpha}_0)\right) \\ &= \mathbf{V}\Sigma^\dagger\mathbf{U}^T\left(D^{obs} - D^{sim}(\hat{\alpha}_0)\right)\end{aligned} \tag{3.17}$$

The algorithm stops when

$$\mathbf{U}^T\left(D^{obs} - D^{sim}(\hat{\alpha}_0)\right) = 0$$

which implies the *necessary condition* $\nabla O(D, \hat{\alpha}) = 0$.

## 3.7 Nongradient Optimization Techniques

Recent advances in information technology and soft computational techniques contribute to a vast literature in nongradient optimization techniques. Some of the prominent nongradient methods are namely:

- Evolutionary Computing, e.g. Genetic Algorithms, Memetic Algorithms, etc.
- Simulated Annealing
- Polytope Algorithms
- Response Surface Methods, others.

Brief explanation of these methods follows.

Evolutionary computing [43, 79, 142] exploits an entire population of potential solutions and evolves them according to some genetically driven phenomena. Genetic algorithms are among the most representative examples of the principle of evolutionary computing. Genetic algorithms are capable of dealing with broad class of tasks in spite of their formulation and the nature of optimization. The genetic algorithm starts with an initial population of $N$ elements in the search space, determines the suitability of survival of its individuals and evolves the population to retain the individuals with the highest values of the fitness function and eliminates the weakest ones. Individual solutions are allowed to recombine and mutate thus emulating the natural selection or adaptation.

Simulated annealing [63, 115, 141, 155] is a generalization of a Monte Carlo method for examining the equations of state and frozen states of $N$-body systems. The concept is based on the manner in which liquids freeze or metals recrystallize in the process of annealing. The original Metropolis scheme was that an initial state of a thermodynamic system was chosen at energy $E$ and temperature $T$, holding $T$ constant the initial configuration is perturbed thus changing the energy $\partial E$. If the change in energy is negative the new configuration is accepted. If the change in energy is positive it is accepted with a probability given by the Boltzmann factor $\exp\{-(\partial E/T)\}$. This processes is then repeated sufficient times to give good sampling statistics for the current temperature, and then the temperature is decreased and the entire process repeated until a frozen state is achieved at $T = 0$.

Polytope algorithms are also known as Downhill Simplex, Nonlinear Simplex, or simply Nelder-Mead Simplex methods [144]. Essentially, these methods start from a Polytope (Simplex), which is a geometrical figure of $N + 1$ vertices (in dimension $N$) and their interconnecting lines. Geometrical operations (reflection, expansion, contraction) are then performed on some candidate vertices in order to move the Polytope in the descent directions.

## 3.8 Search Methods

Overall efficiency of the optimization algorithms hinges on efficient ways to compute search directions and the steps sizes. There are various descent direction search algorithms.

Line-search methods generate the iterates by setting

$$\hat{\alpha}_{k+1} = \hat{\alpha}_k + \lambda_k h_k$$

where $h_k$ is a search direction and $\lambda_k > 0$ is chosen so that

$$O(D, \hat{\alpha}_{k+1}) < O(D, \hat{\alpha}_k).$$

Most line-search versions of the basic Newton method generate the direction $h_k$ by modifying the Hessian matrix $\Delta^2_{\alpha\alpha} O(D, \hat{\alpha}_k)$ to ensure that the quadratic model of the function has a unique minimizer. The *modified Cholesky* decomposition approach adds positive quantities to the diagonal of $\Delta^2_{\alpha\alpha} O(D, \hat{\alpha}_k)$ during the Cholesky factorization. As a result, a diagonal matrix, $E_k$, with nonnegative diagonal entries is generated such that

$$\Delta^2_{\alpha\alpha} O(D, \hat{\alpha}_k) + E_k$$

is positive definite. Given this decomposition, the search direction $h_k$ is obtained by solving

$$\left(\Delta^2_{\alpha\alpha} O(D, \hat{\alpha}_k) + E_k\right) h_k = -\nabla O(D, \hat{\alpha}_k).$$

After $h_k$ is found, a line-search procedure is used to choose an $\lambda_k > 0$ that approximately minimizes $O$ along the ray

$$\{\hat{\alpha}_k + \lambda h_k : \lambda > 0\}.$$

The algorithms for determining $\lambda_k$, in general, rely on quadratic or cubic interpolation of the univariate function

$$\phi(\lambda) = O(D, \hat{\alpha}_k + \lambda h_k)$$

in their search for a suitable $\lambda_k$. An elegant and practical criterion for a suitable step size is to require $\lambda_k$ to satisfy the *sufficient decrease* condition: $O(D, \hat{\alpha}_k + \lambda_k h_k) \leq O(D, \hat{\alpha}_k) + \mu \lambda_k \Delta O(D, \hat{\alpha}_k)^T h_k$ and the *curvature* condition: $|\Delta O(D, \hat{\alpha}_k + \lambda_k h_k)^T| \leq \eta |\Delta O(D, \hat{\alpha}_k)^T h_k|$, where $\mu$ and $\eta$ are two constants with $0 < \mu < \eta < 1$. The sufficient decrease condition guarantees, in particular, that $O(D, \hat{\alpha}_{k+1}) < O(D, \hat{\alpha}_k)$, while the curvature condition requires that $\lambda_k$ be not too far from a minimizer of $\phi$.

A *trust-region* version of Newton's method takes the view that the linear model

$$O(D, \hat{\alpha}_k) + \nabla O(D, \hat{\alpha}_k)^T h$$

of $O(D, \hat{\alpha}_k + h)$ is valid only when $h$ is not too large, and thus places a restriction on the size of the step. In a general trust-region method, the Jacobian matrix is replaced by an approximation, and the step is obtained as an approximate solution of the subproblem

$$\min\{\| O(D, \hat{\alpha}_k) + B_k h \| \ : \ \| S_k h \|_2 \leq \Delta_k\},$$

where $S_k$ is a scaling matrix and $\Delta_k$ is the trust-region radius. The step is accepted if the ratio

$$\rho_k = \frac{|O(D, \hat{\alpha}_k)| - |O(D, \hat{\alpha}_k + h_k)|}{|O(D, \hat{\alpha}_k)| - |O(D, \hat{\alpha}_k) + B_k h_k|}$$

of the actual-to-predicted decrease in $\| O(D, \hat{\alpha}) \|$ is greater than some constant $\sigma_0$ (typically .0001). If the step is not accepted, the trust region radius is decreased and the ratio is recomputed. The trust-region radius may also be updated between iterations according to how close the ratio $\rho_k$ is to its ideal value of 1.

Given an approximation $B_k$ to the Jacobian matrix, a *line-search* method obtains a search direction $h_k$ by solving the system of linear equations

$$B_k h_k = -O(D, \hat{\alpha}_k).$$

The next iterate is then defined as $\hat{\alpha}_{k+1} = \hat{\alpha}_k + \lambda_k h_k$, where the line search parameter $\lambda_k > 0$ is chosen by the line-search procedure so that

$$\| O(D, \hat{\alpha}_{k+1}) \| < \| O(D, \hat{\alpha}_k) \| .$$

When the "approximate" Jacobian is "exact", as in Newton's method, $h_k$ is a downhill direction in $L_2$-norm, so there is certain to be an $\lambda_k > 0$ such that

$$\| O(D, \hat{\alpha}_{k+1}) \|_2 < \| O(D, \hat{\alpha}_k) \|_2 .$$

This descent property does not necessarily hold for other choices of the approximate Jacobian, so line-search methods are used only when $B_k$ is either the exact Jacobian or a close approximation to it.

In an ideal line-search Newton method, we would compute the search direction by solving

$$\nabla O(D, \hat{\alpha}_k)^T h_k = -O(D, \hat{\alpha}_k)$$

and choose the line-search parameter $\lambda_k$ to minimize the scalar function

$$\phi(\lambda) = |O(D, \hat{\alpha}_k + \lambda h_k)|.$$

However, since it is usually too time-consuming to find the $\lambda$ that exactly minimizes $\phi$, we usually settle for an approximate solution $\lambda_k$ that satisfies the conditions

$$\phi(\lambda_k) \leq \phi(0) + \mu \lambda_k \nabla \phi(0), \qquad | \nabla \phi(\lambda_k) | \leq \eta | \nabla \phi(0) |,$$

where $\mu$ and $\eta$ are two constants with $0 < \mu < \eta < 1$. Typical values are $\mu = 0.001$, and $\eta = 0.9$.

The first of these conditions ensures that $\| O(D, \hat{\alpha}) \|_2$ decreases by a significant amount, while the second condition ensures that we move far enough along the search direction by insisting on a significant reduction in the size of the gradient.

Brief discussion on bound constrained optimization problem and its optimality criteria follows in the subsequent section.

## 3.9 Bound Constrained Optimization

Bound-constrained optimization problems play an important role in the development of techniques for dynamic data integration. Formulation of this type of optimization problem is

$$\min\{O(D, \hat{\alpha}) : L \leq \alpha \leq U\} \tag{3.18}$$

where $U$ and $L$ represent the upper and lower constraint vectors constraining the parameter space. The importance of this formulation stems from the fact that parameters describing reservoir properties are not completely arbitrary. These parameters are often believed to lie in a given range, termed *feasibility region*. For example, porosity and permeability take only nonnegative values; high values of permeability are likely to exist in regions of high porosity; and so forth. This range may come from previous inversion or static data integration in reservoir characterization.

Algorithms for unconstrained optimization are much simpler and robust than constrained optimization. Algorithms for "exact" constrained optimization are complicated

and often can only be implemented in an inefficient manner. One of the basic algorithms for bound constrained optimization is *Gradient-Projection Method.*

Algorithms for the solution of bound-constrained problems seek a local minimizer $\hat{\alpha}^*$ of $O$ in the feasible set $\Omega_B = [L, U]$. The second order necessary condition can then be defined by the projection of the gradient on the feasible set $\Omega_B$. This projection can be defined componentwise by

$$P(\nabla O(D,\alpha))_i = \begin{cases} \min\{0, (\nabla O(D,\alpha))_i\} & \text{if} \quad \alpha_i = l_i \\ (\nabla O(D<\alpha))_i & \text{if} \quad l_i < \alpha_i < u_i \\ \max\{0, (\nabla O(D,\alpha))_i\} & \text{if} \quad \alpha_i = u_i \end{cases} \tag{3.19}$$

where $i = 1, \ldots, n_{par}$. The first-order necessary condition is fulfilled in a local minimizer $\hat{\alpha}^*$ if

$$P(\nabla O(D,\alpha^*)) = 0.$$

If the reduced Hessian (with respect to the free variables)

$$\mathbf{I}^T_{\mathcal{F}(\alpha^*)} \nabla^2 O(D,\alpha^*) \mathbf{I}_{\mathcal{F}(\alpha^*)}$$

is positive semi-definite, then the second order necessary condition holds in $\alpha^*$. Here, the index set $\mathcal{F}$ is the set of the free variables

$$\mathcal{F}(\alpha^*) = \{i \in \{1, \ldots, n_{par}\} : l_i < \alpha_i < u_i\}.$$

The complementary set of $\mathcal{F}(\alpha^*)$ is the active set

$$\mathcal{A}(\alpha^*) = \{i \in \{1, \ldots, n_{par}\} : \alpha_i = l_i \text{ or } \alpha_i = u_i\}.$$

### Gradient-Projection Methods

The *gradient-projection* algorithm is the prototypical method that allows large changes in the working set at each iteration. Given $\hat{\alpha}_k$, this algorithm searches along the piecewise linear path

$$P_{\Omega_B}[\hat{\alpha}_k - \lambda \nabla O(D, \hat{\alpha}_k)], \qquad \lambda \geq 0,$$

where $P_{\Omega_B}$ is the projection onto the feasible set given by Equation 3.19. A new point

$$\hat{\alpha}_{k+1} = P_{\Omega_B}[\hat{\alpha}_k - \lambda_k \nabla O(D, \hat{\alpha}_k)]$$

is obtained when a suitable $\lambda_k > 0$ is found. The search for $\lambda_k$ has to be done carefully since the function

$$\phi(\lambda) = O\left(D, P_{\Omega_B}[\hat{\alpha}_k - \lambda_k \nabla O(D, \hat{\alpha}_k)]\right)$$

is only piecewise differentiable.

If properly implemented, the gradient-projection method is guaranteed to identify the active set at a solution in a finite number of iterations. After it has identified the correct active set, the gradient-projection algorithm reduces to the steepest-descent algorithm on the subspace of free variables.

## 3.10 Regularization

Section 3.2 discusses the ill-posedness of inverse problems. A more mathematical discourse of ill-posedness and ways to resolve the problem is given below. If Equation (3.2) is well-posed, then the matrix $\mathbf{F}$ has a well-defined, continuous inverse operator $\mathbf{F}^{-1}$. In particular, $\mathbf{F}^{-1}(\mathbf{F})(\hat{\alpha}) = \hat{\alpha}$ for any $\hat{\alpha} \in \mathcal{H}_1$, where $\mathcal{H}_1 \in \mathbb{R}^{n_{par}}$ is the space of parameter; and $\text{Range}(\mathbf{F}) = \mathcal{H}_2 \in \mathbb{R}^{n_{obs}}$, the space of observable data. If $\mathbf{F}$ is a linear operator, then Equation (3.2) is well-posed if and only if $\text{Null}(\mathbf{F}) = \{\mathbf{0}\}$ and $\text{Range}(\mathbf{F}) = \mathcal{H}_2$. In other words, equation (3.2) is ill-posed when $\mathbf{F}$ is singular or almost singular.

The idea of regularization is to approximate an ill-posed problem with one that is well-posed. It allows computation of one solution of the inverse problem, but, in general, there still is not a unique solution. A regularization operator for $\mathbf{F}$ is a one parameter family of continuous operators $\mathcal{R}_\zeta : \mathcal{H}_2 \to \mathcal{H}_1$, such that $\mathcal{R}_\zeta$ is bounded and $\mathcal{R}_\zeta(z) \to \mathbf{F}^\dagger z$ as $\zeta \to 0 \quad \forall\, z \in \mathcal{D}(\mathbf{F})$, the domain of $\mathbf{F}$. Here $\mathbf{F}^\dagger$ is the generalized inverse operator as defined in Section 3.6.

Regularization of the inverse problem can be achieved in number of ways. Tikhonov regularization is a widely used technique. Tikhonov regularization is given by the following

$$\hat{\alpha}_\zeta = \mathcal{R}_\zeta(D) = \arg \min_{\alpha \in \mathcal{D}(\mathbf{F})} \left( \frac{1}{2} \parallel \mathbf{F}\hat{\alpha} - D \parallel_2^2 + \frac{\zeta}{2} \parallel \hat{\alpha} \parallel_1^2 \right) \tag{3.20}$$

This method can be thought of as penalized least squares with the second term in (3.20) being the penalty term.

Apart from the one discussed above, there are numerous other forms of regularization, namely truncated singular value decomposition, Landweber regularization and so forth. Modified Cholesky decomposition discussed previously in Section 3.9 also achieves some form of regularization via stabilization of the Hessian matrix.

Stabilization of the Hessian matrix in the Gauss-Newton algorithm (Section 3.6) is illustrated next in some detail. From previous discourse, the Gauss-Newton algorithm for the solution of a linear system is given by

$$\mathbf{H}_{GN} \Delta\hat{\alpha} = -\nabla O(D, \hat{\alpha}). \tag{3.21}$$

It was indicated earlier in Section 3.6 that $\mathbf{H}_{GN}$ is usually ill-conditioned or singular. In order to determine the descent direction using (3.21), we need to introduce some changes to $\mathbf{H}_{GN}$ such that $\mathbf{H}_{GN}$ becomes invertible.

This stabilization is achieved in two stages. A diagonal matrix $\mathbf{P}$ is used to scale the diagonal elements of $\mathbf{H}_{GN}$ by the following equation

$$P_{i,i} = (H_{GN_{i,i}})^{-\frac{1}{2}}$$

rendering a modified Gauss-Newton algorithm

$$(\mathbf{P}\mathbf{H}_{GN}\mathbf{P})\mathbf{P}^{-1}\Delta\hat{\alpha} = -\mathbf{P}\nabla O(D, \hat{\alpha})$$

Now the scaled Hessian matrix $\tilde{\mathbf{H}} = \mathbf{P}\mathbf{H}_{GN}\mathbf{P}$ has unity diagonal elements. Moreover, absolute values of the off-diagonal elements become less than unity because of the positive semidefiniteness of the original Hessian matrix. This renders the modified Hessian to be more stable.

If the modified Hessian $\tilde{\mathbf{H}}$ is still ill-conditioned or near singular, a second stage stabilization can be performed by Marquardt method. This stabilization renders

$$\tilde{\mathbf{H}}_{GN} = \mathbf{P}\mathbf{H}_{GN}\mathbf{P} + \zeta \mathbf{I} \tag{3.22}$$

where, $\zeta$ is a small positive number. A check for singularity of the modified Hessian $\tilde{\mathbf{H}}_{GN}$ is performed by Modified Cholesky decomposition. Ill-conditioning is detected by verifying whether the descent direction is sufficient descent direction or not. This means for a positive number $\kappa$ $(0 < \kappa < 1)$,

$$\frac{\nabla O(D, \hat{\alpha})^T \Delta\hat{\alpha}}{\| \nabla O(D, \hat{\alpha}) \| \quad \| \Delta\hat{\alpha} \|} < -\kappa.$$

The value of $\zeta$ in (3.22) is reduced in each successive iteration resulting in a downhill step. However, $\zeta$ is increased whenever the direction appears to be an ascent direction.

Subsequent section describes the inversion technique, Sequential Self-Calibration (SSC) method, which is in the framework of this research. Streamline-based method is applied for fast calculation of such sensitivity coefficients. The method decomposes the multiple-dimensional full flow problem into multiple 1D problems along streamlines. The sensitivity of fractional flow rate at the production well is directly related to the sensitivity of time-of-flight along each individual streamline and the sensitivity of pressure at cells along the streamline. The time-of-flight sensitivity of streamline can be obtained analytically assuming unchanged streamline geometry due to the perturbation of reservoir property. The sensitivity of pressure is obtained as part of a computationally fast single phase flow simulation. The complete set of sensitivity coefficients are obtained simultaneously with one single phase flow simulation, and the perturbations at all master locations are jointly considered. The approach of simultaneous inversion of permeability and porosity builds upon the SSC technique for simple permeability inversion.

## 3.11 Sequential Self-Calibration Technique

SSC technique utilizes a weighted least square formulation. It requires a measure of a mismatch between the inverted model responses and observed data. This measure is termed as a mismatch or objective function for the optimization subproblem. The objective function for the minimization problem in SSC method is given by:

$$O = \sum_i \sum_t W_p(i,t) \left[ p_i^{obs}(t) - p_i^{cal}(t) \right]^2 + \sum_j \sum_t W_f(j,t) \left[ f_j^{obs}(t) - f_j^{cal}(t) \right]^2 \tag{3.23}$$

where $p_i^{obs}(t)$ and $p_i^{cal}(t)$ are the observed and simulated pressure at well $i$ at time $t$. $f_j^{obs}(t)$ and $f_j^{cal}(t)$ are the observed and simulated fractional flow rate at well $i$ at time $t$. $W_p(i,t)$ and $W_f(j,t)$ are weights assigned to pressure and fractional flow rate data at different wells and at different time. For the present problem of simultaneous porosity and permeability inversion, the objective function remains same.

In case of simple permeability inversion, for the optimal permeability perturbations at master locations minimizing the objective function (3.23), sensitivity coefficients of pressure and fractional flow rate at the wells with respect to the permeability perturbations are required for all master points at all time steps. These sensitivity coefficients are:

$$s_{k,p,m,t}(i) = \frac{\partial p_i(t)}{\partial k_m}, \quad \forall i, t, k_m$$

and

$$s_{k,f,m,t}(j) = \frac{\partial f_j(t)}{\partial k_m}, \quad \forall j, t, k_m$$

with $m = 1, \ldots, n_m$ being the index of master points.

In matrix notation, discretization of the flow equation with an implicit scheme leads to the following equation:

$$[A]\{P\}^{t+1} = [B]\{P\}^t + \{f\}^t \tag{3.24}$$

where $[A]$ is the transmissibility matrix which accounts for spatial and temporal discretization, as well as boundary conditions, $[B] = [hc\phi]/\Delta t_{t+1}$, and $\{f\}^t$ is the right hand side matrix that accounts for the load vector (production and injection) and flow boundary conditions. The solution of pressure at time $t+1$ is obtained by inverting matrix $[A]$, that is,

$$\{P\}^{t+1} = [A]^{-1}[B]\{P\}^t + [A]^{-1}\{f\}^t$$

The sensitivity coefficients at time step $t+1$ can be calculated right after the pressure at time $t+1$ is obtained. The perturbation equation of parameter $k_m$ can be written as:

$$[A]\frac{\partial\{P\}^{t+1}}{\partial k_m} + \frac{\partial[A]}{\partial k_m}\{P\}^{t+1} = \frac{\partial[B]}{\partial k_m}\{P\}^t + [B]\frac{\partial\{P\}^t}{\partial k_m} + \frac{\partial\{f\}^t}{\partial k_m}, \qquad m = 1, \ldots, n_m$$

where $n_m$ is the total number of master points, thus,

$$[A]\frac{\partial\{P\}^{t+1}}{\partial k_m} = \frac{\partial[B]}{\partial k_m}\{P\}^t + [B]\frac{\partial\{P\}^t}{\partial k_m} + \frac{\partial\{f\}^t}{\partial k_m} - \frac{\partial[A]}{\partial k_m}\{P\}^{t+1}, \qquad m = 1, \ldots, n_m \tag{3.25}$$

Equation 3.25 has the same form as Equation 3.24 and the matrix $[A]$ is inverted when solving for the pressure $\{P\}^{t+1}$. The sensitivity coefficients can be obtained at the same time step $t+1$ by simple matrix operations, that is,

$$\frac{\partial\{P\}^{t+1}}{\partial k_m} = [A]^{-1}[B]\frac{\partial\{P\}^t}{\partial k_m} + [A]^{-1}\frac{\partial[B]}{\partial k_m}\{P\}^t + [A]^{-1}\frac{\partial\{f\}^t}{\partial k_m} - [A]^{-1}\frac{\partial[A]}{\partial k_m}\{P\}^{t+1},$$
$$m = 1, \ldots, n_m$$

The elements of matrices, $\frac{\partial[A]}{\partial k_m}$, $\frac{\partial[B]}{\partial k_m}$, and $\frac{\partial\{f\}^t}{\partial k_m}$ can be directly computed from the expressions of elements in matrices $[A]$, $[B]$ and $\{f\}$ with $\frac{\partial\{p\}^0}{\partial k_m} = 0$.

The objective function is updated by linearization (i.e., the perturbations of permeability at master locations, $\{\Delta M\} = \{\Delta k_1, \Delta k_2, \ldots, \Delta k_{n_m}, \}^T$). Linearization of the objective function is attained by approximating the pressure data by retaining its first order Taylor expansion, i.e.,

$$\{P^{cal}\}_t^1 \approx \{P^{cal}\}_t^0 + \frac{\partial\{P\}_t}{\partial\{M\}}\{\Delta M\}. \tag{3.26}$$

We define $\{S\}_{k,t} = \partial\{P\}_t/\partial\{M\} = \{S_{k,p,1,t}, S_{k,p,2,t}, \ldots, S_{k,p,n_m,t}\}$, where $S_{k,p,m,t} = \{s_{k,p,m,t}(j),\ j = 1, \ldots, n_w\}^T$ is the sensitivity matrix at time $t$ with respect to the permeability perturbation at location $m$ computed. $\{P^{cal}\}_t^0$ and $\{P^{cal}\}_t^1$ are pressure values at time $t$ before and after introducing a perturbation matrix $\{\Delta M\}$. Using this linear approximation and some manipulation, the objective function (3.23) can be rewritten as following:

$$O(\{P^{cal}\}^1) = O(\{P^{cal}\}^0) + \sum_{t=1}^{n_t}\{D\}_t^T\{\Delta M\} + \sum_{t=1}^{n_t}\{\Delta M\}^T[C]_t\{\Delta M\} \tag{3.27}$$

where the matrices $\{D\}_t$ and $\{C\}_t$ are expressed as follows:

$$\{D\}_t = 2\left(\{P^{cal}\}_t - \{P^{obs}\}_t\right)^T [W]_t\{S\}_t$$

$$\{C\}_t = (\{S\}_t)^T [W]_t\{S\}_t$$

The constraints used for minimizing the objective function (3.27) are simply the possible minimum and maximum values of perturbations, i.e.,

$$\{\Delta k_{\min}\} \leq \{\Delta M\} \leq \{\Delta k_{\max}\}$$

where $\{\Delta k_{\min}\} = \min\{k^0, k_{krig} - \alpha_k \sigma_{k,krig}\}$ and $\{\Delta k_{\max}\} = \max\{k^0, k_{krig} + \alpha_k \sigma_{k,krig}\}$. $\{k^0\}$ is the vector of permeability values at master points in the initial field, $\{k_{krig}\}$ and $\{\sigma_{k,krig}\}$ are kriging estimations and the corresponding kriging standard deviations at the master points based on available measured permeability data. If there is no prior $k$ measurements, $\{k_{krig}\}$ and $\{\sigma_{k,krig}\}$ can be selected as the mean and standard deviation of the desired permeability histogram. $\alpha_k$ is a constant value that specifies the interval size of the constraints.

This single-phase formulation is extended to multiphase system by incorporating fractional flow rate mismatch term in the objective function (Equation 3.23). The underlying bases of this inversion method are (1) the analytical 1D solutions of fractional flow along each streamline [10, 11, 21, 190, 191], (2) the ability to compute sensitivity coefficients of pressure over the entire field from single phase flow solutions, and (3) the assumption that streamline geometry remains unchanged with perturbed permeabilities. The sensitivity coefficients of fractional flow are obtained extremely fast by simple book-keeping of the streamlines in space. The permeability perturbations are jointly considered rather than one at a time as in the perturbation method. This method is implemented within the SSC algorithm for generating geostatistical permeability realizations that simultaneously honor transient pressure and fractional flow rate data. Streamlines are updated in each outer iteration of the SSC inversion (see Figure 3.1). The assumption of streamline geometry remaining unchanged during the perturbation is justified by comparing the SSC inverse results based on both the perturbation method and the analytical method.

### Perturbation Method

A series of measurements of reservoir response $\mathbf{d}^{obs}(\mathbf{u}, t)$ (pressure or fractional flow rate at wells) is observed at location $\mathbf{u} \in A$ and time $t$. $A$ is the entire space. The reservoir data are nonlinear functions of the parameter vector $\mathbf{a}$ (porosity or permeability): $\mathbf{d} = g(\mathbf{a})$. In this case, the function $g$ represents the multiphase flow equations. The inverse problem consists of finding the optimal parameter $\mathbf{a}$ so that the solution $\mathbf{d}^{cal}(\mathbf{u}, t) = g(\mathbf{a})$ matches the observed data $\mathbf{d}^{obs}(\mathbf{u}, t)$. Thus, the mismatch $(\mathbf{d}^{obs} - \mathbf{d}^{cal})^2$ is minimized. For a gradient-based method (e.g., steepest descent, Gauss-Newton or conjugate gradient method), to find the optimal parameter set $\mathbf{a}$, the sensitivity coefficients of $\mathbf{d}$ with respect to the parameters in $\mathbf{a}$ are required.

The simplest way of computing such sensitivity coefficients is the so- called substitution or perturbation method. The first order approximation of the sensitivity coefficient is computed in this method using a finite difference procedure. The SSC method is adapted to the perturbation method to find the optimal permeability fields that match the fractional

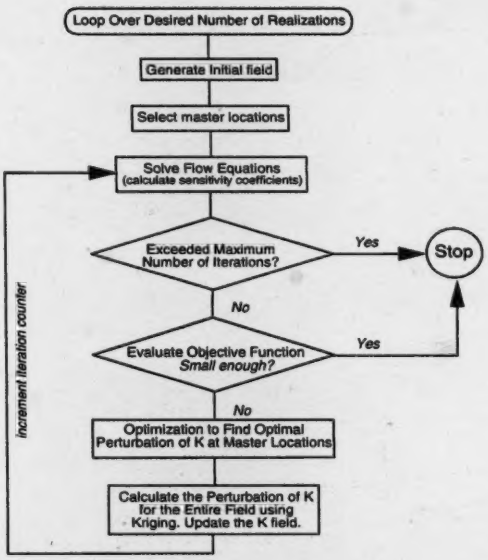


Figure 3.1: Flowchart of the Sequential Self-Calibration method.

flow data $f_j(t)$. An initial permeability field, $\mathbf{a}_0 = \mathbf{k}_0 = \{k_0(\mathbf{u}_i), i = 1, \ldots, N\}$, is selected. $N$ is the number of cells in the model. The flow equations are solved for fractional flow rate, $f_j(0)$, at all wells and at all time steps using the initial permeability field.

For all master point locations $m = 1, \ldots, n_m$ ($\ll N$ usually), a small perturbation $\Delta k_m$ is introduced individually to the initial permeability at master locations $\mathbf{u}_m$. The field $\Delta \mathbf{k}_m = \{\Delta k(\mathbf{u}_i), i = 1, \ldots, N\}$ due to the perturbation $\Delta k_m = \Delta k(\mathbf{u}_m)$, at locations $\mathbf{u}_m$ is calculated by kriging. This kriged perturbation field is then added to the initial permeability field to obtain the perturbed permeability field $\mathbf{k}' = \mathbf{k}_0 + \Delta \mathbf{k}_m$. The flow equations are solved using this perturbed field $\mathbf{k}'$ to obtain the new fractional flow rate solution, $f'_j(t)$ induced by the perturbation at master point $\mathbf{u}_m$. The sensitivity coefficient of fractional flow rate with respect to the permeability change at master location $m$ can then be computed as:

$$s_{k,f,m,t}(j) = \frac{f'_j(t) - f_j(0)}{\Delta k_m}$$

Thus, for each outer-iteration of the SSC method (see Figure 3.1), a total of $n_m + 1$ flow simulation runs are needed to obtain all sensitivity coefficients required, which is very computationally intensive. In addition, the values of $s_{k,f,m,t}(j)$, computed with this substitution method, are sensitive to the perturbation magnitude, $\Delta k_m$, particularly when the function $f$ is nonlinear. More importantly, the substitution method computes sensitivity coefficients of each parameter independently. Thus, it does not account for joint perturbations at all $n_m$ master locations. The spatial relationship of different master locations is not accounted for. This is crucial for optimization, which will be elaborated later.

### Streamline-Based Analytical Method

The sensitivity coefficients are calculated based on the streamline algorithm and the analytical relationship between fractional flow rate and the time-of-flight of streamline [10, 192].

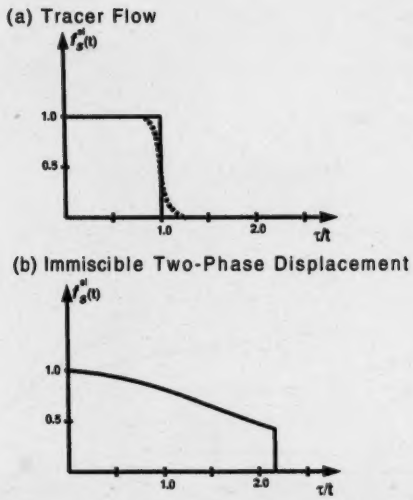


Figure 3.2: (a) Analytical 1D solution of tracer flow and its approximation using a Gaussian cumulative function (dashed line), and (b) analytical 1D solution of immiscible two-phase displacement.

The key assumption is that the streamline geometry is insensitive to the relatively small perturbations of the permeability field. This assumption is appropriate if the perturbations are kept small and all streamlines are updated after each outer loop of the SSC inversion. The complete set of sensitivity coefficients at all master points are obtained simultaneously. The spatial correlation of perturbation at multiple master locations is accounted for by using kriging weights computed for all master locations to propagate the perturbations from the master locations to the entire field.

In the streamline-based method, the fractional flow for a given producing well $j$ at time $t$ is expressed as [10]:

$$f_j(t) = \frac{\sum_{s=1}^{n_j^{sl}} q_s^{sl} f_s^{sl}(t)}{\sum_{s=1}^{n_j^{sl}} q_s^{sl}}$$

where $q_s^{sl}$ is the flow rate associated with streamline $s$, and $f_s^{sl}(t_f)$ is the fractional flow of streamline $s$ at time $t$. $n_j^{sl}$ is the total number of streamlines arriving to well $w_j$. The derivative of $f_j(t)$ with respect to the permeability perturbation at master point $m$ is then:

$$s_{k,f,m,t}(j) = \frac{\partial f_j(t)}{\partial k_m} = \frac{1}{\sum_{s=1}^{n_j^{sl}} q_s^{sl}} \sum_{s=1}^{n_j^{sl}} q_s^{sl} \frac{\partial f_s^{sl}(t)}{\partial k_m}$$

Depending on the flow regime, the fractional flow rate $f_s^{sl}(t)$ of streamline $s$ can be expressed as a function of time-of-flight $\tau_s$, that is, $f_s^{sl}(t) \sim (\frac{\tau_s}{t})$. Examples of the function $f_s^{sl}(t)$ for tracer flow and immiscible two-phase displacement are shown in Figure 3.2. These functions can either be obtained analytically or numerically [10]. Thus, for $\frac{\partial f_s^{sl}(t)}{\partial k_m}$, it is only required to compute $\frac{\partial \tau_s}{\partial k_m}$.

For simplification, a non-diffusive tracer flow (unit mobility ratio and matched fluid

density) is considered. In such case, the fractional flow rate is (see Figure 3.2a):

$$f_s^{sl}(t) = \begin{cases} 1, & if\ \tau_s \leq t \\ 0, & if\ \tau_s > t \end{cases} \tag{3.28}$$

Since Equation (3.28) is not differentiable at $\tau_s/t = 1$, a Gaussian cumulative function $F(\tau_s/t)$ with small variance is used to approximate the 1D tracer solution (Figure 3.2a):

$$f_s^{sl}(t) \approx 1 - F\left(\frac{\tau_s}{t}\right)$$

hence,

$$\frac{\partial f_s^{sl}(t)}{\partial k_m} = -\frac{1}{t} G\left(\frac{\tau_s}{t}\right) \frac{\partial \tau_s}{\partial k_m}$$

where

$$G\left(\frac{\tau_s}{t}\right) = \frac{1}{\sqrt{2\pi}\sigma} e^{-\frac{(\tau_s - t)^2}{2t^2\sigma^2}}$$

is a Gaussian distribution function with mean 1 and variance $\sigma^2$. The variance $\sigma^2$ should be small so that the approximation is close. The influence of that variance on the sensitivity coefficients is investigated later.

In the case of two-phase immiscible displacement as shown in Figure 3.2b, the derivatives of fractional flow with respect to the time-of-flight can be directly computed from Buckley-Leverett solution.

The time-of-flight of streamline $s$ is a function of total flow velocity itself is a function of permeability and total pressure along the streamline:

$$\tau_s = \int_0^s \frac{1}{v_s} ds.$$

In a discretized numerical model (see Figure 3.3), the time- of-flight of streamline $s$ from injector to producer is the sum of the time-of- flight in each cell that streamline $s$ passes through, that is,

$$\tau_s = \sum_{c=1}^{n_{s,c}} \triangle\tau_{s,c} \tag{3.29}$$

$n_{s,c}$ being the number of cells crossed by streamline $s$ from injector to producer, and $\triangle\tau_{s,c}$ is the associated time-of-flight for streamline $s$ to pass through cell $c$.

In Figure 3.3, for example, the total number of cells crossed by the streamline from injector to producer is 13 ($= n_{s,c}$). Based on the semi-analytical solution [51, 161], that is, assuming linear variation of velocity in all directions within a numerical cell, the cell (or differential) time-of-flights are:

- if the streamline exits the cell $c$ in the $X$-direction,

$$\triangle\tau_{s,c} = \triangle\tau_{s,c,x} = \frac{1}{J_x} \ln\left\{\frac{v_{x,0} + J_x(x_e - x_0)}{v_{x,0} + J_x(x_i - x_0)}\right\} \tag{3.30}$$

- if the streamline exits the cell $c$ in the $Y$-direction,

$$\triangle\tau_{s,c} = \triangle\tau_{s,c,y} = \frac{1}{J_y} \ln\left\{\frac{v_{y0} + J_y(y_e - y_0)}{v_{y0} + J_y(y_i - y_0)}\right\} \tag{3.31}$$

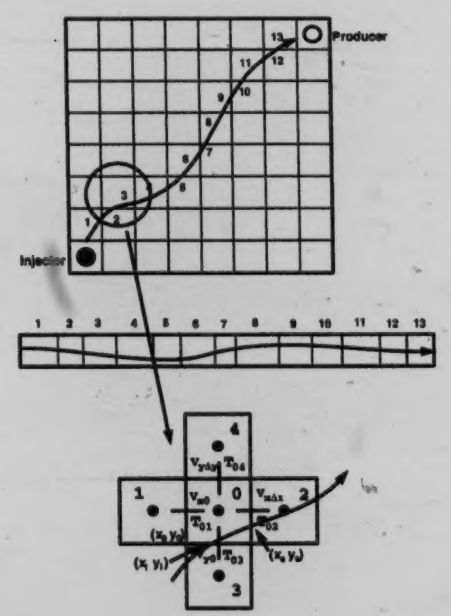


Figure 3.3: Schematic illustration of tracking a streamline through a discretized numerical model.

where

$$J_x = \frac{v_{x,\triangle x} - v_{x,0}}{\triangle x}$$

$$J_y = \frac{v_{y,\triangle y} - v_{y,0}}{\triangle y}$$

$$\begin{aligned}
v_{x,0} &= -T_{01}\frac{p_0 - p_1}{\triangle x \phi \mu}, & T_{01} &= \frac{2k_0k_1}{k_0 + k_1} \\
v_{x,\triangle x} &= -T_{02}\frac{p_2 - p_0}{\triangle x \phi \mu}, & T_{02} &= \frac{2k_0k_2}{k_0 + k_2} \\
v_{y,0} &= -T_{03}\frac{p_0 - p_3}{\triangle y \phi \mu}, & T_{03} &= \frac{2k_0k_3}{k_0 + k_3} \\
v_{y,\triangle y} &= -T_{04}\frac{p_4 - p_0}{\triangle y \phi \mu}, & T_{04} &= \frac{2k_0k_4}{k_0 + k_4}
\end{aligned} \tag{3.32}$$

where $\triangle x$ and $\triangle y$ are the cell size in $X$ and $Y$ directions, $\phi$ the porosity, $T_{01}$ to $T_{04}$ the transmissibilities for the four interfaces of the cell intersected by the streamline (cell 0 in Figure 3.3), $p_0$ to $p_4$ and $k_0$to $k_4$ the pressure and permeability values at the current (0) and the surrounding (1 to 4) cells, respectively (see Figure 3.3). $(x_i, y_i)$ and $(x_e, y_e)$ are the inlet and exit coordinates of the streamline in current cell 0, and $(x_0, y_0)$ is the coordinate of the lower-left corner of current cell 0.

From Equations (3.29) to (3.32), the derivatives of time-of- flights with respect to permeabilities are derived to be:

$$\frac{\partial \tau_s}{\partial k_j} = \sum_{c=1}^{n_{s,c}} \left\{ \sum_{g=1}^{4} \frac{\partial \triangle \tau_{s,c}}{\partial T_{0g}} \frac{\partial T_{0g}}{\partial k_j} + \sum_{l=0}^{4} \frac{\partial \triangle \tau_{s,c}}{\partial p_l} \frac{\partial p_l}{\partial k_j} \right\}$$

$\frac{\partial \Delta \tau_{s,c}}{\partial T_{0g}}$ and $\frac{\partial \Delta \tau_{s,c}}{\partial p_l}$ can be computed from Equations (3.30) and (3.31). $\frac{\partial p_l}{\partial k_j}$ are the sensitivity coefficients of pressure with respect to permeability change. Finally [81]

$$\frac{\partial T_{0g}}{\partial k_j} = \frac{T_{0g}^2}{2}\left\{\frac{\alpha_{k,j,0}}{k_0^2} + \frac{\alpha_{k,j,g}}{k_g^2}\right\}$$

$\alpha_{k,j,0}$ and $\alpha_{k,j,g}$ are the permeability kriging weights attributed to master point $j$, cells 0 and $g$ ($g = 1, \ldots, 4$). Since the kriging weights are computed accounting for all master points [114], the resulting sensitivity coefficients account for the spatial distribution of all master points. The permeability perturbations at all master locations are now considered jointly rather that one at a time. The complete set of sensitivity coefficients at all master points are obtained simultaneously. In addition, there is no need to choose a specific value of $\Delta k_j$ before computing sensitivity coefficients.

## Derivation of Time-of-Flight and Derivatives

The derivations of the time-of-flights and their derivatives or the sensitivity coefficients are laid out in this section. Essentially, this calculation reduces to a simple book-keeping of the streamlines in the simulation model. This is both mathematically simple and computationally efficient. Extension of this method to other types of flow, such as immiscible two-phase flow and 3D flow, should be straightforward.

From Equations (3.30) to (3.32), the cell time-of-flights, derived, are:

$$\Delta\tau_{s,c,x} = \frac{-\Delta x^2 \phi}{A_x} \ln\left\{\frac{\Delta x T_{01}(p_0 - p_1) + A_x(x_e - x_0)}{\Delta x T_{01}(p_0 - p_1) + A_x(x_i - x_0)}\right\} \tag{3.33}$$

$$\Delta\tau_{s,c,y} = \frac{-\Delta y^2 \phi}{A_y} \ln\left\{\frac{\Delta y T_{01}(p_0 - p_3) + A_y(y_e - y_0)}{\Delta y T_{01}(p_0 - p_3) + A_y(y_i - y_0)}\right\} \tag{3.34}$$

where $A_x = T_{01}(p_1 - p_0) + T_{02}(p_2 - p_0)$, and $A_y = T_{03}(p_3 - p_0) + T_{04}(p_4 - p_0)$.

The derivatives, required in Equation (3.11) in the $x$- direction, are stated below (refer to Figure 3.3). Taking partial derivatives of Equation 3.33 with respect to $T_{01}$, $T_{02}$, $T_{03}$, $T_{04}$, $p_0$, $p_1$, $p_2$, $p_3$ and $p_4$, respectively, Equations (3.35) to (3.41) are obtained.

$$\frac{\partial \Delta \tau_{s,c,x}}{\partial T_{01}} = \frac{-\Delta x^2 \phi (p_0 - p_1)}{A_x^2}\left\{\ln\frac{D_x}{C_x} + A_x\frac{[\Delta x - (x_e - x_0)]\,C_x - [\Delta x - (x_i - x_0)]\,D_x}{C_x D_x}\right\} \tag{3.35}$$

$$\frac{\partial \Delta \tau_{s,c,x}}{\partial T_{02}} = \frac{-\Delta x^2 \phi (p_0 - p_2)}{A_x^2}\left\{\ln\frac{D_x}{C_x} + A_x\frac{-(x_e - x_0)C_x + (x_i - x_0)D_x}{C_x D_x}\right\} \tag{3.36}$$

$$\frac{\partial \Delta \tau_{s,c,x}}{\partial T_{03}} = \frac{\partial \Delta \tau_{i,s,x}}{\partial T_{04}} = 0 \tag{3.37}$$

$$\frac{\partial \Delta \tau_{s,c,x}}{\partial p_0} = \frac{-\Delta x^2 \phi}{A_x^2}\left\{-(T_{01} + T_{02})\ln\left(\frac{D_x}{C_x}\right) + A_x\frac{[\Delta x T_{01} - (T_{01} + T_{02})(x_e - x_0)]\,C_x - [\Delta x T_{01} - (T_{01} + T_{02})(x_i - x_0)]\,D_x}{C_x D_x}\right\} \tag{3.38}$$

$$\frac{\partial \triangle \tau_{s,c,x}}{\partial p_1} = \frac{-\triangle x^2 \phi}{A_x^2} \left\{ T_{01} \ln\left(\frac{D_x}{C_x}\right) + A_x \frac{[-\triangle x T_{01} + T_{01}(x_e - x_0)]\, C_x - [\triangle x T_{01} + T_{01}(x_i - x_0)]\, D_x}{C_x D_x} \right\} \tag{3.39}$$

$$\frac{\partial \triangle \tau_{s,c,x}}{\partial p_2} = \frac{-\triangle x^2 \phi}{A_x^2} \left\{ T_{02} \ln\left(\frac{D_x}{C_x}\right) + A_x \frac{T_{02}(x_e - x_0) C_x - T_{02}(x_i - x_0) D_x}{C_x D_x} \right\} \tag{3.40}$$

$$\frac{\partial \triangle \tau_{s,c,x}}{\partial p_3} = \frac{\partial \triangle \tau_{i,s,x}}{\partial p_4} = 0 \tag{3.41}$$

where $C_x = \triangle x T_{01}(p_0 - p_1) + A_x(x_i - x_0)$ and $D_x = \triangle x T_{01}(p_0 - p_1) + A_x(x_e - x_0)$.

Similarly, in the $y$-direction, taking partial derivatives of Equation 3.34 with respect to $T_{03}$, $T_{04}$, $T_{01}$, $T_{02}$, $p_0$, $p_3$, $p_4$, $p_1$ and $p_2$, respectively, Equations (3.42) to (3.48) are obtained.

$$\frac{\partial \triangle \tau_{s,c,y}}{\partial T_{03}} = \frac{-\triangle y^2 \phi (p_0 - p_3)}{A_y^2} \left\{ \ln \frac{D_y}{C_y} + A_y \frac{[\triangle y - (y_e - y_0)]\, C_y - [\triangle y - (y_i - y_0)]\, D_y}{C_y D_y} \right\} \tag{3.42}$$

$$\frac{\partial \triangle \tau_{s,c,y}}{\partial T_{04}} = \frac{-\triangle y^2 \phi (p_0 - p_4)}{A_y^2} \left\{ \ln \frac{D_y}{C_y} + A_x \frac{-(y_e - y_0) C_y + (y_i - y_0) D_y}{C_y D_y} \right\} \tag{3.43}$$

$$\frac{\partial \triangle \tau_{s,c,y}}{\partial T_{01}} = \frac{\partial \triangle \tau_{s,c,y}}{\partial T_{02}} = 0 \tag{3.44}$$

$$\frac{\partial \triangle \tau_{s,c,y}}{\partial p_0} = \frac{-\triangle y^2 \phi}{A_y^2} \left\{ -(T_{03} + T_{04}) \ln\left(\frac{D_y}{C_y}\right) + A_y \frac{[\triangle y T_{03} - (T_{03} + T_{04})(y_e - y_0)]\, C_y - [\triangle y T_{03} - (T_{03} + T_{04})(y_i - y_0)]\, D_y}{C_y D_y} \right\} \tag{3.45}$$

$$\frac{\partial \triangle \tau_{s,c,y}}{\partial p_3} = \frac{-\triangle y^2 \phi}{A_y^2} \left\{ T_{03} \ln\left(\frac{D_y}{C_y}\right) + A_y \frac{[-\triangle y T_{03} + T_{03}(y_e - y_0)]\, C_y - [\triangle y T_{03} + T_{03}(y_i - y_0)]\, D_y}{C_y D_y} \right\} \tag{3.46}$$

$$\frac{\partial \triangle \tau_{s,c,y}}{\partial p_4} = \frac{-\triangle y^2 \phi}{A_y^2} \left\{ T_{04} \ln\left(\frac{D_y}{C_y}\right) + A_y \frac{T_{04}(y_e - y_0) C_y - T_{04}(y_i - y_0) D_y}{C_y D_y} \right\} \tag{3.47}$$

$$\frac{\partial \triangle \tau_{s,c,y}}{\partial p_1} = \frac{\partial \triangle \tau_{s,c,y}}{\partial p_2} = 0 \tag{3.48}$$

where $C_y = \triangle y T_{03}(p_0 - p_3) + A_y(y_i - y_0)$ and $D_y = \triangle y T_{03}(p_0 - p_3) + A_y(y_e - y_0)$.

This elegant account of the streamline derivatives is an essential feature of the streamline-based analytical technique. For increasingly large grid sizes, this method with simple book-keeping of streamlines proves to be far more efficient than the perturbation methods. The derivatives here have been derived for 2D grids, which can easily be extended to 3D grids.

A simplification to the computation of the time-of-flights derivatives can be implemented. One can assume that the contribution of the second term of the derivation shown in Equation 3.32 is negligible. So the derivatives of time-of-flights with respect to permeabilities will now be:

$$\frac{\partial \tau_s}{\partial k_j} = \sum_{c=1}^{n_{s,c}} \left\{ \sum_{g=1}^{4} \frac{\partial \triangle \tau_{s,c}}{\partial T_{0g}} \frac{\partial T_{0g}}{\partial k_j} \right\}$$

with the notations having earlier implications. Further simplification, which precludes a few computational steps, can be implemented if one considers $\frac{\partial \triangle \tau_{s,c}}{\partial k_c} \frac{\partial k_c}{\partial k_j}$ instead of $\frac{\partial \triangle \tau_{s,c}}{\partial T_{0g}} \frac{\partial T_{0g}}{\partial k_j}$, where $k_c$ is the permeability at cell $c$. This reduces the necessary derivative equation to:

$$\frac{\partial \tau_s}{\partial k_j} = \sum_{c=1}^{n_{s,c}} \frac{\partial \triangle \tau_{s,c}}{\partial k_j} = \sum_{c=1}^{n_{s,c}} \frac{\partial \triangle \tau_{s,c}}{\partial k_c} \frac{\partial k_c}{\partial k_j}. \tag{3.49}$$

The partial derivatives in Equation 3.49 can be derived from the basic equations. Combining Equations 3.11, 3.29 and Darcy's law one can obtain:

$$\triangle \tau_{s,c} = \int_{s_{in}}^{s_{out}} \frac{1}{v_{s,c}} dr = \int_{s_{in}}^{s_{out}} \frac{\phi_c \mu}{k_c |J|} dr$$

where $\phi$, $\mu$ and $k_c$ are porosity, viscosity and permeability at cell $c$, and $|J|$ is the absolute value of the pressure gradient. Assuming independence of the time-of- flights to the pressure gradient, the partial derivatives can be approximated to be:

$$\frac{\partial \triangle \tau_{s,c}}{\partial k_c} = -\frac{\triangle \tau_{s,c}}{k_c}.$$

Applying the above to Equation 3.49, the derivative equation will be reduced to:

$$\frac{\partial \tau_s}{\partial k_j} = \sum_{c=1}^{n_{s,c}} \frac{\partial \triangle \tau_{s,c}}{\partial k_c} \frac{\partial k_c}{\partial k_j} = -\sum_{c=1}^{n_{s,c}} \frac{\triangle \tau_{s,c}}{k_c} \alpha_{k,j,c}$$

where $\alpha_{k,j,c}$ is the permeability kriging weight of master point $j$ to cell $c$, which accounts for the correlation of permeability at the two locations. Studies indicate faster convergence using this simplified approach with little loss of accuracy.

# Chapter 4

# Simultaneous Inversion of $\phi/\ln(k)$ Using Multiple Well Production Data

In this chapter, we present an inversion algorithm for simultaneous generation of porosity and permeability models using available production data and static information. Applications with synthetic and realistic examples are discussed. A number of implementation issues and sensitivity studies are also discussed.

## 4.1 Simultaneous Inversion Problem

It is a common practice to build geostatistical reservoir porosity models by kriging-based simulation techniques [67] and then generate permeability models by collocated cokriging-based simulation [210] using porosity values. The inversion algorithm described here is based on the same underlying geostatistical equations.

The approach uses simple kriging of porosity ($\phi$) at all locations, then collocated cokriging to estimate $y = \ln(k)$. The simple kriging equation for $\phi$ at location $i$ is:

$$\phi_i = \sum_{j=1}^{n_{mp}} \tau_{i,j}^{\phi} \phi_j \tag{4.1}$$

where $\phi_j,\ j = 1, \ldots, n_{mp}$ are the porosity values at the master points, $n_{mp}$ is the number of master points, and $\tau_{i,j}^{\phi}$ are the kriging weights at a location $i$ for porosity value at master point $\phi_j$. While the collocated cokriging equations for $y_i$ at location $i$ is given by

$$y_i = \sum_{j=1}^{n_{mp}} \tau_{i,j}^{y} y_j + \xi_i \phi_i \tag{4.2}$$

where $y_j,\ j = 1, \ldots, n_{mp}$ are the log permeability values at the master points, $\tau_{i,j}^{y}$ are the kriging weights at location $i$ for $y_j$ value at any master point, $\xi_i$ is the collocated kriging weight at location $i$ for the collocated secondary variable $\phi_i$.

A Markov assumption is then used that entails a linear regression model between $y$ and $\phi$:

$$y = \rho\phi + r \tag{4.3}$$

where $\rho$ is the global correlation coefficient between $y$ and $\phi$, and $r$ a random component.

Relationship (4.3) is used as a closure. Combining above relationships, we have:

$$\frac{\partial y_i}{\partial y_j} = \tau^y_{i,j} + \xi_i \frac{\partial \phi_i}{\partial y_j} = \tau^y_{i,j} + \xi_i \frac{\partial \phi_i}{\partial \phi_j}\frac{\partial \phi_j}{\partial y_j} = \tau^y_{i,j} + \xi_i \tau^\phi_{i,j}\frac{1}{\rho} \tag{4.4}$$

This equation describes the change of $y$ at any location $i$ due to the change of $y$ at a given master point $j$. The second term is set to zero if $\rho = 0$; then the collocated kriging equation becomes a simple kriging equation.

Based on this, we can build the correlation relationship into the flow equations to get the sensitivity of pressure on $y$ and $\phi$. Details follow.

Discretization of flow equation with an implicit scheme leads to the following equation:

$$\mathbf{A}\mathbf{p}^{n+1} = \mathbf{B}\mathbf{p}^n + \mathbf{f}^n \tag{4.5}$$

$\mathbf{A}$, $\mathbf{B}$, and $\mathbf{f}$ have closed form functional relation. It is possible to obtain the derivatives of $\mathbf{A}$, $\mathbf{B}$, and $\mathbf{f}$ with respect to $y$. Note that $\mathbf{A}$ and $\mathbf{B}$ are explicit functions of $k = \exp(y)$, and only the diagonal terms of these matrices have terms depending on $\phi$; however, since $y$ is correlated to $\phi$ (as shown in Equation 4.2), non-diagonal terms of both $\mathbf{A}$ and $\mathbf{B}$ are also dependent on $\phi$. Thus, we need to consider $\phi$ as a variable as well.

Elements of $\mathbf{A}$ are the sum of transmissibilities. Using geometric averages of permeabilities in the transmissibility calculation, we have the following for any two adjacent grid cells 1 and 2

$$T_{1,2} = \sqrt{k_1 k_2} = \exp\left\{\frac{y_1 + y_2}{2}\right\} \tag{4.6}$$

where $y_1 = \log(k_1)$ and $y_2 = \log(k_2)$. Consequently, the derivatives are computed as

$$\frac{\partial T_{1,2}}{\partial y_j} = \frac{1}{2} T_{1,2}\left(\frac{\partial y_1}{\partial y_j} + \frac{\partial y_2}{\partial y_j}\right) \tag{4.7}$$

The sensitivity coefficients in the above equation can be calculated using (4.4).

For terms of $\mathbf{A}$ and $\mathbf{B}$ having $\phi$ variable, we need

$$\frac{\partial \phi_i}{\partial y_j} = \frac{\partial \phi_i}{\partial \phi_j}\frac{\partial \phi_j}{\partial y_j} = \frac{\tau^\phi_{i,j}}{\rho} \tag{4.8}$$

Again, the right hand side of the above equation is set to 0 when $\rho = 0$. Using Equations 4.7 and 4.8, we can compute derivatives of $\mathbf{A}$, $\mathbf{B}$, and $\mathbf{f}$ with respect to $y$, and obtain the sensitivity of pressure on $y$, that is, $\partial p_i / \partial y_j$.

The sensitivity of pressure on porosity can be similarly calculated. In order to compute derivatives of $\mathbf{A}$, $\mathbf{B}$, and $\mathbf{f}$ with respect to $\phi$ at any master point $j$, we need the sensitivity coefficients of $y_i$ with respect to $\phi_j$. Applying Equation 4.4 and chain rule, we have

$$\frac{\partial y_i}{\partial \phi_j} = \frac{\partial y_i}{\partial y_j}\frac{\partial y_j}{\partial \phi_j} = \rho\frac{\partial y_i}{\partial y_j} = \rho\left(\tau^y_{i,j} + \xi_i \tau^\phi_{i,j}\frac{1}{\rho}\right) = \rho\tau^y_{i,j} + \xi_i \tau^\phi_{i,j} \tag{4.9}$$

Introducing the above relationships into the derivative of Equation 4.5, we get

$$\frac{\partial p_i}{\partial \phi_j} = \frac{\partial p_i}{\partial y_j}\frac{\partial y_j}{\partial \phi_j} = \rho\frac{\partial p_i}{\partial y_j} \tag{4.10}$$

The above relationship indicates that we do not need to solve separately for sensitivity coefficient of porosity. The linear regression relationship can be used to get the sensitivity coefficients of the response variables with respect to $\phi$ from those with respect to $y$. Again, when $\rho = 0$, Equation 4.10 can not be used, and we need to use 4.9 to compute the derivatives in Equation 4.5 to get the sensitivity coefficients with respect to porosity. Such calculation would be simple since there is no permeability term. It is now possible to perform the optimization to find the optimal $\Delta y_j$ and $\Delta\phi_j$, $j = 1, \ldots, n_{mp}$ .

The optimal perturbations must then be propagated to the entire domain using collocated cokriging (Equations 4.1 and 4.2). The algorithm for the simultaneous porosity and permeability inversion:

1. Select master point locations $j = 1, \ldots, n_{mp}$.
2. Perform simple kriging of $\phi$ to get kriging weights $\tau_{i,j}^{\phi}$ at location $i$ for $\phi_j$, $j = 1, \ldots, n_{mp}$.
3. Perform collocated cokriging with Markov-type assumption and obtain cokriging weights $\tau_{i,j}^{y}$ and $\xi_i$.
4. Solve pressure equations.
5. Compute derivatives of matrices in Equation 4.5 with respect to $y_j$ for all master points.
6. Compute sensitivity coefficients with respect to $y$.
7. Compute sensitivity coefficients with respect to $\phi$ using Equation 4.9 or 4.10.
8. Perform optimization to compute optimal change of $\Delta y_j$ and $\Delta\phi_j$.
9. Propagate changes to entire domain.
10. Update $\phi$ and $y$ fields.
11. Repeat Step (1) to (10) until convergence is achieved.

The algorithm for computing the sensitivity coefficients is based on the kriging equations for porosity and collocated cokriging equation for permeability modeling. We use the relationship between porosity and permeability in the kriging equations and permeability sensitivity of the pressure equation. This drastically reduces the computation time compared to separate porosity and permeability sensitivity calculation.

A facility for histogram transformation of the inverted $\phi$ and $\ln(k)$ fields to some global distributions is imcorporated in the integration algorithm. This transformation may be perfomed after Step (10) in the above mentioned workflow. In order to honor hard data at well locations, the constraints are set up using very low variance values. Thus, there is a flexibility of variation within narrow range to account for the error components in the hard data. The code allows one to input these variances at the hard data location explicitly. However, at other master points the constraints are given by the kriging variances.

Allocation of master points is performed in a random manner. However, to maintain an areally unclustered distribution of the locations of the master points, they are allocated in a 2D random grid selection procedure. The locations of the master points can be changed

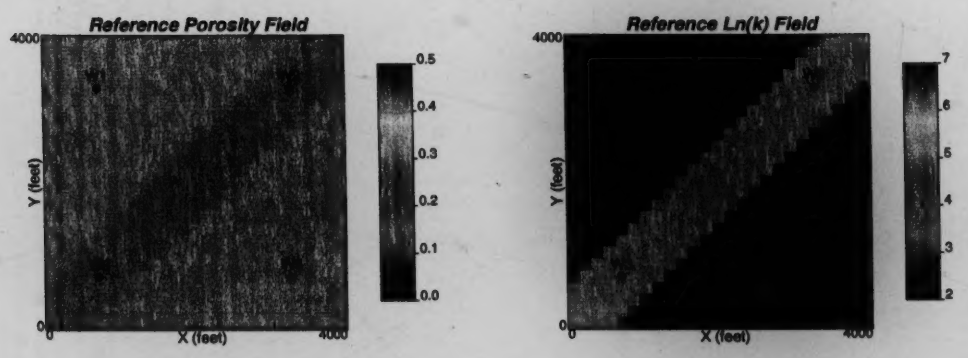


Figure 4.1: Reference $\phi$ and $\ln(k)$ fields: Deterministic Example.

after a fixed number of outer iterations. This number is provided as a parameter at the start of the execution. It should be noted that at all well blocks with production data, master points are assigned automatically.

Subsequent sections discuss the application of the algorithm with some synthetic reservoir models. Some implementation issues and sensitivity analyses are also documented.

## 4.2 Example 1: A Deterministic Example

A synthetic example is used here to evaluate the ability of the algorithm to generate models of porosity and permeability from multiple well production data. The reference $\phi$ and $\ln(k)$ models are constructed, and then, the dynamic pressure responses at a number of wells, caused by changing flow rates, are obtained by flow simulation. The dynamic flow rate and pressure data and information on the variograms of $\phi$ and $\ln(k)$ are used to invert for both $\phi$ and $\ln(k)$. Then, the inverted fields are compared with the reference field to evaluate the capability of the algorithm.

The 2D 4,000-ft square domain will be discretized into 25 $\times$ 25 grid cells of 160 $\times$ 160 ft. There is a high porosity (0.25) and high permeability (500 mD) band connecting the lower-left corner and upper-right corner. The porosity and the permeability in other areas are 0.175 and 10 mD, respectively. Figure 4.1 shows the reference $\phi$ and $\ln(k)$ fields. There are four wells: W1 at the center of the cell (5,21), W2 at (21,21),W3 at (5,5), and W4 at (21,5). Wells are shown in Figure 4.1. The four boundaries are no-flow boundaries, reservoir thickness is 100 ft, viscosity is 0.2 cp, formation compressibility is $10^{-6}$ psi$^{-1}$, and well radius is 0.3 ft. For global distribution of $\phi$ and $\ln(k)$, we used the reference bimodal distributions.

Figure 4.2 shows the imposed producing rates and the corresponding pressure responses at the different wells solved numerically. Different shut-in times for different wells create well interference so that more information on spatial variations of $\phi$ and $\ln(k)$ is contained in the production data.

There are many implementation options. Results obtained using various options are informative. Sensitivity of the inverted models to the selection of various anisotropy, initial fields, optimization parameters will be demonstrated later.

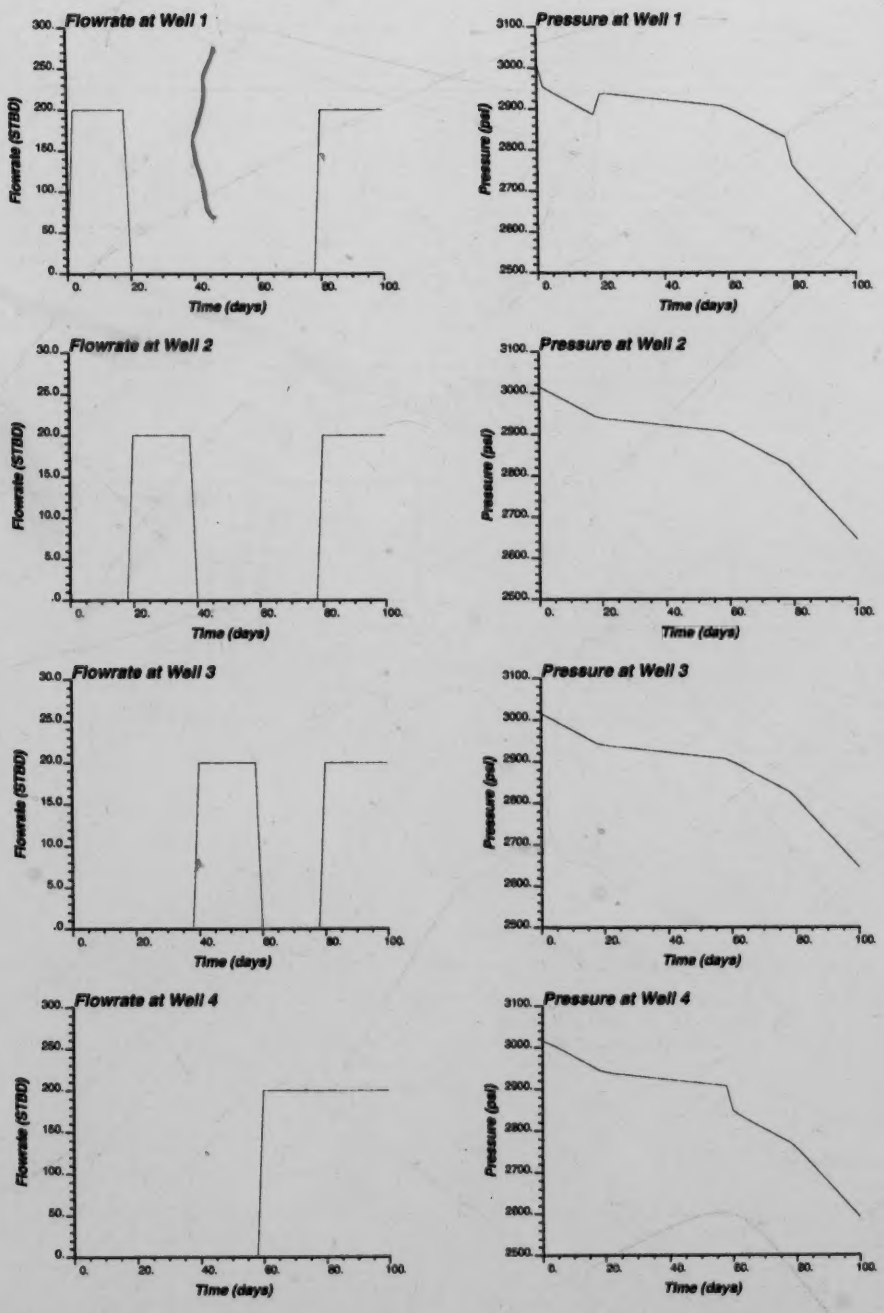


Figure 4.2: Production data (pressure and flow rates) obtained from the reference field: Deterministic Example.

| V. No. | Type | Sill | Range X - Y (ft) | Angle ($^o$) |
|---|---|---|---|---|
| 0 | Nugget | 0.05 | | |
| 1 | Sph | 0.95 | 8000 - 1100 | 45 |

Table 4.1: Prior variogram information used for $\phi$: Example 1.

| V. No. | Type | Sill | Range X - Y (ft) | Angle ($^o$) |
|---|---|---|---|---|
| 0 | Nugget | 0.05 | | |
| 1 | Sph | 0.95 | 8100 - 1000 | 45 |

Table 4.2: Prior variogram information used for $\ln(k)$ in Example 1.

For all the runs below, we used constant initial $\phi$ and $\ln(k)$ fields of $\phi = 0.4$ and $\ln(k) = 3.15$. Anisotropic variograms with very long correlation length (about 8,000 ft) in the $45^0$ direction for both $\phi$ and $\ln(k)$ were employed. The prior variogram models used in the following runs (unless stated otherwise) for $\phi$ and $\ln(k)$ are given in Tables 4.1 and 4.2:

### Run 1: Inversion with production data, global histogram, prior information on variography, and local hard data

Local hard data used are shown in Figure 4.3. The inverted models are obtained after 17 outer iterations (75 seconds in 733 MHz dual processor workstation). The pressure responses in the updated porosity and permeability fields converge to the reference pressure data. These inverted models are shown in Figure 4.4. The connected high porosity/permeability band connecting W2 and W3 is clearly evident. Figure 4.5 shows the pressure values at the four wells computed from the true (from reference), initial and final updated porosity and permeability fields. Pressure responses in the initial field deviate significantly from the true values because of the poor model; however, the updated fields accurately reproduce the pressure data from all wells. The objective function values of the inversion process is shown in Figure 4.6. Final average pressure mismatch (in $L^2$ norm sense) for 200 data was 4.1 psi, which is remarkably small as evident from the pressure match in Figure 4.5. Updated porosity and permeability fields after each outer iteration of the inversion method are shown in Figures 4.7 and 4.8.

It is interesting to see $\phi$ and $\ln(k)$ models and their pressure responses when only static information is used. Figure 4.9 shows conditionally simulated porosity and permeability fields using local hard data, prior global distribution and information on variography. Thus, no production data information is captured in these models. The models themselves appear to have the major features of the reference models. Nevertheless, the pressure responses (shown in Figure 4.10) computed from these models deviate from those in the reference field significantly.

If the global distribution is not used in static inversion (conditional simulation), the models and the pressure responses deviate drastically from those of the reference model. Figure 4.11 shows these conditionally simulated porosity and permeability fields. Figure 4.12 shows the computed pressure responses of these models. Comparison with the models inverted using production data (Figure 4.5) gives us an idea of what information can be

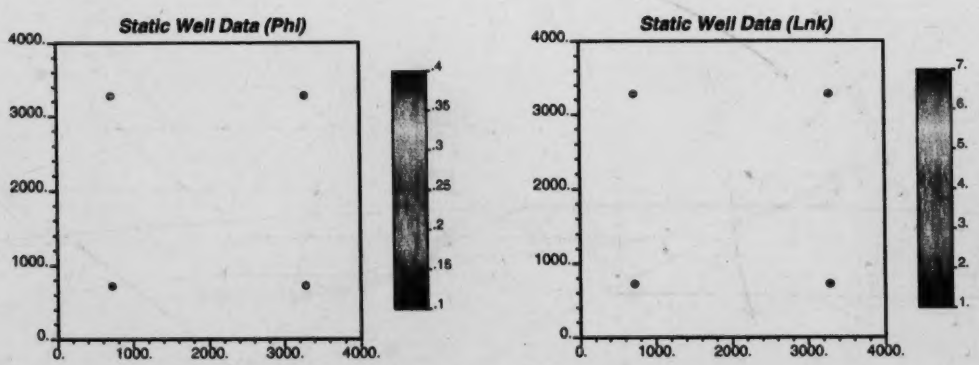


Figure 4.3: Static well data for $\phi$ and $\ln(k)$: Deterministic Example Run 1.

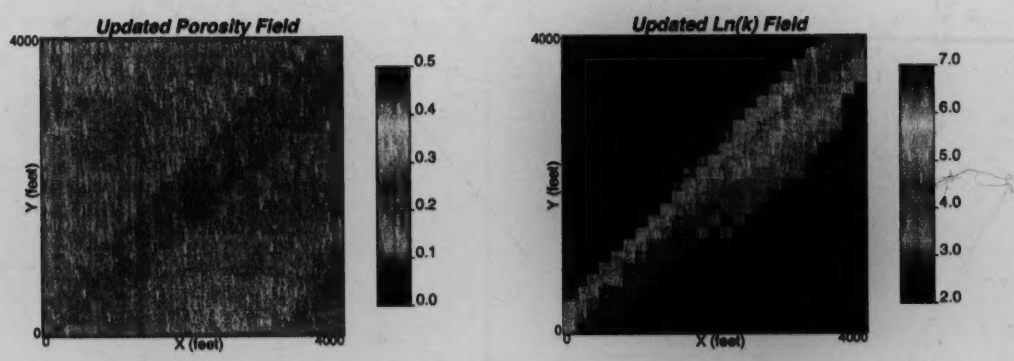


Figure 4.4: Updated $\phi$ and $\ln(k)$ fields: Deterministic Example Run 1.

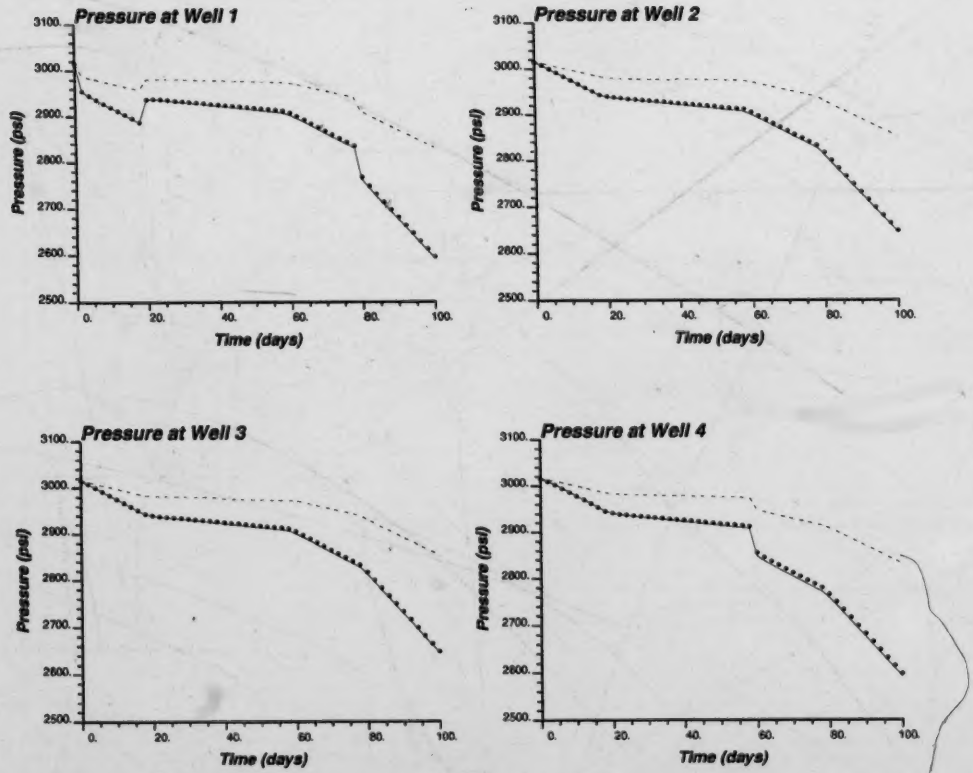


Figure 4.5: Pressure responses computed from initial (dashed lines) and updated (bullets) $\phi$ and $\ln(k)$ fields with the true data (solid lines): Deterministic Example Run 1.

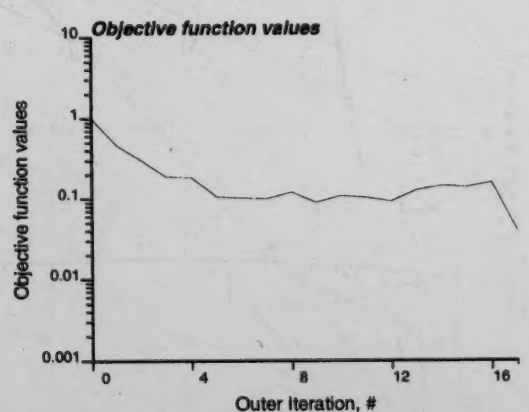


Figure 4.6: Objective function values of the inversion process: Deterministic Example Run 1.

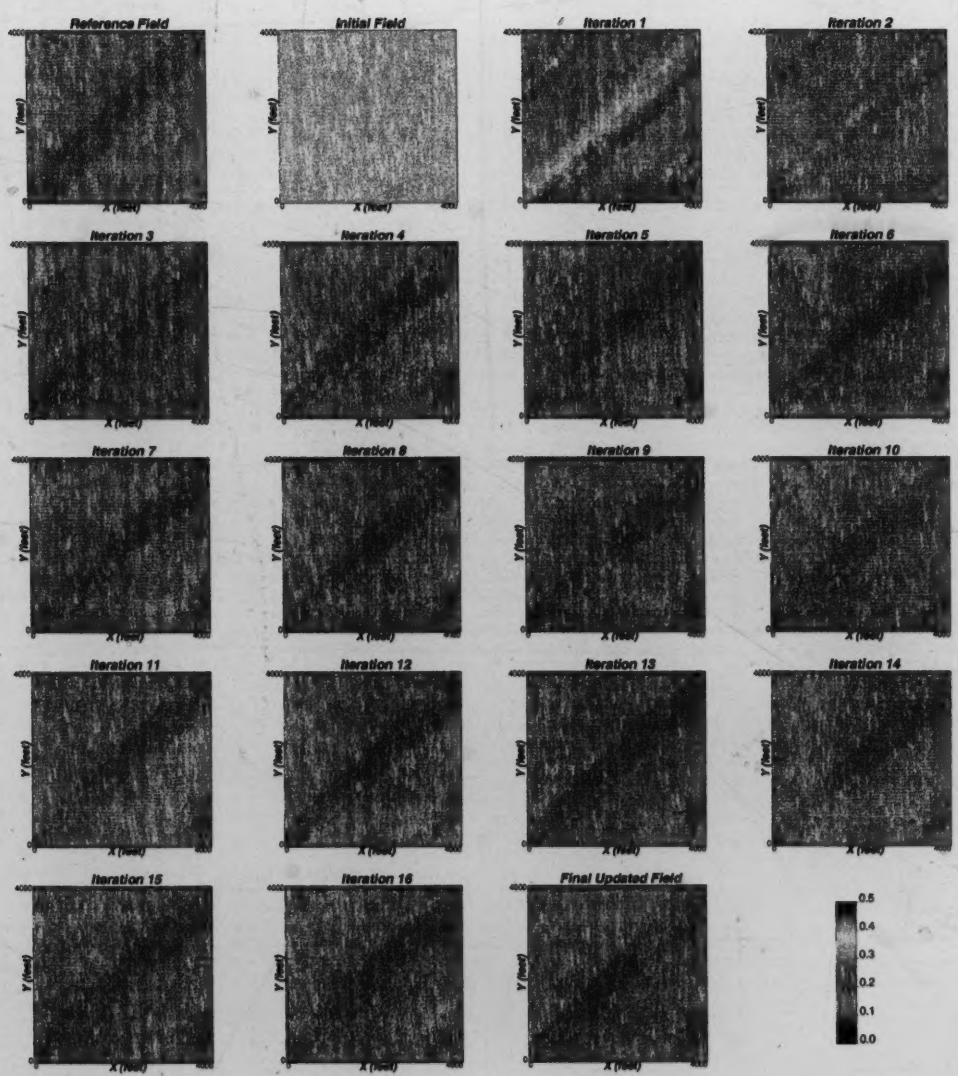


Figure 4.7: Updated $\phi$ fields at each iteration of the inversion process: Deterministic Example Run 1.

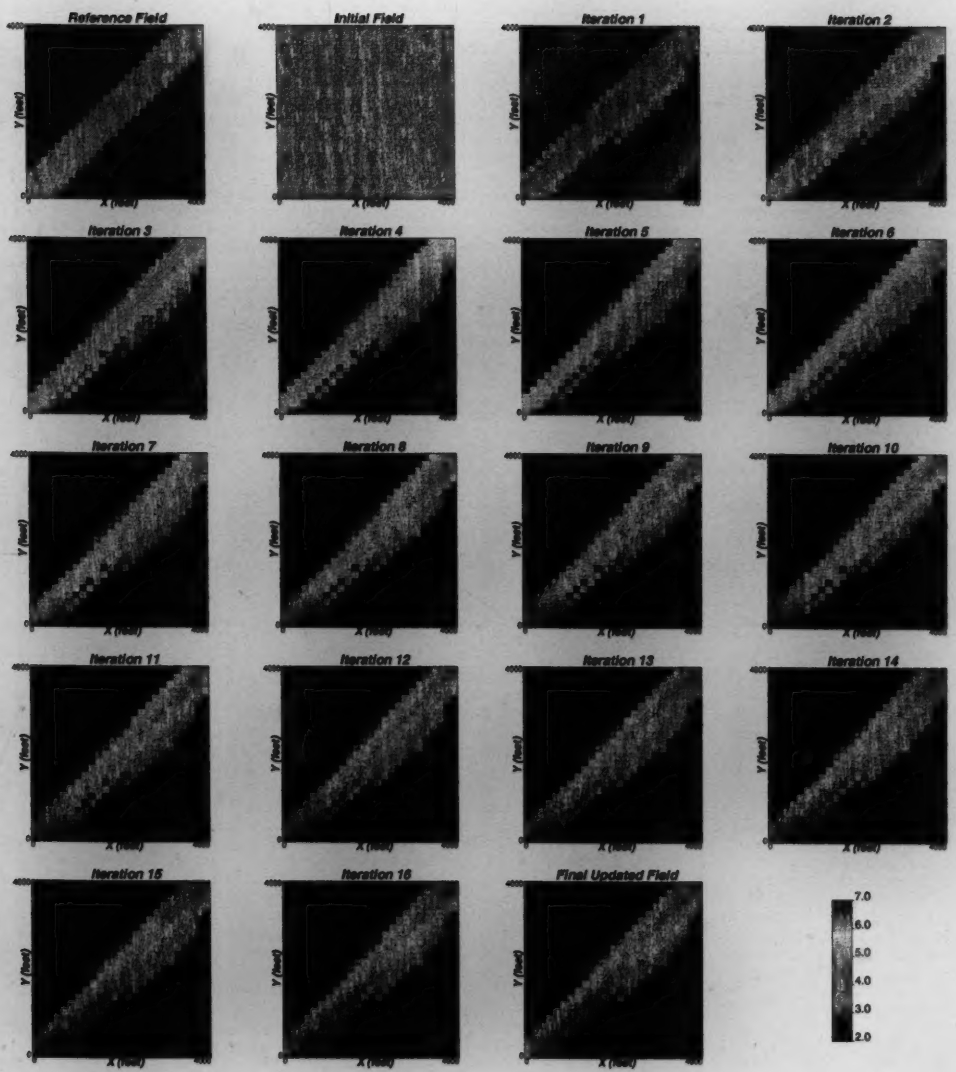


Figure 4.8: Updated $\ln(k)$ fields at each iteration of the inversion process: Deterministic Example Run 1.

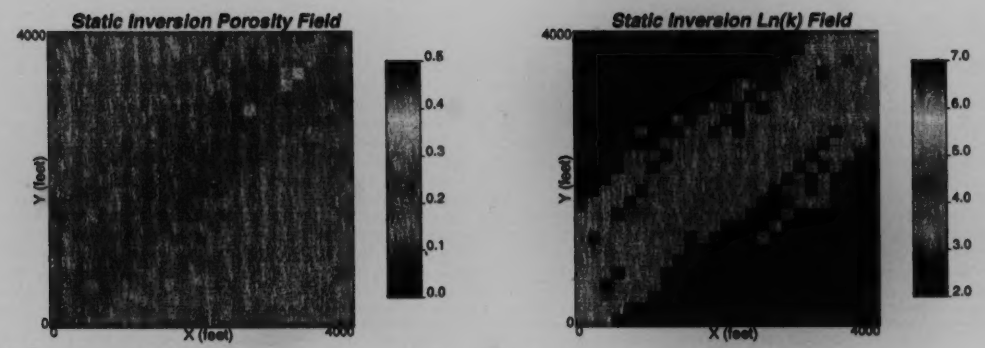


Figure 4.9: Conditional simulation of $\phi$ and $\ln(k)$ fields honoring only static information (local data, global distribution and prior variography).

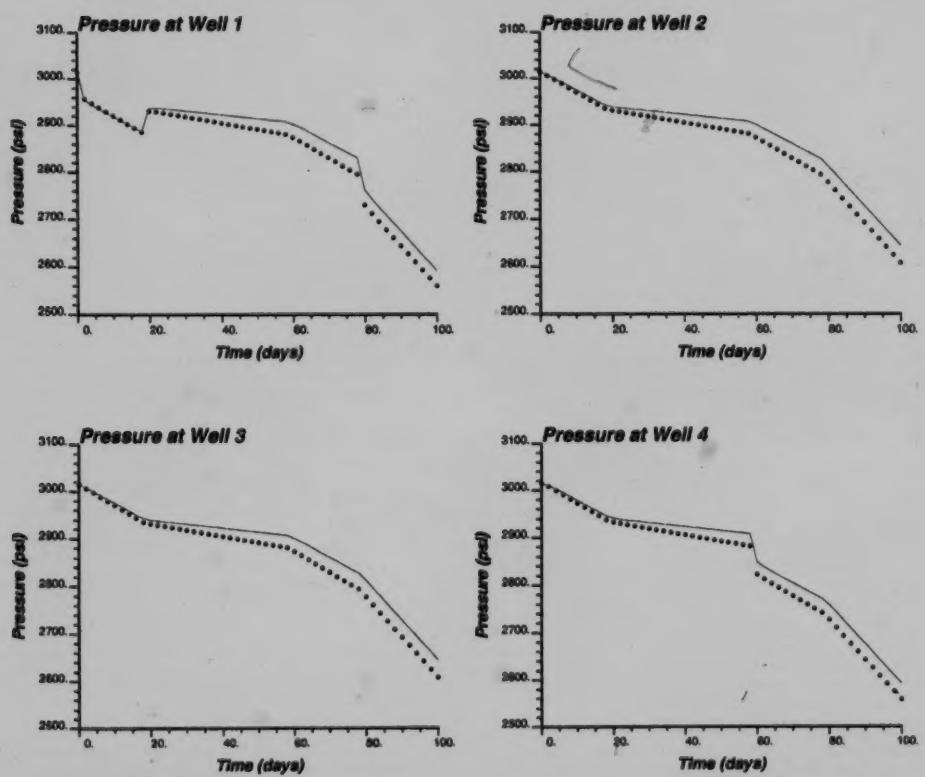


Figure 4.10: Pressure responses computed from conditionally simulated (bullets) $\phi$ and $\ln(k)$ fields with the true data (solid lines).

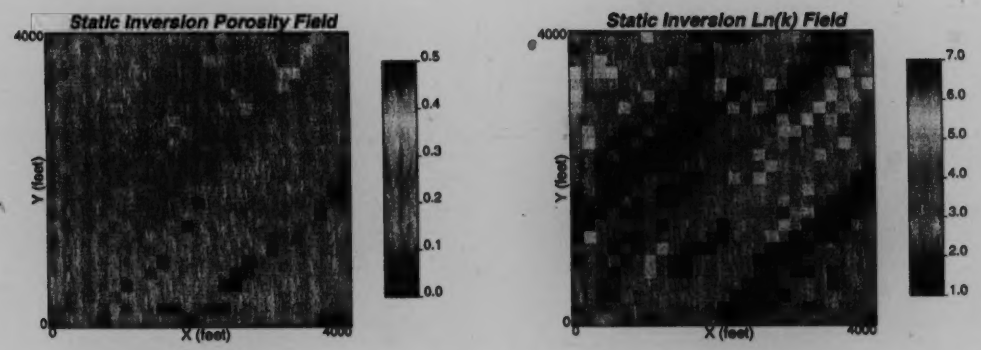


Figure 4.11: Conditional simulation of $\phi$ and $\ln(k)$ fields honoring only static local data, and prior variography information.

resolved using production data. Of course, more data leads to the better resolved model. Conflicting data will lead to a poor model and lack of convergence.

### Run 2: Inversion with production data, global histogram, prior information on variography, but no local hard data

The inverted models are obtained after 5 outer iterations (26 seconds in 733 MHz dual processor workstation). The pressure responses in the updated porosity and permeability fields converge to the reference pressure data. These inverted models are shown in Figure 4.13. The connected high porosity/permeability band connecting W2 and W3 is clearly evident. Figure 4.14 shows the pressure values at the four wells computed from the true (from reference), initial and final updated porosity and permeability fields. Note that the pressure match in this case is even better than the previous case. The objective function values of the inversion process are shown in Figure 4.15. Final average pressure mismatch (in $L^2$ norm sense) for 200 data was 1.7 psi (compared to 4.1 psi in Run 1). Near-wellbore featrues are captured in the inverted models. However, close inspection of the final models tells us that these models do not accurately capture the high porosity/permeability streak in the boundary regions away from the wells. Perhaps it can be explained by the notion that static hard data play a greater role through kriged estimation in the regions that cannot be informed by production data. Updated porosity and permeability fields after each outer iteration of the inversion method are shown in Figures 4.16 and 4.17.

### Run 3: Inversion with production data, prior information on variography and local hard data, but no global distribution

Local hard data used are shown in Figure 4.3 (same as in Run 1). The inverted models are obtained after 7 outer iterations (44 seconds in 733 MHz dual processor workstation). The pressure responses in the updated porosity and permeability fields converge to the reference pressure data. These inverted models are shown in Figure 4.18. The connected high porosity/permeability band connecting W2 and W3 is clearly evident. Figure 4.19 shows the pressure values at the four wells computed from the true (from reference), initial and final updated porosity and permeability fields. The objective function values of the

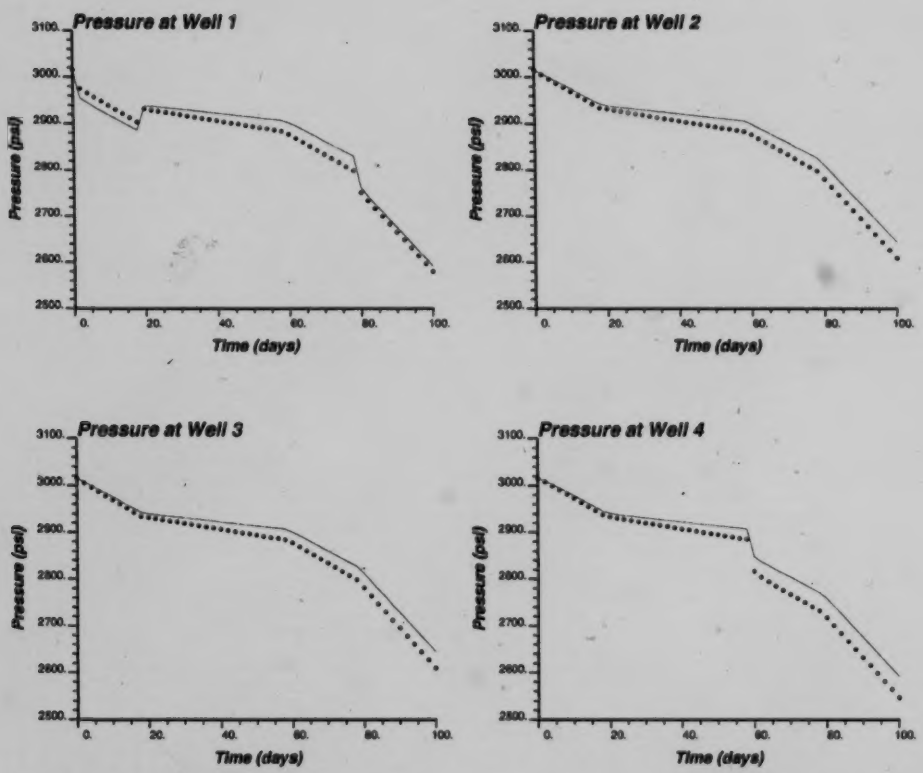


Figure 4.12: Pressure responses computed from conditionally simulated (bullets) $\phi$ and $\ln(k)$ fields with the true data (solid lines).

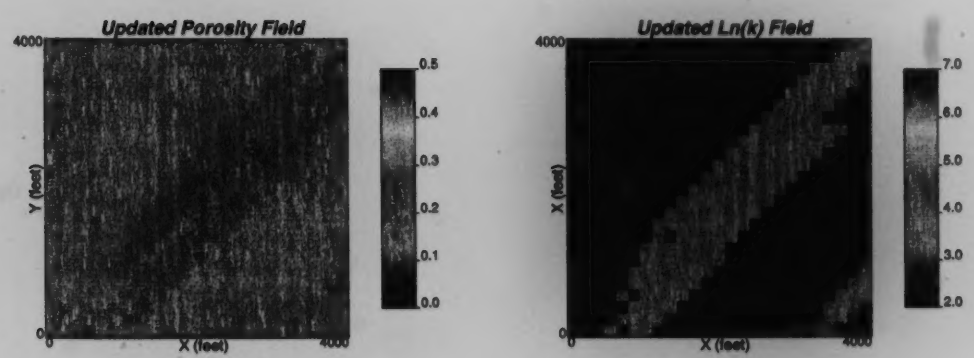


Figure 4.13: Updated $\phi$ and $\ln(k)$ fields: Deterministic Example Run 2.

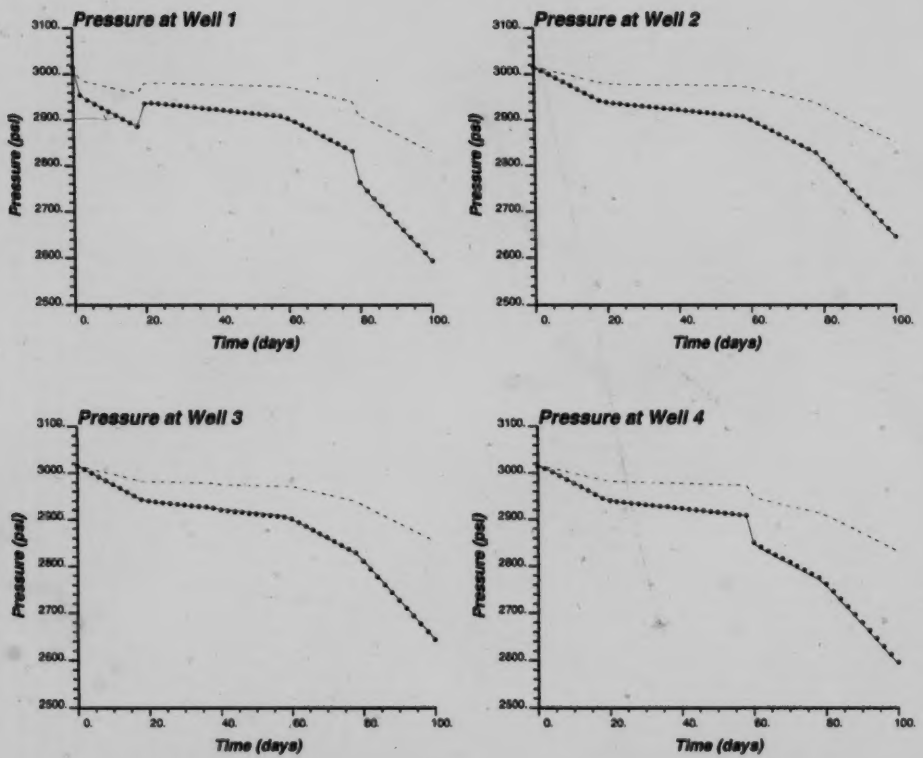


Figure 4.14: Pressure responses computed from initial (dashed lines) and updated (bullets) $\phi$ and $\ln(k)$ fields with the true data (solid lines): Deterministic Example Run 2.

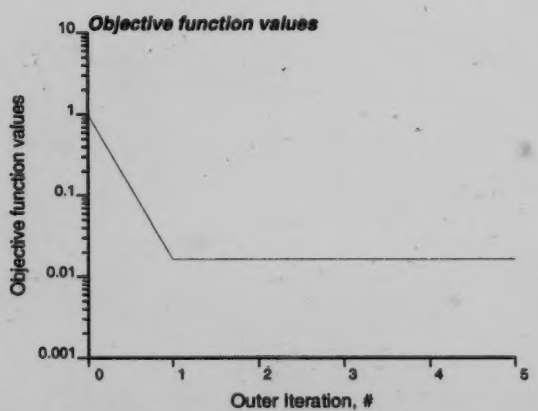


Figure 4.15: Objective function values of the inversion process: Deterministic Example Run 2.

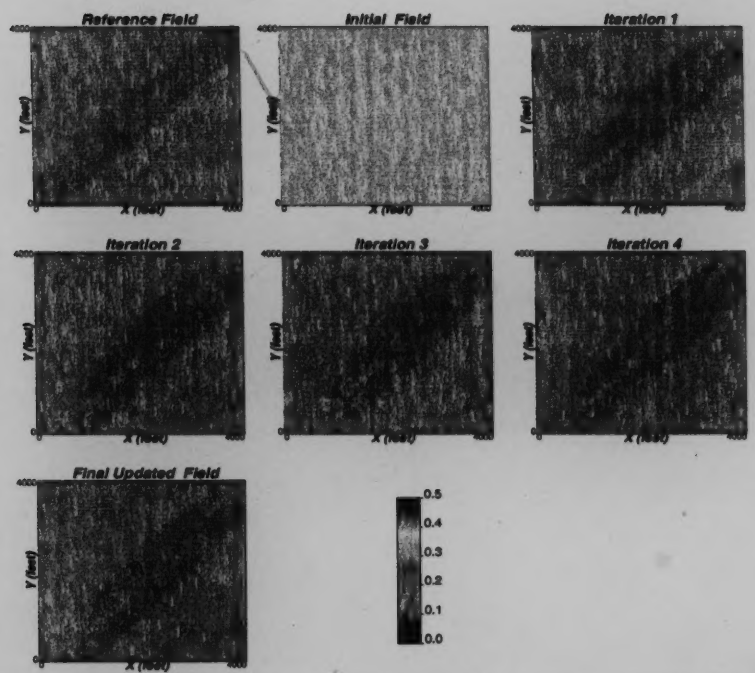


Figure 4.16: Updated $\phi$ fields at each iteration of the inversion process: Deterministic Example Run 2.

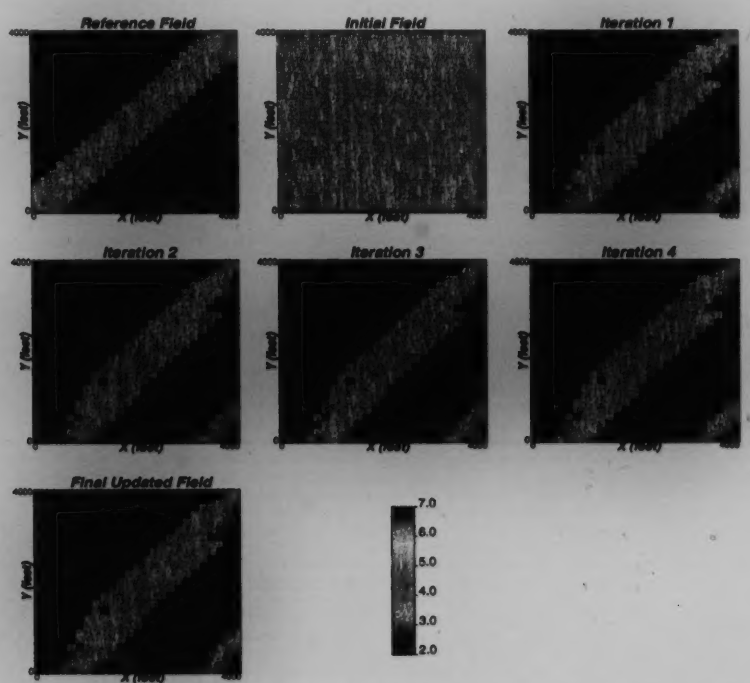


Figure 4.17: Updated $\ln(k)$ fields at each iteration of the inversion process: Deterministic Example Run 2.

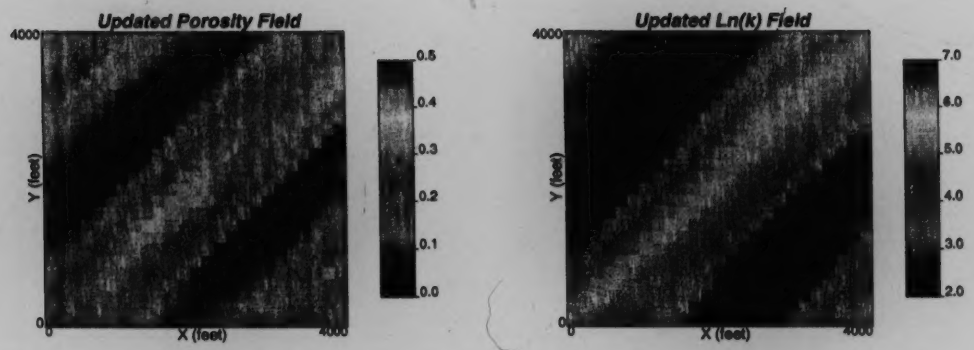


Figure 4.18: Updated $\phi$ and $\ln(k)$ fields: Deterministic Example Run 3.

inversion process is shown in Figure 4.20. Final average pressure mismatch (in $L^2$ norm sense) for 200 data was 9.1 psi. Compared to the first two runs, this is a relatively high number. Updated porosity and permeability fields after each outer iteration of the inversion method are shown in Figures 4.21 and 4.22.

### Run 4: Inversion with production data and prior information on variography, but no local hard data or global distribution

The inverted models are obtained after 10 outer iterations (47 seconds in 733 MHz dual processor workstation). The pressure responses in the updated porosity and permeability fields converge to the reference pressure data. These inverted models are shown in Figure 4.23. The connected high porosity/permeability band connecting W2 and W3 is clearly evident. Figure 4.24 shows the pressure values at the four wells computed from the true (from reference), initial and final updated porosity and permeability fields. The objective function values of the inversion process is shown in Figure 4.25. Final average pressure mismatch (in $L^2$ norm sense) for 200 data was 33.3 psi, which is a relatively high value. This poor match is evident in the pressure match in Figure 4.24. Updated porosity and permeability fields after each outer iteration of the inversion method are shown in Figures 4.26 and 4.27.

## 4.3 Some Sensitivity Studies

We performed a number of sensitivity studies to establish the robustness of the approach to simultaneous inversion of $\phi$ and $\ln(k)$.

### Sensitivity to initial $\phi$ and $\ln(k)$ fields

The dynamic data integration algorithm relies on a minimization subproblem. In a gradient based minimization technique,the initial model is an important factor for convergence. Thus, in our data integration problem, $\phi$ and $\ln(k)$ could be vital in the convergence of the algorithm. In order to illustrate the sensitivity of the inversion response to initial fields, we performed a number of exercises starting from initial fields of different constant $\phi$ and

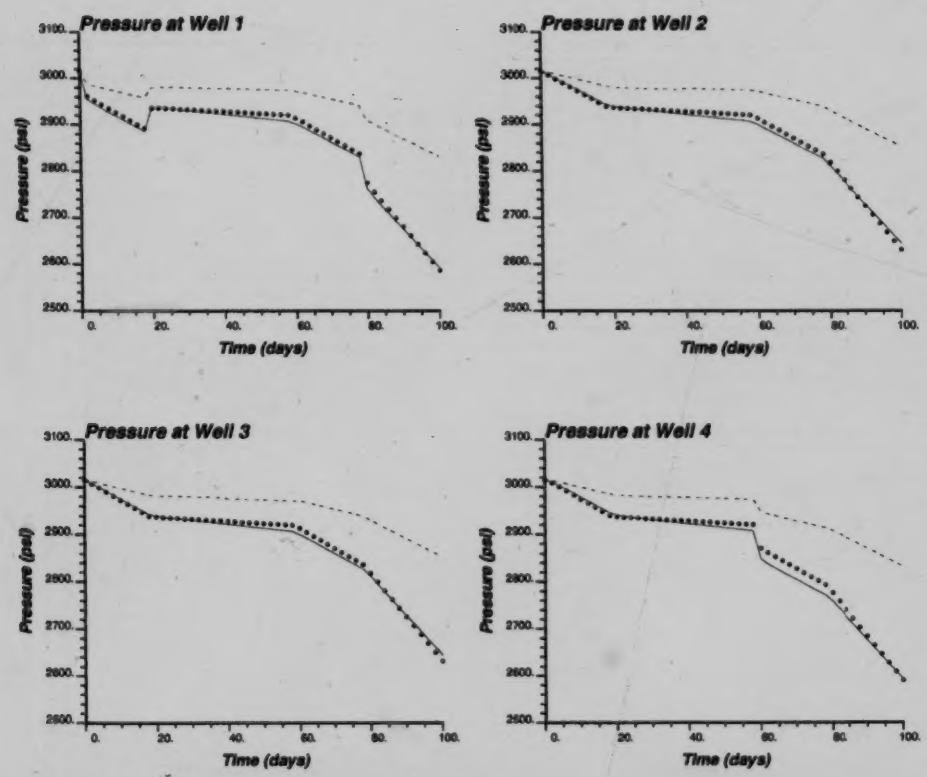


Figure 4.19: Pressure responses computed from initial (dashed lines) and updated (bullets) $\phi$ and $\ln(k)$ fields with the true data (solid lines): Deterministic Example Run 3.

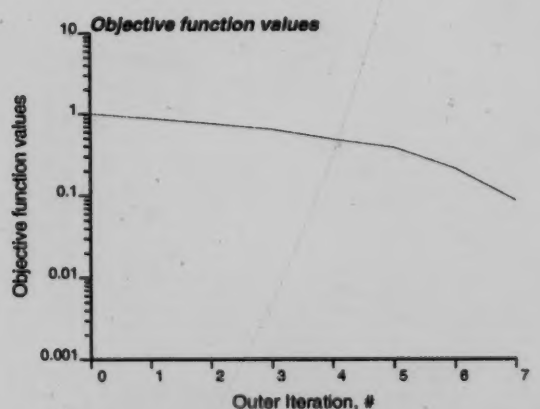


Figure 4.20: Objective function values of the inversion process: Deterministic Example Run 3.

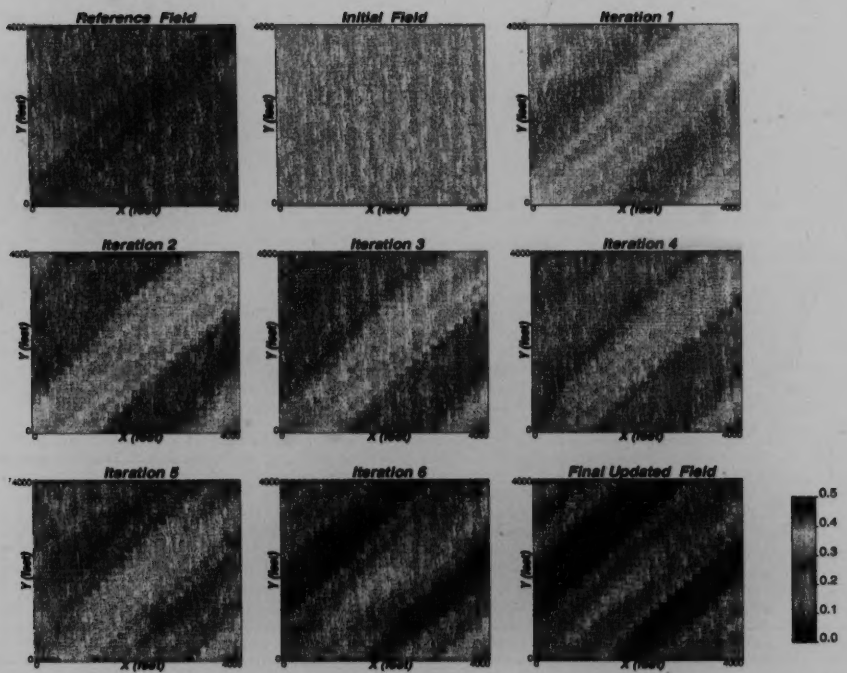


Figure 4.21: Updated $\phi$ fields at each iteration of the inversion process: Deterministic Example Run 3.

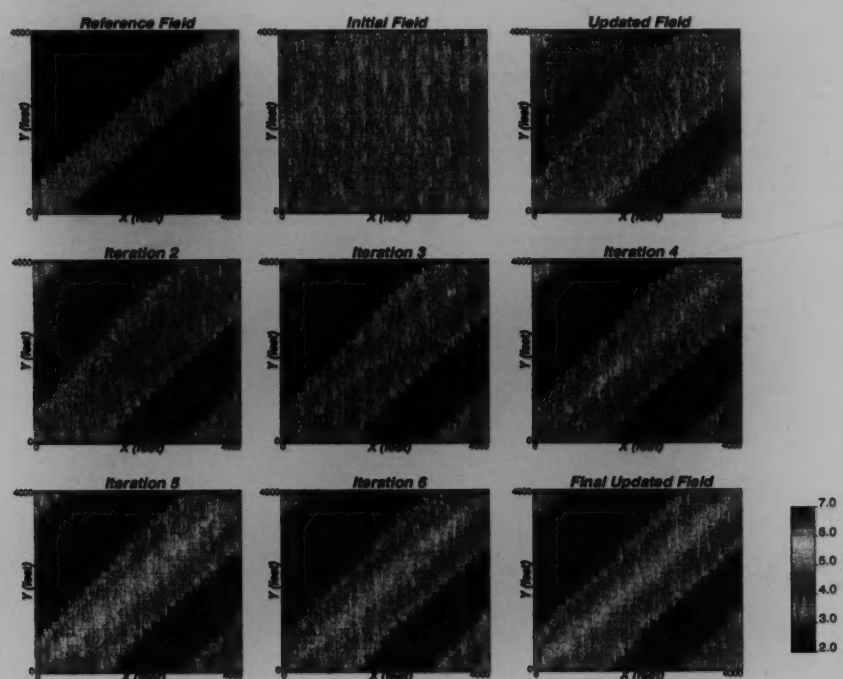


Figure 4.22: Updated $\ln(k)$ fields at each iteration of the inversion process: Deterministic Example Run 3.

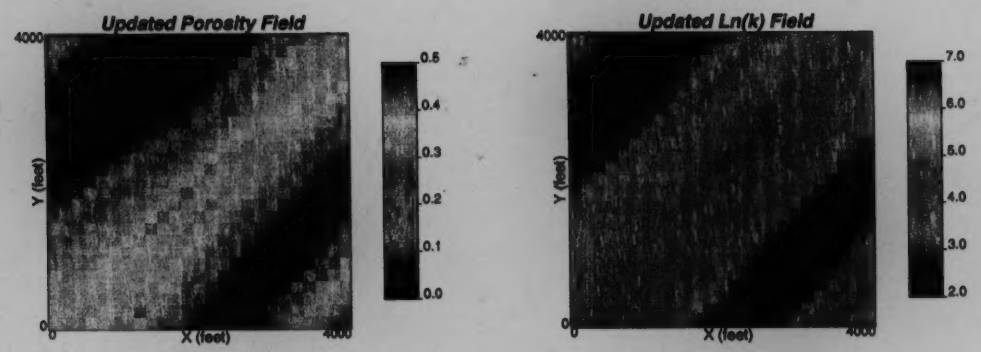


Figure 4.23: Updated $\phi$ and $\ln(k)$ fields: Deterministic Example Run 4.

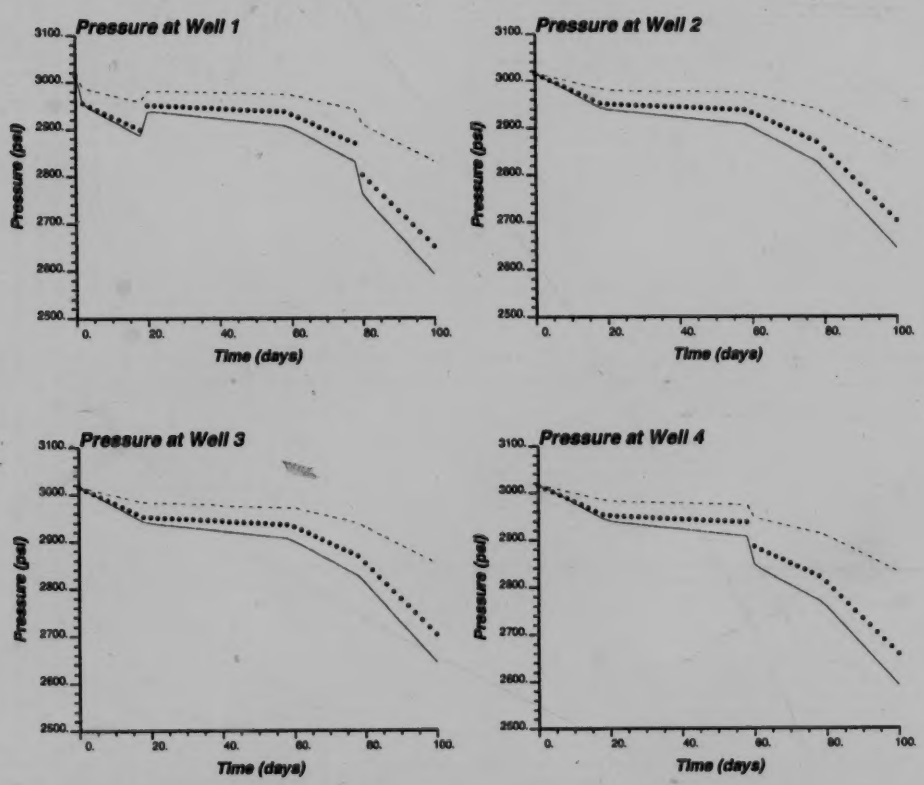


Figure 4.24: Pressure responses computed from initial (dashed lines) and updated (bullets) $\phi$ and $\ln(k)$ fields with the true data (solid lines): Deterministic Example Run 4.

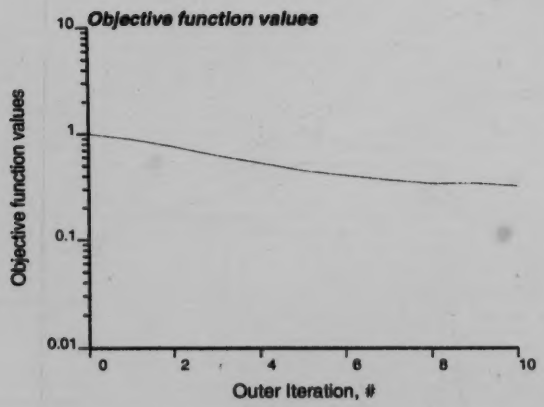


Figure 4.25: Objective function values of the inversion process: Deterministic Example Run 4.

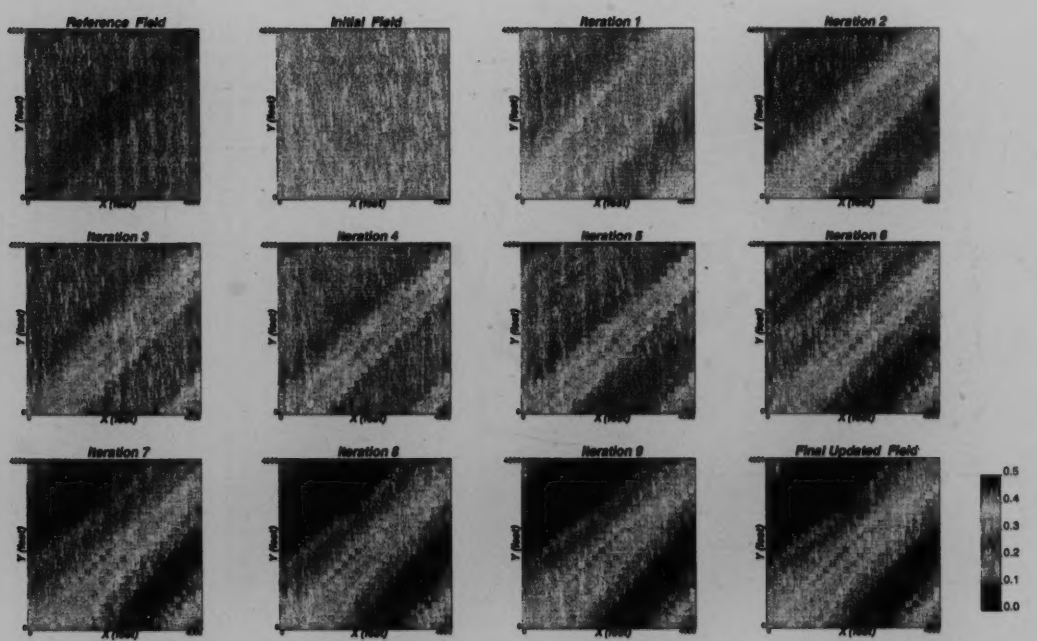


Figure 4.26: Updated $\phi$ fields at each iteration of the inversion process: Deterministic Example Run 4.

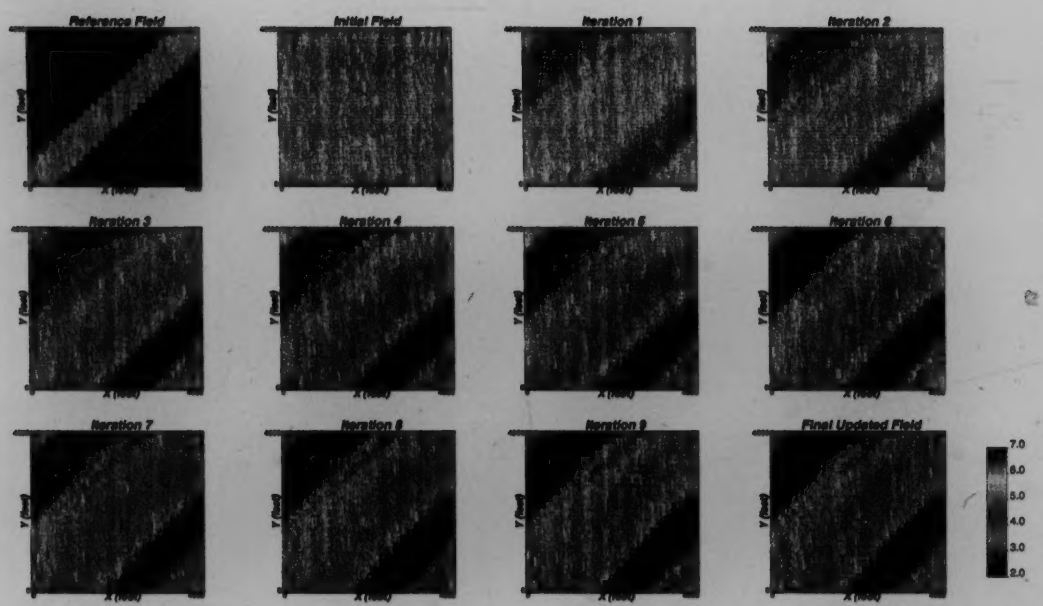


Figure 4.27: Updated $\ln(k)$ fields at each iteration of the inversion process: Deterministic Example Run 4.

| S. No. | Initial $\phi$ p.u. | Initial $\ln(k)$ | Avg Mismatch psi ($L^2$ norm) | Outer Iter | CPU Time sec |
|---|---|---|---|---|---|
| 1 | 0.2 | 1.0 | 5.82 | 9 | 37 |
| 2 | 0.2 | 3.15 | 4.38 | 16 | 76 |
| 3 | 0.2 | 6.0 | 4.18 | 18 | 75 |
| Run 1 | 0.4 | 3.15 | 4.1 | 17 | 75 |

Table 4.3: Summarized responses of sensitivity exercise to initial $\phi$ and $\ln(k)$ fields.

$\ln(k)$ values. The responses are tabulated in Table 4.3. The performance of Deterministic Example Run 1 is shown for comparison.

The inverted models from the three sensitivity runs are shown in Figures 4.28, 4.29, and 4.30. The connected high $\phi$ and $\ln(k)$ band connecting W2 and W3 is evident in all the inverted models except for the last one where the initial porosity and permeability fields were 0.2 and 6.0, respectively. Interestingly, we find that the last run has the best average pressure match (see Table 4.3). Possible reason for poor inversion in this case may be the solution is stuck within a local minimum.

The algorithm is reasonably robust with respect to the initial field. However, the fact that there is no optimality criteria for global minima makes it impossible to state definite conclusions. Some initial fields will fare better than others. Also, this sensitivity study reveals that looking only at the pressure match may not be sufficient.

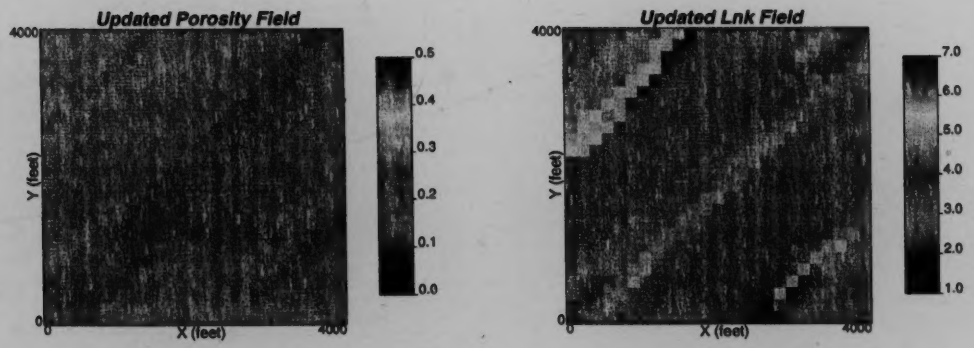


Figure 4.28: Updated $\phi$ and $\ln(k)$ fields: Initial Field $\phi = 0.2$ and $\ln(k) = 1.0$.

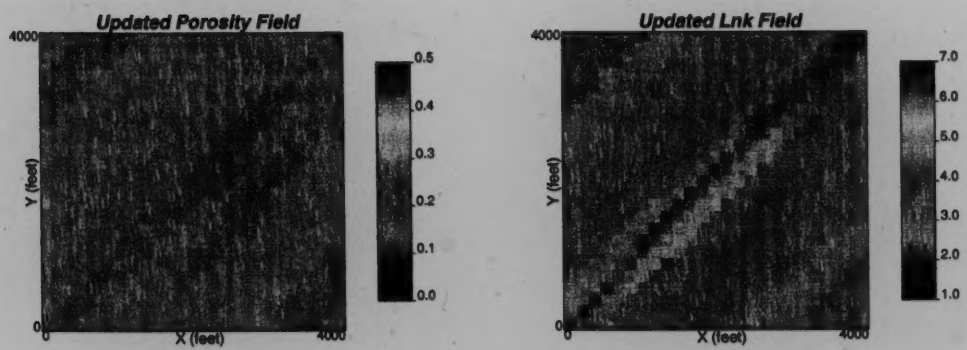


Figure 4.29: Updated $\phi$ and $\ln(k)$ fields: Initial Field $\phi = 0.2$ and $\ln(k) = 3.15$.

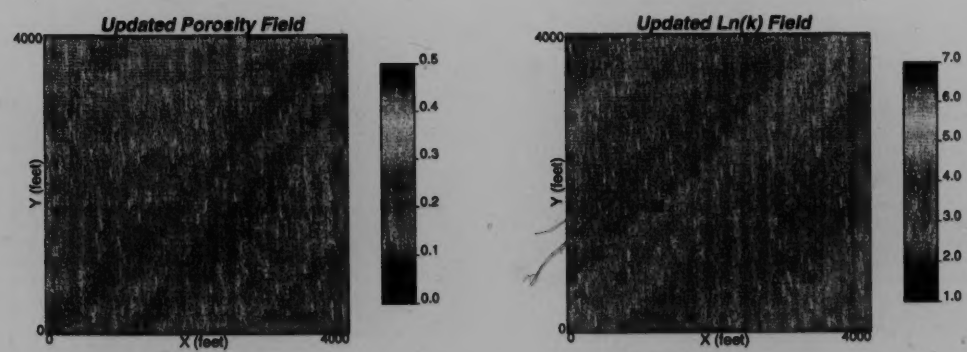


Figure 4.30: Updated $\phi$ and $\ln(k)$ fields: Initial Field $\phi = 0.2$ and $\ln(k) = 6.0$. (Poor inversion)

| S. No. | No. of Master Points $X$ - $Y$ | Avg Mismatch psi ($L^2$ norm) | Outer Iter | CPU Time sec |
|---|---|---|---|---|
| 1 | 2 - 2 | 3.01 | 15 | 15 |
| 2 | 3 - 3 | 2.24 | 12 | 20 |
| 3 | 4 - 4 | 4.52 | 12 | 35 |
| 4 | 6 - 6 | 3.22 | 18 | 92 |
| 5 | 7 - 7 | 4.65 | 10 | 112 |
| Run 1 | 5 - 5 | 4.1 | 17 | 75 |

Table 4.4: Summarized responses of sensitivity exercise to number of master points.

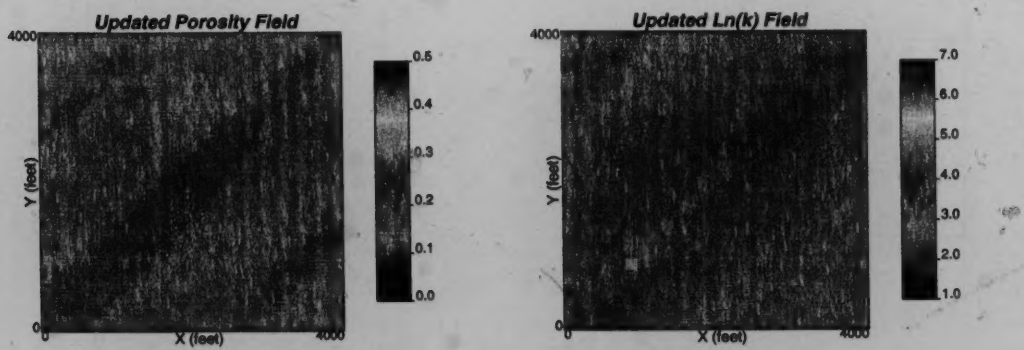


Figure 4.31: Updated $\phi$ and $\ln(k)$ fields: $2 \times 2$ Master Points Case.

## Sensitivity to number of master points

Master points are the cells of the model where porosity and permeability values are iteratively updated in order to minimize the pressure mismatch. Convergence of the inversion problem depends on the relative amount of data and unknown parameters involved. Thus, the number of master points could be an important element in the solution of the data integration algorithm.

In order to illustrate the sensitivity to the number of master points, number of master points was varied from $2 \times 2$ to $7 \times 7$. The responses are tabulated in Table 4.4. Also shown is the performance of Deterministic Example Run 1 for comparison.

The inverted models from these sensitivity runs are shown in Figures 4.31, 4.32, 4.33, 4.34, and 4.35, respectively. The spatially connected high $\phi$ and $\ln(k)$ band connecting W2 and W3 is evident in all the inverted models. The objective function values of the inversion processes in Table 4.4 are all reasonably good.

Increasing the number of master points may not improve the inversion pressure match. Having too few or too many master points may make it more difficult to capture the major features. It should be noted that the CPU time goes up as the number of master points increases.

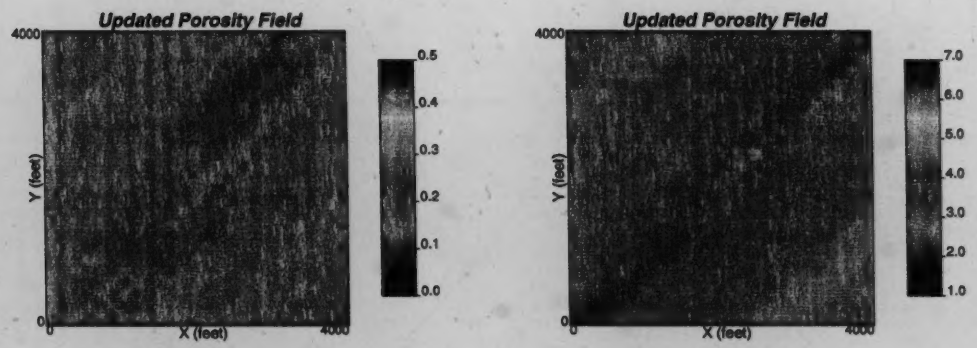


Figure 4.32: Updated $\phi$ and $\ln(k)$ fields: 3 × 3 Master Points Case.

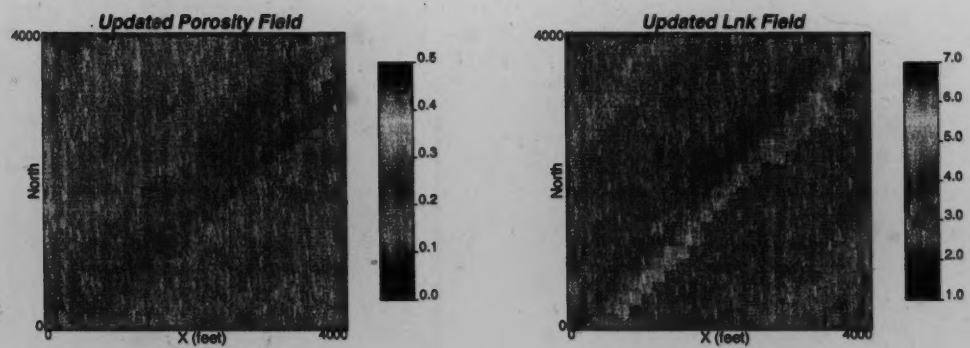


Figure 4.33: Updated $\phi$ and $\ln(k)$ fields: 4 × 4 Master Points Case.

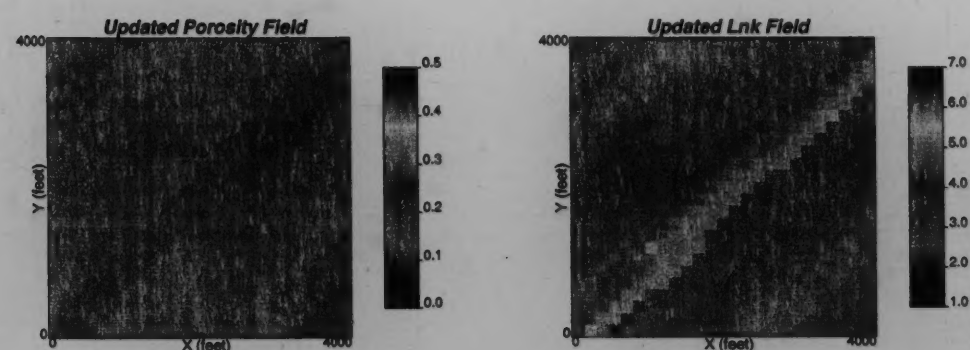


Figure 4.34: Updated $\phi$ and $\ln(k)$ fields: 6 × 6 Master Points Case.

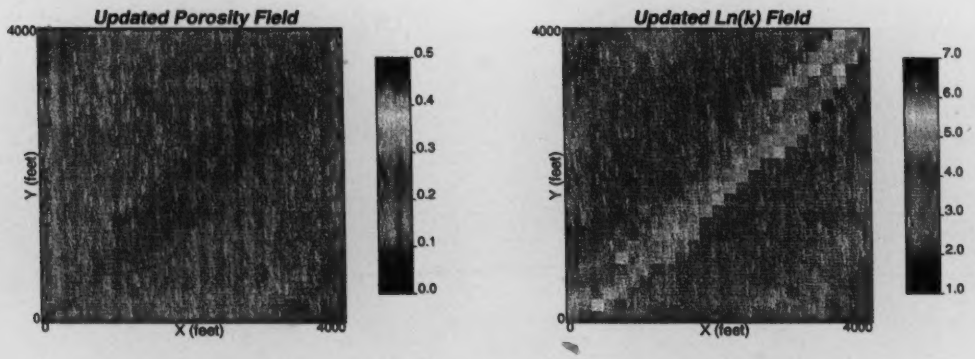


Figure 4.35: Updated $\phi$ and $\ln(k)$ fields: $7 \times 7$ Master Points Case.

| S. No. | Updating Freq | Avg Mismatch psi ($L^2$ norm) | Outer Iter | CPU Time sec |
|---|---|---|---|---|
| 1 | 1 | 6.30 | 8 | 46 |
| 2 | 2 | 6.26 | 13 | 64 |
| 3 | 3 | 1.62 | 15 | 70 |
| 4 | 4 | 7.35 | 16 | 72 |
| 5 | 8 | 8.27 | 16 | 74 |
| 6 | 10 | 4.45 | 9 | 40 |
| Run 1 | 5 | 4.1 | 17 | 75 |

Table 4.5: Summarized responses of sensitivity exercise to master point locations.

### Sensitivity to master point locations

The previous section dealt with the number of master points. It is conjectured that updating or changing the locations of the master points has a significant effect in the inversion process. The basis for this conjecture is that it may be possible to shift away from the local minima to elsewhere in the feasible space by changing the locations of the master points.

A number of exercises are performed with updating the master points after every few outer iterations. The frequency of updating the master point locations are varied from 1 to 10. The responses of the sensitivity exercise are tabulated in Table 4.5. Also shown in the table is the performance of Deterministic Example Run 1 for comparison. It should be noted that $5 \times 5$ master points were used in Deterministic Example Run 1.

The inverted models from these sensitivity runs are shown in Figures 4.36, 4.37, 4.38, 4.39, 4.40 and 4.41, respectively. The inverted models appear almost exactly the same. The objective function values of the inversion processes (Table 4.5) vary from 1.6 to 8.3 in $L^2$ norm sense. Updating master point locations affects the number of outer iterations required to have the minimum mismatch; however, it appears that location updating does not have a large impact on convergence.

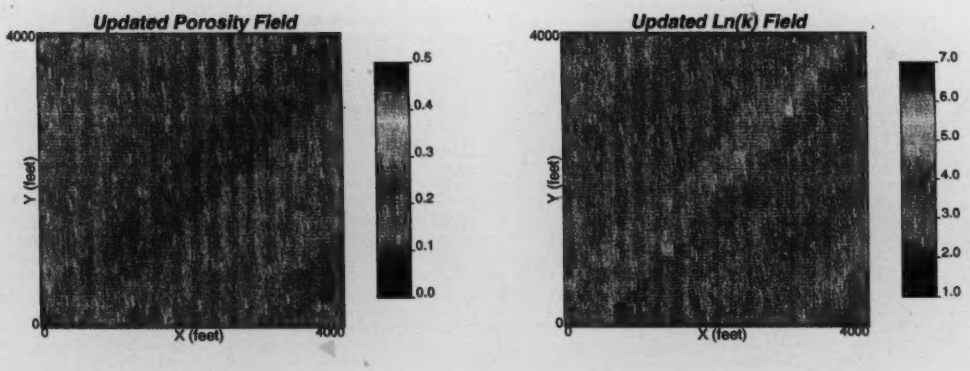


Figure 4.36: Updated $\phi$ and $\ln(k)$ fields: Updating frequency - every 1 iteration.

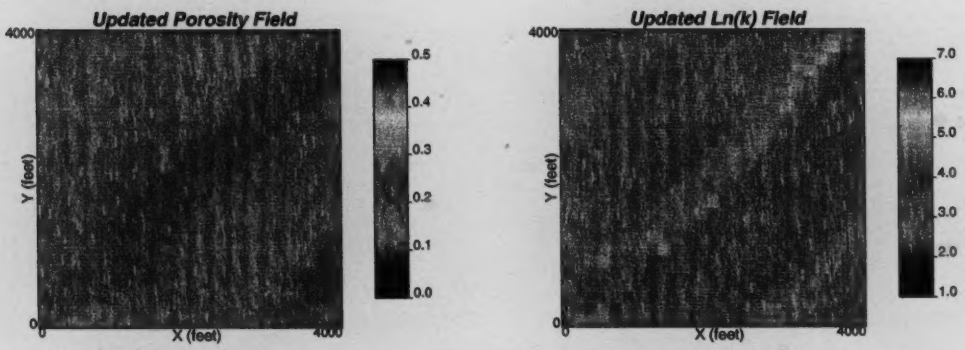


Figure 4.37: Updated $\phi$ and $\ln(k)$ fields: Updating frequency - every 2 iterations.

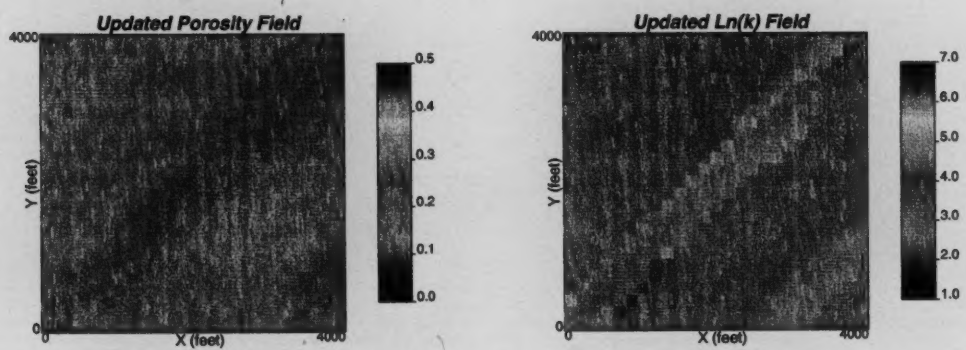


Figure 4.38: Updated $\phi$ and $\ln(k)$ fields: Updating frequency - every 3 iterations.

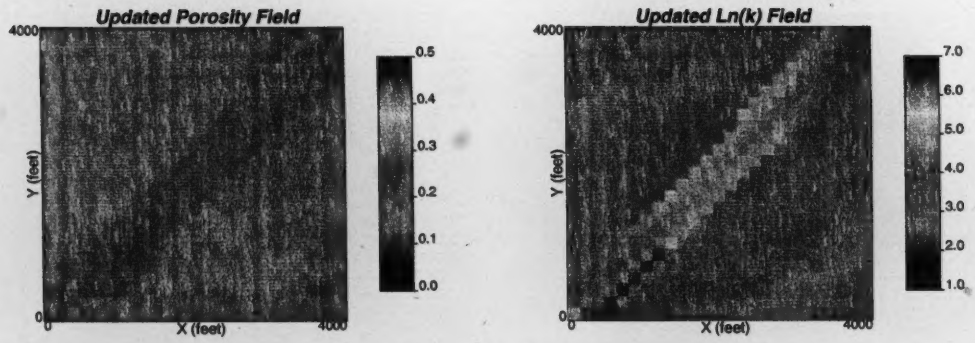


Figure 4.39: Updated $\phi$ and $\ln(k)$ fields: Updating frequency - every 4 iterations.

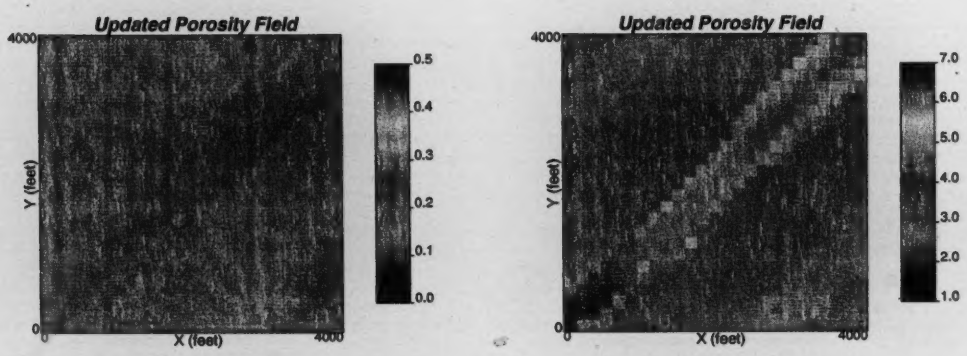


Figure 4.40: Updated $\phi$ and $\ln(k)$ fields: Updating frequency - every 8 iterations.

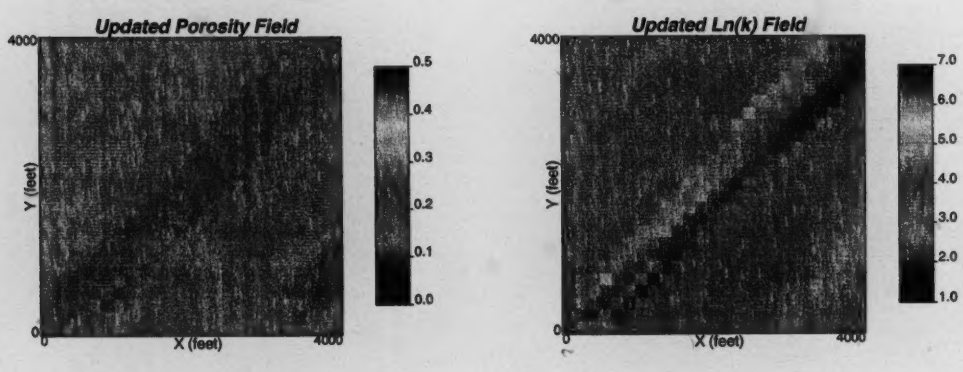


Figure 4.41: Updated $\phi$ and $\ln(k)$ fields: Updating frequency - every 10 iterations.

| S. No. | ln($k$) Range X - Y (ft) | ln($k$) Angle ($^o$) | $\phi$ Range X - Y (ft) | $\phi$ Angle ($^o$) |
|---|---|---|---|---|
| 1 | 8100 - 1000 | 20 | 8000 - 1100 | 20 |
| 2 | 8100 - 1000 | 70 | 8000 - 1100 | 70 |
| 3 | 6100 - 1000 | 45 | 6000 - 1100 | 45 |
| 4 | 4100 - 1000 | 45 | 4000 - 1100 | 45 |
| Run 1 | 8100 - 1000 | 45 | 8000 - 1100 | 45 |

Table 4.6: Prior variogram information used in sensitivity exercise.

| S. No. | Avg Mismatch psi ($L^2$ norm) | Outer Iter | CPU Time sec |
|---|---|---|---|
| 1 | 2.80 | 20 | 89 |
| 2 | 2.35 | 12 | 63 |
| 3 | 3.40 | 14 | 66 |
| 4 | 2.23 | 16 | 76 |
| Run 1 | 4.1 | 17 | 75 |

Table 4.7: Summarized responses of sensitivity exercise to prior variography information.

### Sensitivity to prior variogram information

Prior variogram information is an important factor in a good reservoir characterization study. From the first exercise in the previous section, it was evident that variography has a significant impact on the inverted models; however, the right variogram is extremely difficult to infer from limited well data. A sensitivity study of the results with different variograms will help determine how well the algorithm resolve reservoir parameters with uncertain input parameters.

In order to illustrate the sensitivity of the inversion response to variography, consider the variograms tabulated in Table 4.6. Variogram anisotropy was changed from a ratio of about 8:1 to 4:1. Anisotropy angle was varied from $20^o$ to $70^o$. The responses of the sensitivity exercise with different prior variography information are tabulated in Table 4.7. Also shown in the table is the performance of Deterministic Example Run 1 for comparison.

The inverted models from these sensitivity runs are shown in Figures 4.42, 4.43, 4.44, and 4.45, respectively. Inverted models appear almost exactly the same. The objective function values of the inversion processes in Table 4.7 varies from about 2.2 to 4.1 in $L^2$ norm sense. These are all reasonably good pressure matches.

### Sensitivity to inner optimization parameters

In the inner optimization module, the objective is to search for a primal local minima under bound constraints of the $\phi$, ln($k$) correction values. An approximate subproblem of our original data integration problem is formulated for the minimization. The importance of this inner optimization and consequences of relaxing the stopping criteria are relevant sensitivities.

In order to demonstrate the sensitivity of the inversion response to inner optimization parameters, we vary the tolerance values for objective function convergence and norm of the

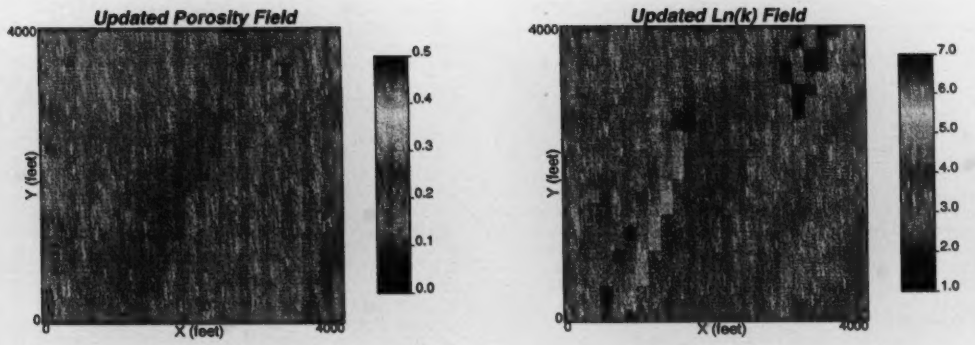


Figure 4.42: Updated $\phi$ and $\ln(k)$ fields: Prior Variogram Set 1 in Table 4.6.

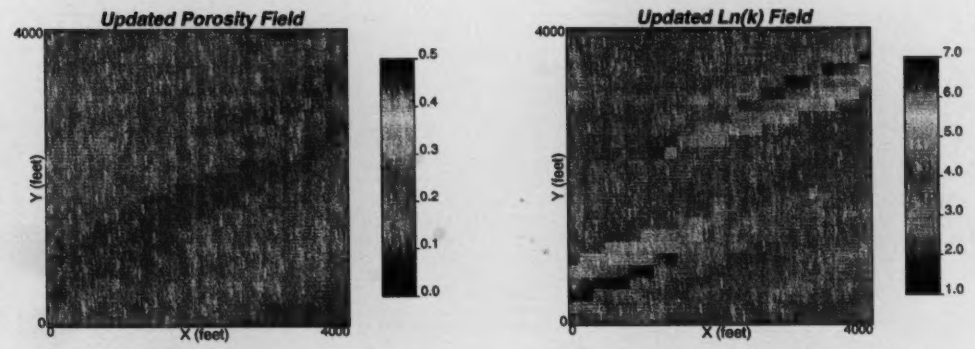


Figure 4.43: Updated $\phi$ and $\ln(k)$ fields: Prior Variogram Set 2 in Table 4.6.

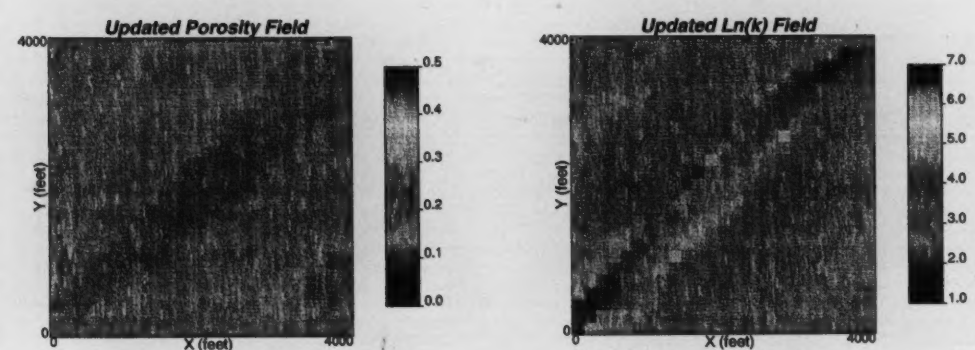


Figure 4.44: Updated $\phi$ and $\ln(k)$ fields: Prior Variogram Set 3 in Table 4.6.

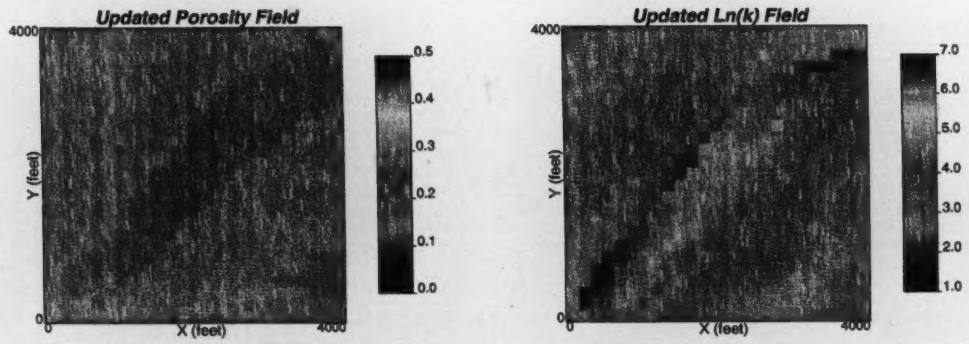


Figure 4.45: Updated $\phi$ and $\ln(k)$ fields: Prior Variogram Set 4 in Table 4.6.

| S. No. | Gradient Norm Tol | Obj Func Tol | Obj Func Conv No. |
|---|---|---|---|
| 1 | $5.0 \times 10^{-4}$ | $1.0 \times 10^{-5}$ | 40 |
| 2 | $5.0 \times 10^{-4}$ | $1.0 \times 10^{-5}$ | 10 |
| 3 | $5.0 \times 10^{-5}$ | $1.0 \times 10^{-5}$ | 10 |
| 4 | $5.0 \times 10^{-4}$ | $1.0 \times 10^{-4}$ | 40 |
| Run 1 | $5.0 \times 10^{-5}$ | $1.0 \times 10^{-5}$ | 40 |

Table 4.8: Inner optimization parameters used in sensitivity exercise.

gradient. The inner optimization parameters used for the sensitivity studies are tabulated in Table 4.8. The responses of the sensitivity exercise with different inner optimization parameters are tabulated in Table 4.9. Also shown in the table is the performance of Deterministic Eexample Run 1 for comparison.

Inverted models (not shown here) capture major heterogeneity features of the reference field. However, the objective function values of the inversion processes in Table 4.9 varies significantly from about 2.5 to 6.9 in $L^2$ norm sense. When the tolerance for gradient comparison is $5 \times 10^{-4}$, the number of function and gradient evaluation remains at the assigned minimum of 50 after first few outer iterations; however when this value is fixed at $5 \times 10^{-5}$ (more stringent tolerance), this termination criteria is not met and the number of function evaluation is much higher (over 1000).

| S. No. | Avg Mismatch psi ($L^2$ norm) | Outer Iteration | CPU Time sec |
|---|---|---|---|
| 1 | 2.51 | 18 | 79 |
| 2 | 6.93 | 14 | 50 |
| 3 | 3.72 | 7 | 32 |
| 4 | 3.35 | 10 | 36 |
| Run 1 | 4.1 | 17 | 75 |

Table 4.9: Summarized responses of sensitivity exercise to inner optimization parameters.

## 4.4 An Implementation Issue: Propagation of Optimal Corrections

The optimal corrections from the inner optimization at master point locations are propagated onto the entire field by kriging. We use kriging equation (Equation 4.1) for $\phi$ corrections $\Delta\phi_i$, whereas we employ the collocated cokriging equation (Equation 4.2) for $y = \ln(k)$ corrections $\Delta y_i$. The correction propagation equations are given below:

$$\Delta\phi_i = \sum_{j=1}^{n_{mp}} \tau_{i,j}^{\phi} \Delta\phi_j \tag{4.11}$$

$$\Delta y_i = \sum_{j=1}^{n_{mp}} \tau_{i,j}^{y} \Delta y_j + \xi_i \Delta\phi_i \tag{4.12}$$

The average corrections $\overline{\Delta}$ will approach zero as convergence is attained; however, it may be non-zero in the initial iterations, especially when the initial model is not that good. In the latter case, the above optimal correction equations could be modified to account for the non-zero overall mean correction:

$$\Delta\phi_i = \sum_{j=1}^{n_{mp}} \tau_{i,j}^{\phi} \Delta\phi_j + \left(1 - \sum_{j=1}^{n_{mp}} \tau_{i,j}^{\phi}\right) \overline{\Delta\phi} \tag{4.13}$$

$$\Delta y_i = \sum_{j=1}^{n_{mp}} \tau_{i,j}^{y} \Delta y_j + \xi_i(\Delta\phi_i - \overline{\Delta\phi}) + \left(1 - \sum_{j=1}^{n_{mp}} \tau_{i,j}^{y}\right) \overline{\Delta y} \tag{4.14}$$

where $\overline{\Delta\phi}$ and $\overline{\Delta y}$ are average $\Delta\phi$ and $\Delta y$, respectively.

It was found that this alternative using an experimental mean is more likely to get into degeneracy problems. In order to illustrate the difference between the two implementation, we performed the deterministic example Run 1 inversion and compared the performance.

With $\overline{\Delta} \neq 0$, the inverted models are obtained after 16 outer iterations (77 seconds in 733 MHz dual processor workstation). These inverted models are shown in Figure 4.46. The spatially connected high $\phi$ and $\ln(k)$ band connecting W2 and W3 is evident in the inverted models. However, the major features are not captured with as much detail as it was obtained using $\overline{\Delta} = 0$. Figure 4.47 shows the pressure values at the four wells computed from the true (from reference), initial and final updated porosity and permeability fields. The objective function values of the inversion process is shown in Figure 4.48. Comparing the objective functions curves for the cases (Figures 4.6 and 4.48), it can be seen that implementation with $\overline{\Delta} = 0$ is smoother than the other. Final average pressure mismatch (in $L^2$ norm sense) for 200 data in both the implementations is 4.13 psi.

## 4.5 Example 2: A Stochastic Example

A more realistic example is demonstrated here to evaluate the ability of the algorithm to generate models of porosity and permeability from multiple well production data. Reference porosity and permeability models are constructed first. Dynamic pressure responses at a

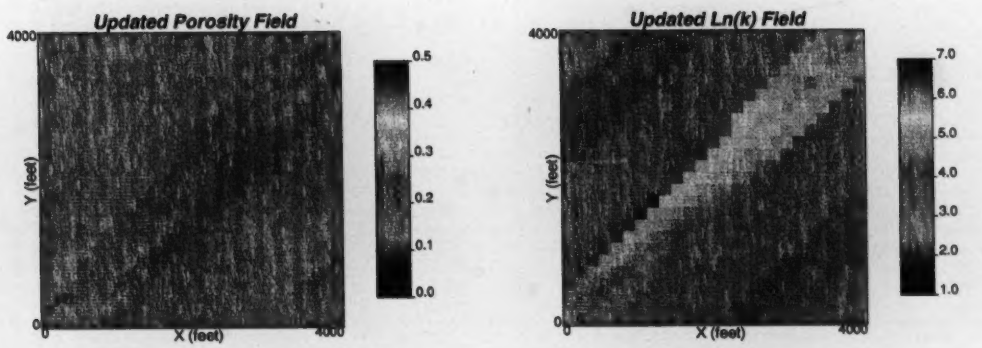


Figure 4.46: Updated $\phi$ and $\ln(k)$ fields: Base Case $\overline{\Delta} = 0$.

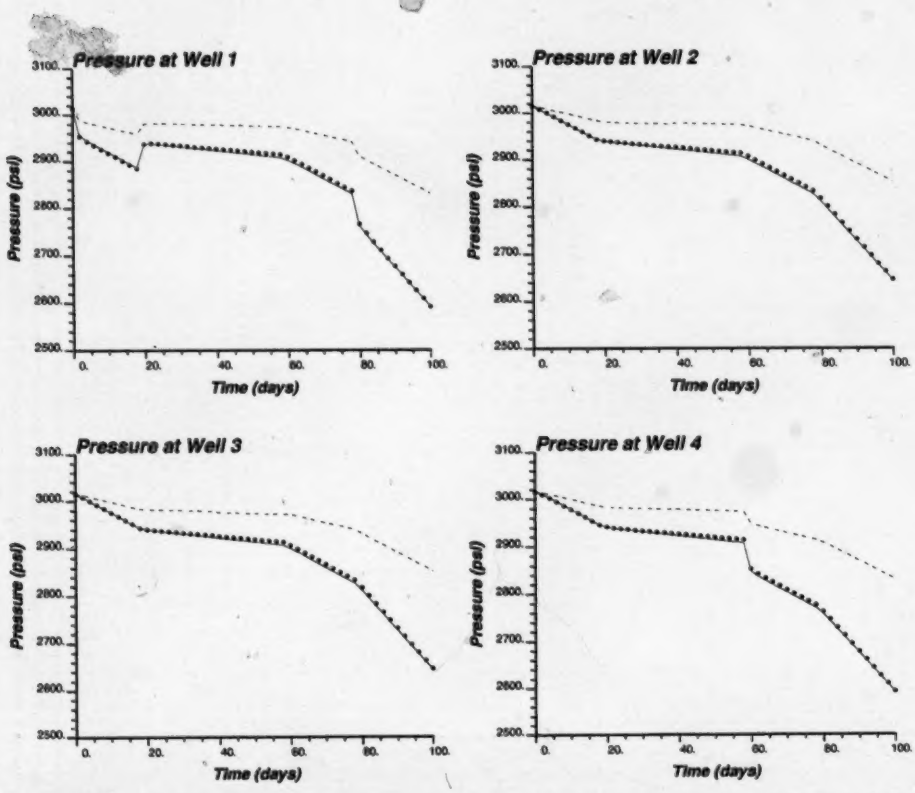


Figure 4.47: Pressure responses computed from initial (dashed lines) and updated (bullets) $\phi$ and $\ln(k)$ fields with the true data (solid lines): Base Case.

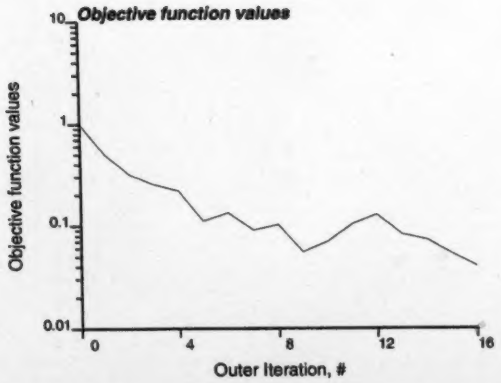


Figure 4.48: Objective function values of the inversion process: Base Case.

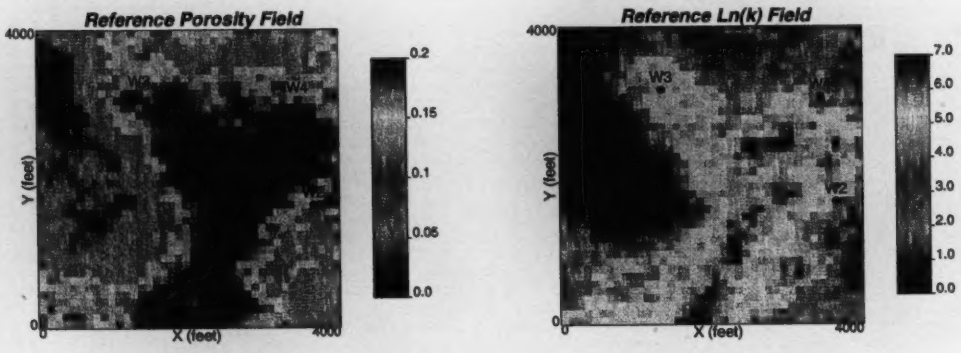


Figure 4.49: Reference $\phi$ and $\ln(k)$ fields: Stochastic Example.

number of wells are obtained by flow simulation. The inverted fields are compared with the reference fields to evaluate the capability of the algorithm.

A 2D 4,000-ft square domain is discretized into 40 $\times$ 40 grid cells of 100 $\times$ 100 ft. Porosity and permeability fields are shown in Figure 4.49. There are four wells: W1 at the center of the cell (24,10), W2 at (37,17), W3 at (14,32), and W4 at (35,31), see Figure 4.49. Reservoir parameters are similar to the deterministic example unless stated otherwise. Figure 4.50 shows the imposed production rates and the corresponding pressure responses. It should be noted that the production rates are not very high, however the pressure decline is significant. This type of situation would arise when the storativity of the reservoir is not high. The low permeability and good communication between the wells entails that any measurable change in one well would be reflected in the pressure responses of the other wells. The histograms the scatter-plot of $\phi$ and $\ln(k)$ are shown in Figures 4.51 and 4.52. Mean and standard deviation of reference distributions are 0.13 and 0.04 for $\phi$, and 3.37 and 2.09 for $\ln(k)$, respectively. We used the reference $\phi$ and $\ln(k)$ distributions in the inversion exercise for the global distributions. The correlation coefficient of $\phi$ and $\ln(k)$ is 0.82. The variogram parameters are shown in Table 4.10.

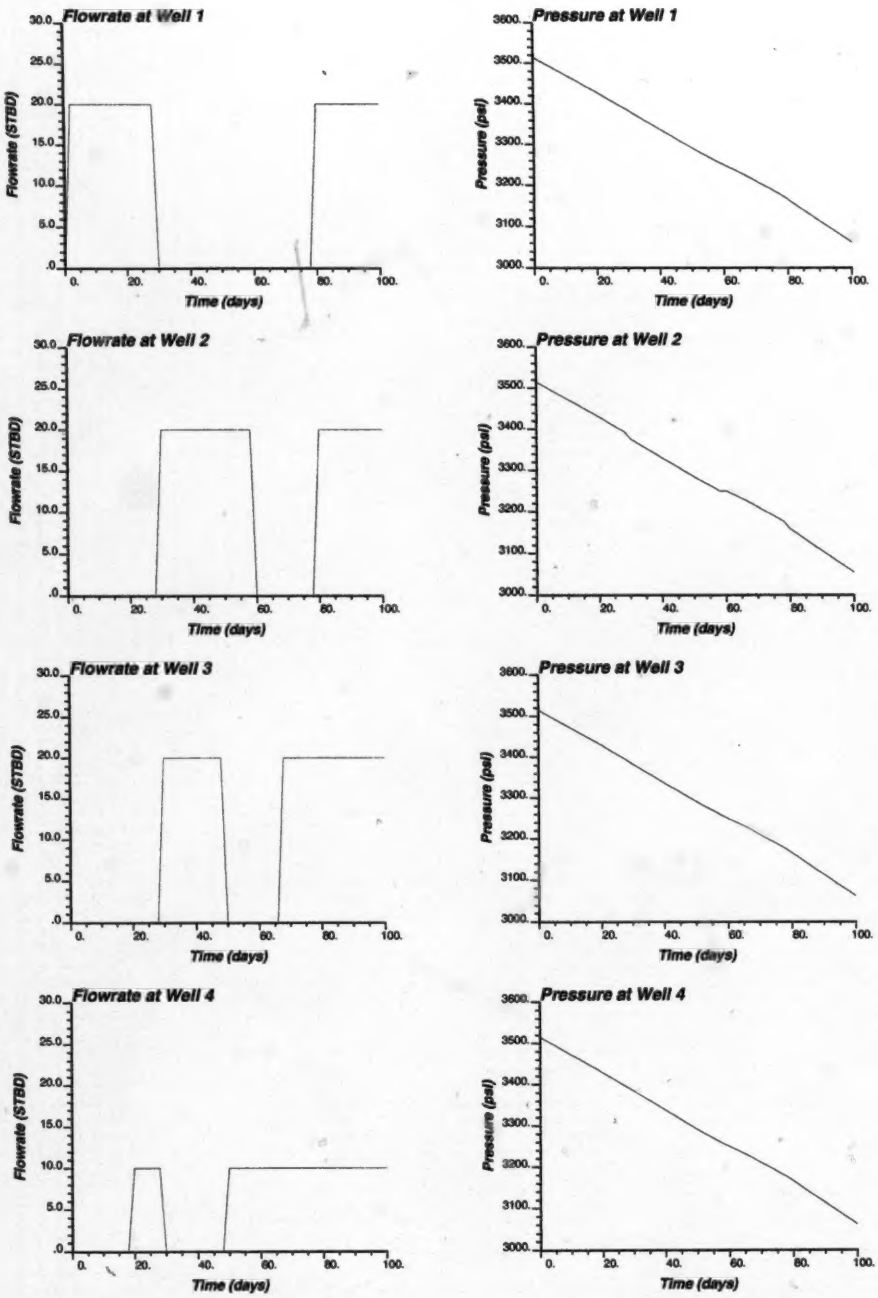


Figure 4.50: Production data (pressure and flow rates) obtained from the reference field: Stochastic Example.

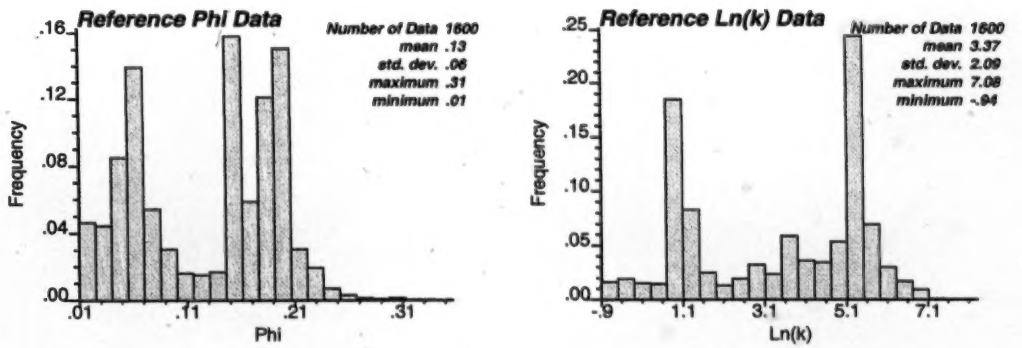


Figure 4.51: Histograms of reference $\phi$ and $\ln(k)$ fields: Stochastic Example.

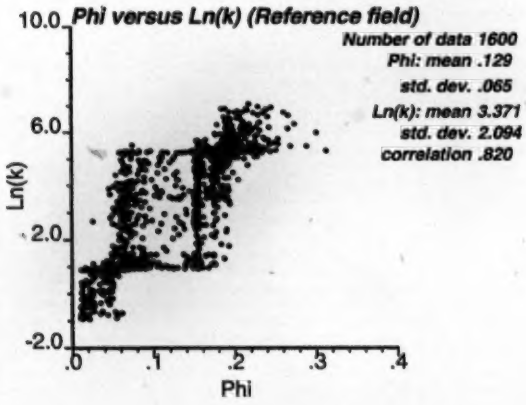


Figure 4.52: Scatterplot of reference $\phi$ and $\ln(k)$ distributions: Stochastic Example.

| V. No. | Type | Sill | Range X - Y (ft) | Angle ($^o$) |
|---|---|---|---|---|
| 0 | Nugget | 0.0 | | |
| 1 | Sph | 0.6 | 2500 - 3600 | 0 |
| 2 | Sph | 0.4 | 4000 - 3250 | 0 |

Table 4.10: Variogram information used for both $\phi$ and $\ln(k)$: Stochastic Example Run 1.

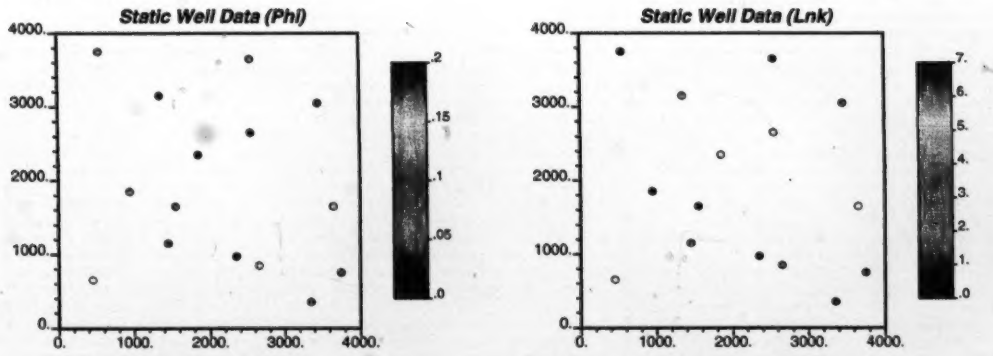


Figure 4.53: Static well data for $\phi$ and $\ln(k)$: Stochastic Example Run 1.

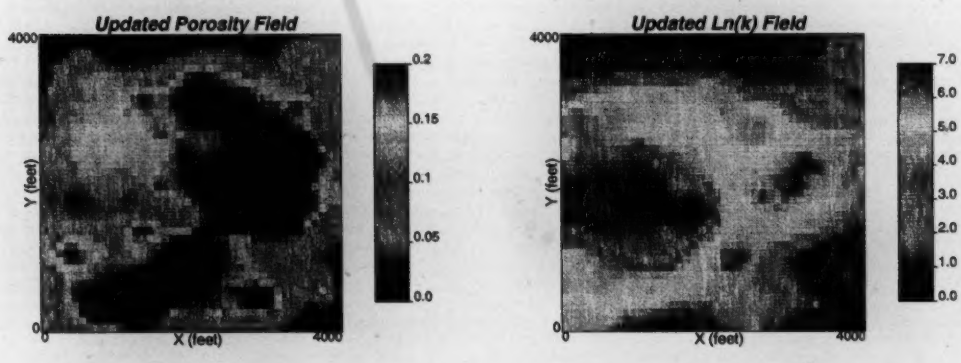


Figure 4.54: Updated $\phi$ and $\ln(k)$ fields: Stochastic Example Run 1.

### Run 1: Inversion with production data, global histogram, reference variogram information, and reference local hard data

For this inversion exercise, we used homogeneous initial porosity and permeability fields of $\phi = 0.4$ and $\ln(k) = 3.15$ ln(mD). Reference global distributions, the reference variograms, and the local hard data shown in Figure 4.53 are used.

The inverted models are obtained after 7 outer iterations (134 seconds in 733 MHz dual processor workstation). The pressure responses in the updated porosity and permeability fields converge to the reference pressure data. These inverted models are shown in Figure 4.54. Figure 4.55 shows the pressure values at the four wells computed from the true (from reference), initial and final updated $\phi$ and $\ln(k)$ fields. Although the pressure match of the updated fields is not close particularly in the late time period, there is a significant reduction of the mismatch from the initial field responses. The objective function values of the inversion process is shown in Figure 4.56. Final average pressure mismatch (in $L^2$ norm sense) for 200 data was 10.4 psi. Updated $\phi$ and $\ln(k)$ fields after each outer iteration of the inversion method are shown in Figures 4.57 and 4.58.

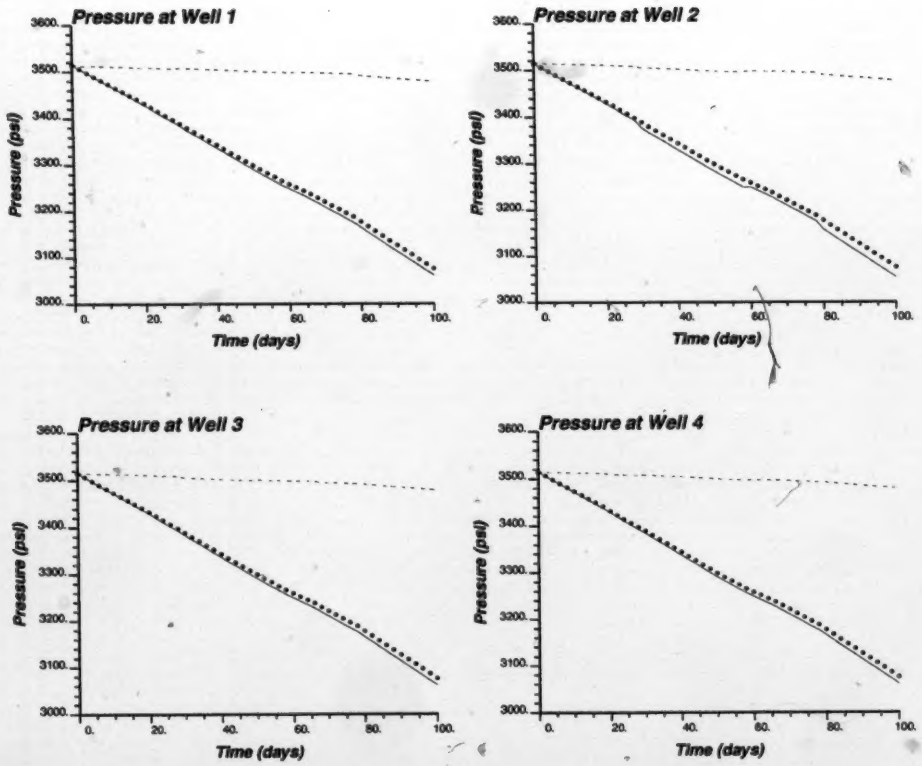


Figure 4.55: Pressure responses computed from initial (dashed lines) and updated (bullets) $\phi$ and $\ln(k)$ fields with the true data (solid lines): Stochastic Example Run 1.

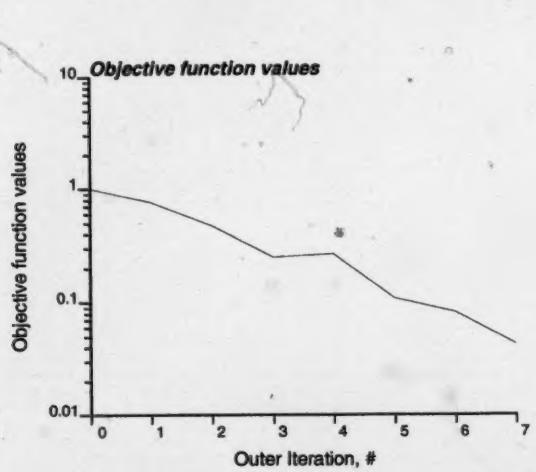


Figure 4.56: Objective function values of the inversion process: Stochastic Example Run 1.

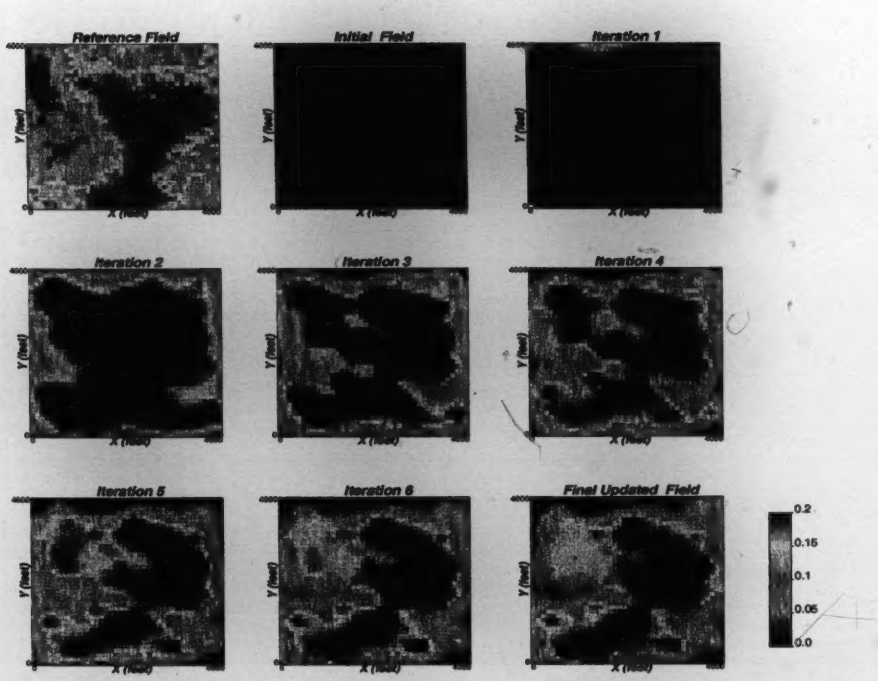


Figure 4.57: Updated $\phi$ fields at each iteration of the inversion process: Stochastic Example Run 1.

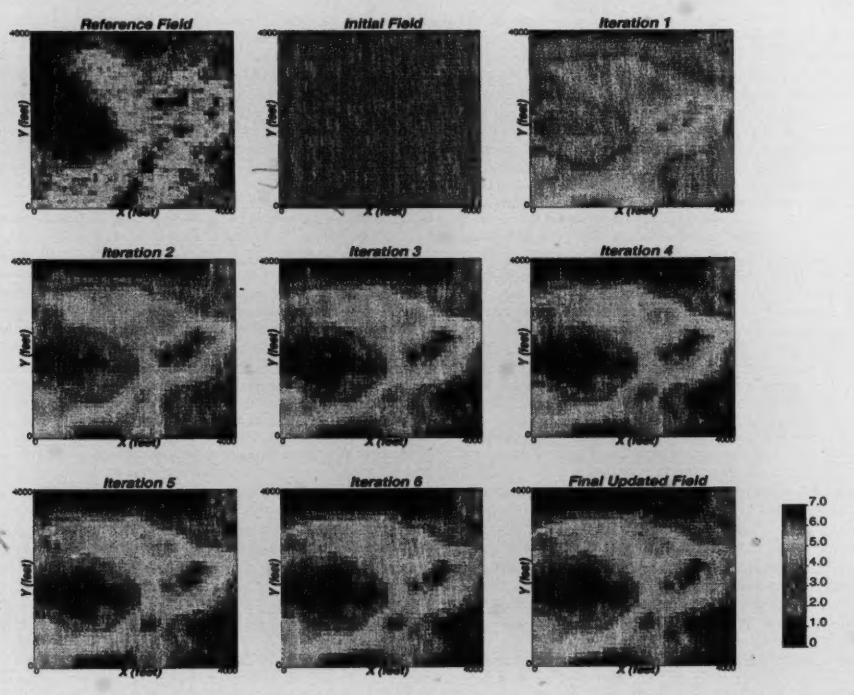


Figure 4.58: Updated $\ln(k)$ fields at each iteration of the inversion process: Stochastic Example Run 1.

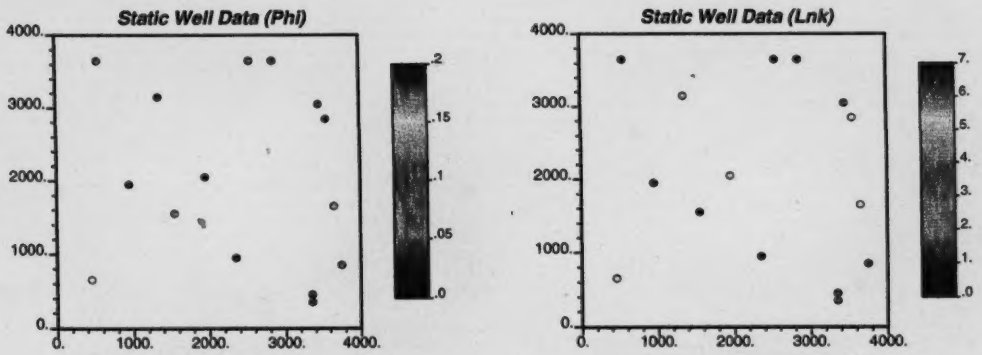


Figure 4.59: Static well data for $\phi$ and $\ln(k)$: Stochastic Example Run 2.

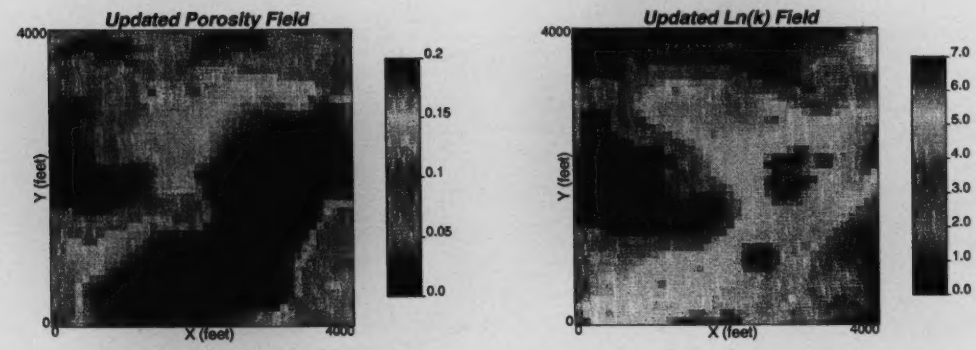


Figure 4.60: Updated $\phi$ and $\ln(k)$ fields: Stochastic Example Run 2.

### Run 2: Inversion with production data, global histogram, reference variogram information, but different local hard data

In this case, we used the same homogeneous initial porosity and permeability fields of $\phi = 0.4$ and $\ln(k) = 3.15$ ln(mD). Reference global distributions are used along with reference variograms; however a different set of local hard data (extracted from the reference fields) are also used in the inversion run below (shown in Figure 4.59). The idea for the exercise is to determine how much information was incorporated into the final models.

The inverted models are obtained after 15 outer iterations (254 seconds in 733 MHz dual processor workstation). The pressure responses in the updated porosity and permeability fields converge to the reference pressure data. These inverted models are shown in Figure 4.60. Figure 4.61 shows the pressure values at the four wells computed from the true (from reference), initial and final updated $\phi$ and $\ln(k)$ fields. Pressure match of the updated fields, in this case, is better than that of Run 1. The objective function values of the inversion process are much lower and smooth (shown in Figure 4.62). Final average pressure mismatch (in $L^2$ norm sense) for 200 data was 6.9 psi. Updated $\phi$ and $\ln(k)$ fields after each outer iteration of the inversion method are shown in Figures 4.63 and 4.64.

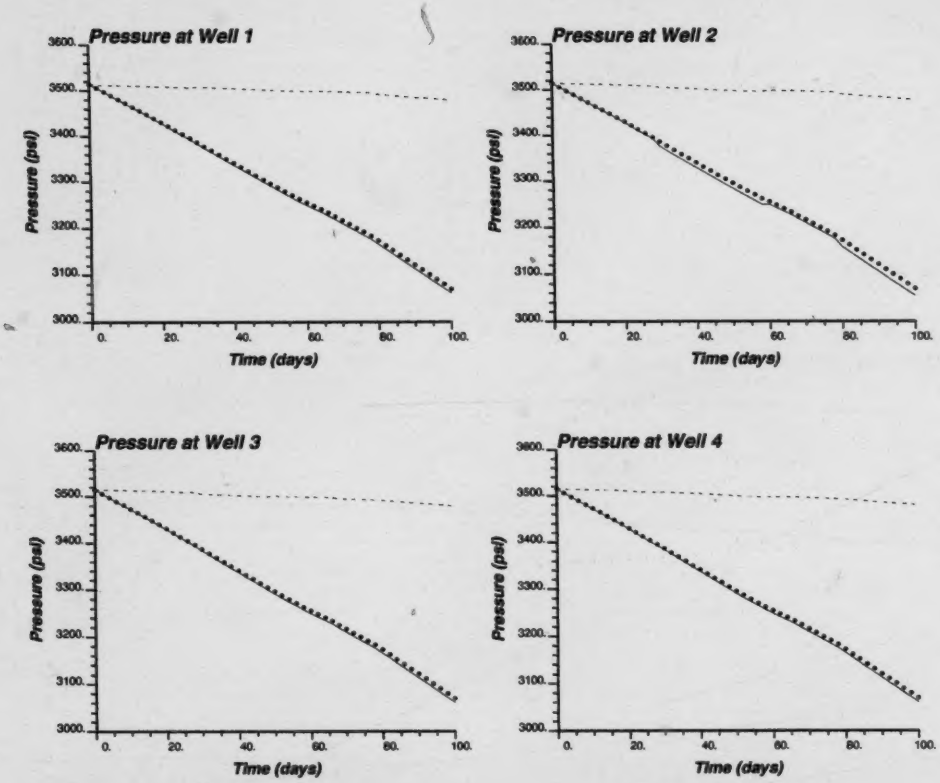


Figure 4.61: Pressure responses computed from initial (dashed lines) and updated (bullets) $\phi$ and $\ln(k)$ fields with the true data (solid lines): Stochastic Example Run 2.

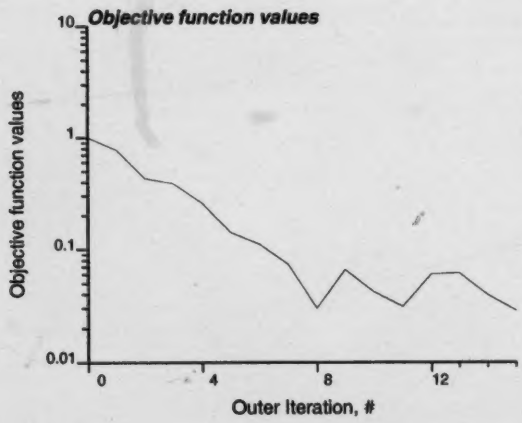


Figure 4.62: Objective function values of the inversion process: Stochastic Example Run 2.

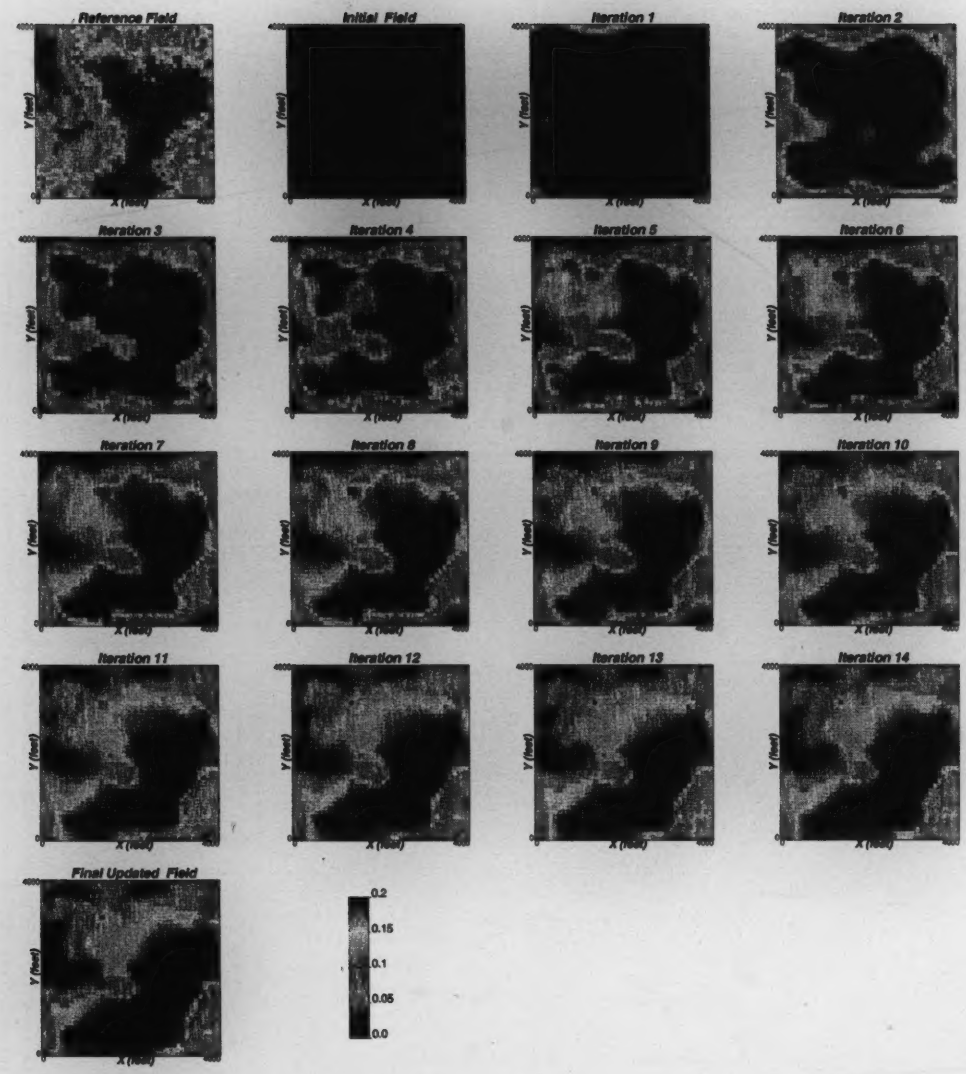


Figure 4.63: Updated $\phi$ fields at each iteration of the inversion process: Stochastic Example Run 2.

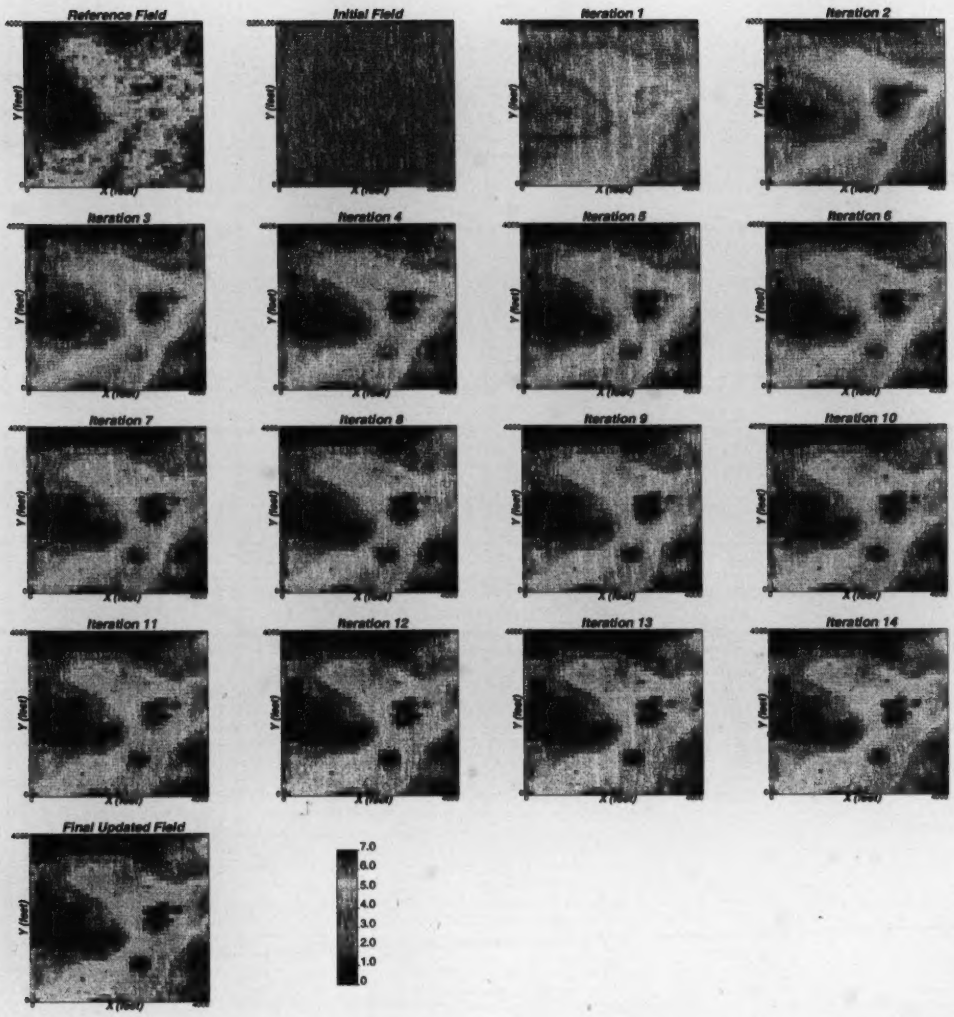


Figure 4.64: Updated $\ln(k)$ fields at each iteration of the inversion process: Stochastic Example Run 2.

## 4.6 Discussion

In this chapter, we presented a newly developed algorithm for simultaneous inversion of porosity and permeability via collocated cokriging. The implemented code has been demonstrated with a synthetic and realistic reservoir example. Some sensitivity studies have been performed to investigate the robustness of the algorithm. Some implementation issues have been addressed. Inversion results are positive and informative. However, there are scopes of improvement in this area of research.

Some of the findings from the illustrated examples and sensitivity analyses in this chapter include:

- inversion with only production data and prior variography information may not be sufficient to capture heterogeneity features
- global distribution information is important in inversion performance
- minimum pressure mismatch criterion by itself may not lead to the best inverted model attainable
- unrealistic initial porosity and permeability fields may affect the inversion responses
- constraints are important for the overall inversion process
- number of master points affects the solution. Inversion with too few master points may lead to poor inversion; on the contrary, inversion with too many master points increases the execution time and at the same time may not guarantee better inversion solution
- increasing the frequency of master point location updating may reduce the possibility of getting stuck in local minima, but may not guarantee it
- prior variography information can be critical to inversion performance.

# Chapter 5

# Simultaneous Inversion of Unique $\phi/\ln(k)$ Features From Production Data

We presented an algorithm for simultaneous inversion of $\phi$ and $K$ in Chapter 4. The ability and the effectiveness of the algorithm was discussed in that chapter. In this chapter, we analyze the inversion experiment with reservoir models with unique $\phi/\ln(k)$ features.

## 5.1 A Synthetic Reservoir Model with Unique $\phi/\ln(k)$ Features

Consider a 2D example of 4,000 ft by 4,000 ft domain that is discretized into 40 $\times$ 40 grid cells of 100 $\times$ 100 ft. Porosity and permeability fields are shown in Figure 5.1. It is evident from the figure that reference porosity field has large continuity in the North-South direction. Porosity values gradually decrease in the Westward direction. Whereas, the permeability field has large continuity in Southwest-Northeast direction. In the Southeast portion of the reservoir the permeability values are high. Permeability decreases gradually in Northeastward direction. There are 8 wells: W1 at the center of the cell (34,33), W2 at (33,8), W3 at (25,12), W4 (18,27), W5 (14,6), W6 (30,17), W7 (8,33), and W8 (35,12), respectively. Wells are shown in Figure 5.1. The four boundaries are no-flow boundaries, reservoir thickness is 100 ft, viscosity is 0.2 cp, formation compressibility is $10^{-6}$ psi$^{-1}$, and well radius is 0.3 ft. Figure 5.2 shows the imposed production rates and the corresponding numerically simulated pressure responses at the different wells. The global histograms of the reference distributions and the scatter-plot between porosity and $\ln(k)$ are shown in Figures 5.3 and 5.4, respectively. Mean and standard deviation of reference distributions are 0.129 and 0.056 for $\phi$, and 1.33 and 1.608 for $\ln(k)$. The low average porosity confirms the low storativity of the reservoir. Correlation coefficient of the two distributions is 0.31. Variogram for both $\phi$ and $\ln(k)$ of the reference fields are shown in Figure 5.5.

We employ the reference distributions as the global distribution information. It is true that we do not have this information a priori, in that case we could use an approximate global distribution informed by some secondary data such as seismic data. Static well data used in the example are shown in Figure 5.6. We perform the inversion with a number of prior variogram models and analyze the inverted models in each of the runs.

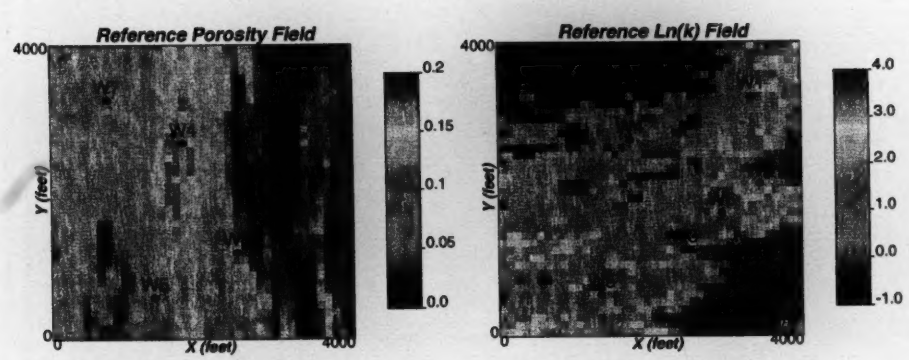


Figure 5.1: Reference $\phi$ and $\ln(k)$ fields.

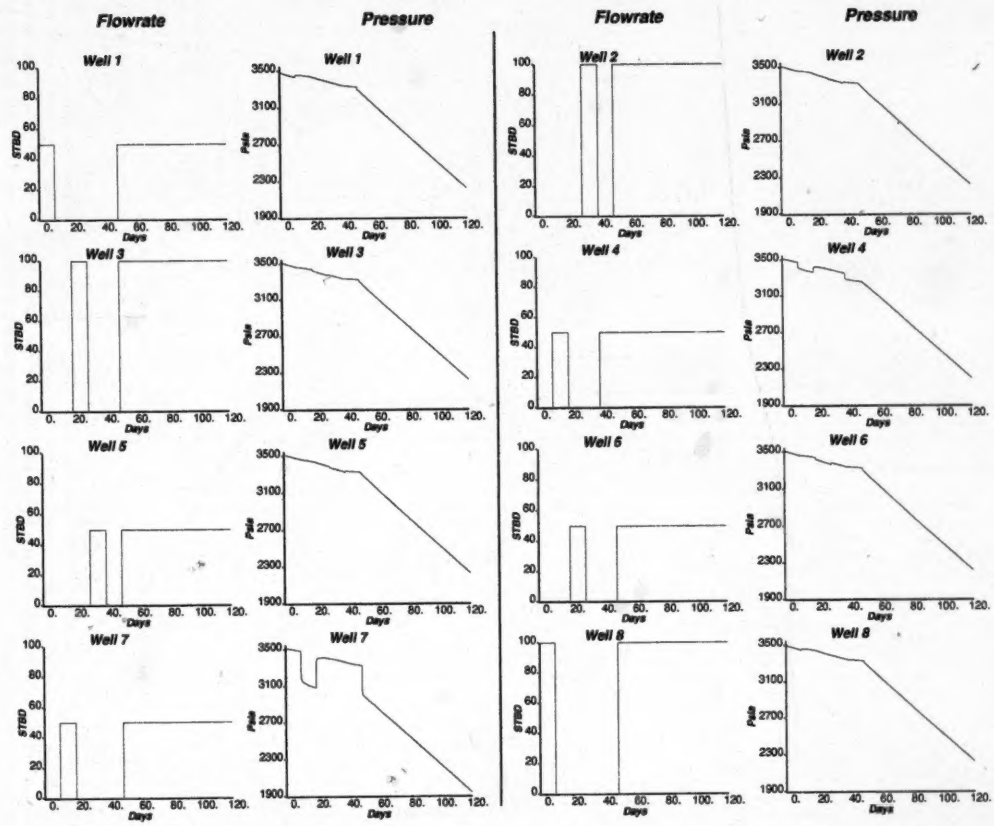


Figure 5.2: Production data (pressure and flow rates) obtained for 8 wells from the reference field.

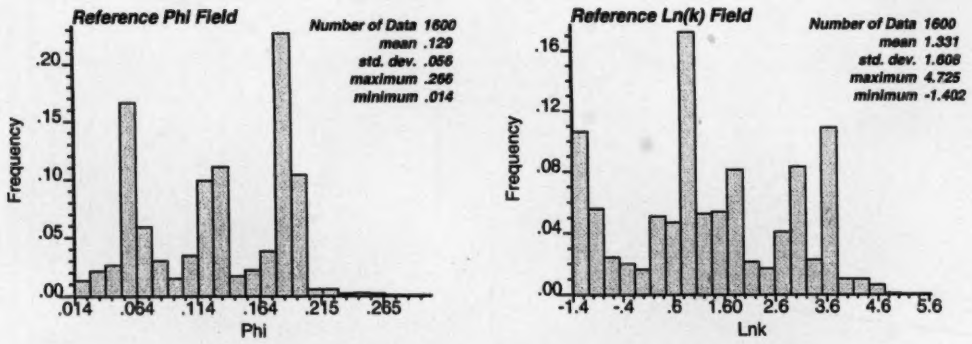


Figure 5.3: Histograms of reference $\phi$ and $\ln(k)$ fields.

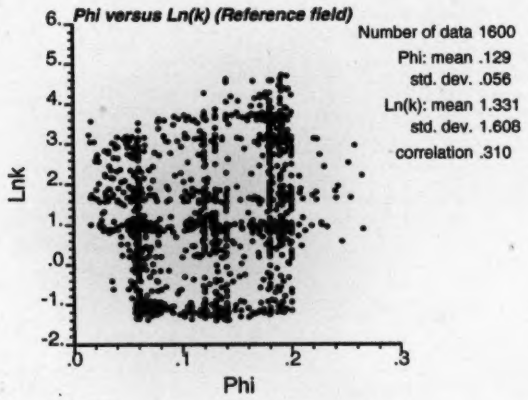


Figure 5.4: Scatterplot of reference $\phi$ and $\ln(k)$ values.

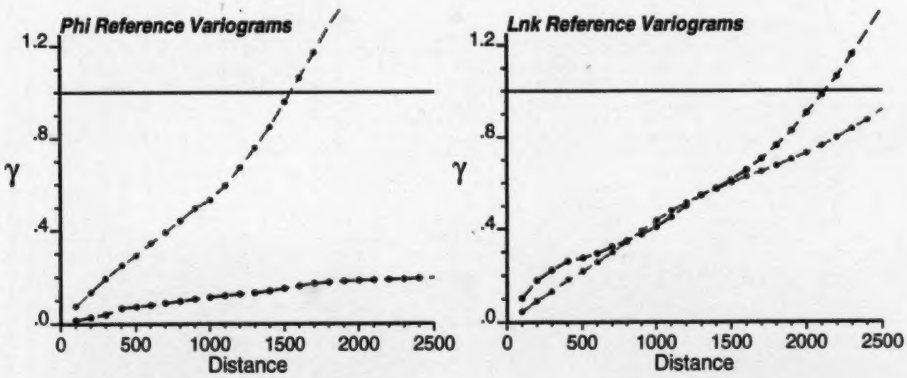


Figure 5.5: Variograms of reference $\phi$ and $\ln(k)$. (X direction - light, Y direction - dark)

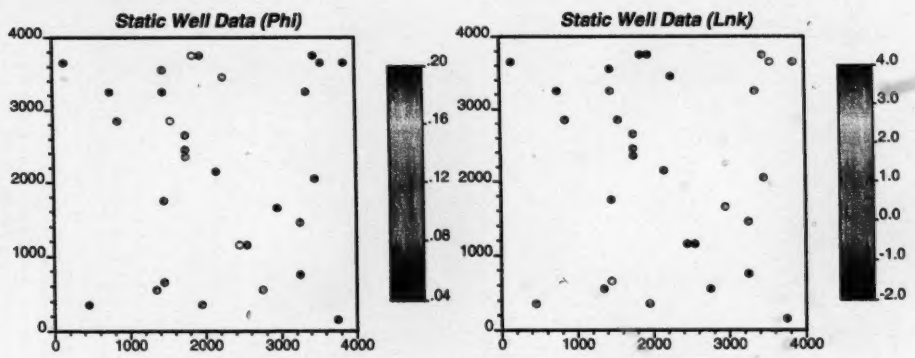


Figure 5.6: Static well data for $\phi$ and $\ln(k)$.

| V. No. | Type | Sill | Range X - Y (ft) | Angle ($^o$) |
|---|---|---|---|---|
| 0 | Nugget | 0.05 | | |
| 1 | Sph | 0.55 | 14000 - 4000 | 0 |
| 2 | Sph | 0.4 | 13000 - 10000 | 0 |

Table 5.1: Prior variogram information used for $\phi$: Run 1.

### Run 1

The prior variogram model used in this run is shown in Tables 5.1 and 5.2 for $\phi$ and $\ln(k)$. The inversion was run for 16 outer iterations using 6 $\times$ 6 (=36) master points in each iteration. CPU time for the run was only 315 seconds in a 1.8 GHz Pentium 4 machine. The pressure responses in the updated porosity and permeability fields converge to the reference pressure data. These inverted models are shown in Figure 5.7. Figure 5.8 shows the pressure values at the eight wells computed from the true (from reference), initial and final updated porosity and permeability fields. The updated fields by the new method accurately reproduce the true pressure data at all wells except Well W4 which is located at (1750.0, 2650.0). The objective function values of the inversion process are shown in Figure 5.9. Final average pressure mismatch in $L^2$ norm sense was 14.7 psi. Updated porosity and permeability fields after each outer iteration of the inversion method are shown in Figures 5.10 and 5.11.

| V. No. | Type | Sill | Range X - Y (ft) | Angle ($^o$) |
|---|---|---|---|---|
| 0 | Nugget | 0.05 | | |
| 1 | Sph | 0.5 | 14000 - 9000 | 0 |
| 2 | Sph | 0.45 | 13000 - 10000 | 0 |

Table 5.2: Prior variogram information used for both $\ln(k)$: Run 1.

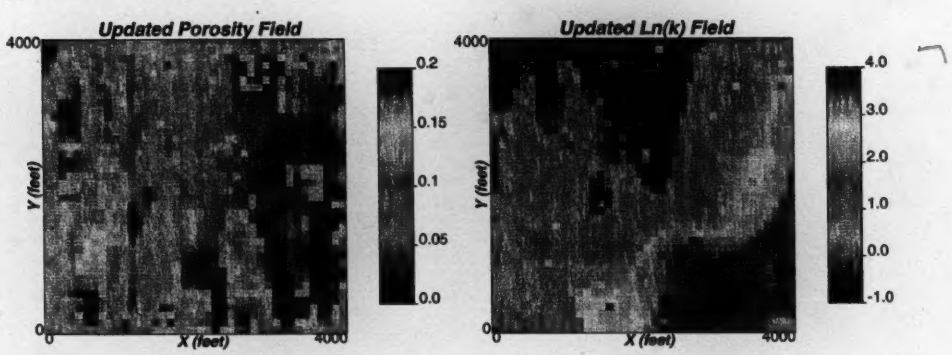


Figure 5.7: Updated $\phi$ and $\ln(k)$ fields: Run 1.

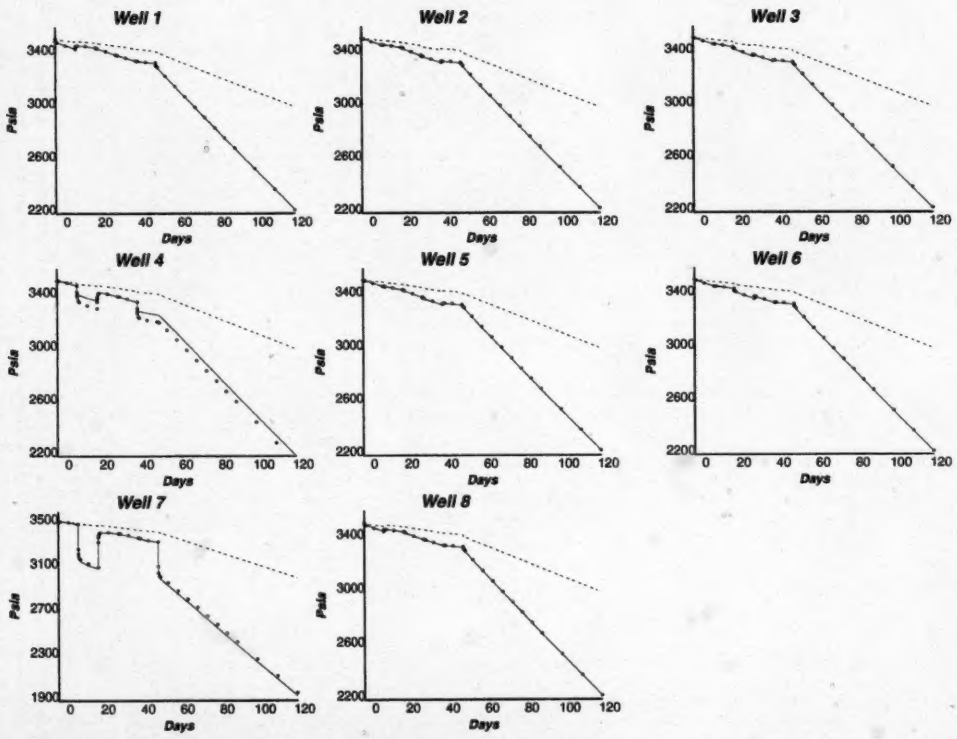


Figure 5.8: Pressure responses computed from initial (dashed lines) and updated (bullets) $\phi$ and $\ln(k)$ fields with the true data (solid lines): Run 1.

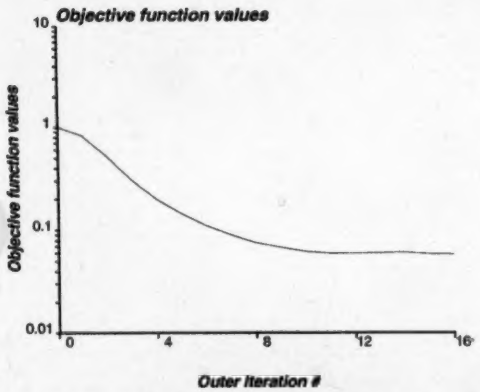


Figure 5.9: Objective function values of the inversion process: Run 1.

| V. No. | Type | Sill | Range X - Y (ft) | Angle ($^o$) |
|---|---|---|---|---|
| 0 | Nugget | 0.05 | | |
| 1 | Sph | 0.55 | 4000 - 10000 | 0 |
| 2 | Sph | 0.4 | 10000 - 12000 | 0 |

Table 5.3: Prior variogram information used for $\phi$: Run 2.

### Run 2

The prior variogram model used in this run is shown in Tables 5.3 and 5.4 for $\phi$ and $\ln(k)$. The inversion was run for 17 outer iterations using 6 $\times$ 6 (=36) master points in each iteration. CPU time for the run was only 331 seconds in a 1.8 GHz Pentium 4 machine. The pressure responses in the updated porosity and permeability fields converge to the reference pressure data. These inverted models are shown in Figure 5.12. Figure 5.13 shows the pressure values at the eight wells computed from the true (from reference), initial and final updated porosity and permeability fields. The updated fields by the new method accurately reproduce the true pressure data at all wells except the same Well W4 as in Run 1. However, the mismatch in this case has reduced. The objective function values of the inversion process are shown in Figure 5.14. Final average pressure mismatch in $L^2$ norm sense was 12.5 psi. Updated porosity and permeability fields after each outer iteration of the inversion method are shown in Figures 5.15 and 5.16.

Having analyzed the inverted models from the two runs, it could be concluded that the algorithm provides reasonably good models. However, better models are obtained for

| V. No. | Type | Sill | Range X - Y (ft) | Angle ($^o$) |
|---|---|---|---|---|
| 0 | Nugget | 0.05 | | |
| 1 | Sph | 0.5 | 4000 - 9000 | 0 |
| 2 | Sph | 0.45 | 10000 - 10000 | 0 |

Table 5.4: Prior variogram information used for $\ln(k)$: Run 2.

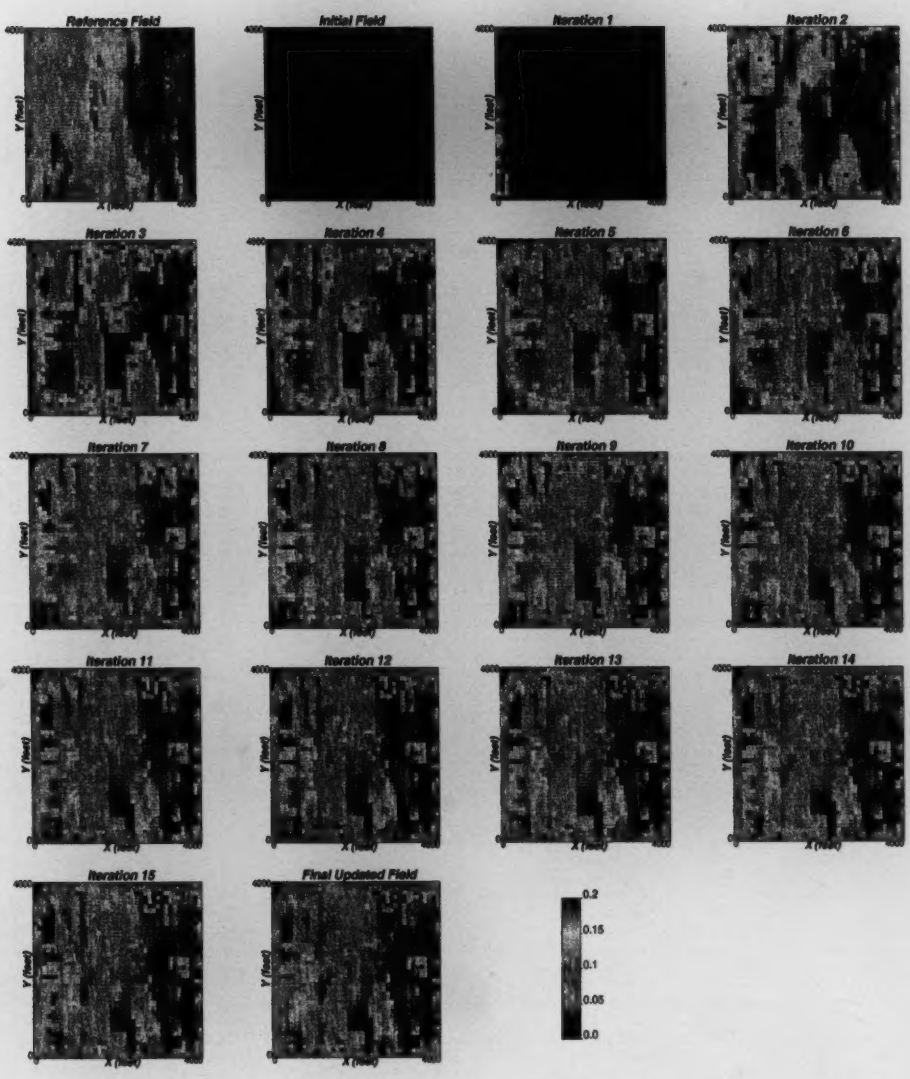


Figure 5.10: Updated $\phi$ fields at each iteration of the inversion process: Run 1.

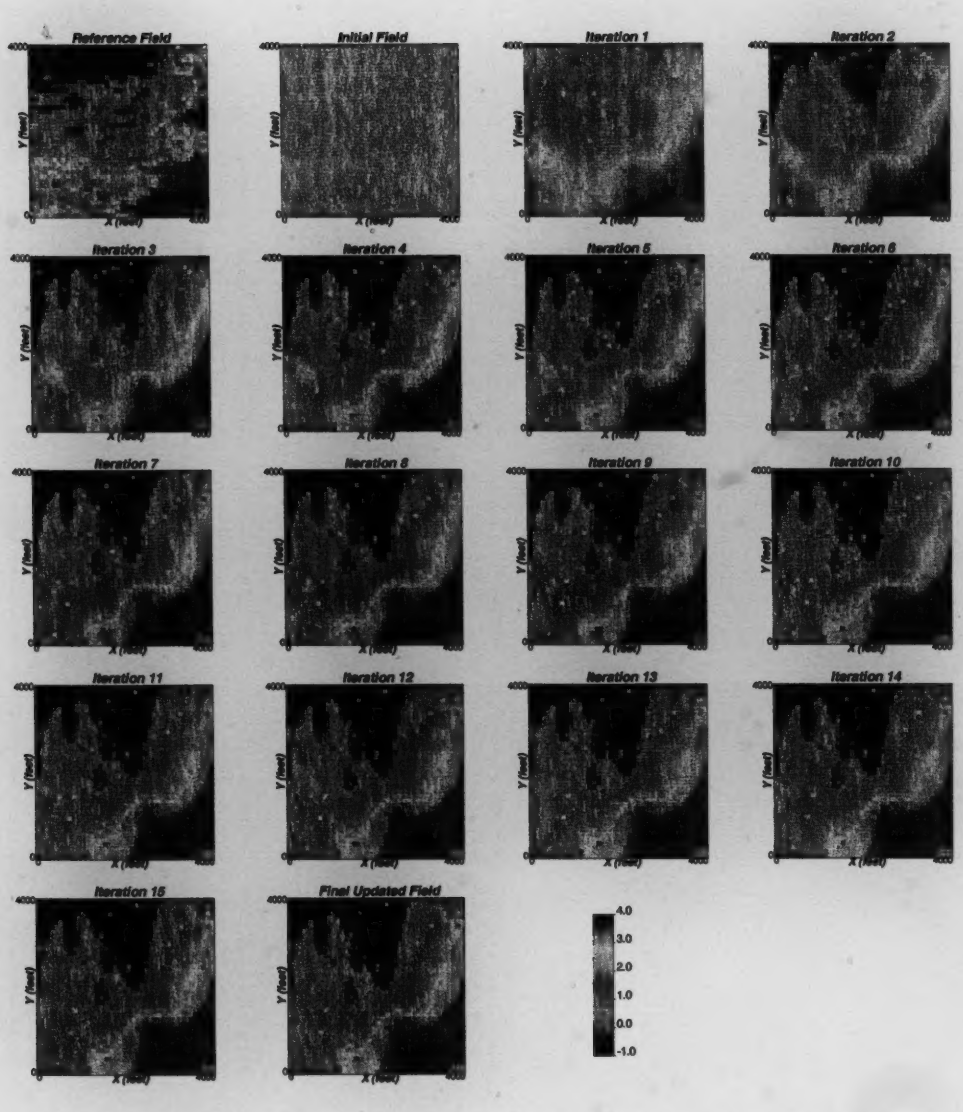


Figure 5.11: Updated $\ln(k)$ fields at each iteration of the inversion process: Run 1.

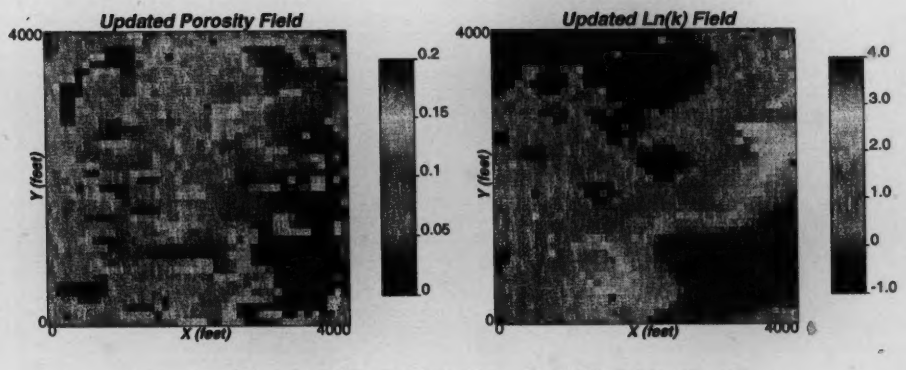


Figure 5.12: Updated $\phi$ and $\ln(k)$ fields: Run 2.

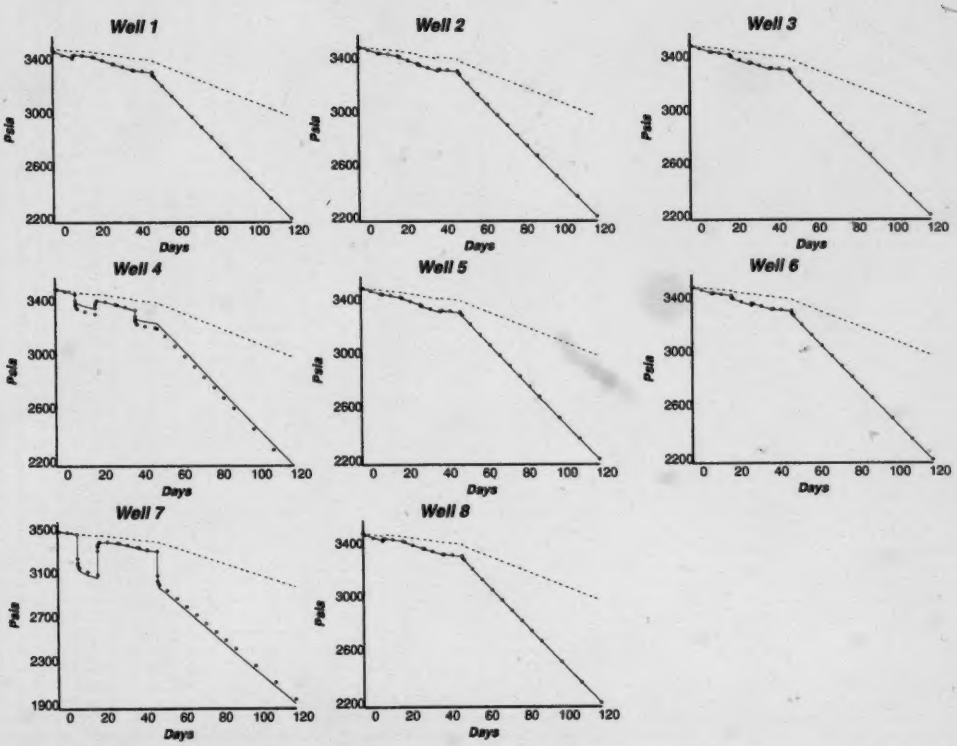


Figure 5.13: Pressure responses computed from initial (dashed lines) and updated (bullets) $\phi$ and $\ln(k)$ fields with the true data (solid lines): Run 2.

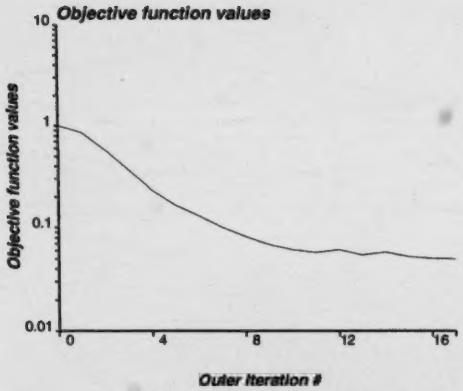


Figure 5.14: Objective function values of the inversion process: Run 2.

permeability than those for porosity. In the first run, we started with a prior variogram model with high continuity in the North-South direction for both $\phi$ and $\ln(k)$, the inverted models had right heterogeneity structure for $\ln(k)$. In the second run, we started with an almost isotropic model. In this case also we retrieve the right structure for $\ln(k)$. However, for $\phi$ the nugget effect is exaggerated. Well W4 (1750.0, 2650.0) in both runs had the highest mismatch. In the reference models, $\phi$ and $\ln(k)$ values in this grid block are 0.131 and 0.542; average values for both variables. Inspecting the inverted fields, we could see poor inverted values around this block.

Note that the termination criteria for the outer loop of the inversion algorithm are maximum number of outer iterations or a tolerance value for the objective function. If the second criterion is not met, we first perform the inversion with a large value for the number of outer iterations. Then we examine the objective function curve and in the next run we set the number of outer iterations to this value. This could be automated in the code by storing the best model and the number of outer loops, and reporting the outputs up to this outer iteration.

## 5.2 Effect of Production Data

In this section, we investigate the effect of production data on the inversion outcome. We reduce the number of wells to 6 and 4, and perform the inversion. We employ similar parameters as in the previous section apart from the production data.

### 6 Well Case

The 6 wells are: W1 at the center of the cell (34,33), W2 at (33,8), W3 at (25,12), W4 (18,27), W5 (14,6), and W6 (30,17), respectively. The wells are shown in Figure 5.1. Figure 5.17 shows the imposed production rates and the corresponding numerically simulated pressure responses at these wells. The anisotropic low nugget prior variogram model used in this run is shown in Tables 5.3 and 5.4 for $\phi$ and $\ln(k)$. The inversion was run for 7 outer iterations using $6 \times 6$ (=36) master points in each iteration. CPU time for the run was only 143 seconds in a 1.8 GHz Pentium 4 machine. The pressure responses in the updated porosity and permeability fields converge to the reference pressure data. These inverted models

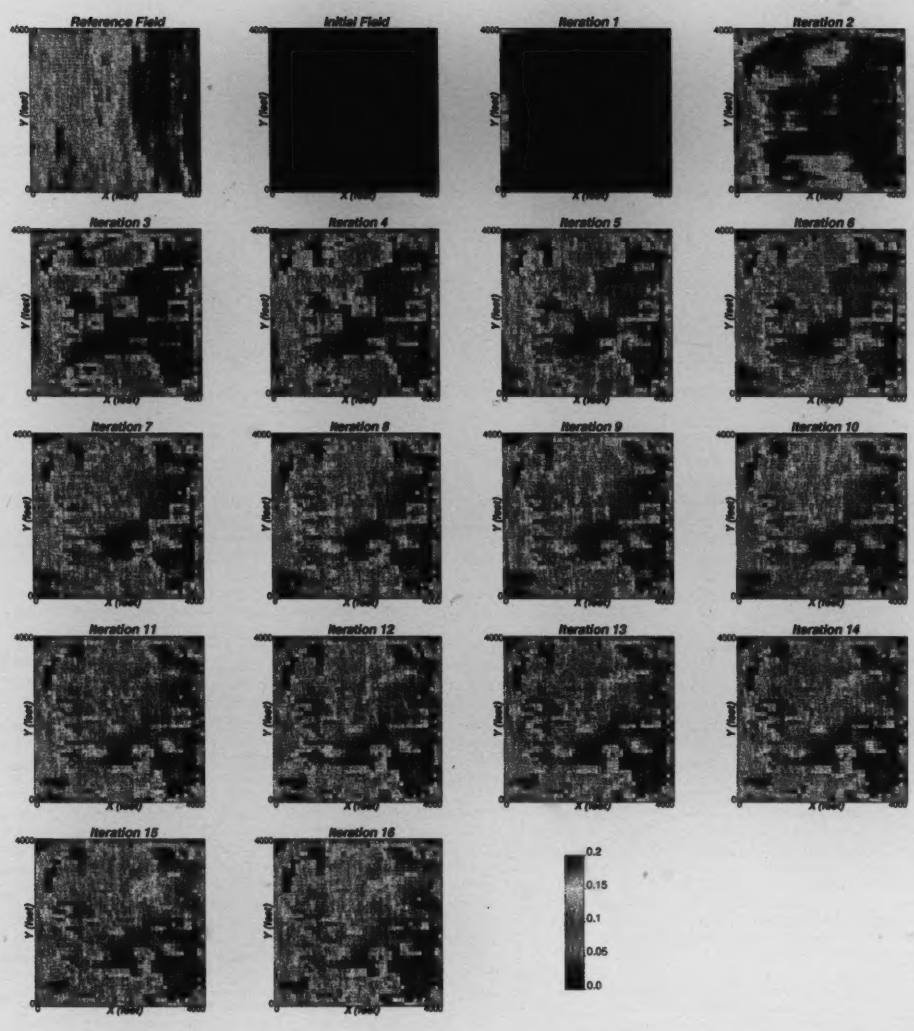


Figure 5.15: Updated $\phi$ fields at each iteration of the inversion process: Run 2.

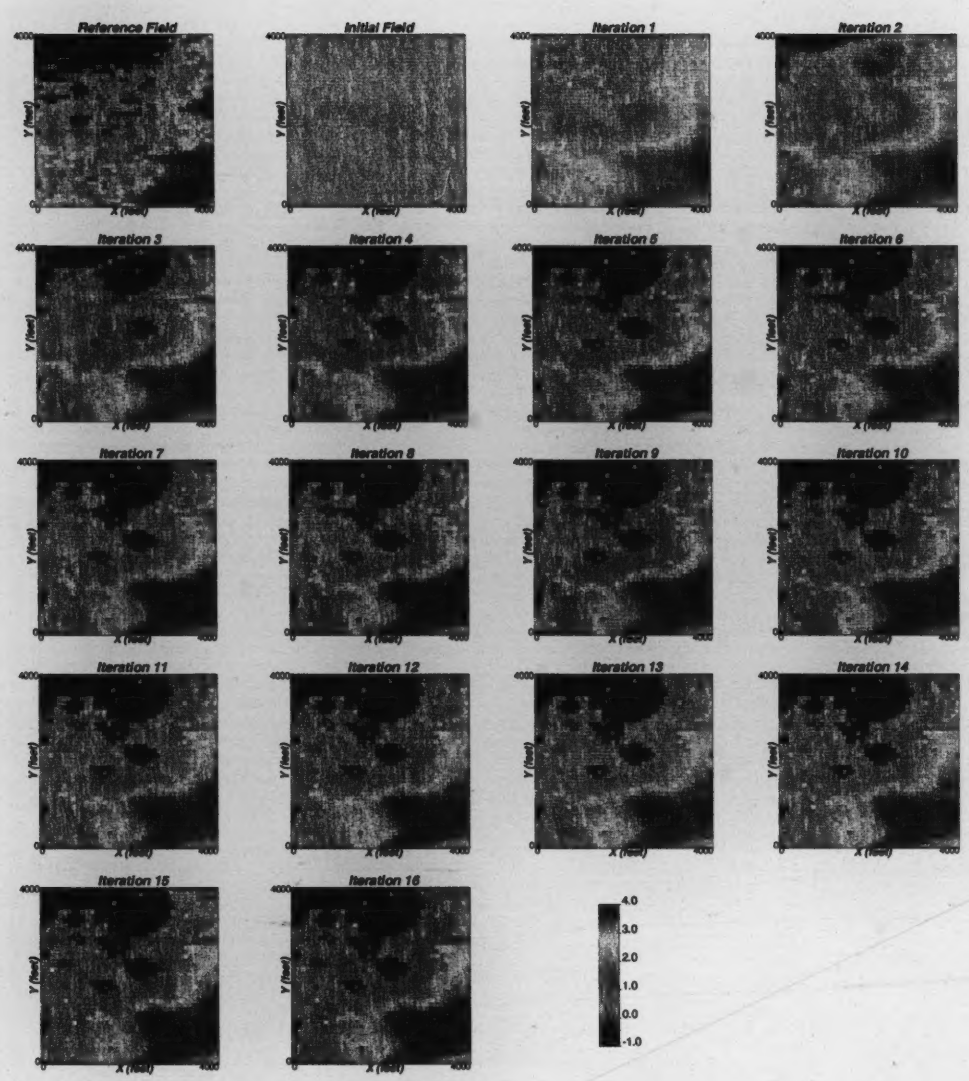


Figure 5.16: Updated $\ln(k)$ fields at each iteration of the inversion process: Run 2.

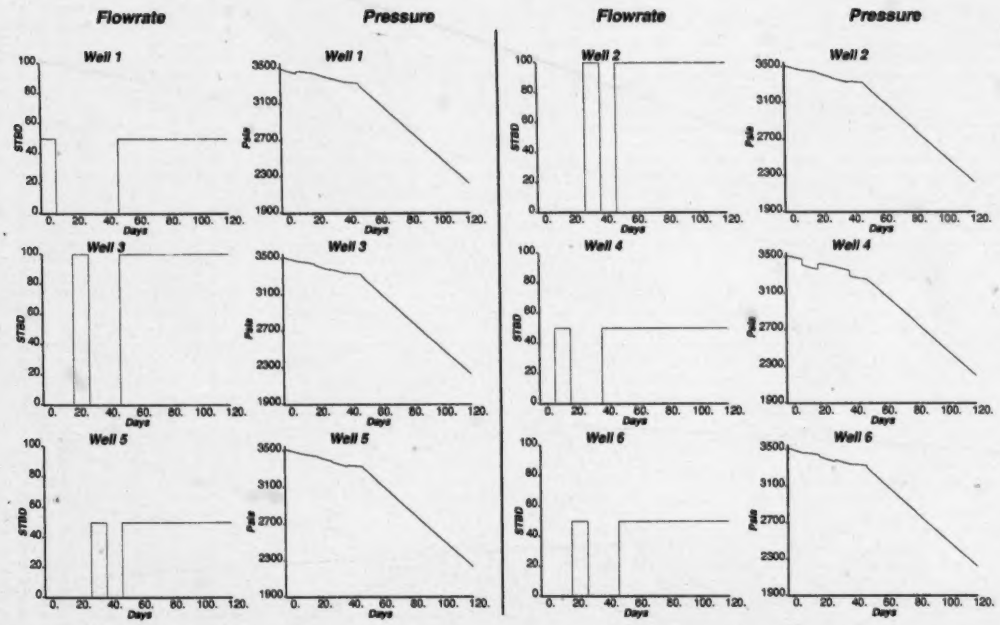


Figure 5.17: Production data (pressure and flow rates) obtained from the reference field: 6 Well Case.

are shown in Figure 5.18. Figure 5.19 shows the pressure values at the six wells computed from the true (from reference), initial and final updated porosity and permeability fields. The updated fields by the new method accurately reproduce the true pressure data at all wells except Well W4 that is located at (1750.0, 2650.0). The objective function values of the inversion process is shown in Figure 5.20. Final average pressure mismatch in $L^2$ norm sense was 6.35 psi. Updated porosity and permeability fields after each outer iteration of the inversion method are shown in Figures 5.21 and 5.22.

## 4 Well Case

The 4 wells are: W1 at the center of the cell (34,33), W2 at (33,8), W3 at (25,12), and W4 (18,27). The wells are shown in Figure 5.1. Figure 5.23 shows the imposed production rates and the corresponding numerically simulated pressure responses at these wells. The prior variogram model used in this run is shown in Tables 5.3 and 5.4 for $\phi$ and $\ln(k)$. The inversion was run for 7 outer iterations using $6 \times 6$ (=36) master points in each iteration. CPU time for the run was only 143 seconds in a 1.8 GHz Pentium 4 machine. The pressure responses in the updated porosity and permeability fields converge to the reference pressure data. These inverted models are shown in Figure 5.24. Figure 5.25 shows the pressure values at the four wells computed from the true (from reference), initial and final updated porosity and permeability fields. The updated fields by the new method accurately reproduce the true pressure data at all wells except Well W4 that is located at (1750.0, 2650.0). The objective function values of the inversion process is shown in Figure 5.26. Final average

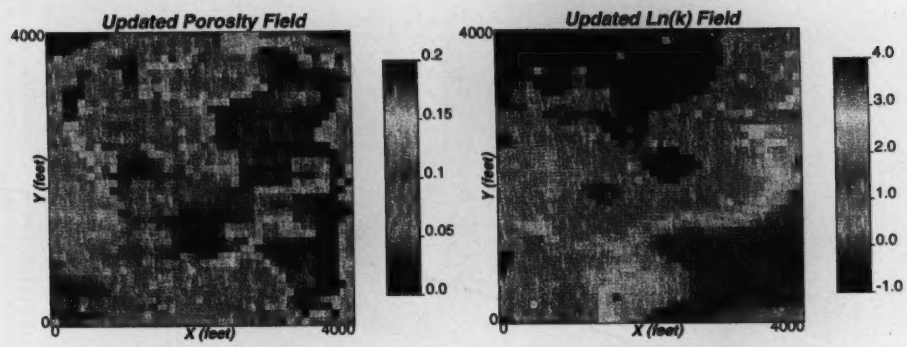


Figure 5.18: Updated $\phi$ and $\ln(k)$ fields: 6 Well Case.

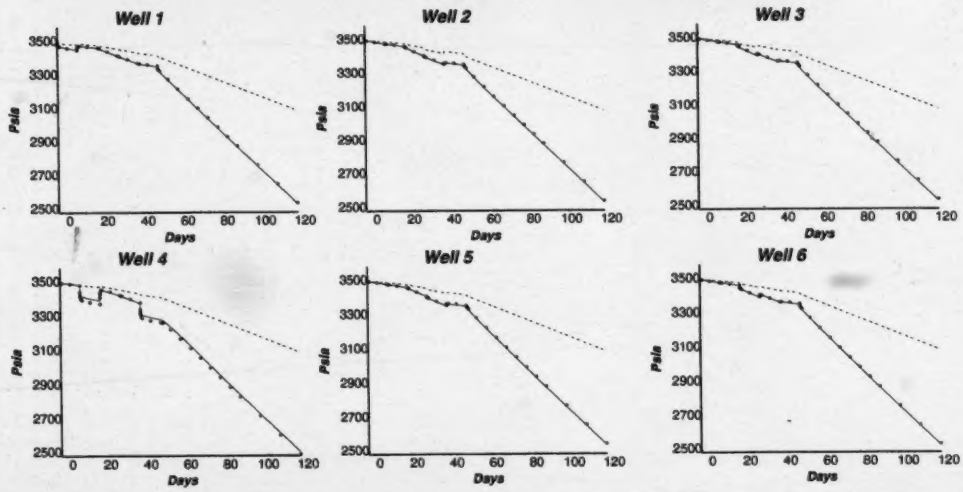


Figure 5.19: Pressure responses computed from initial (dashed lines) and updated (bullets) $\phi$ and $\ln(k)$ fields with the true data (solid lines): 6 Well Case.

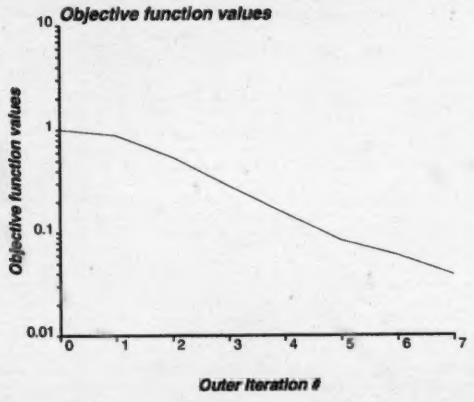


Figure 5.20: Objective function values of the inversion process: 6 Well Case.

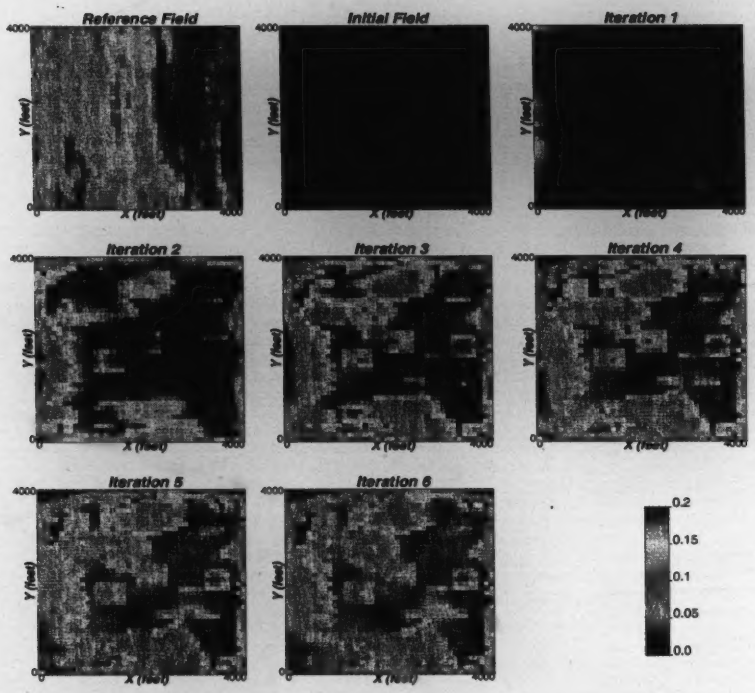


Figure 5.21: Updated $\phi$ fields at each iteration of the inversion process: 6 Well Case.

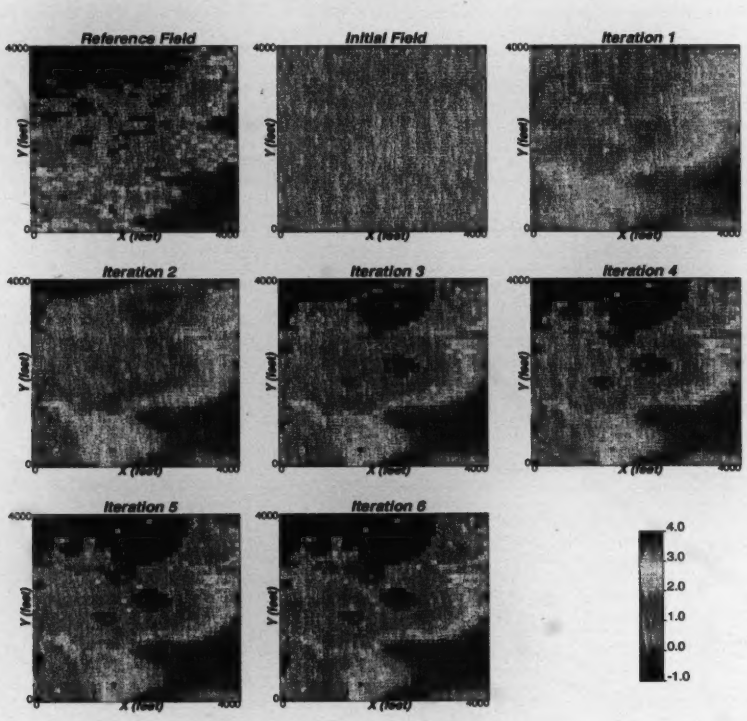


Figure 5.22: Updated $\ln(k)$ fields at each iteration of the inversion process: 6 Well Case.

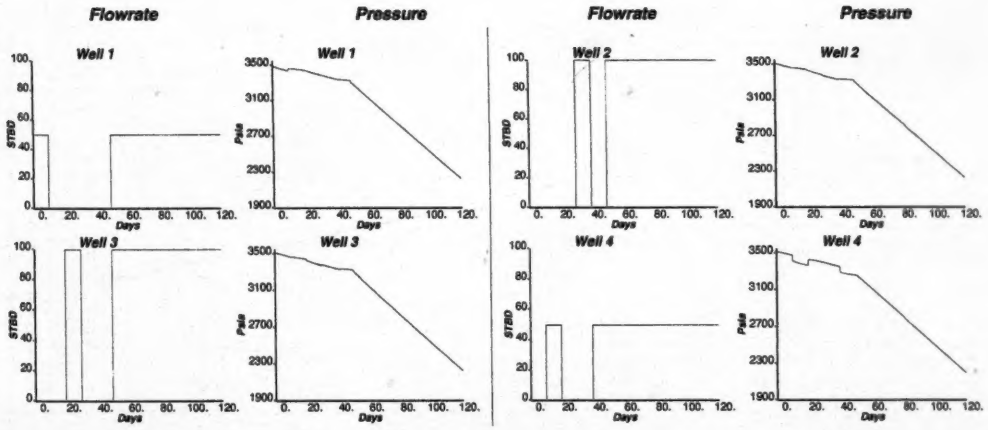


Figure 5.23: Production data (pressure and flow rates) obtained from the reference field: 4 Well Case.

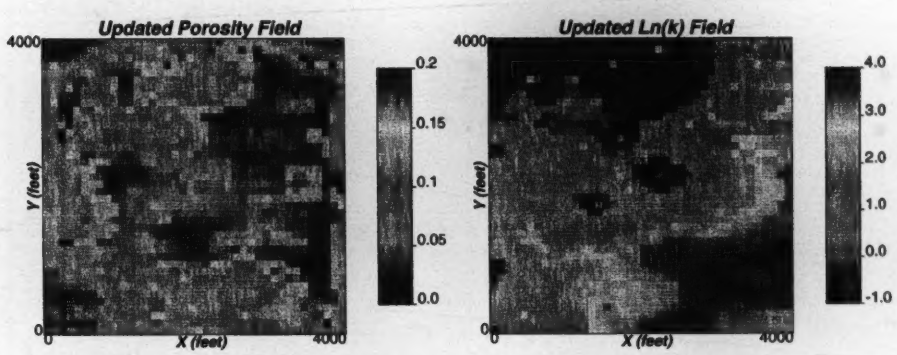


Figure 5.24: Updated $\phi$ and $\ln(k)$ fields: 4 Well Case.

pressure mismatch in $L^2$ norm sense was 7.69 psi. Updated porosity and permeability fields after each outer iteration of the inversion method are shown in Figures 5.27 and 5.28.

## Conclusion

It could be concluded that using 4, 6 or 8 wells for porosity, permeability inversion leads to similar models for the present synthetic reservoir model with unique heterogeneity features. Originally, the intention was to investigate whether the developed algorithm can invert $\phi$, $\ln(k)$ models where in some portions of the reservoir the correlation between the two petrophysical variables is poor. The responses of the inversion runs and the sensitivities performed confirm that it is possible to invert for this kind of models. However, it appears $\ln(k)$ models obtained through this algorithm retrieves heterogeneity features better than that of $\phi$. A possible solution of this limitation may be to calculate the $\phi$ gradients independently from the flow and constitutive equations involved.

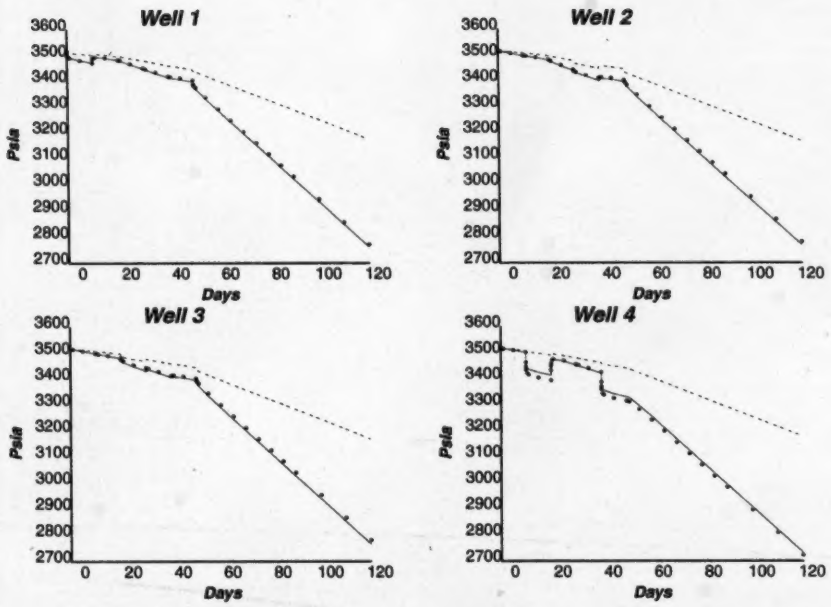


Figure 5.25: Pressure responses computed from initial (dashed lines) and updated (bullets) $\phi$ and $\ln(k)$ fields with the true data (solid lines): 4 Well Case.

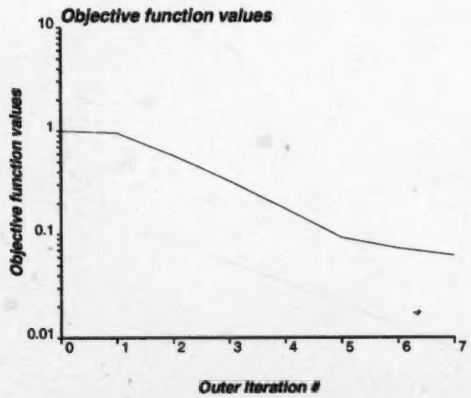


Figure 5.26: Objective function values of the inversion process: 4 Well Case.

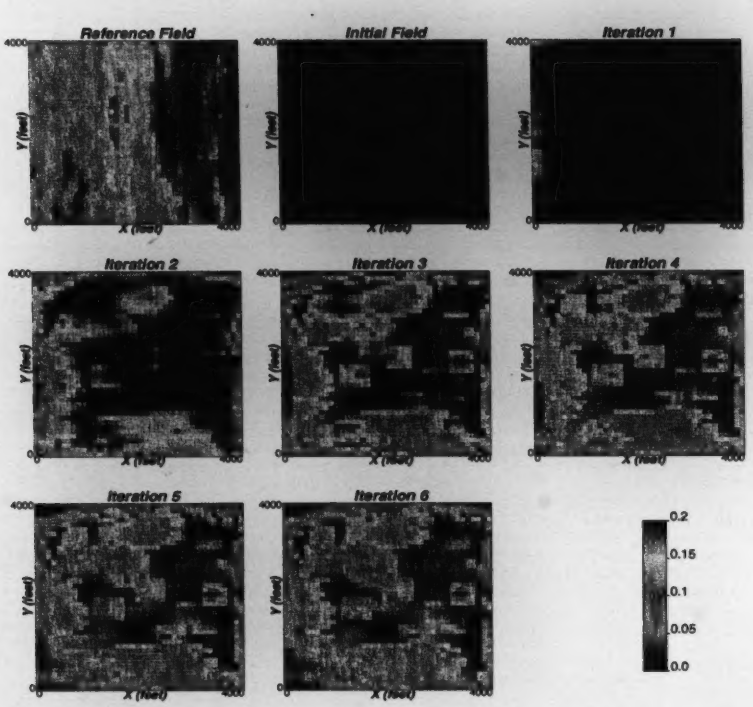


Figure 5.27: Updated $\phi$ fields at each iteration of the inversion process: 4 Well Case.

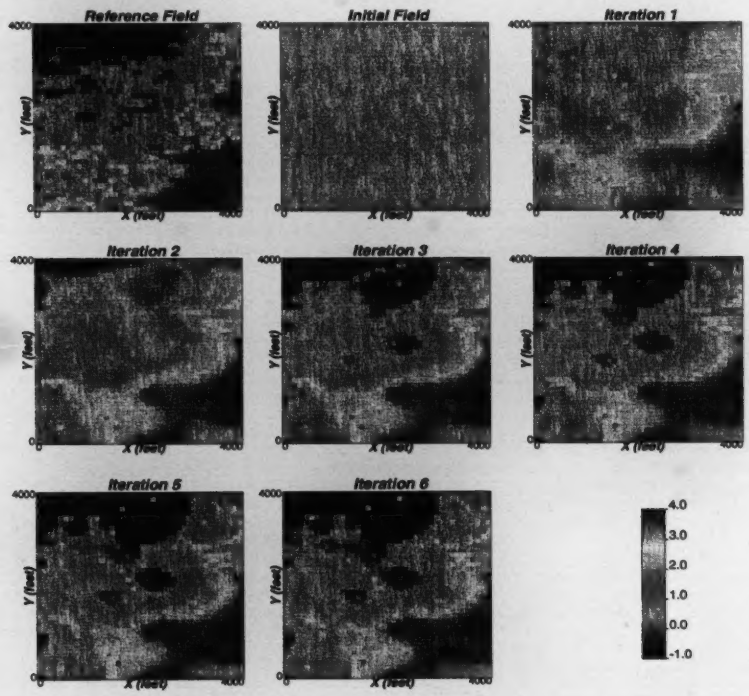


Figure 5.28: Updated $\ln(k)$ fields at each iteration of the inversion process: 4 Well Case.

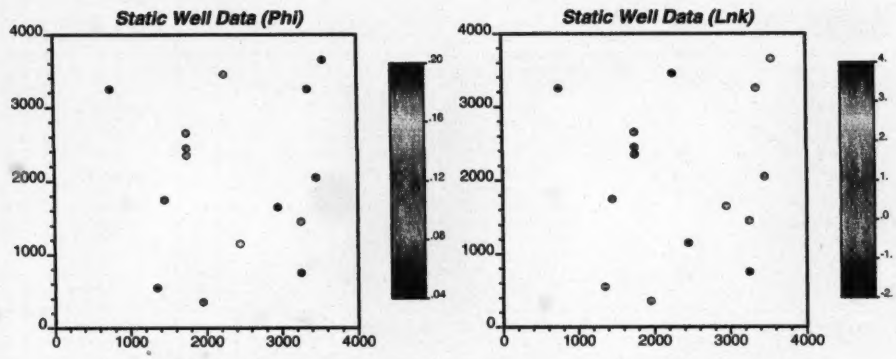


Figure 5.29: Static well data for $\phi$ and $\ln(k)$: 15 Local Data Case.

## 5.3 Influence of Local Data

In all the previous inversion runs, we performed the inversion using "many" local data (30 precisely). It would be interesting to see how much incremental contribution of these local data is in the inverted models. In order to investigate this we perform the inversion by varying the number of local data to 15 and 0. We use similar parameters as used in the previous section for 6 well case. The 6 wells are: W1 at the center of the cell (34,33), W2 at (33,8), W3 at (25,12), W4 (18,27), W5 (14,6), and W6 (30,17). Wells are shown in Figure 5.1. Figure 5.17 shows the imposed production rates and the corresponding numerically simulated pressure responses at these wells. The prior variogram model used in this run is shown in Tables 5.3 and 5.4 for $\phi$ and $\ln(k)$.

### 15 Local Data Case

Local data used in this run are shown in Figure 5.29. The inversion was run for 6 outer iterations using 6 $\times$ 6 (=36) master points in each iteration. CPU time for the run was only 125 seconds in a 1.8 GHz Pentium 4 machine. The pressure responses in the updated porosity and permeability fields converge to the reference pressure data. These inverted models are shown in Figure 5.30. Figure 5.31 shows the pressure values at the six wells computed from the true (from reference), initial and final updated porosity and permeability fields. The updated fields by the new method accurately reproduce the true pressure data at all wells. Even Well W4 located at (1750.0, 2650.0) pressure match is good in this case. The objective function values of the inversion process is shown in Figure 5.32. Final average pressure mismatch in $L^2$ norm sense was 4.05 psi. This mismatch value compared to that (6.35) with 30 local data is even better. Updated porosity and permeability fields after each outer iteration of the inversion method are shown in Figures 5.33 and 5.34.

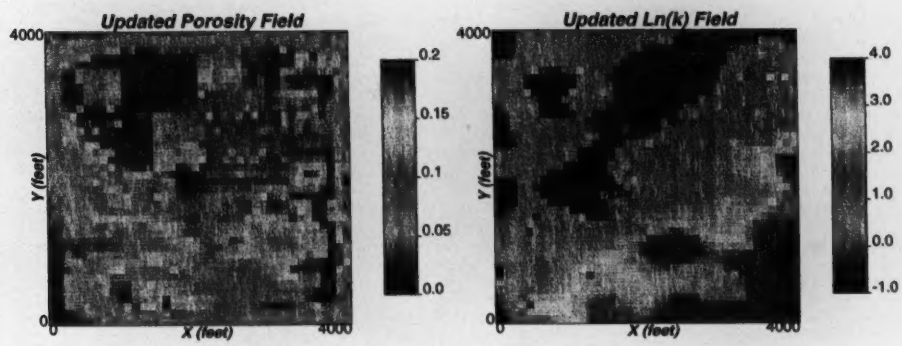


Figure 5.30: Updated $\phi$ and $\ln(k)$ fields: 15 Local Data Case.

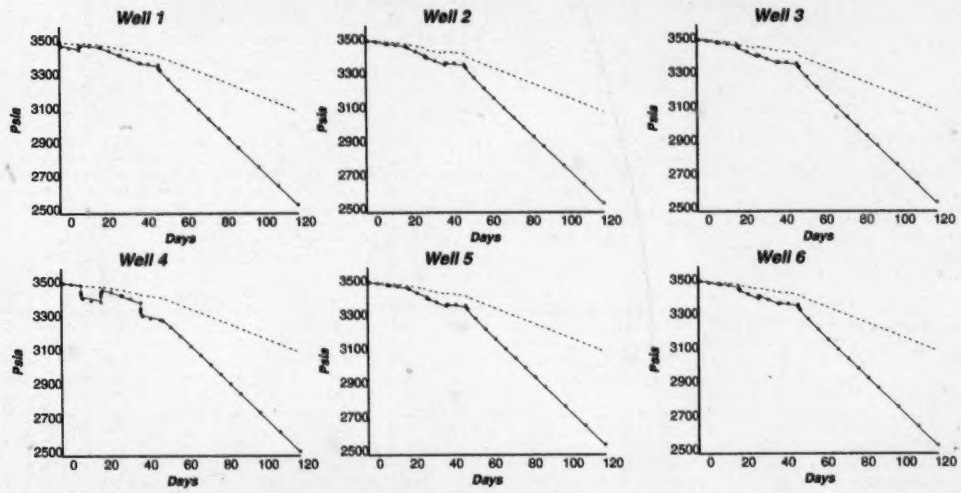


Figure 5.31: Pressure responses computed from initial (dashed lines) and updated (bullets) $\phi$ and $\ln(k)$ fields with the true data (solid lines): 15 Local Data Case.

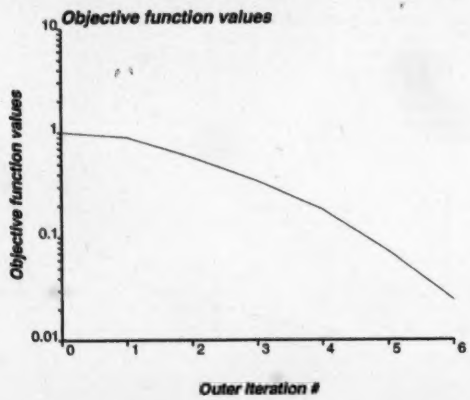


Figure 5.32: Objective function values of the inversion process: 15 Local Data Case.

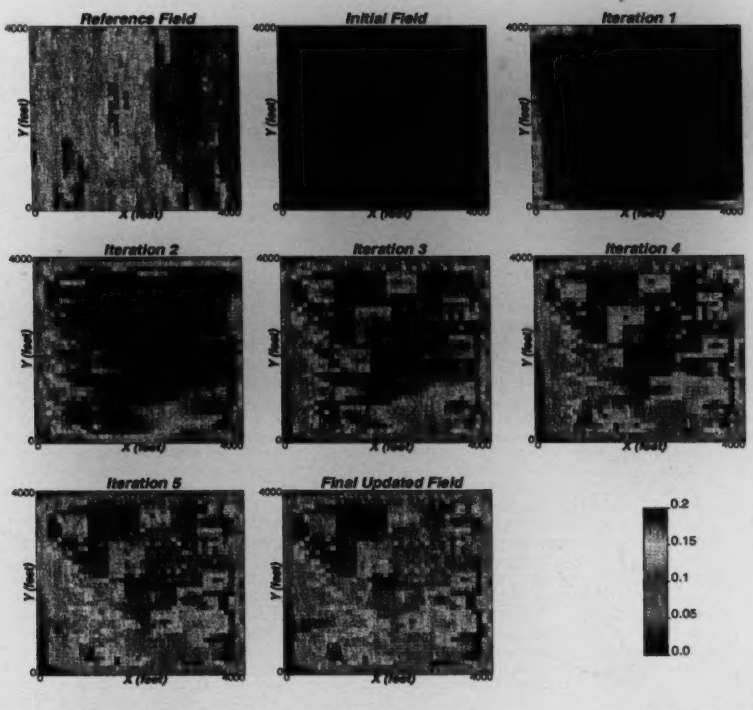


Figure 5.33: Updated $\phi$ fields at each iteration of the inversion process: 15 Local Data Case.

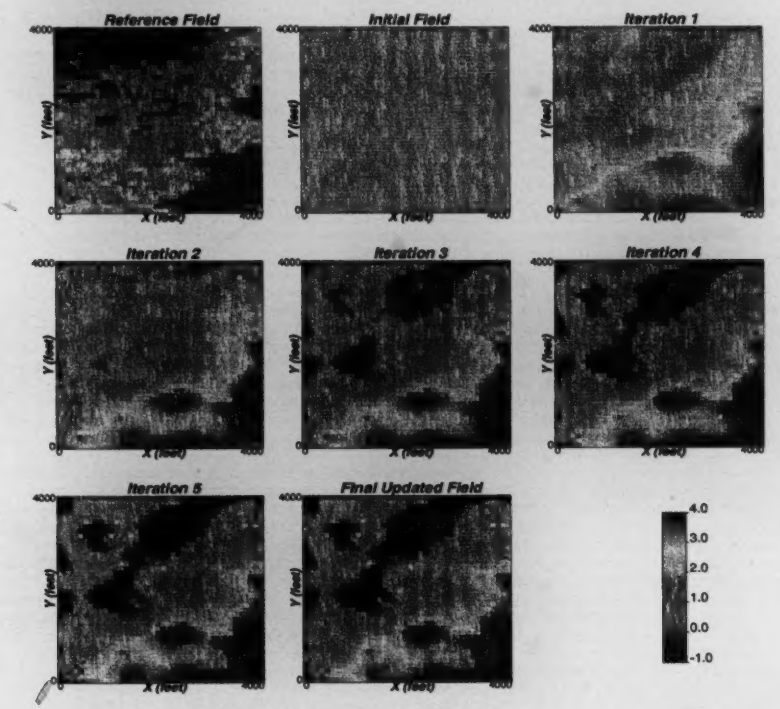


Figure 5.34: Updated $\ln(k)$ fields at each iteration of the inversion process: 15 Local Data Case.

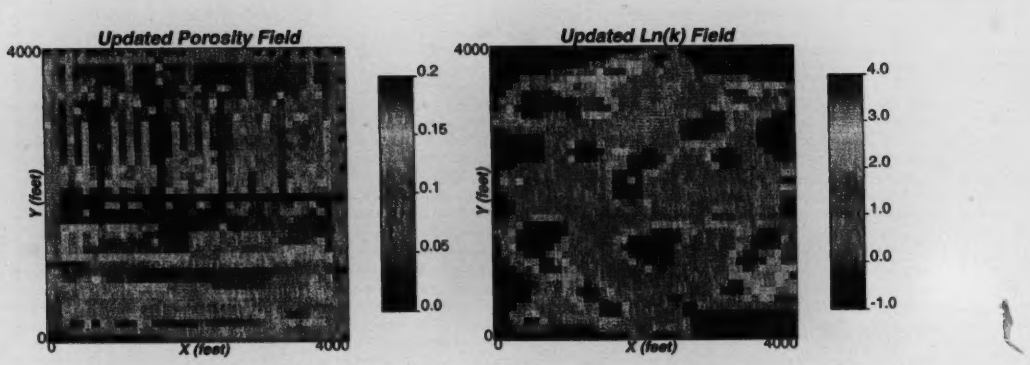


Figure 5.35: Updated $\phi$ and $\ln(k)$ fields: No Local Data Case. Poor Convergence.

## No Local Data Case

This inversion run was performed without any local data. The inversion was run for 6 outer iterations using 36 master points in each iteration. CPU time for the run was only 115 seconds in a 1.8 GHz Pentium 4 machine. The pressure responses in the updated $\phi$ and $\ln(k)$ fields do not converge to the reference pressure data. These inverted models are shown in Figure 5.35. Figure 5.36 shows the pressure values at the six wells computed from the true (from reference), initial and final updated porosity and permeability fields. The updated fields by the new method accurately reproduce the true pressure data at Wells W2, W3 and W6 only. Well W1 pressure match curve reveals early and late time mismatch indicating improper heterogeneity capture in both the vicinity and the distant grid blocks. Well W4, located at (1750.0, 2650.0), has the greatest mismatch as was evident in most of the previous inversion exercises. The objective function values of the inversion process is shown in Figure 5.37. It is evident from the figure that realistically no improvement took place after the second outer iteration. It appears that the solution is stuck in some kind of local minimum that is far from the global minimum. Final average pressure mismatch in $L^2$ norm sense was 17.24 psi, a significantly high value. Updated porosity and permeability fields after each outer iteration of the inversion method are shown in Figures 5.38 and 5.39.

## Conclusion

From the above sensitivity exercise, it could be concluded that integration of both local data and dynamic production is important for good inverted models. This confirms the hypothesis that different sources of data contain valuable information. One needs to appropriately combine all available information. The extremely poor inversion outcomes in case of no local data reveals that in order to constrain $\phi$ and $\ln(k)$ values properly, some local data is essential. However, this does not imply that the more the local data being used, the better the inverted models. This is revealed by comparing the cases using 15 and 30 local data cases.

Local data helps regularize the nonlinear inverse problem. The inherent non-uniqueness of inverse problem causes the solution to be stuck in some local minimum unless some regularization scheme is used.

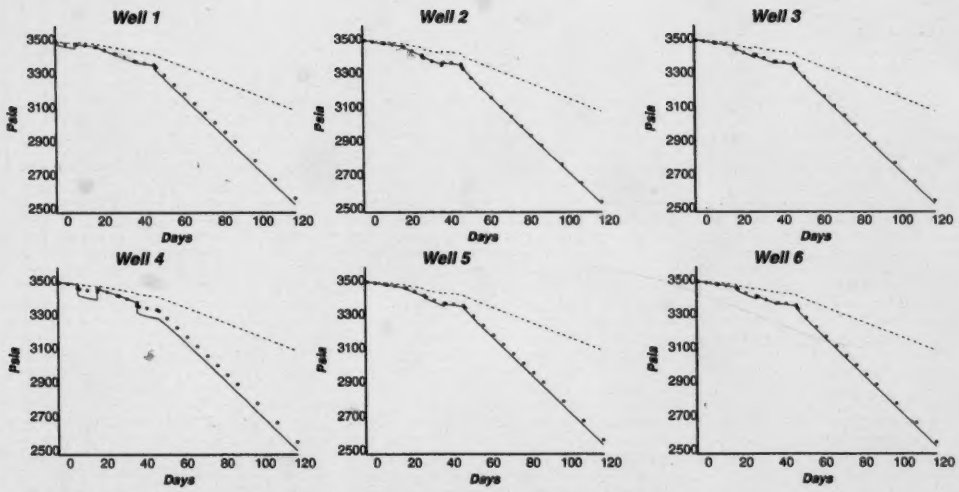


Figure 5.36: Pressure responses computed from initial (dashed lines) and updated (bullets) $\phi$ and $\ln(k)$ fields with the true data (solid lines): No Local Data Case.

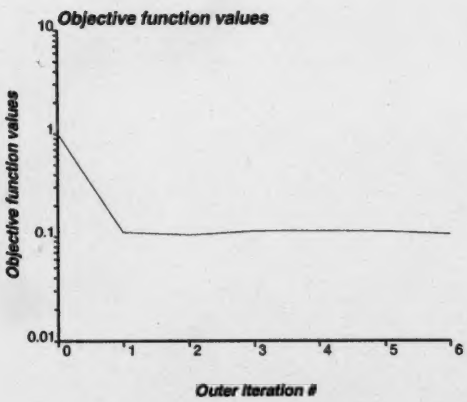


Figure 5.37: Objective function values of the inversion process: No Local Data Case.

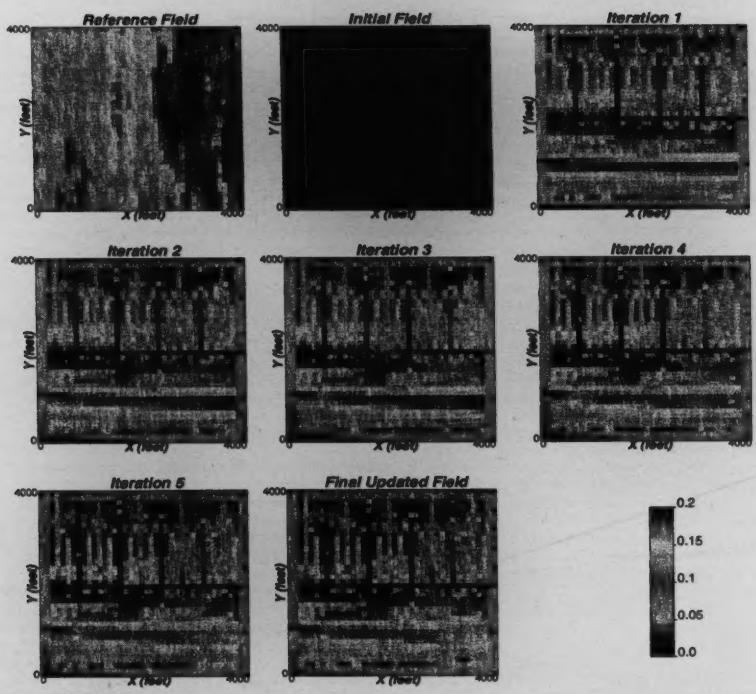


Figure 5.38: Updated $\phi$ fields at each iteration of the inversion process: No Local Data Case.

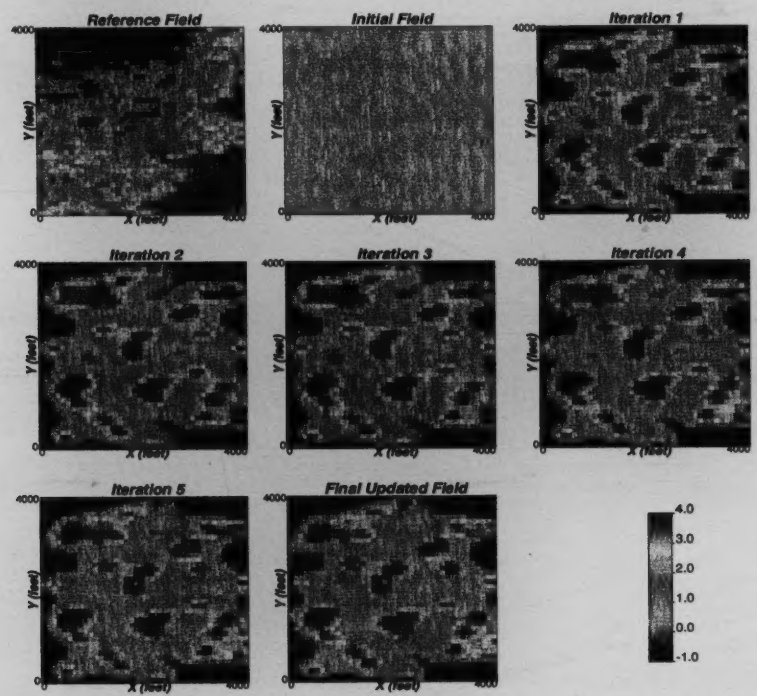


Figure 5.39: Updated $\ln(k)$ fields at each iteration of the inversion process: No Local Data Case.

# Chapter 6

# Simultaneouos Inversion with Variogram Updating

There are rarely enough data to calculate reliable variograms. This is particularly true in petroleum reservoir characterization. It is hardly possible to model reasonably good horizontal variograms with a few well data. Expert modeler would use experience or analogue information; however, each reservoir is unique and the reasonableness of analogue data can always be questioned. In this chapter, we present a technique to assist with variogram inference by using information available from production history or well test data. The new algorithm further improves upon the inversion solutions that are obtained using the algorithm presented in Chapter 4.

The algorithm will be explained. We demonstrate the results of the developed code with some synthetic realistic reservoir models. The outcome of this approach in addressing the problem is remarkable when sufficient production data exist.

## 6.1 Variogram Inversion Algorithm

The algorithm developed here builds upon the algorithm presented in Chapter 4. We extend this dynamic data integration algorithm for petrophysical property modeling to invert for spatial continuity parameters. In order to achieve this, we have implemented a module to determine updated experimental variograms of the property models, and another module to automatically fit these dynamically updated experimental variograms. The automatic variogram fitting module relies on an 'almost' exhaustive search algorithm in a $L^2$ norm basis. The $L^2$ norm is calculated using an inverse squared distance weighting approach where short distances are emphasized.

The inversion code requires additional parameters for variogram inversion. One needs the parameters required for experimental variogram calculation. Namely, the number of lags, lag distance, lag tolerance, azimuth angles, angle tolerance and bandwidths.

### Extension for Variogram Updating

The incorporation of experimental variogram calculation and automatic variogram modeling module is as follows:

1. Perform Steps (1) to (10) discussed for simultaneous inversion algorithm in Chapter 4 using a priori variogram information.

2. Calculate experimental variograms of updated $\phi$ and $\ln(k)$ fields.

3. Perform automatic variogram modeling with an 'almost' exhaustive search algorithm based on a weighted $L^2$ norm.

4. Update the prior variogram parameters with the new ones.

5. Repeat Steps (1) to (4) until convergence is achieved in the inversion process.

In this modified algorithm the variogram models that are to be used for kriging at each outer iteration are updated. This updating is naturally informed to some extent by the production data at each outer iteration. In the original version of the algorithm, the variogram models are kept unchanged. Thus, even if incremental information is captured from production data, the initial variogram information of is used at each outer iteration. The new algorithm removes some of these restictions by dynamically updating the variogram models. The parameters that are fitted in the updating module are the ranges of each variogram structure, sill contribution, angle of anistropy, and nugget effect.

## 6.2 A Synthetic Application

A synthetic example is presented here to evaluate the ability of the algorithm to invert for variogram parameters using multiple well production data. Reference porosity and permeability models are constructed first. Pressure responses at a number of wells are obtained through flow simulation.

The 2D 4,000-ft square domain is discretized into 40 $\times$ 40 grid cells of 100 $\times$ 100 ft. Porosity and permeability fields are shown in Figure 6.1. There are four wells: W1 at the center of the cell (24,10), W2 at (37,17), W3 at (14,32), and W4 at (35,31). Wells are shown in Figure 6.1. The four boundaries are constant pressure boundaries, reservoir thickness is 100 ft, viscosity is 0.2 cp, formation compressibility is $10^{-6}$ $\text{psi}^{-1}$, and well radius is 0.3 ft. Figure 6.2 shows the imposed production rates and the corresponding numerically simulated pressure responses at the different wells. The global histograms and the scatter-plot between porosity and $\ln(k)$ are shown in Figures 6.3 and 6.4, respectively. Mean and standard deviation of reference distributions are 0.13 and 0.06 for $\phi$, and 1.43 and 1.96 for $\ln(k)$. The low average porosity confirms the low storativity of the reservoir. Correlation coefficient of the two distributions is 0.79. Variogram for both $\phi$ and $\ln(k)$ of the reference fields are shown in Figure 6.5. The well data is inadequate for variogram inference. Using only this many data, one can hardly model or infer horizontal variograms. Even with unusually large lag tolerance and bandwidth used in variogram estimation, realistic variograms could not be estimated (shown in Figure 6.6). We do not have much confidence in the variograms estimated from the well data. Our objective here is to account for production data and estimate a realistic variogram model for the reservoir.

The data integration algorithm devised here requires the well data, the production history (or well test data), global distribution information and a prior guess of the variogram model. We employ the reference distributions as the global distribution information. It is true that we do not have this information a priori; we could use an approximate global

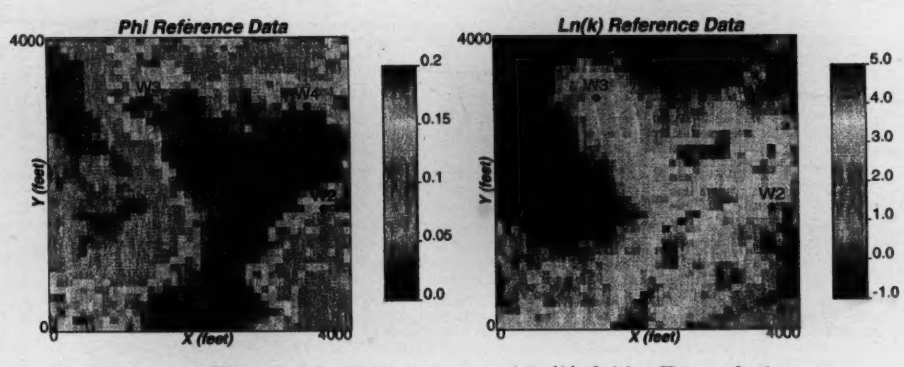


Figure 6.1: Reference $\phi$ and $\ln(k)$ fields: Example 1.

distribution informed by some secondary data (for instance, seismic data). Static well used in the example are shown in Figure 6.7.

In order to demonstrate the ability of the developed code for variogram estimation and uncertainty, we use a number of prior variogram models and analyze the updated variograms in each of the runs.

## Run 1

The prior variogram models used in this run for $\phi$ and $\ln(k)$ are given in Equations 6.1 and 6.2:

$$\gamma_\phi(h) = 0.05 + 0.5Sph(h)\begin{matrix} a_x = 7000 \\ a_y = 7000 \end{matrix} + 0.45Sph(h)\begin{matrix} a_x = 4000 \\ a_y = 4000 \end{matrix} \tag{6.1}$$

and

$$\gamma_y(h) = 0.05 + 0.55Sph(h)\begin{matrix} a_x = 3500 \\ a_y = 3500 \end{matrix} + 0.4Sph(h)\begin{matrix} a_x = 6000 \\ a_y = 6000 \end{matrix} \cdot \tag{6.2}$$

The data integration code was run for 15 outer iterations using $6 \times 6$ (=36) master points in each iteration. CPU time for the run was only 320 seconds in a 1.8 GHz Pentium 4 personal computer. The updated variograms for $\phi$ and $\ln(k)$ are shown in Figures 6.8, 6.9, 6.10, and 6.11, for directions with azimuth 0 and 90. A close look at the variograms indicates improvement of the estimated variograms with the iterations. The dynamic data integration mismatch in $L^2$ norms for each iteration is shown in Figure 6.12. The final $L^2$ norm of the pressure march was 6.51. The prior initial variogram models were isotropic for both $\phi$ and $\ln(k)$, however the estimated variograms at each iteration reveals a reasonable anisotropy. It should be pointed that with inverse squared distance mismatch norm for variogram updating, it is difficult to good match at large lag distances in the updated model. The reason being the higher weights given to short lag distances. After 15 iterations, the final updated variogram models are given in Tables 6.1 and 6.2, respectively for $\phi$ and $\ln(k)$. It is evident that this approach can provide a more realistic variogram than what we get from the experimental variogram (Figure 6.6) using only static well data.

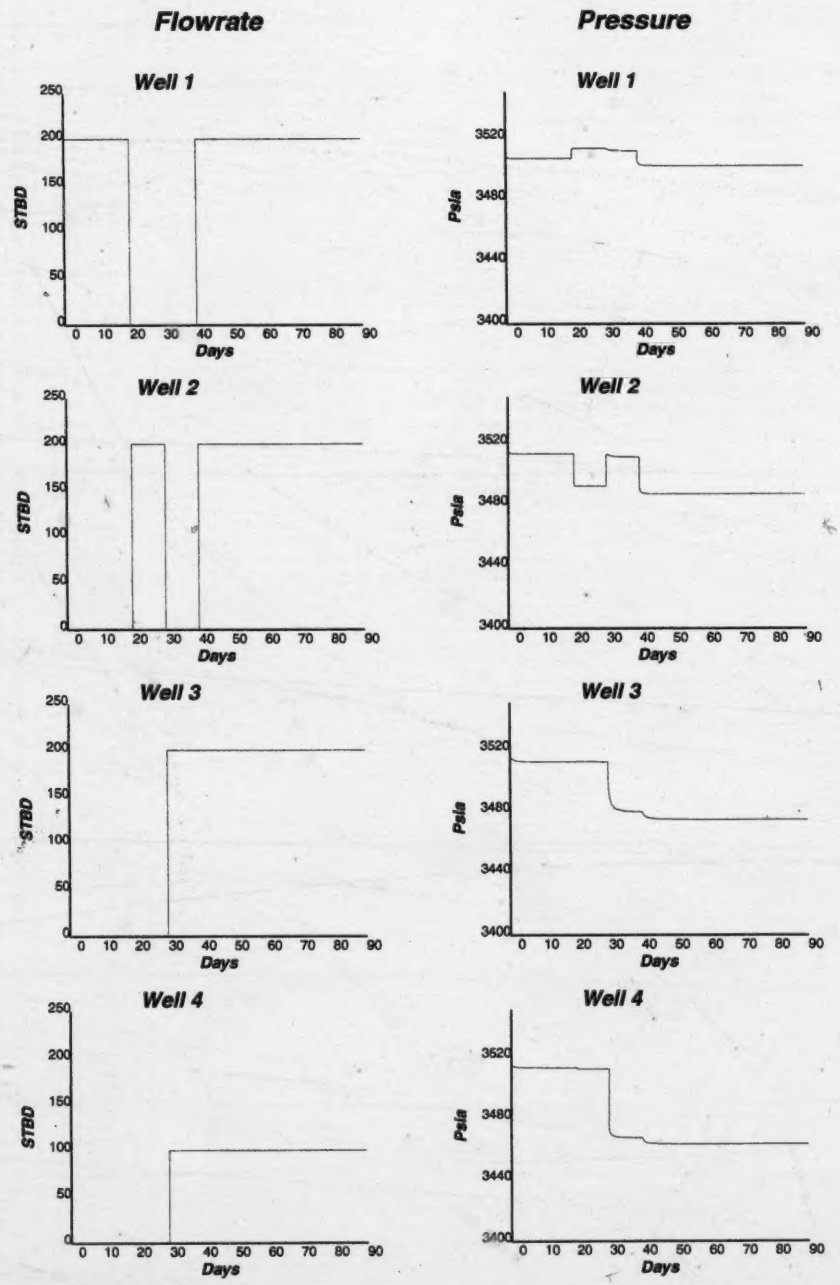


Figure 6.2: Production data (pressure and flow rates) obtained from the reference field: Example 1.

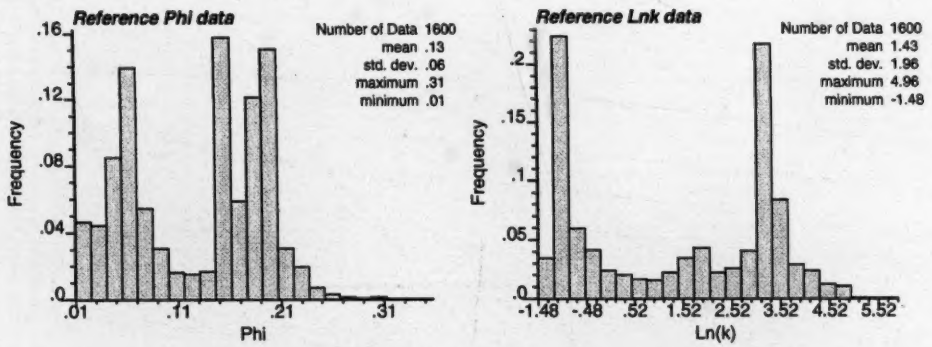


Figure 6.3: Histograms of reference $\phi$ and $\ln(k)$ fields: Example 1.

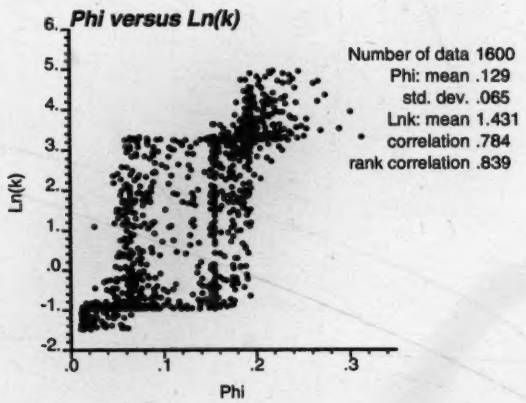


Figure 6.4: Scatterplot between reference $\phi$ and $\ln(k)$ values: Example 1.

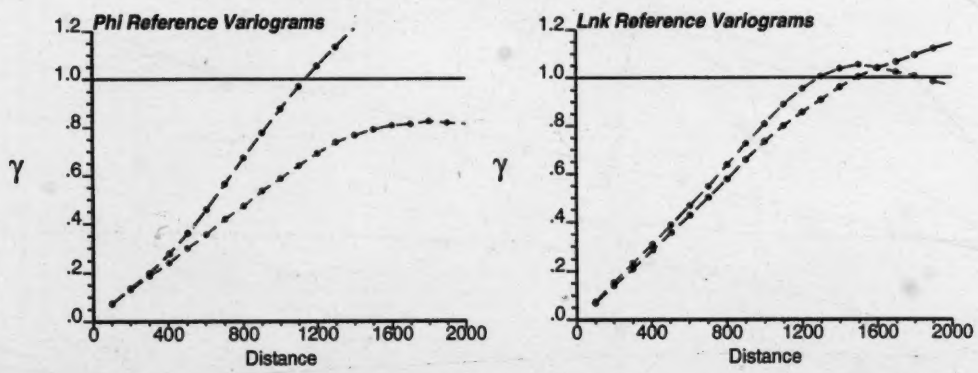


Figure 6.5: Variograms of reference $\phi$ and $\ln(k)$ distributions: Example 1. (X direction - dark, Y direction - light)

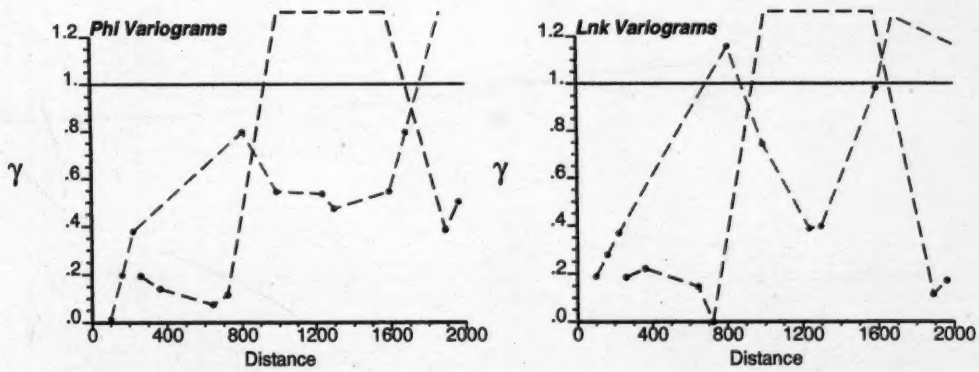


Figure 6.6: Variograms estimated from well data for $\phi$ and $\ln(k)$: Example 1. (X direction - dark, Y direction - light)

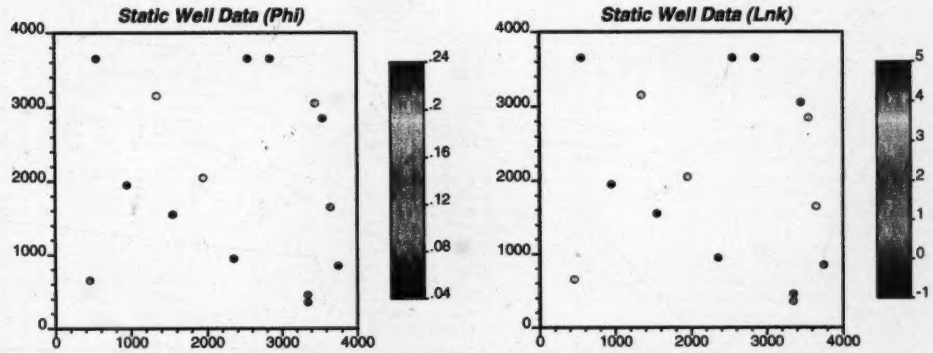


Figure 6.7: Static well data for $\phi$ and $\ln(k)$: Example 1.

| V. No. | Type | Sill | Range X - Y (ft) | Angle ($^o$) |
|---|---|---|---|---|
| 0 | Nugget | 0.0 | | |
| 1 | Sph | 0.141 | 1000 - 9720 | 0 |
| 2 | Sph | 0.859 | 1475 - 1135 | 0 |

Table 6.1: Final variogram model obtained for $\phi$ after 15 iterations: Example 1 Run 1.

| V. No. | Type | Sill | Range X - Y (ft) | Angle ($^o$) |
|---|---|---|---|---|
| 0 | Nugget | 0.008 | | |
| 1 | Sph | 0.482 | 1425 - 1062 | 0 |
| 2 | Sph | 0.51 | 1600 - 1184 | 0 |

Table 6.2: Final variogram model obtained for $\ln(k)$ after 15 iterations: Example 1 Run 1.

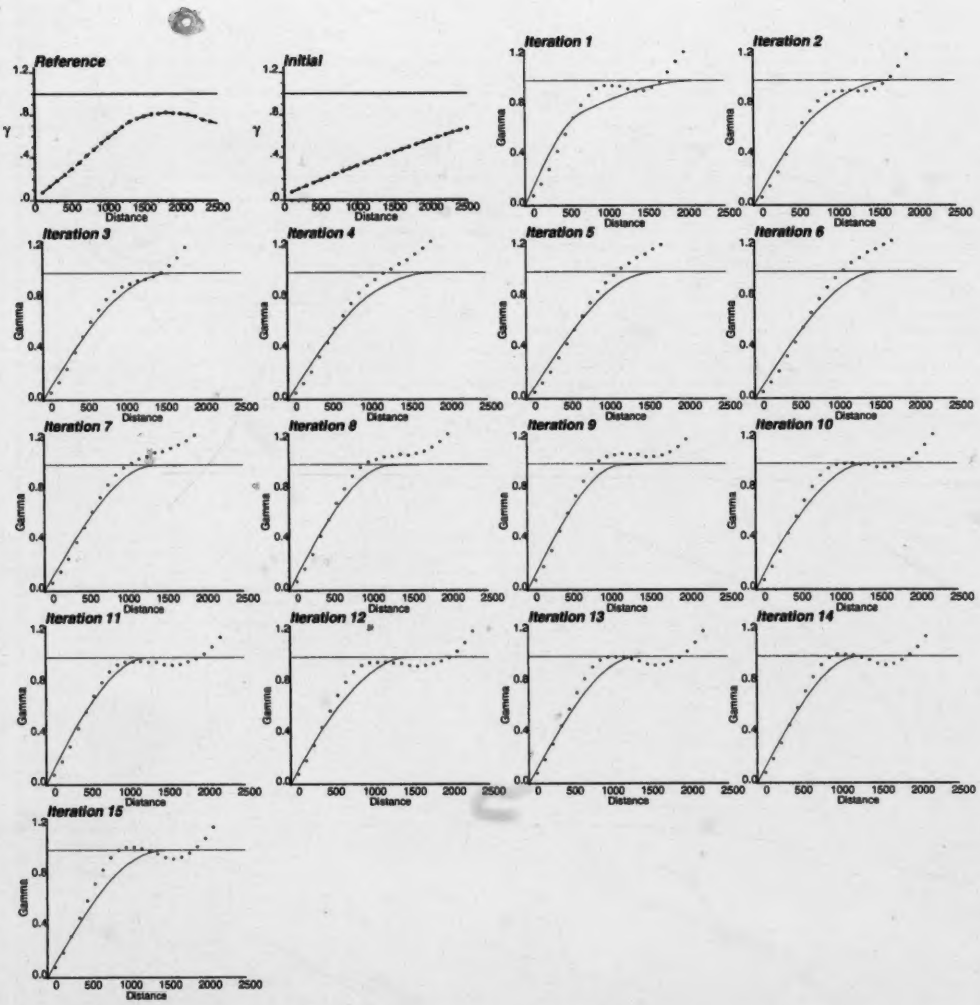


Figure 6.8: Reference, prior and updated variograms (experimental - dotted line, model - solid line) for $\phi$ at each outer iteration: Example 1 Run 1. (Direction with azimuth 0)

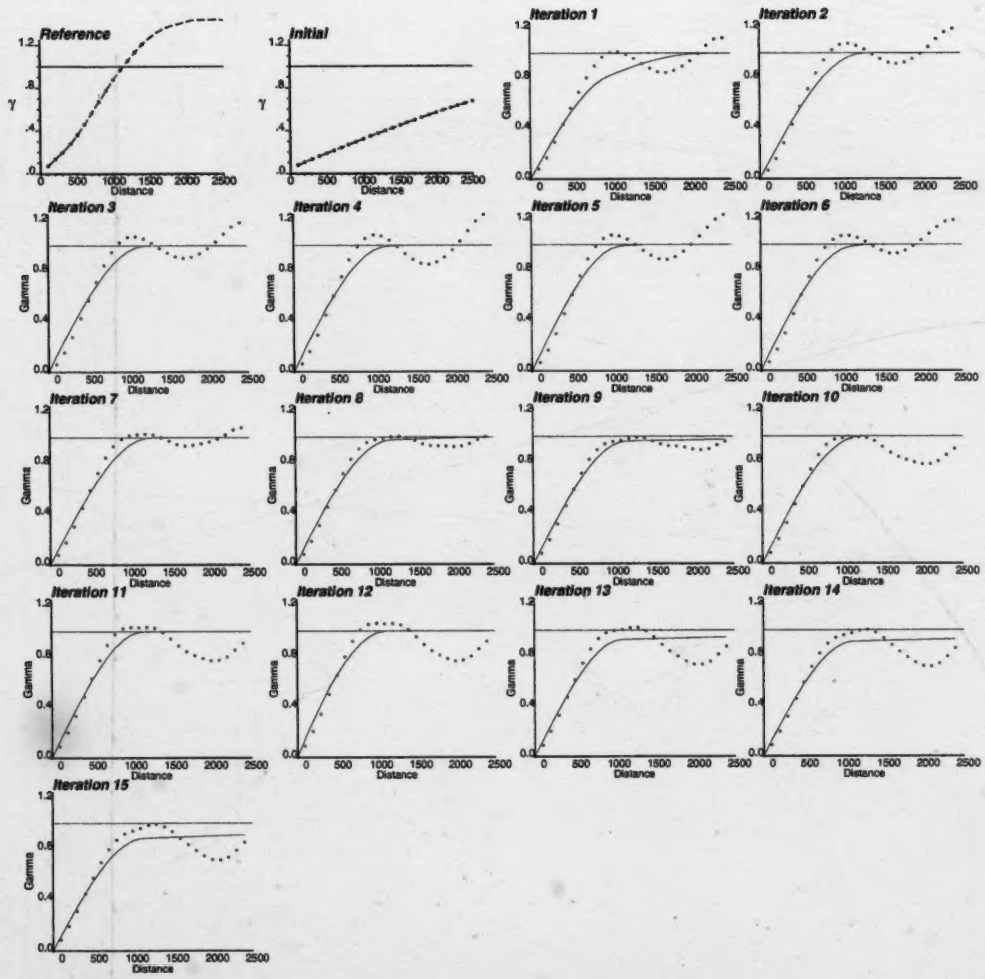


Figure 6.9: Reference, prior and updated variograms (experimental - dotted line, model - solid line) for $\phi$ at each outer iteration: Example 1 Run 1. (Direction with azimuth 90)

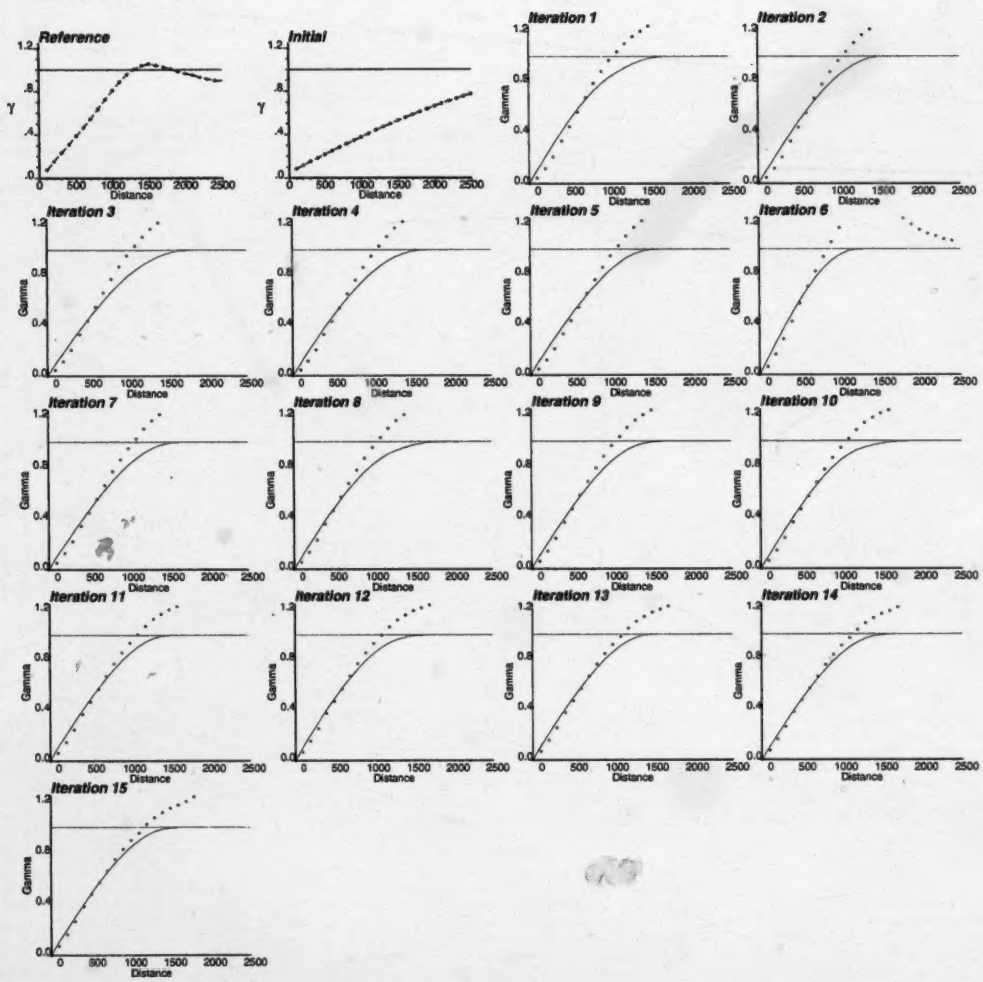


Figure 6.10: Reference, prior and updated variograms (experimental - dotted line, model - solid line) for $\ln(k)$ at each outer iteration: Example 1 Run 1. (Direction with azimuth 0)

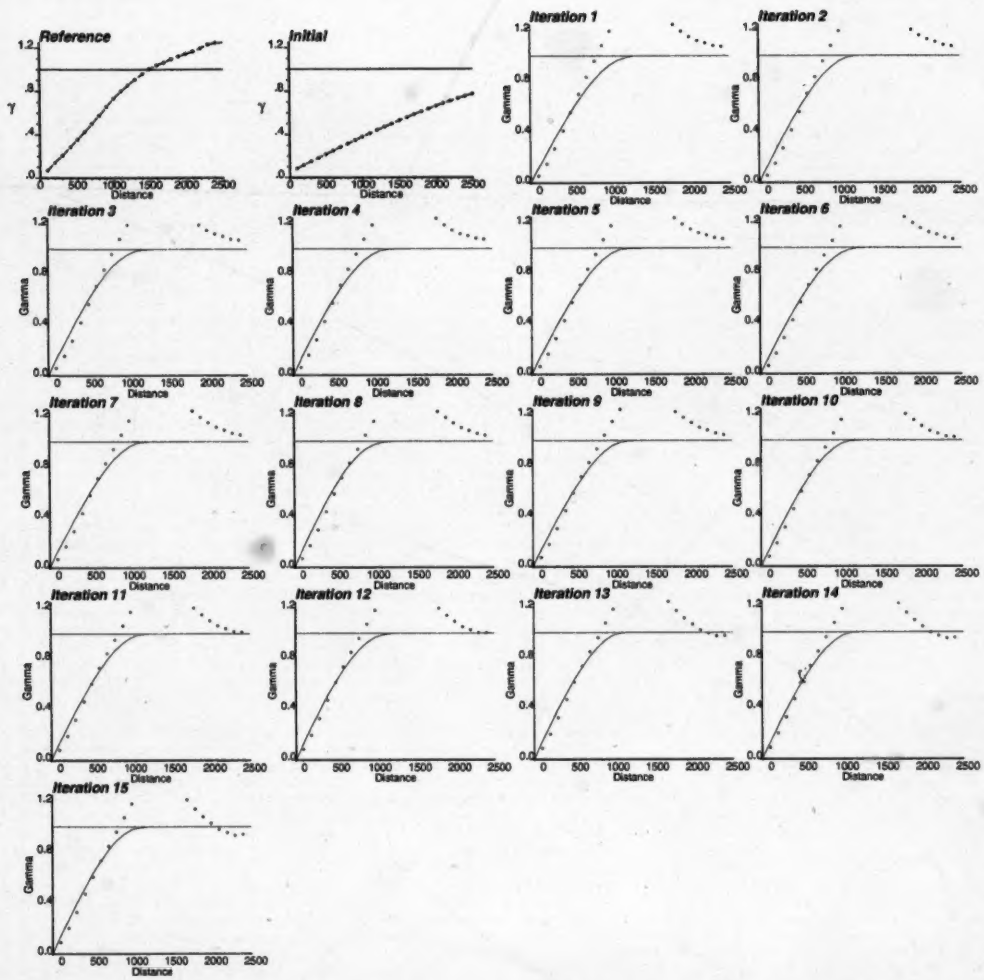


Figure 6.11: Reference, prior and updated variograms (experimental - dotted line, model - solid line) for $\ln(k)$ at each outer iteration: Example 1 Run 1. (Direction with azimuth 90)

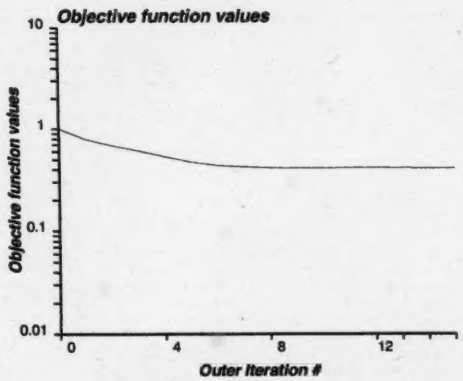


Figure 6.12: Mismatch norm of data integration at each outer iteration: Example 1 Run 1.

### Run 2

The prior variogram models used in this run for $\phi$ and $\ln(k)$ are given in Equations 6.3 and 6.4:

$$\gamma_\phi(h) = 0.25 + 0.5Sph(h)\begin{matrix} a_x = 1000 \\ a_y = 1000 \end{matrix} + 0.25Sph(h)\begin{matrix} a_x = 4000 \\ a_y = 4000 \end{matrix} \tag{6.3}$$

and

$$\gamma_y(h) = 0.25 + 0.55Sph(h)\begin{matrix} a_x = 1500 \\ a_y = 1500 \end{matrix} + 0.2Sph(h)\begin{matrix} a_x = 6000 \\ a_y = 6000 \end{matrix}. \tag{6.4}$$

The nugget effect in the prior variograms is increased and the ranges are decreased for both $\phi$ and $\ln(k)$ compared to those used in Run 1. The data integration code was run for 15 outer iterations using $6 \times 6$ (=36) master points in each iteration. CPU time for the run was only 295 seconds in a 1.8 GHz Pentium 4 personal computer. The updated variograms for $\phi$ and $\ln(k)$ are shown in Figures 6.13, 6.14, 6.15, and 6.16, for directions with azimuth 0 and 90. A close look at the variograms indicates improvement of the estimated variograms with the iterations. The dynamic data integration mismatch in $L^2$ norms for each iteration is shown in Figure 6.17. The final $L^2$ norm of the pressure march was 6.04. The prior initial variogram models were isotropic for both $\phi$ and $\ln(k)$, however the estimated variograms at each iteration reveals a reasonable anisotropy. After 15 outer iterations, the final updated variogram models are given in Tables 6.3 and 6.4, respectively for $\phi$ and $\ln(k)$. It is evident that this approach can provide a more realistic variogram than what we get from the experimental variogram (Figure 6.6) obtained using only static well data. The prior variogram models had a nugget effect of 0.25 that was updated to almost negligible nugget effect which is closer to the reference.

### Run 3

The prior variogram models used in this run for $\phi$ and $\ln(k)$ are given in Equations 6.5 and 6.6:

$$\gamma_\phi(h) = 0.75 + 0.05Sph(h)\begin{matrix} a_x = 1000 \\ a_y = 1000 \end{matrix} + 0.2Sph(h)\begin{matrix} a_x = 7000 \\ a_y = 7000 \end{matrix} \tag{6.5}$$

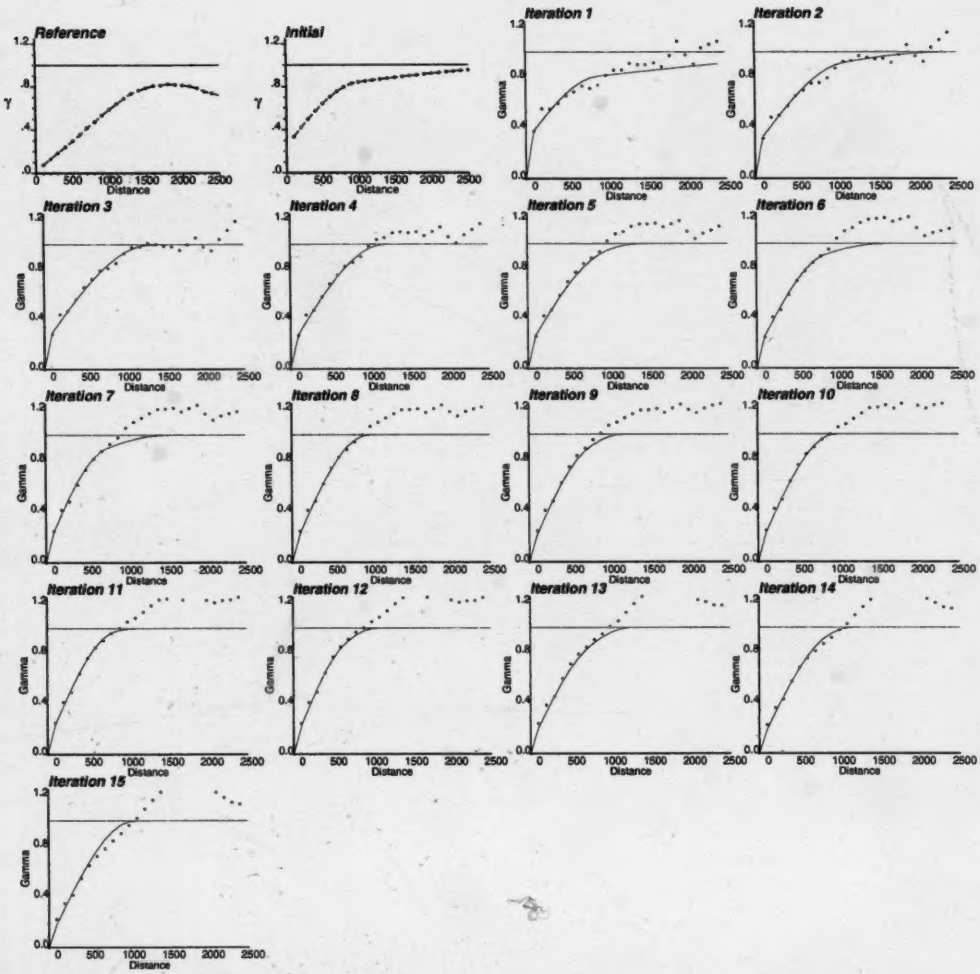


Figure 6.13: Reference, prior and updated variograms (experimental - dotted line, model - solid line) for $\phi$ at each outer iteration: Example 1 Run 2. (Direction with azimuth 0)

| V. No. | Type | Sill | Range X - Y (ft) | Angle ($^o$) |
|---|---|---|---|---|
| 0 | Nugget | 0.047 | | |
| 1 | Sph | 0.176 | 1050 - 911 | 0 |
| 2 | Sph | 0.777 | 1062 - 861 | 0 |

Table 6.3: Final variogram model obtained for $\phi$ after 15 iterations: Example 1 Run 2.

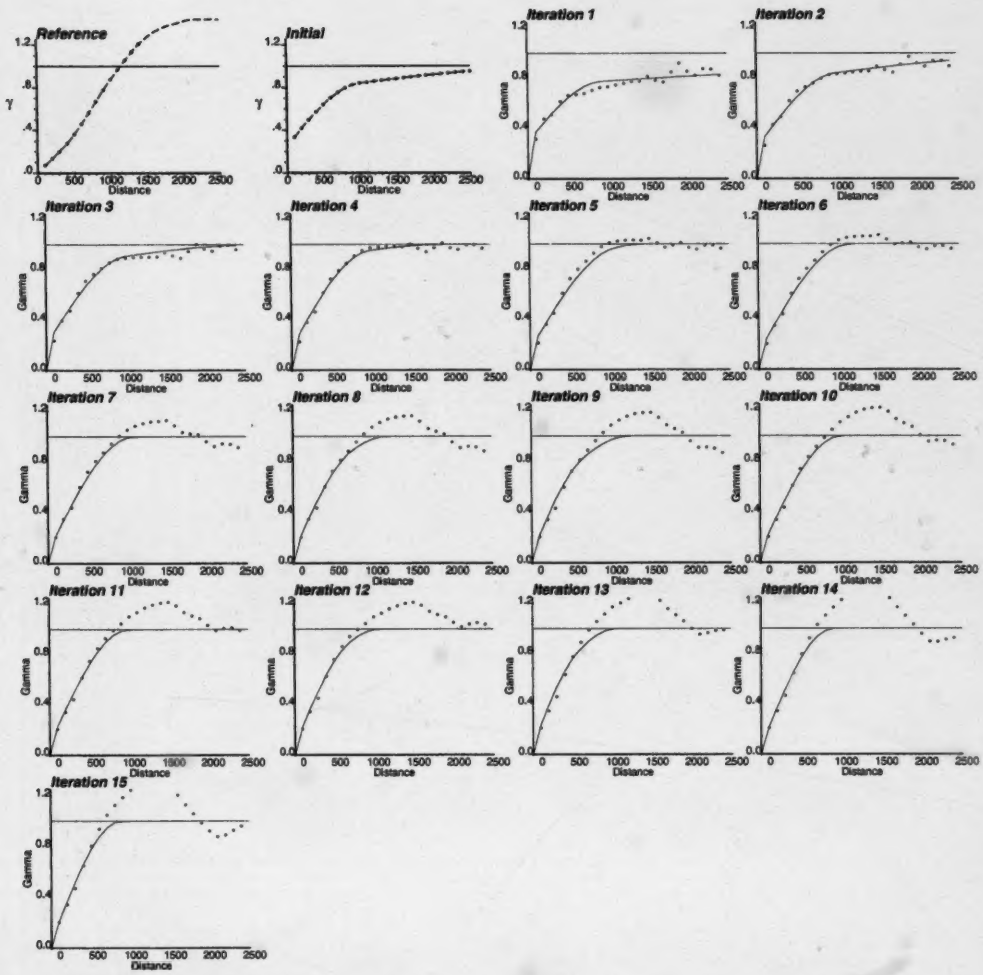


Figure 6.14: Reference, prior and updated variograms (experimental - dotted line, model - solid line) for $\phi$ at each outer iteration: Example 1 Run 2. (Direction with azimuth 90)

| V. No. | Type | Sill | Range X - Y (ft) | Angle ($^o$) |
|---|---|---|---|---|
| 0 | Nugget | 0.001 | | |
| 1 | Sph | 0.058 | 800 - 420 | 0 |
| 2 | Sph | 0.941 | 1312 - 1100 | 0 |

Table 6.4: Final variogram model obtained for $\ln(k)$ after 15 iterations: Example 1 Run 2.

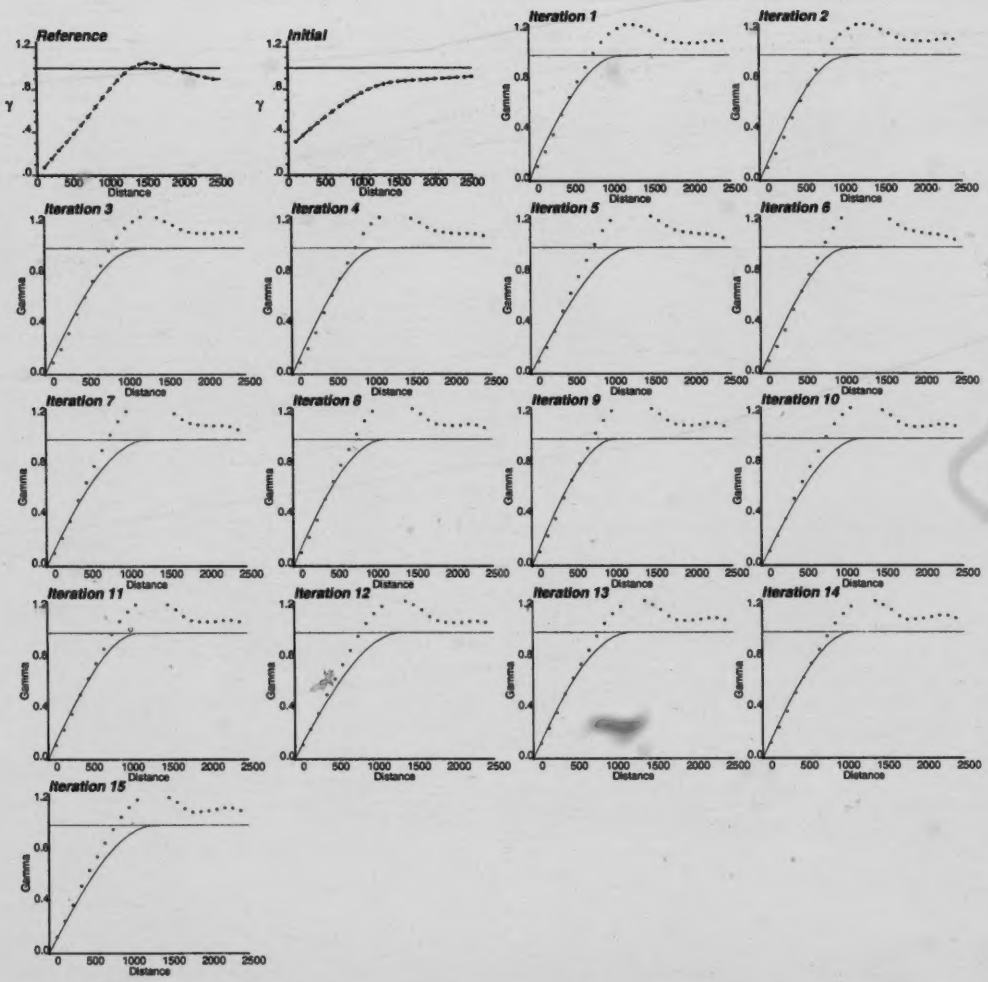


Figure 6.15: Reference, prior and updated variograms (experimental - dotted line, model - solid line) for $\ln(k)$ at each outer iteration: Example 1 Run 2. (Direction with azimuth 0)

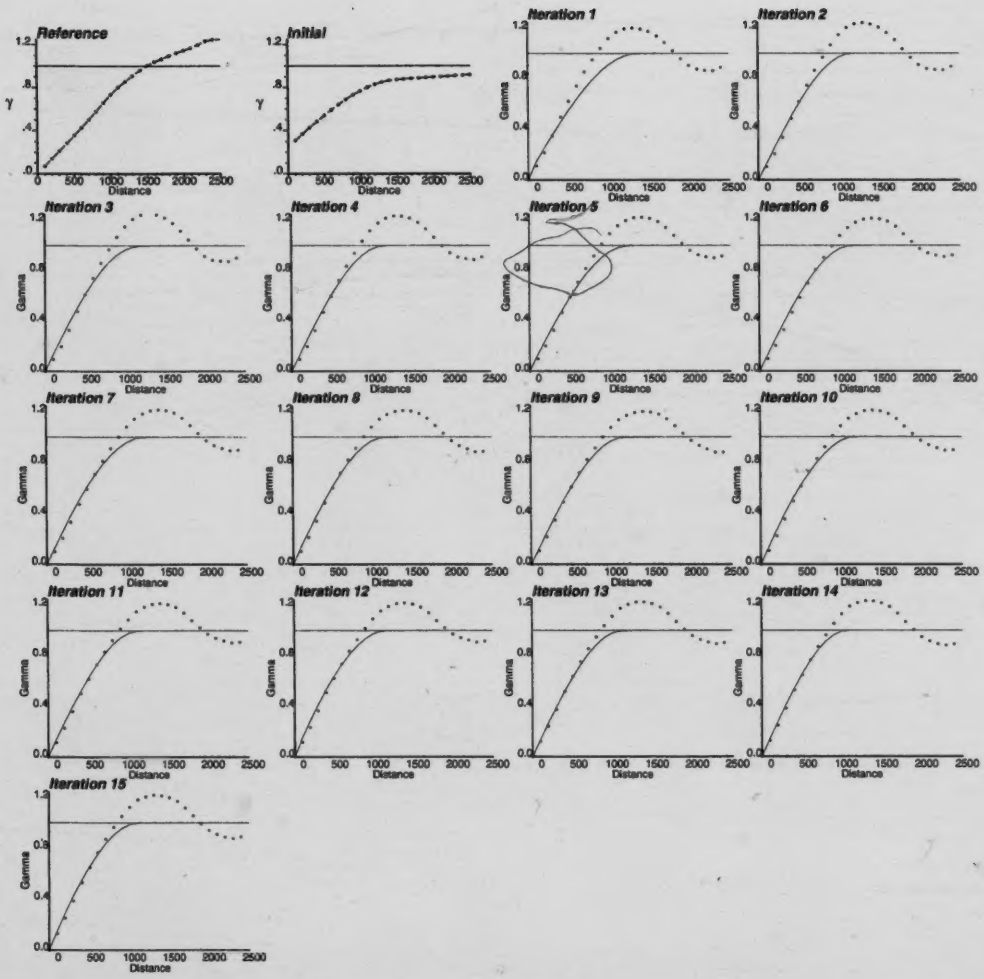


Figure 6.16: Reference, prior and updated variograms (experimental - dotted line, model - solid line) for $\ln(k)$ at each outer iteration: Example 1 Run 2. (Direction with azimuth 90)

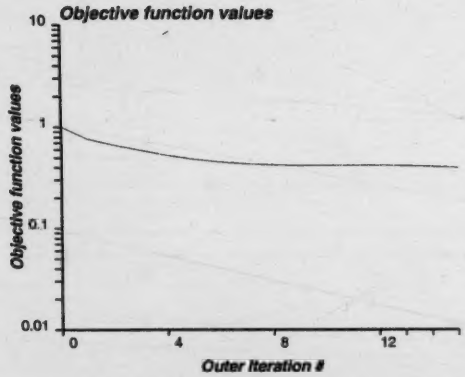


Figure 6.17: Mismatch norm of data integration at each outer iteration: Example 1 Run 2.

| V. No. | Type | Sill | Range X - Y (ft) | Angle ($^o$) |
|---|---|---|---|---|
| 0 | Nugget | 0.063 | | |
| 1 | Sph | 0.649 | 850 - 3404 | 0 |
| 2 | Sph | 0.288 | 5937 - 831 | 0 |

Table 6.5: Final variogram model obtained for $\phi$ after 16 iterations: Example 1 Run 3.

and

$$\gamma_y(h) = 0.75 + 0.05Sph(h)\begin{matrix} a_x = 1500 \\ a_y = 1500 \end{matrix} + 0.2Sph(h)\begin{matrix} a_x = 8000 \\ a_y = 8000 \end{matrix} \cdot \tag{6.6}$$

The nugget effect in the prior variograms is increased to 75% for both $\phi$ and $\ln(k)$ in this case. The data integration code was run for 16 outer iterations using $6 \times 6$ (=36) master points in each iteration. CPU time for the run was only 312 seconds in a 1.8 GHz Pentium 4 personal computer. The updated variograms for $\phi$ and $\ln(k)$ are shown in Figures 6.18, 6.19, 6.20, and 6.21, for directions with azimuth 0 and 90. A close look at the variograms indicates improvement of the estimated variograms with the iterations. The dynamic data integration mismatch in $L^2$ norms for each iteration is shown in Figure 6.22. The final $L^2$ norm of the pressure march was 0.588, a remarkably low mismatch value. The prior initial variogram models were isotropic for both $\phi$ and $\ln(k)$, however the estimated variograms at each iteration reveals a reasonable anisotropy. After 16 outer iterations, the final updated variogram models are given in Tables 6.5 and 6.6 for $\phi$ and $\ln(k)$. It is evident that this approach can provide a more realistic variogram than what we get from the experimental variogram (Figure 6.6). The prior variogram model with high nugget effect of 0.75 led to final updated variogram model with a low nugget effect close to the reference value.

### Some Conclusions From Example One

Having analyzed the updated variograms in the first example, it could be concluded that the developed code provides reasonably good variogram models using multiple well production data. Some of the salient features of variogram information extraction from production data in this example are the following.

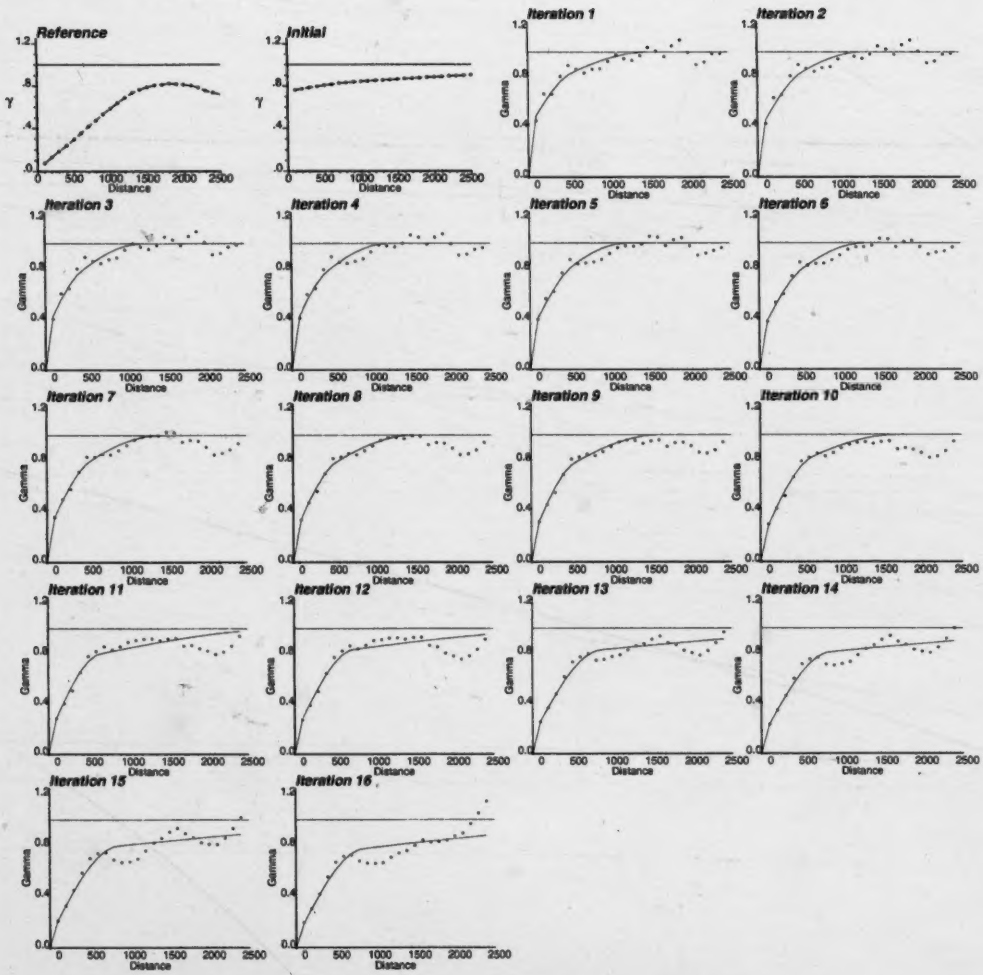


Figure 6.18: Reference, prior and updated variograms (experimental - dotted line, model - solid line) for $\phi$ at each outer iteration: Example 1 Run 3. (Direction with azimuth 0)

| V. No. | Type | Sill | Range X - Y (ft) | Angle ($^o$) |
|---|---|---|---|---|
| 0 | Nugget | 0.072 | | |
| 1 | Sph | 0.053 | 1312 - 220 | 0 |
| 2 | Sph | 0.875 | 1400 - 2310 | 0 |

Table 6.6: Final variogram model obtained for $\ln(k)$ after 16 iterations: Example 1 Run 3.

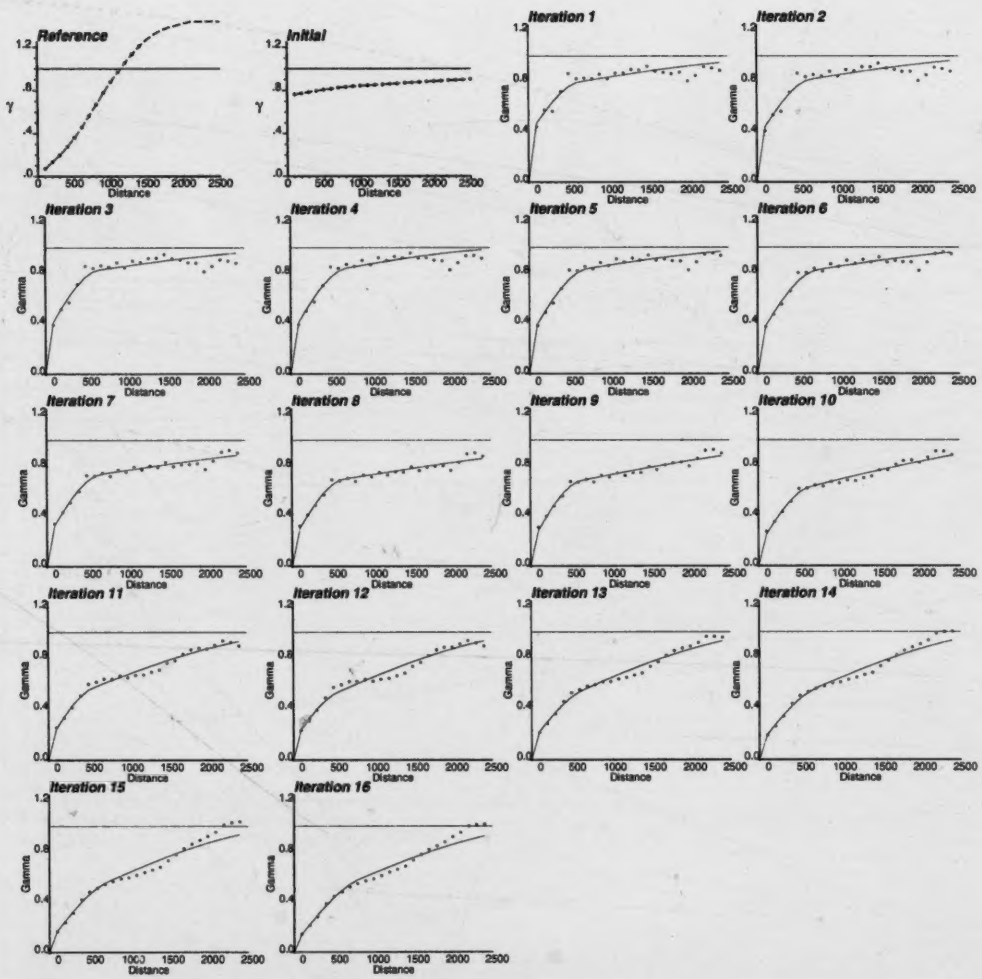


Figure 6.19: Reference, prior and updated variograms (experimental - dotted line, model - solid line) for $\phi$ at each outer iteration: Example 1 Run 3. (Direction with azimuth 90)

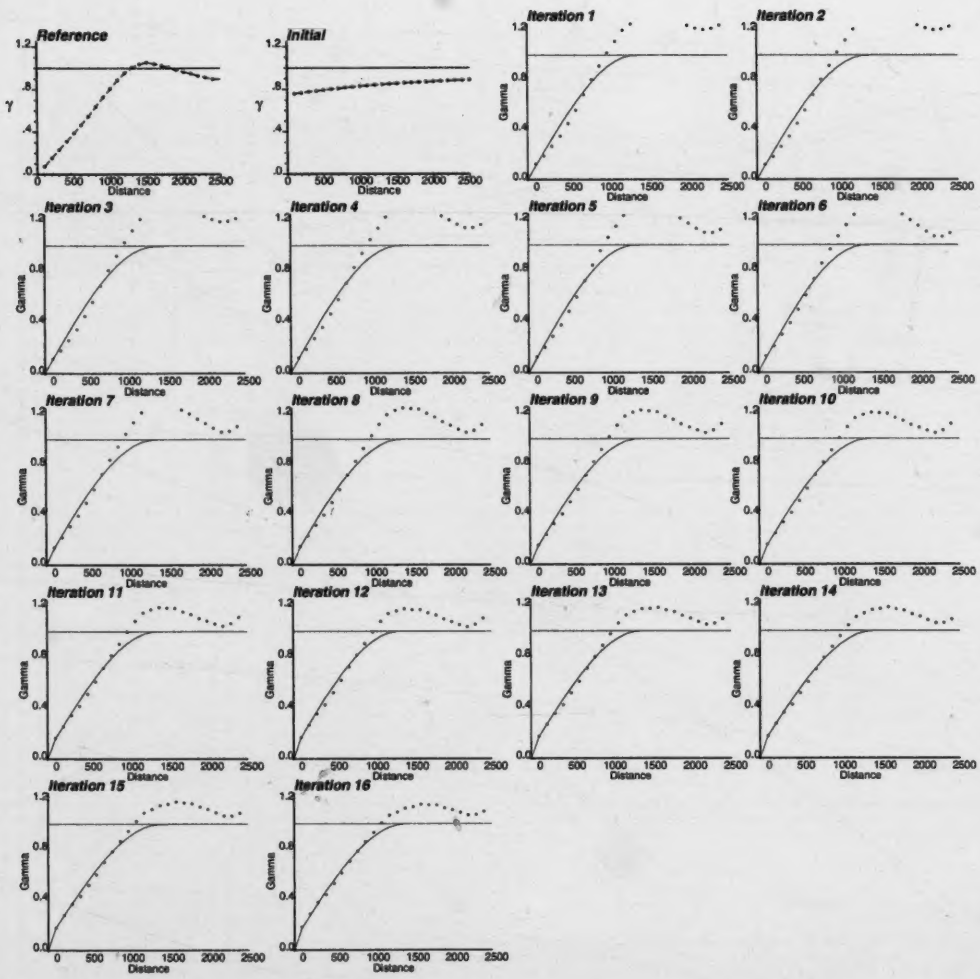


Figure 6.20: Reference, prior and updated variograms (experimental - dotted line, model - solid line) for $\ln(k)$ at each outer iteration: Example 1 Run 3. (Direction with azimuth 0)

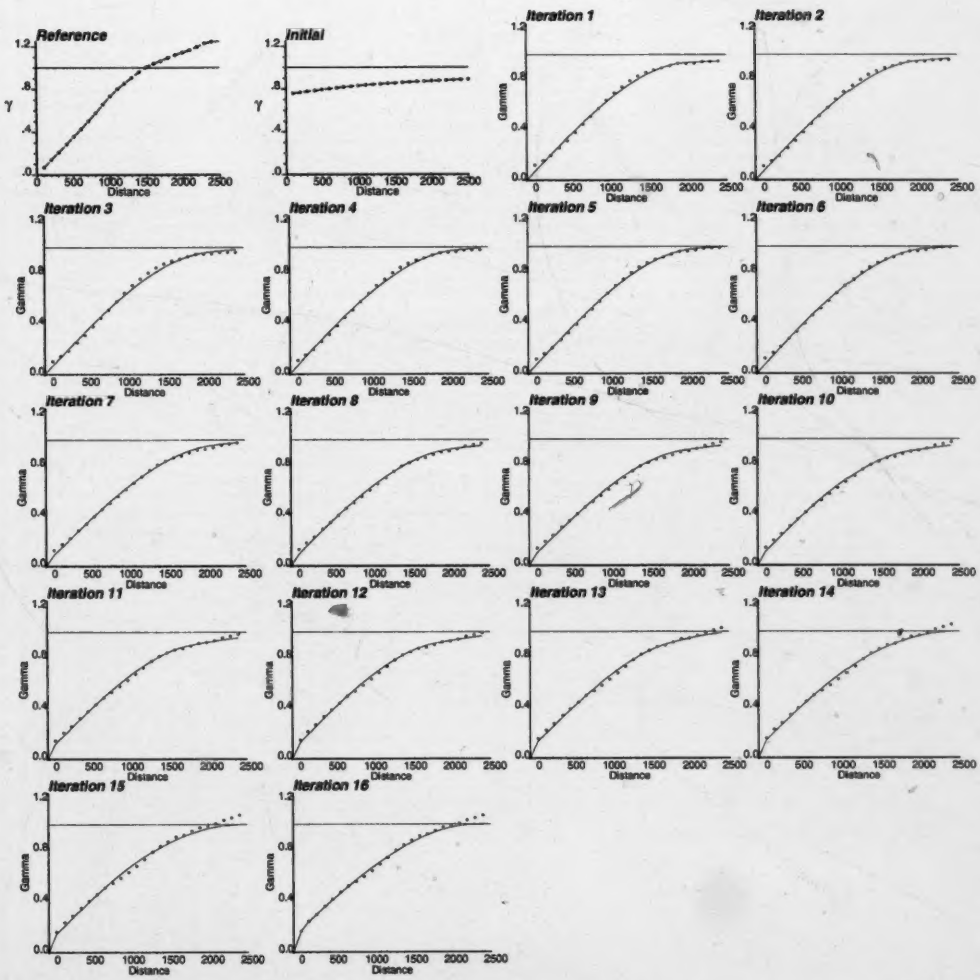


Figure 6.21: Reference, prior and updated variograms (experimental - dotted line, model - solid line) for $\ln(k)$ at each outer iteration: Example 1 Run 3. (Direction with azimuth 90)

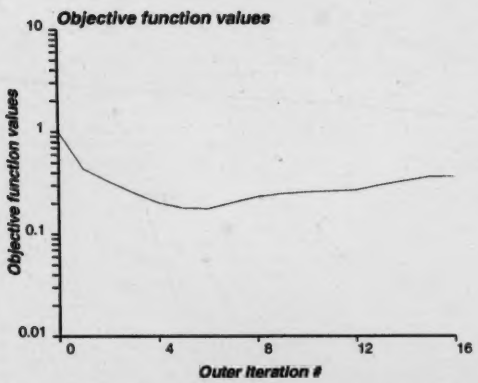


Figure 6.22: Mismatch norm of data integration at each outer iteration: Example 1 Run 3.

- Irrespective of prior variogram models with high or low nugget effect, we get back the low nugget effect of the reference distribution. It should be noted that the experimental variograms are obtained from gridded distribution, thus the smallest lag distance depends on the smallest dimension of the grid blocks.
- Range convergence is good for both $\phi$ and $\ln(k)$.
- Anisotropy convergence is also captured reasonably well in the final updated variogram models.

In the subsequent section, we will investigate the response of the developed code in the event of high nugget effect in the reference distribution. Given the diffusive nature of flow data, it would be interesting to see if the inversion algorithm can retrieve high spatial randomness in the reference distribution.

## 6.3 High Nugget Effect Inversion Using Production Data

It is expected that inverted variogram models using production data will have very low nugget effect. The reason for such a hypothesis is the fact that subsurface reservoir fluid flow is diffusive in nature. Nevertheless, it would be interesting to perform some study of nugget effect inversion.

As in the earlier example, reference porosity and permeability models are constructed first. Pressure responses at a number of wells are obtained through flow simulation.

This 2D example of 4,000-ft square domain is discretized into 40 × 40 grid cells of 100 × 100 ft. Porosity and permeability fields are shown in Figure 6.23. There are 10 wells: Well W1 at the center of the cell (24,10), Wells W2, W3, W4, W5, W6, W7, W8, W9 and W10 at cells (37,17), (14,32), (35,31), (34,23), (28,13), (13,33), (16,29), (19,10), and (9,17), respectively. Wells are shown in Figure 6.23. Other reservoir properties are similar to the previous example. Figure 6.24 shows the imposed production rates and the corresponding numerically simulated pressure responses at the different wells. The histograms and the scatter-plot between $\phi$ and $\ln(k)$ are shown in Figures 6.25 and 6.26. Mean and standard deviation of reference distributions are 0.13 and 0.08 for $\phi$, and 1.38 and 2.06 for $\ln(k)$.

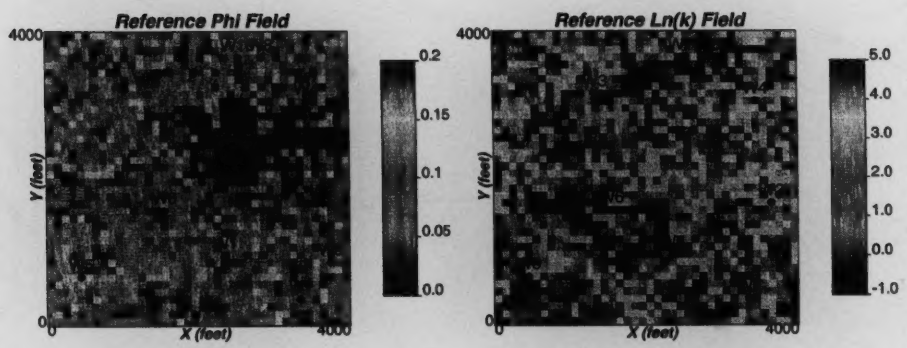


Figure 6.23: Reference $\phi$ and $\ln(k)$ fields: High Nugget Effect Example.

Correlation coefficient of the two distributions is 0.658. Variogram for both $\phi$ and $\ln(k)$ of the reference fields are shown in Figure 6.27.

For the inversion, we employ the reference distributions as the global distribution information. Static well data used in the example are shown in Figure 6.28. Realistic experimental variograms could not be obtained using these static data.

The inversion was tried with a number of prior variogram models. It is not possible to capture high spatial randomness in the inverted distributions. We have employed prior variogram models with nugget effect from 0.05 to 0.75. In fact in the case of prior variogram models with low nugget effect, the mismatch function in the inversion increases instead of decreases. With a nugget effect of 0.75, inversion was possible however with a very poor mismatch of 47.3.

The prior variogram model used for the run with an initial nugget of 75% is shown in Tables 6.7 and 6.8 for $\phi$ and $\ln(k)$. The data integration code was run for 7 outer iterations using $6 \times 6$ (=36) master points in each iteration. CPU time for the run was only 157 seconds in a 1.8 GHz Pentium 4 personal computer. The updated variograms for $\phi$ and $\ln(k)$ are shown in Figures 6.29, 6.30, 6.31, and 6.32, for directions with azimuth 0 and 90. The mismatch in $L^2$ norms for each iteration is shown in Figure 6.33. The final $L^2$ norm of the pressure march was 47.3, an extremely high mismatch value. After 7 iterations, the final updated variogram models are given in Tables 6.9 and 6.10 for $\phi$ and $\ln(k)$.

From the perspective of the geostatistical scaling laws in the context of small scale core data (perhaps with a nugget effect) and with block data (that is $10^4$ times larger), one would expect the nugget effect to smeared at the coarser scale. The heterogeneities one expects from production data integration are large scale caused by facies/stratigraphic boundaries or from faults. There really will be no nugget effect between "continuous" blocks. Moreover, even if we believed there was a nugget effect at the block scale, it would almost certainly be informed from densely spaced well log or core data. Our main task is to determine horizontal ranges and anisotropy (including perhaps, zonal anisotropy).

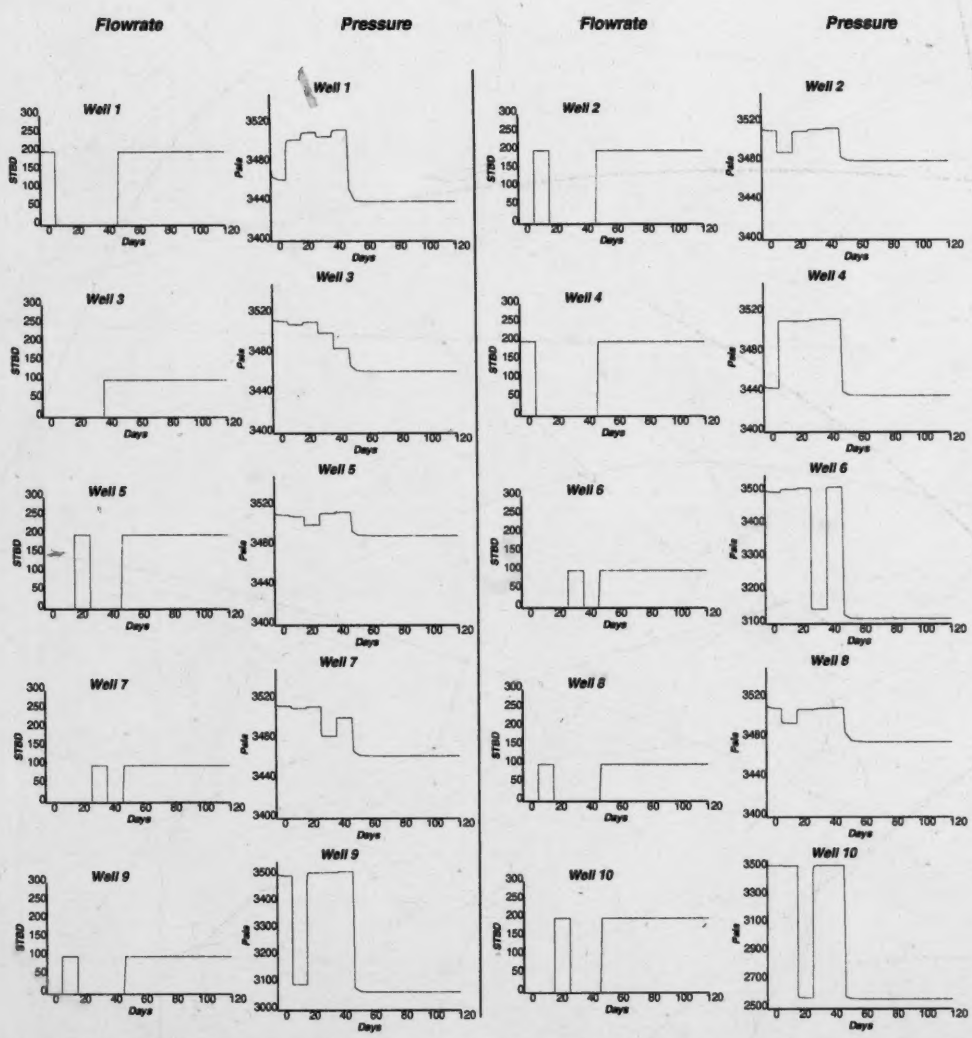


Figure 6.24: Production data (pressure and flow rates) obtained from the reference field: High Nugget Effect Example.

| V. No. | Type | Sill | Range X - Y (ft) | Angle ($^o$) |
|---|---|---|---|---|
| 0 | Nugget | 0.05 | | |
| 1 | Sph | 0.5 | 7000 - 7000 | 0 |
| 2 | Sph | 0.45 | 4000 - 4000 | 0 |

Table 6.7: Prior variogram information used for $\phi$: High Nugget Effect Example.

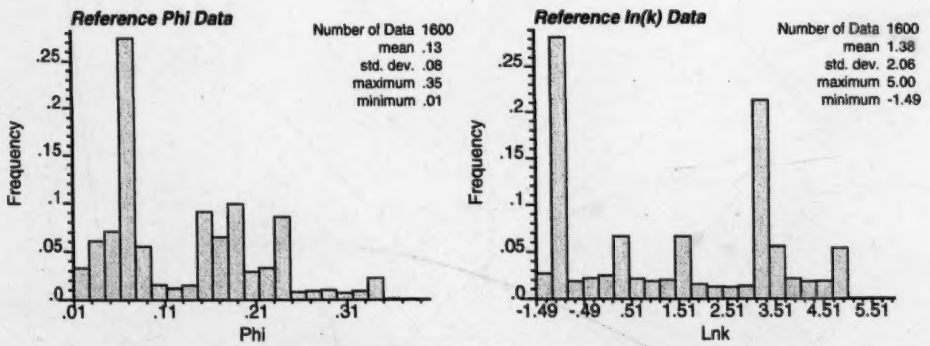


Figure 6.25: Histograms of reference $\phi$ and $\ln(k)$ fields: High Nugget Effect Example.

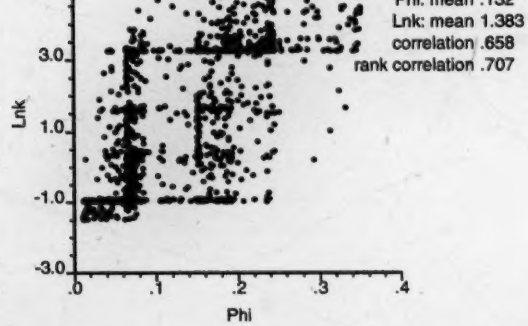


Figure 6.26: Scatterplot between reference $\phi$ and $\ln(k)$ values: High Nugget Effect Example.

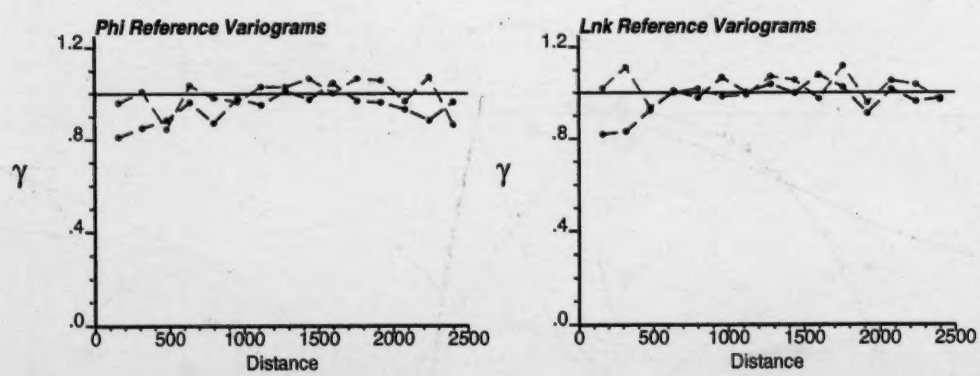


Figure 6.27: Variograms of reference $\phi$ and $\ln(k)$ distributions: High Nugget Effect Example. (X direction - dark, Y direction - light)

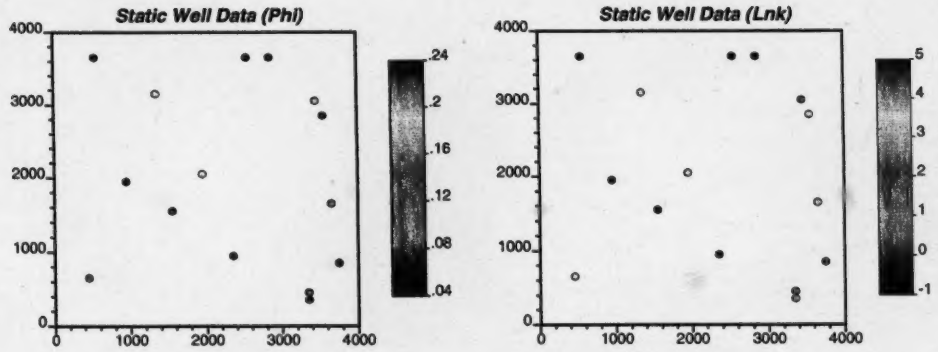


Figure 6.28: Static well data for $\phi$ and $\ln(k)$: High Nugget Effect Example.

| V. No. | Type | Sill | Range X - Y (ft) | Angle ($^o$) |
|---|---|---|---|---|
| 0 | Nugget | 0.05 | | |
| 1 | Sph | 0.55 | 3500 - 3500 | 0 |
| 2 | Sph | 0.4 | 6000 - 6000 | 0 |

Table 6.8: Prior variogram information used for $\ln(k)$: High Nugget Effect Example.

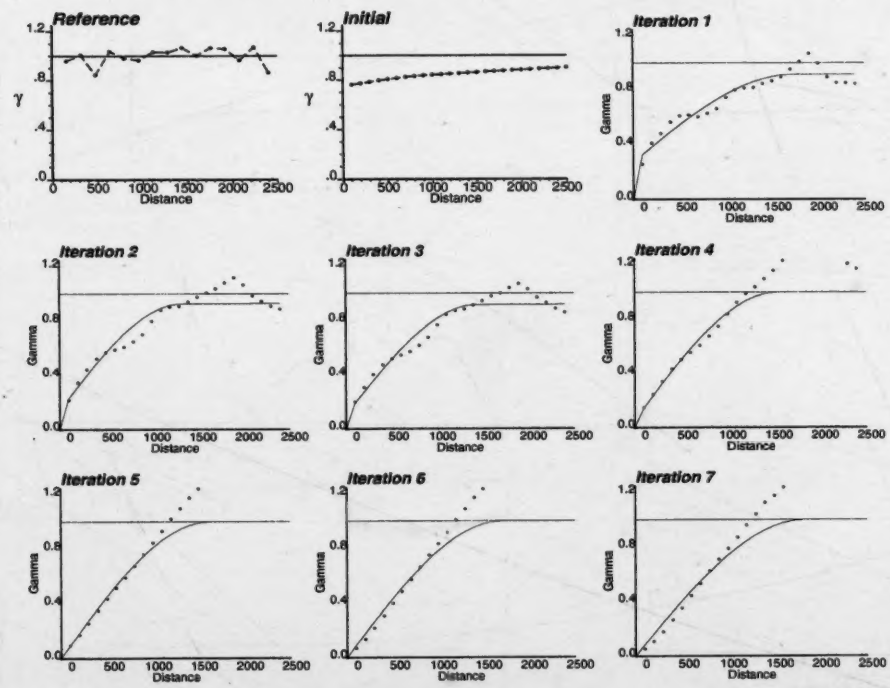


Figure 6.29: Reference, prior and updated variograms (experimental - dotted line, model - solid line) for $\phi$ at each outer iteration: High Nugget Effect Example. (Direction with azimuth 0)

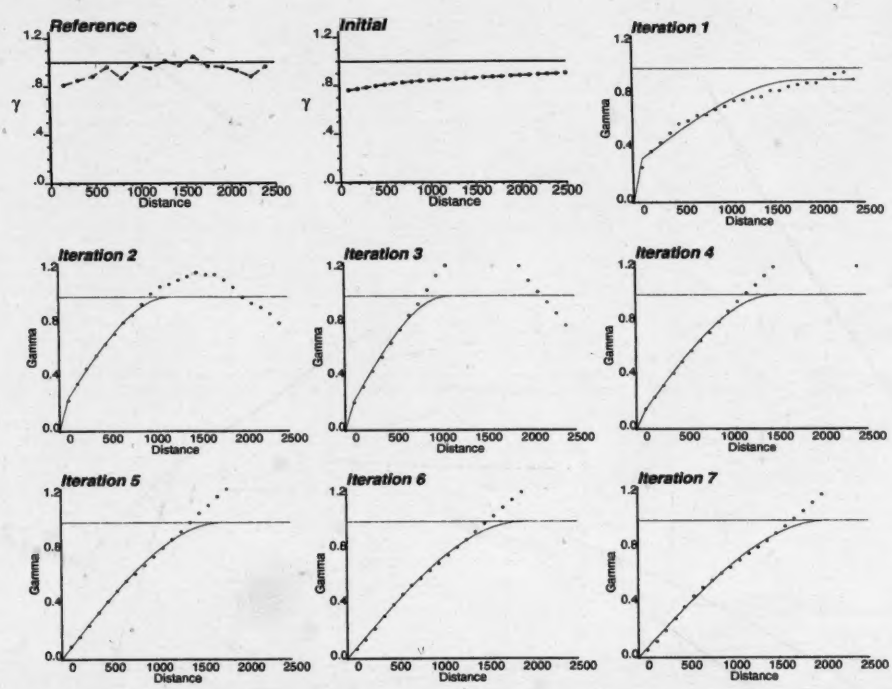


Figure 6.30: Reference, prior and updated variograms (experimental - dotted line, model - solid line) for $\phi$ at each outer iteration: High Nugget Effect Example. (Direction with azimuth 90)

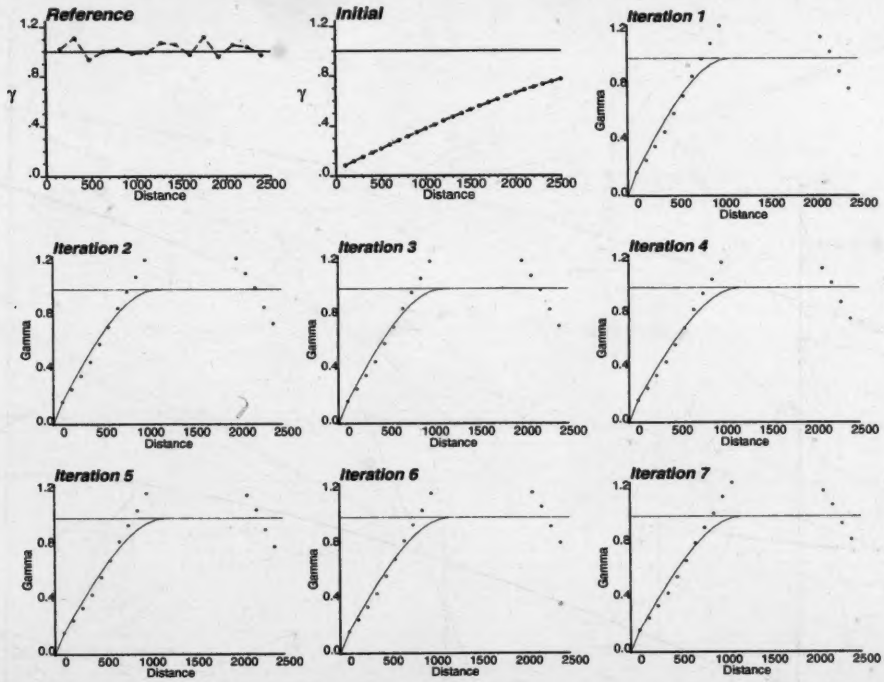


Figure 6.31: Reference, prior and updated variograms (experimental - dotted line, model - solid line) for $\ln(k)$ at each outer iteration: High Nugget Effect Example. (Direction with azimuth 0)

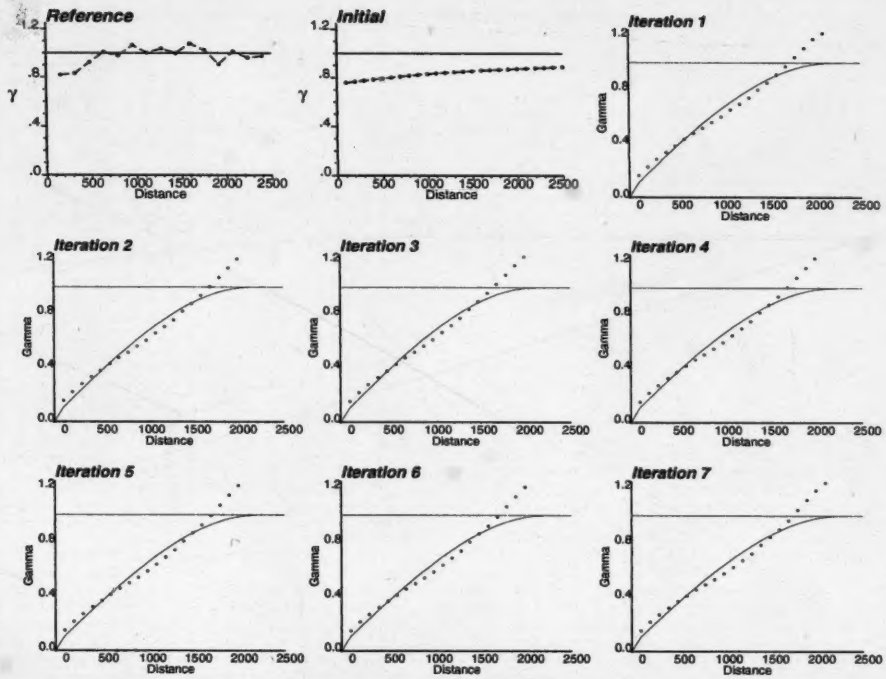


Figure 6.32: Reference, prior and updated variograms (experimental - dotted line, model - solid line) for $\ln(k)$ at each outer iteration: High Nugget Effect Example. (Direction with azimuth 90)

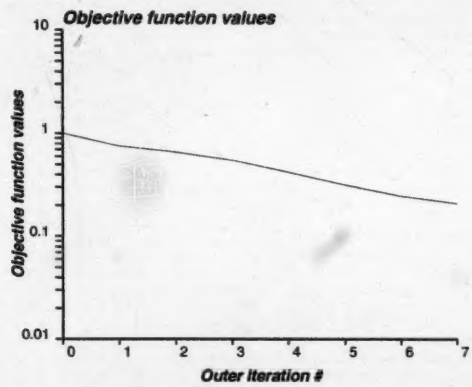


Figure 6.33: Mismatch norm of data integration at each outer iteration: High Nugget Effect Example.

| V. No. | Type | Sill | Range X - Y (ft) | Angle ($^o$) |
|---|---|---|---|---|
| 0 | Nugget | 0.0 | | |
| 1 | Sph | 0.95 | 1825 - 2049 | 0 |
| 2 | Sph | 0.05 | 1800 - 2016 | 0 |

Table 6.9: Final variogram model obtained for $\phi$ after 7 iterations: High Nugget Effect Example.

| V. No. | Type | Sill | Range X - Y (ft) | Angle ($^o$) |
|---|---|---|---|---|
| 0 | Nugget | 0.044 | | |
| 1 | Sph | 0.593 | 1200 - 2268 | 0 |
| 2 | Sph | 0.363 | 1200 - 2232 | 0 |

Table 6.10: Final variogram model obtained for $\ln(k)$ after 7 iterations: High Nugget Effect Example.

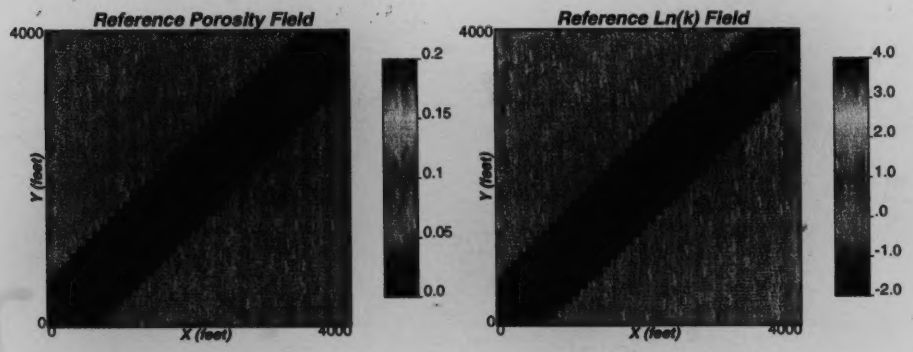


Figure 6.34: Reference $\phi$ and $\ln(k)$ fields: Production Data Sensitivity Example.

## 6.4 Effect of Production Data

Variogram inversion requires production data having information about the reservoir heterogeneity. The amount of information captured in the inverted models depends on the quality and amount of production data. Here we investigate the effect of the quantity of dynamic data on updated variogram models.

We perform the inversion on a synthetic reservoir model with varying number of wells with production data. The updated variograms models are compared and analyzed to determine the effect of the amount of production data on the resulting variogram.

Consider our familiar 2D 4,000-ft square domain discretized into 40 $\times$ 40 grid cells of 100 $\times$ 100 ft. Porosity and permeability fields are shown in Figure 6.34. The boundaries on all four sides are no-flow boundaries. Reservoir properties are the same as those discussed in the previous sections unless stated otherwise. There is a high porosity-permeability band connecting the lower-left corner and upper-right corner. The histograms and the scatterplot between $\phi$ and $\ln(k)$ are shown in Figures 6.35 and 6.36. The distribution is bimodal. The correlation coefficient of the two distributions is 1.0. Mean and standard deviation of reference distributions are 0.13 and 0.046 for $\phi$, and 0.683 and 2.108 for $\ln(k)$. Variogram for both $\phi$ and $\ln(k)$ of the reference fields are shown in Figure 6.37. We employ the reference distributions as the global distribution information. The prior variogram model used in this exercise is shown in Tables 6.11 and 6.12 for $\phi$ and $\ln(k)$.

We perform the inversion 3 times with production data from 4, 6 and 8 wells. The well locations for each case are shown in Figure 6.38. Figures 6.39, 6.40, and 6.41 show the imposed production rates and the corresponding numerically simulated pressure responses for the 3 cases. Only the well porosity and permeability values are used for the inversion.

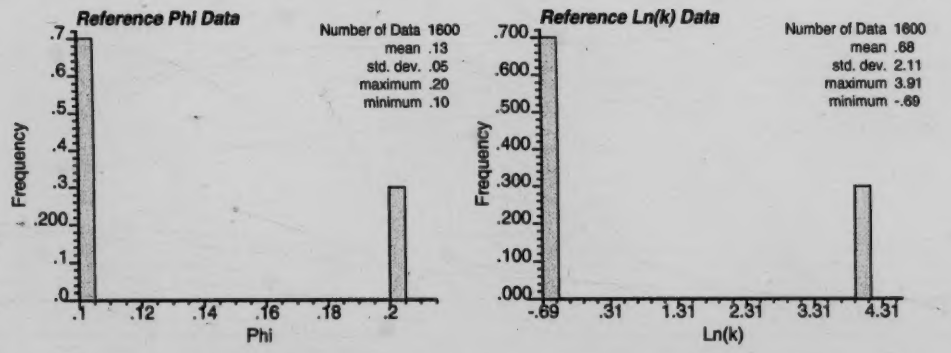


Figure 6.35: Histograms of reference $\phi$ and $\ln(k)$ fields: Production Data Sensitivity Example.

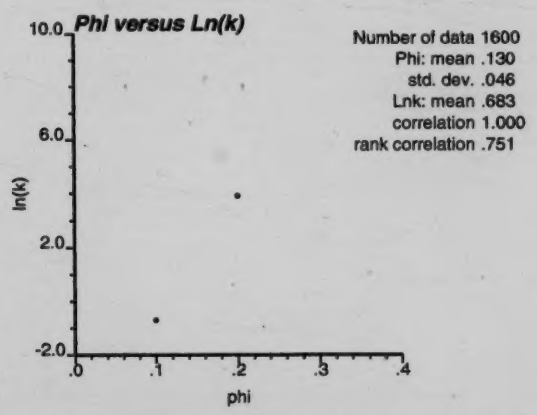


Figure 6.36: Scatterplot between reference $\phi$ and $\ln(k)$ values: Production Data Sensitivity Example.

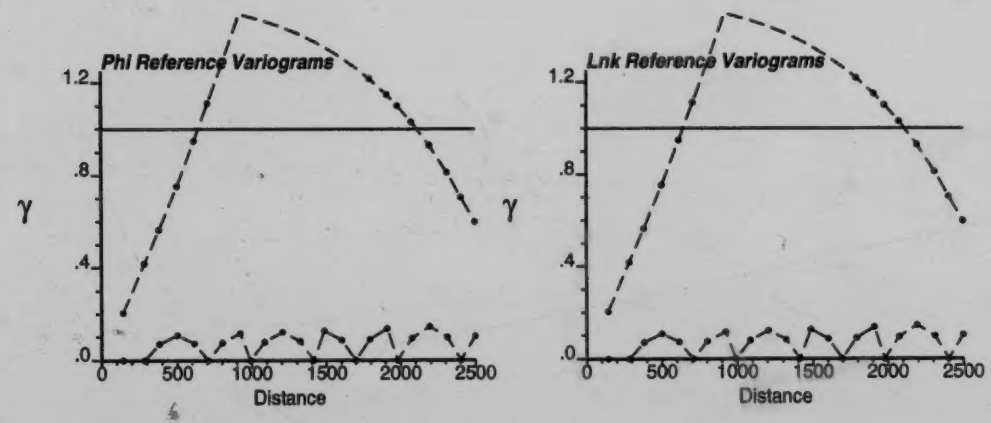


Figure 6.37: Variograms of reference $\phi$ and $\ln(k)$ distributions: Production Data Sensitivity Example. (X direction - dark, Y direction - light)

| V. No. | Type | Sill | Range X - Y (ft) | Angle ($^o$) |
|---|---|---|---|---|
| 0 | Nugget | 0.05 | | |
| 1 | Sph | 0.55 | 14000 - 2000 | 45.0 |
| 2 | Sph | 0.4 | 13000 - 10000 | 45.0 |

Table 6.11: Prior variogram information used for $\phi$: Production Data Sensitivity Example.

| V. No. | Type | Sill | Range X - Y (ft) | Angle ($^o$) |
|---|---|---|---|---|
| 0 | Nugget | 0.05 | | |
| 1 | Sph | 0.5 | 14000 - 2000 | 45.0 |
| 2 | Sph | 0.45 | 13000 - 10000 | 45.0 |

Table 6.12: Prior variogram information used for $\ln(k)$: Production Data Sensitivity Example.

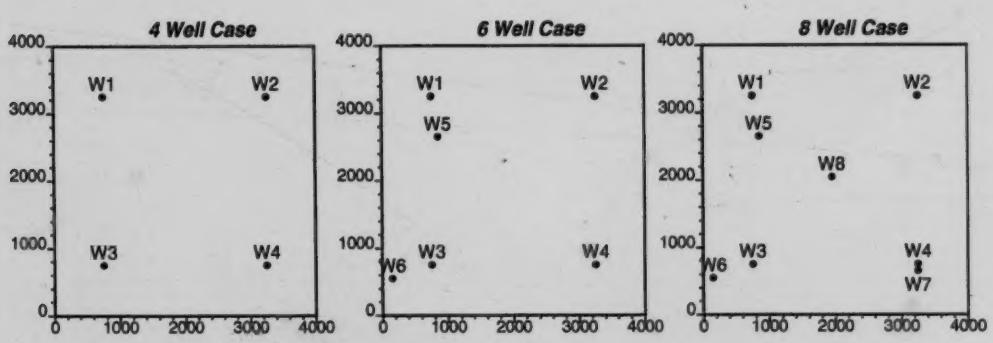


Figure 6.38: Well locations for the 3 cases: 4, 6 and 8 well case.

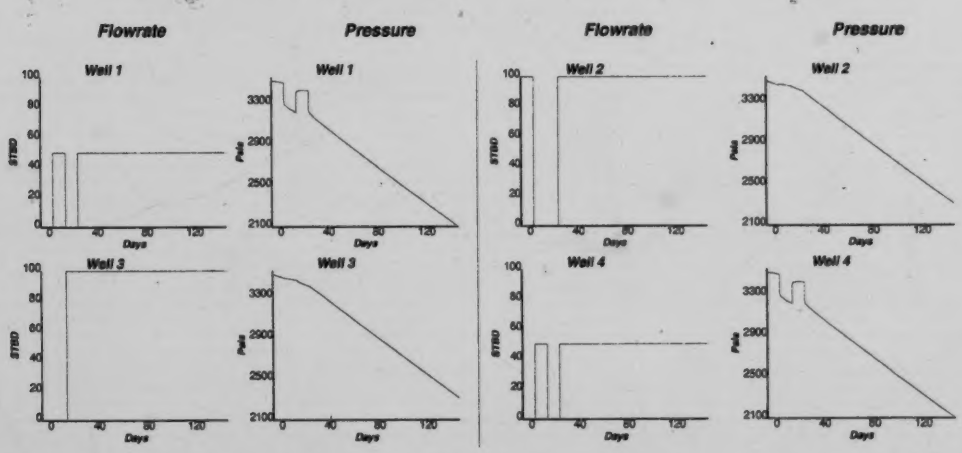


Figure 6.39: Production data (pressure and flow rates) obtained from the reference field: 4 well case.

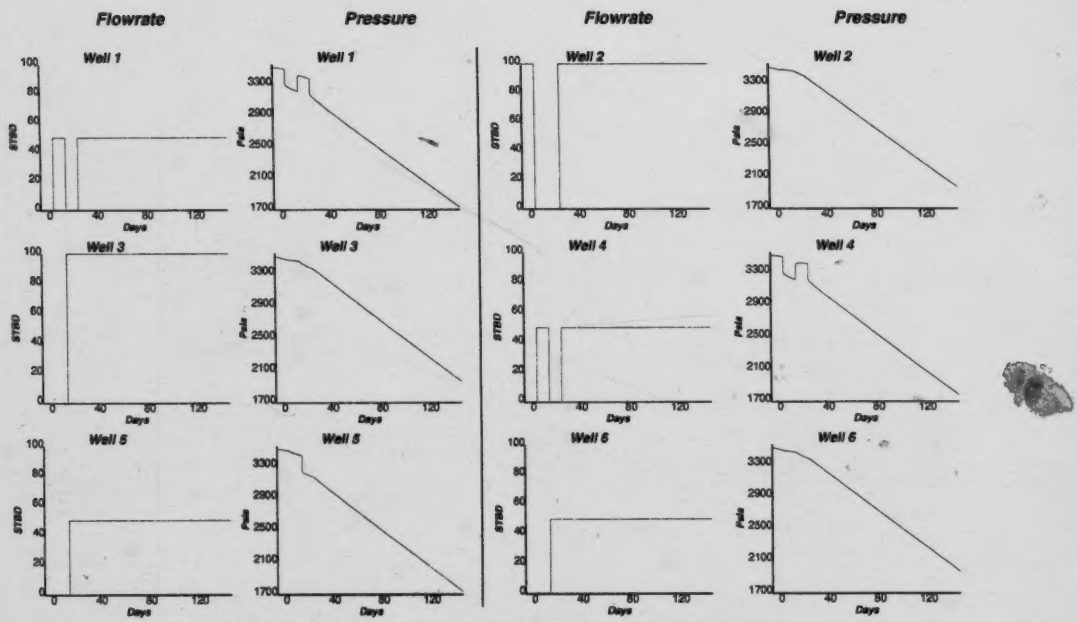


Figure 6.40: Production data (pressure and flow rates) obtained from the reference field: 6 well case.

| V. No. | Type | Sill | Range X - Y (ft) | Angle ($^o$) |
|---|---|---|---|---|
| 0 | Nugget | 0.0 | | |
| 1 | Sph | 0.555 | 2787 - 983 | 45 |
| 2 | Sph | 0.445 | 925 - 194 | 45 |

Table 6.13: Final variogram model obtained for $\phi$ after 11 iterations: 4 Well case.

## 4 Well Case

The inversion was performed for 11 outer iterations. CPU time for the run was only 213 seconds in a 1.8 GHz Pentium 4 personal computer. The updated variograms for $\phi$ and $\ln(k)$ are shown in Figures 6.42, 6.43, 6.44, and 6.45, for directions with azimuth 45 and 135. The mismatch in $L^2$ norms for each iteration is shown in Figure 6.46. The final $L^2$ norm of the pressure march was 10.91. After 11 iterations, the final updated variogram models are given in Tables 6.13 and 6.14 for $\phi$ and $\ln(k)$.

## 6 Well Case

The inversion was performed for 13 outer iterations. CPU time for the run was only 252 seconds in a 1.8 GHz Pentium 4 personal computer. The updated variograms for $\phi$ and $\ln(k)$ are shown in Figures 6.47, 6.48, 6.49, and 6.50, for directions with azimuth 45 and 135. The mismatch in $L^2$ norms for each iteration is shown in Figure 6.51. The final $L^2$ norm of the pressure march was 11.39. After 13 iterations, the final updated variogram models are given in Tables 6.15 and 6.16 for $\phi$ and $\ln(k)$.

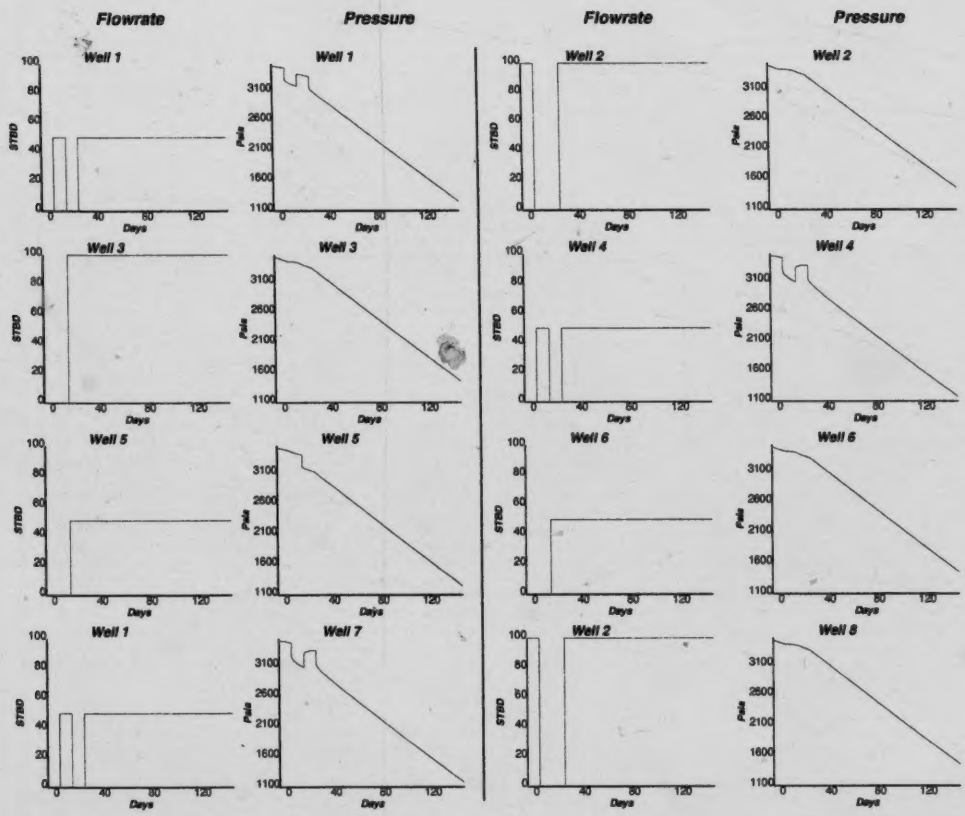


Figure 6.41: Production data (pressure and flow rates) obtained from the reference field: 8 well case.

| V. No. | Type | Sill | Range X - Y (ft) | Angle ($^o$) |
|---|---|---|---|---|
| 0 | Nugget | 0.003 | | |
| 1 | Sph | 0.86 | 10900 - 903 | 45 |
| 2 | Sph | 0.137 | 2600 - 895 | 45 |

Table 6.14: Final variogram model obtained for $\ln(k)$ after 11 iterations: 4 Well case.

| V. No. | Type | Sill | Range X - Y (ft) | Angle ($^o$) |
|---|---|---|---|---|
| 0 | Nugget | 0.001 | | |
| 1 | Sph | 0.575 | 10650 - 669 | 45 |
| 2 | Sph | 0.424 | 500 - 31 | 45 |

Table 6.15: Final variogram model obtained for $\phi$ after 13 iterations: 6 Well case.

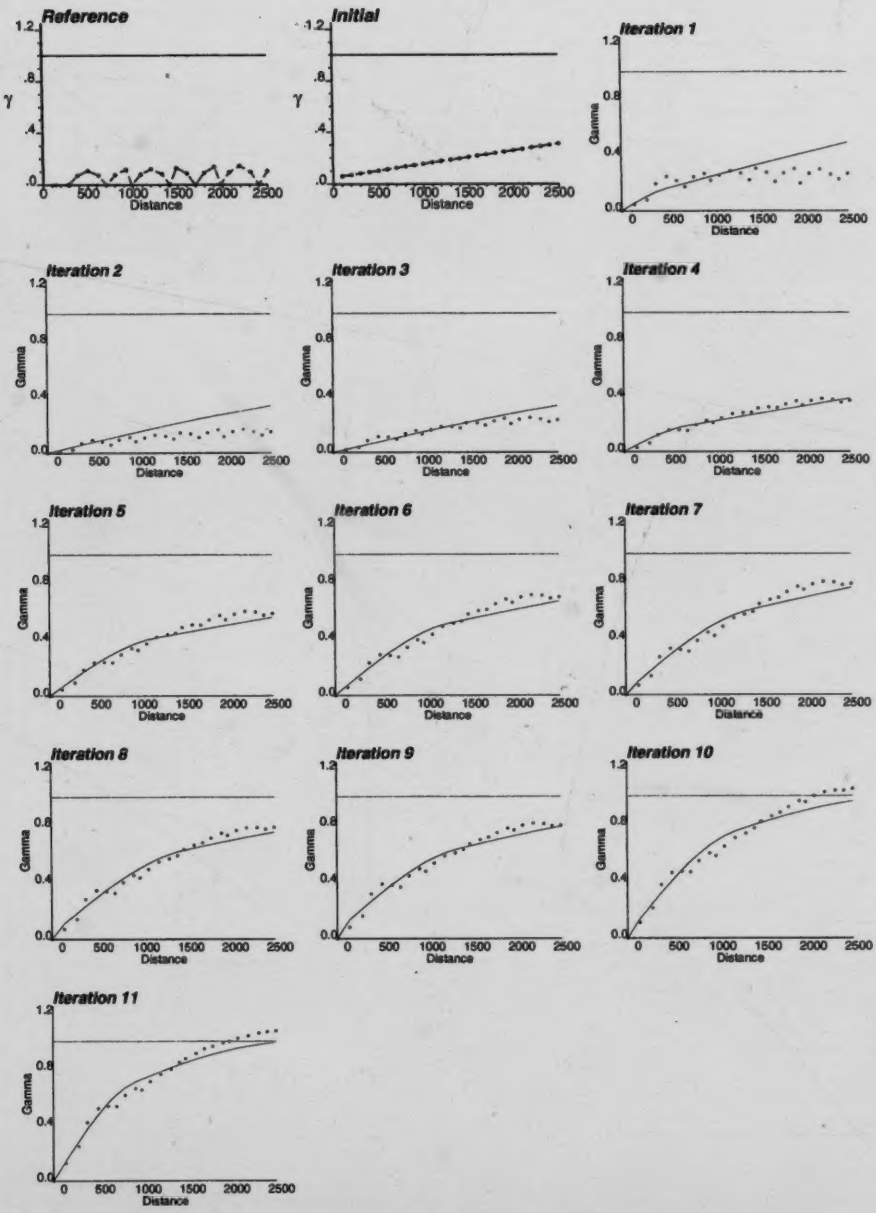


Figure 6.42: Reference, prior and updated variograms (experimental - dotted line, model - solid line) for $\phi$ at each outer iteration: 4 Well case. (Direction with azimuth 45)

| V. No. | Type | Sill | Range X - Y (ft) | Angle ($^o$) |
|---|---|---|---|---|
| 0 | Nugget | 0.001 | | |
| 1 | Sph | 0.933 | 13100 - 922 | 45 |
| 2 | Sph | 0.066 | 450 - 72 | 45 |

Table 6.16: Final variogram model obtained for $\ln(k)$ after 13 iterations: 6 Well case.

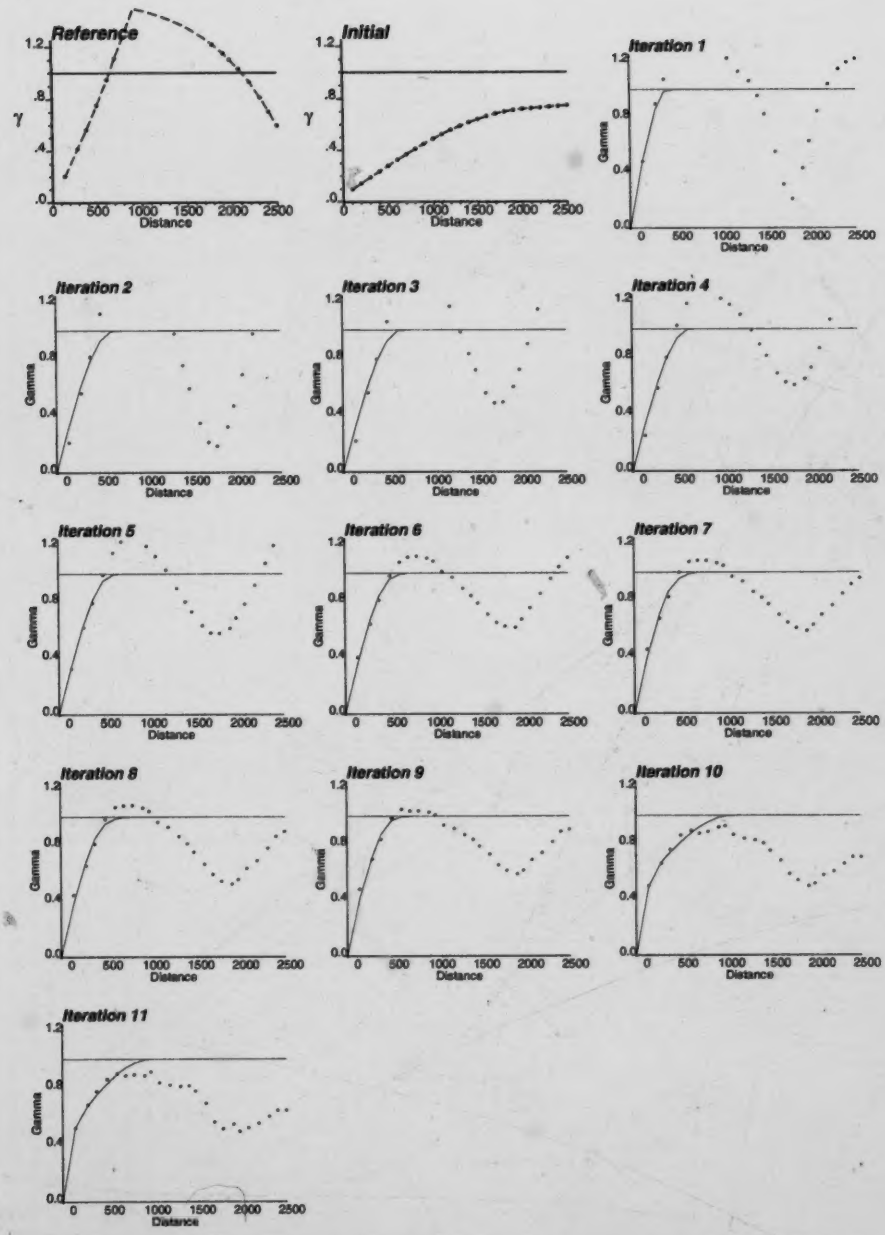


Figure 6.43: Reference, prior and updated variograms (experimental - dotted line, model - solid line) for $\phi$ at each outer iteration: 4 Well case. (Direction with azimuth 135)

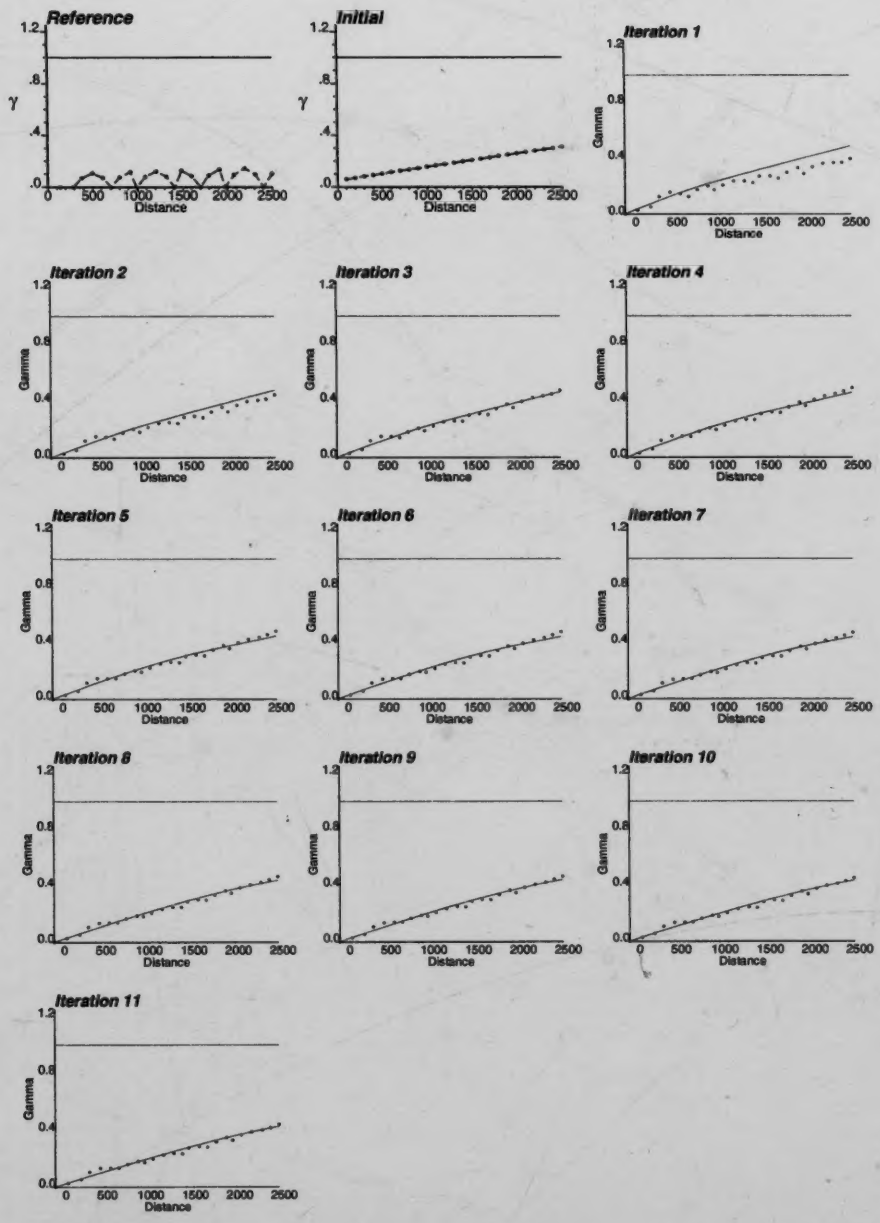


Figure 6.44: Reference, prior and updated variograms (experimental - dotted line, model - solid line) for $\ln(k)$ at each outer iteration: 4 Well case. (Direction with azimuth 45)

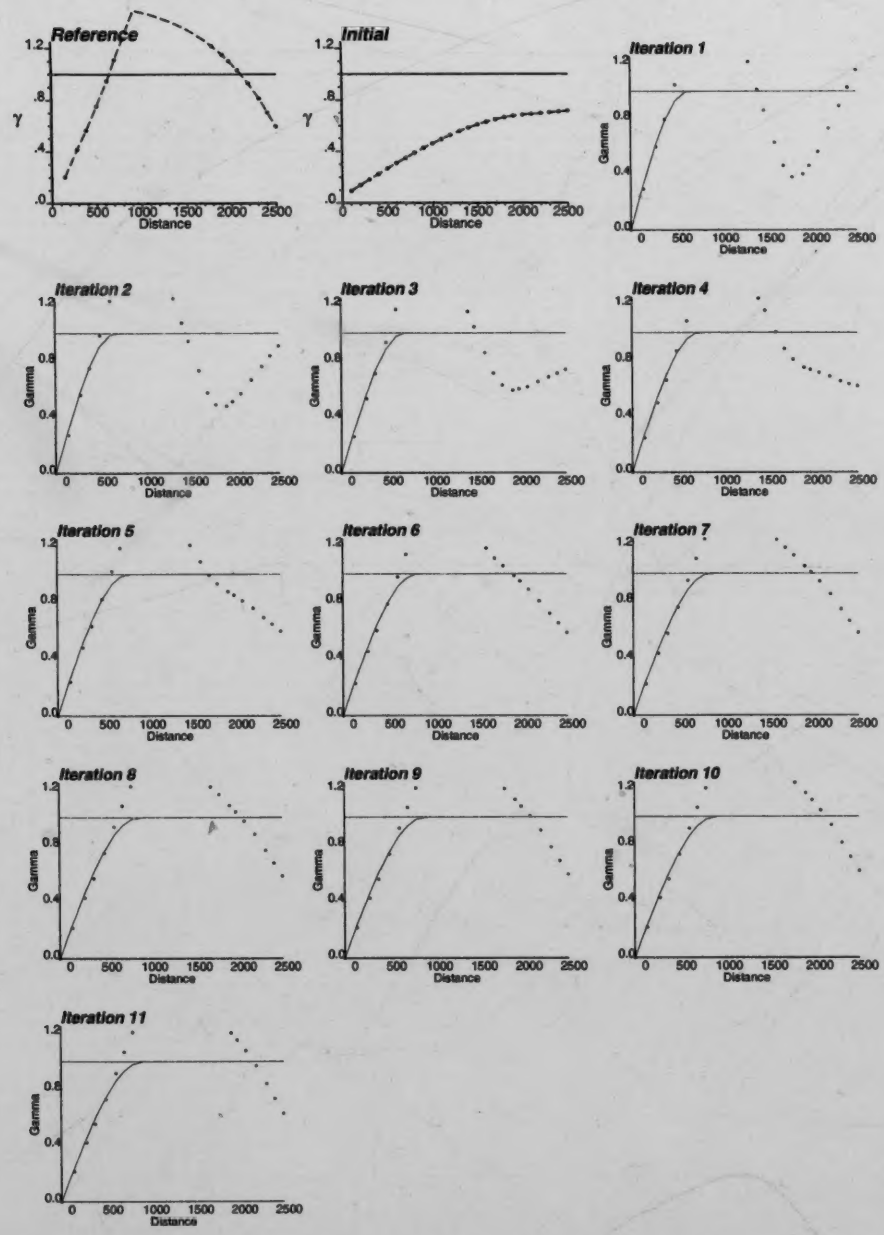


Figure 6.45: Reference, prior and updated variograms (experimental - dotted line, model - solid line) for $\ln(k)$ at each outer iteration: 4 Well case. (Direction with azimuth 135)

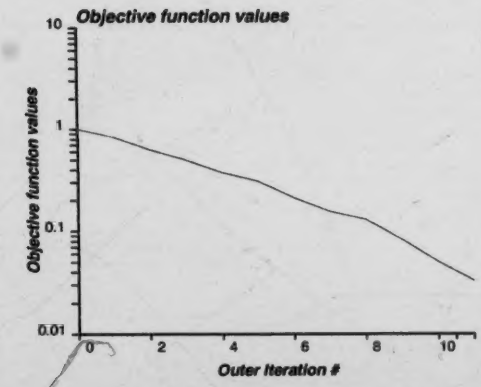


Figure 6.46: Mismatch norm of data integration at each outer iteration: 4 Well case.

| V. No. | Type | Sill | Range X - Y (ft) | Angle ($^o$) |
|---|---|---|---|---|
| 0 | Nugget | 0.0 | | |
| 1 | Sph | 0.339 | 575 - 220 | 45 |
| 2 | Sph | 0.661 | 10050 - 545 | 45 |

Table 6.17: Final variogram model obtained for $\phi$ after 10 iterations: 8 Well case.

### 8 Well Case

The inversion was performed for 10 outer iterations. CPU time for the run was only 195 seconds in a 1.8 GHz Pentium 4 personal computer. The updated variograms for $\phi$ and $\ln(k)$ are shown in Figures 6.52, 6.53, 6.54, and 6.55, for directions with azimuth 45 and 135. The mismatch in $L^2$ norms for each iteration is shown in Figure 6.56. The final $L^2$ norm of the pressure march was 27.34. After 10 iterations, the final updated variogram models are given in Tables 6.17 and 6.18 for $\phi$ and $\ln(k)$.

### Some Conclusions on Effect of Production Data

Production data contains information about reservoir heterogeneity. The question is how much information we can retrieve with our developed algorithm. Having analyzed the responses, we can definitely improve the variogram parameters using production data. Some of the observations are the following.

- Variogram inversion for $\ln(k)$ is relatively better than that for $\phi$.

| V. No. | Type | Sill | Range X - Y (ft) | Angle ($^o$) |
|---|---|---|---|---|
| 0 | Nugget | 0.003 | | |
| 1 | Sph | 0.903 | 12000 - 934 | 45 |
| 2 | Sph | 0.094 | 600 - 96 | 45 |

Table 6.18: Final variogram model obtained for $\ln(k)$ after 10 iterations: 8 Well case.

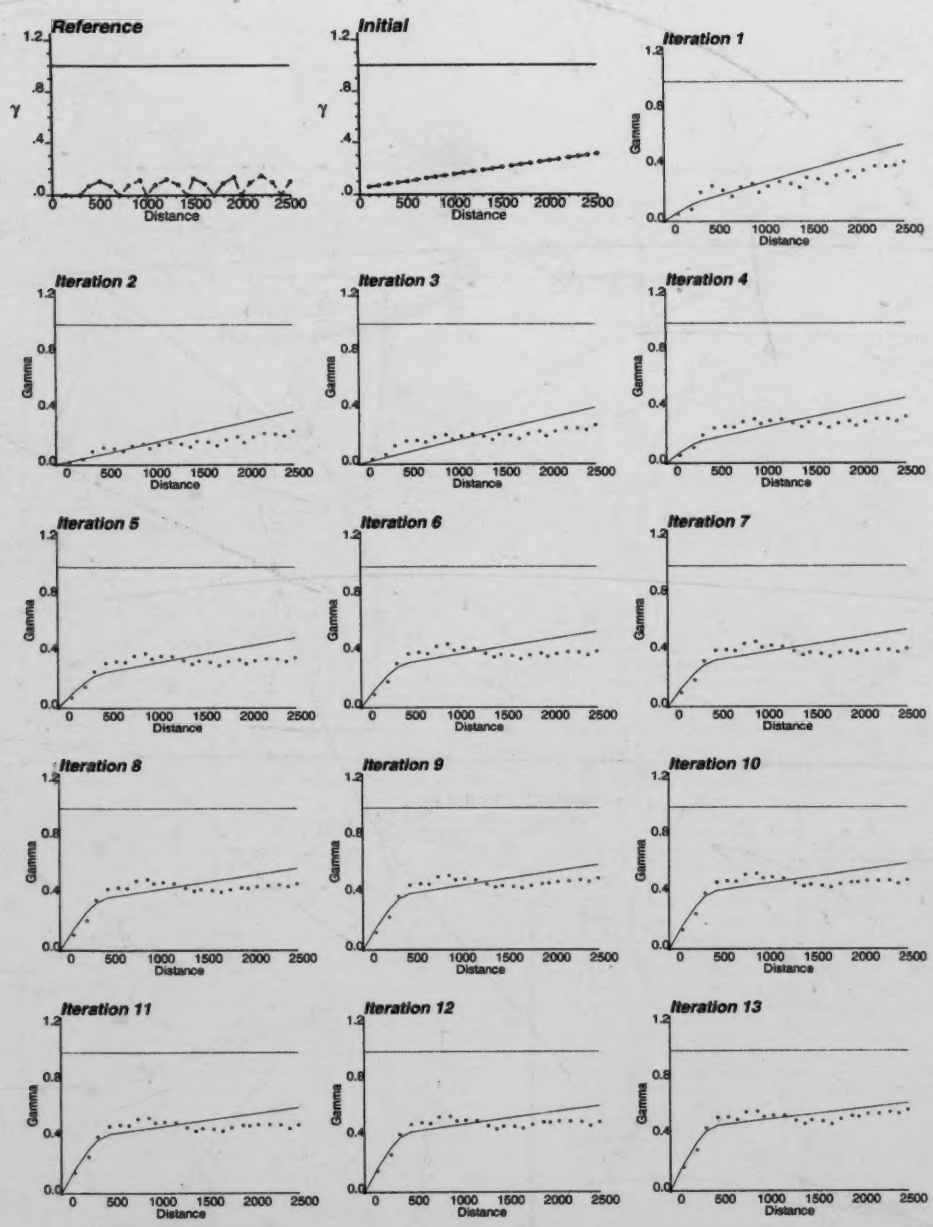


Figure 6.47: Reference, prior and updated variograms (experimental - dotted line, model - solid line) for $\phi$ at each outer iteration: 6 Well case. (Direction with azimuth 45)

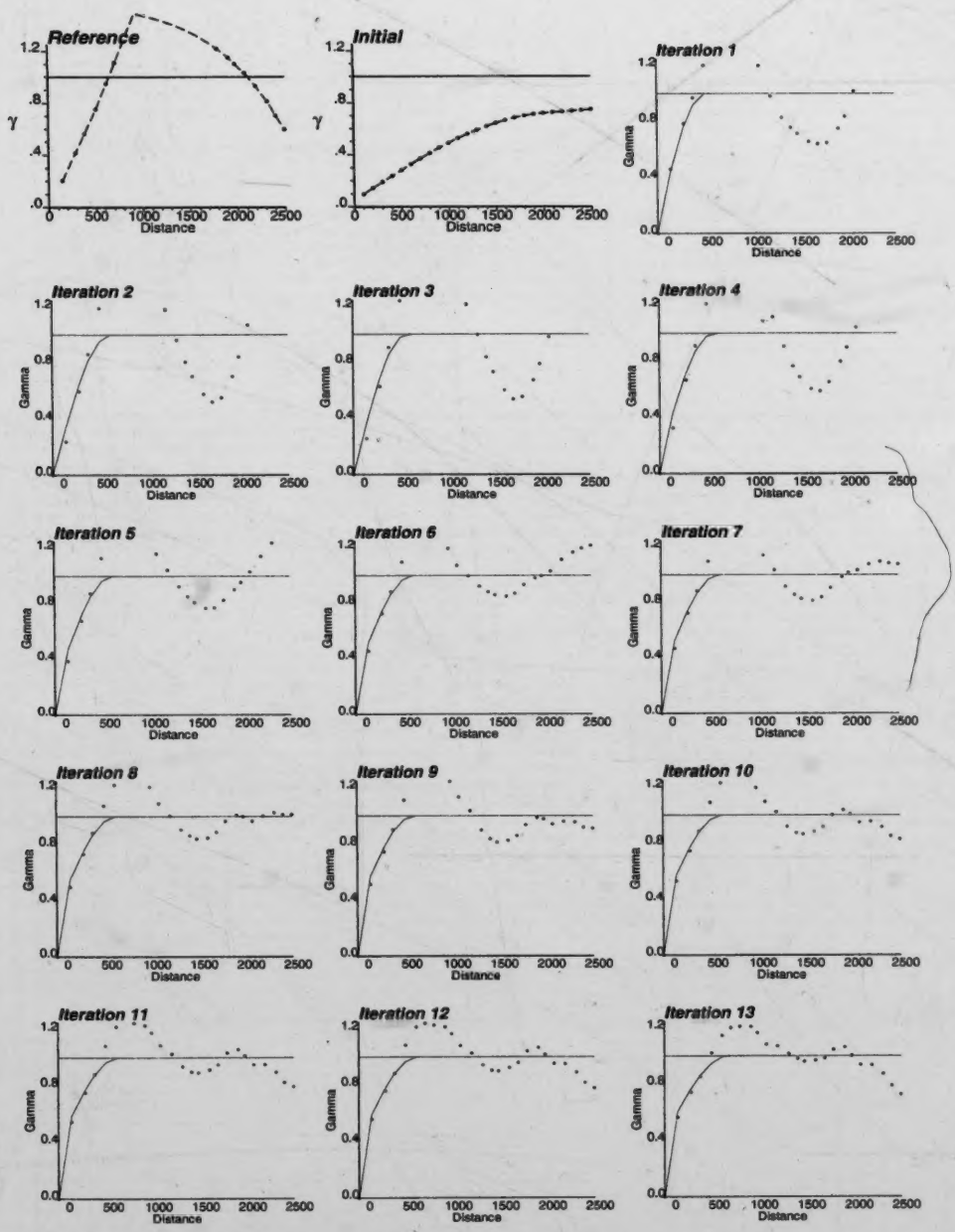


Figure 6.48: Reference, prior and updated variograms (experimental - dotted line, model - solid line) for $\phi$ at each outer iteration: 6 Well case. (Direction with azimuth 135)

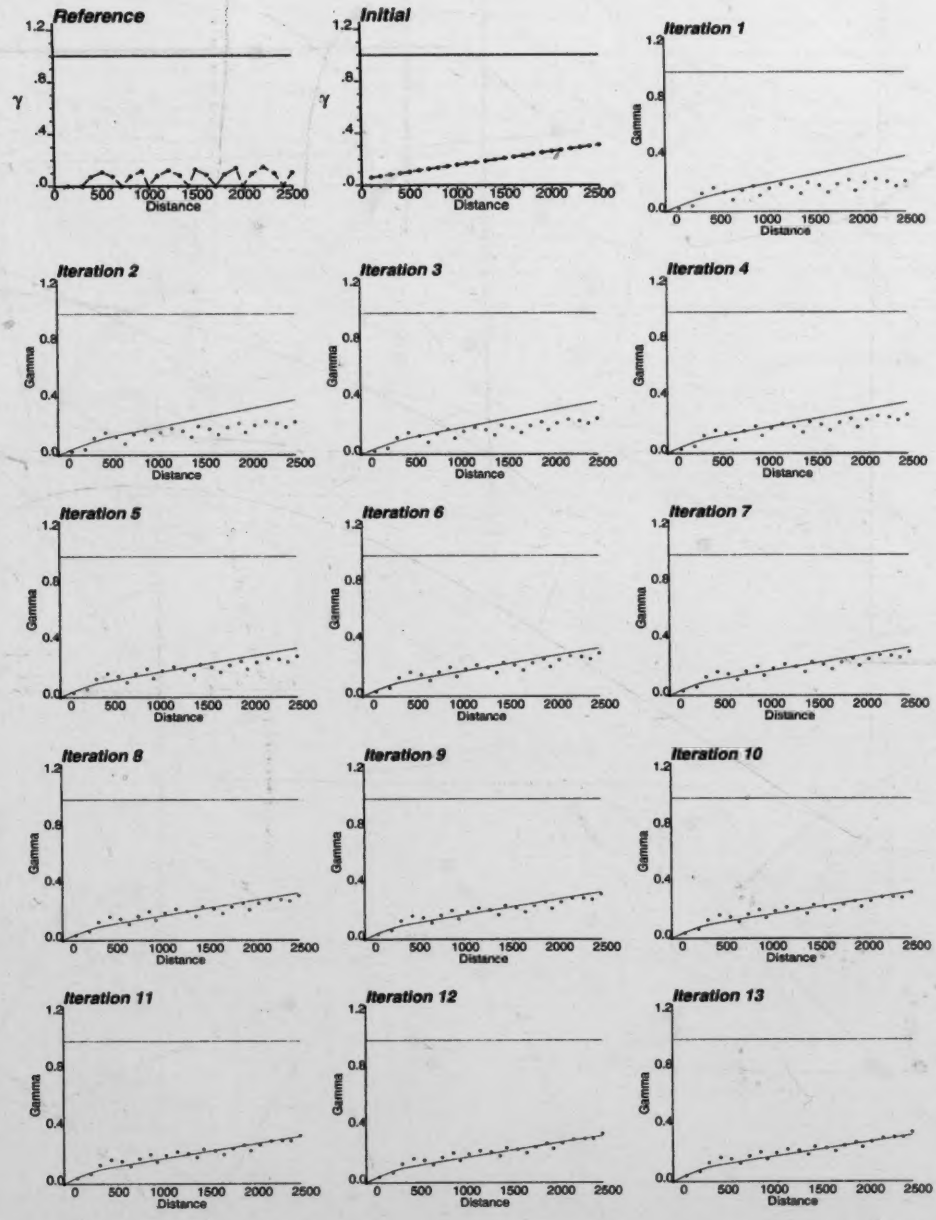


Figure 6.49: Reference, prior and updated variograms (experimental - dotted line, model - solid line) for $\ln(k)$ at each outer iteration: 6 Well case. (Direction with azimuth 45)

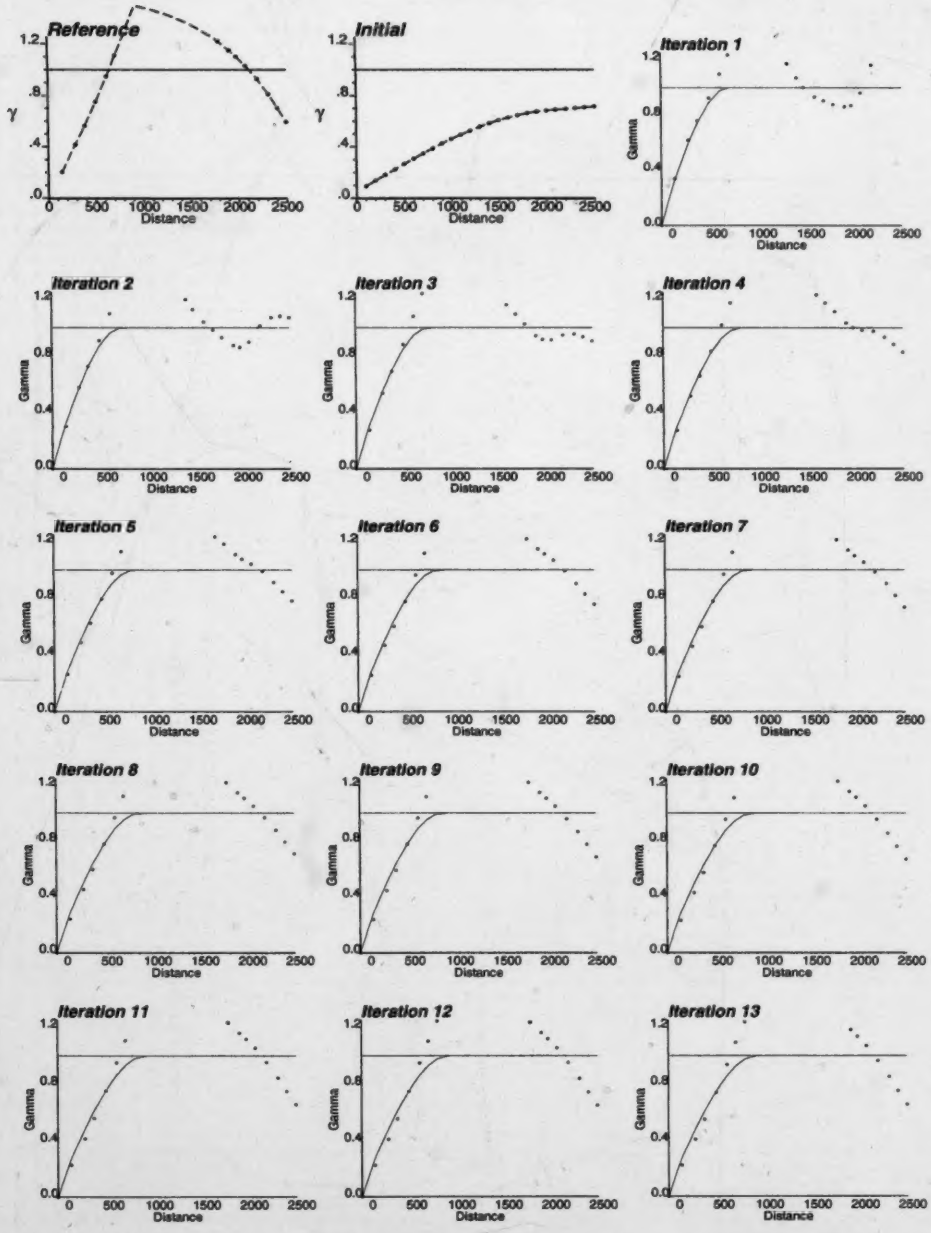


Figure 6.50: Reference, prior and updated variograms (experimental - dotted line, model - solid line) for $\ln(k)$ at each outer iteration: 6 Well case. (Direction with azimuth 135)

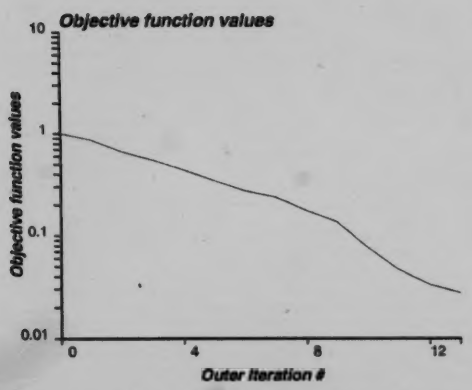


Figure 6.51: Mismatch norm of data integration at each outer iteration: 6 Well case.

- More production data will improve the inverted variogram models, provided the information is captured in the inversion. A low mismatch value is an index for such evaluation; however, more production data increases the complexity in the nonlinear inverse problem leading to a possible poor match.
- In spite of our objective of getting back the right variogram from production data, we need to start with reasonable variogram models. Gradient-based algorithm requires an initial solution close to the optimal solution.
- The quality of the inverted models depends on the in-built variogram modeling module. It may be possible to further improve on this module by trying different variogram types.
- It might be a good idea to perform the inversion with a prior model having large variogram range values to retrieve the anisotropy information better.
- It also seems that starting with high nugget effect of constant values (no prior structure) works best.

## 6.5 Some Remarks on Variogram Modeling Module

The in-built automatic variogram modeling module is implemented with an inverse squared distance weighted scheme. Thus, short lag distances are given more weights than the larger distances. Consequently, the updated variogram models do not have good match at large distances.

The perturbation is done on variogram range first, then anisotropy and finally the sill contributions for each nested structure. This cycle is repeated until a convergence with a criterion of threshold number of changes performed. The variograms are modeled to the total sill equal to the variance. No perturbation is done on the variogram type.

Nugget effect is an important parameter for any variogram model. However in a gridded domain, the nugget effect information is limited by the smallest dimension of the grid blocks. A possible solution could be to devise an artificial nugget effect information in the experimental variograms through the use of slopes near the origin (zero lag distance).

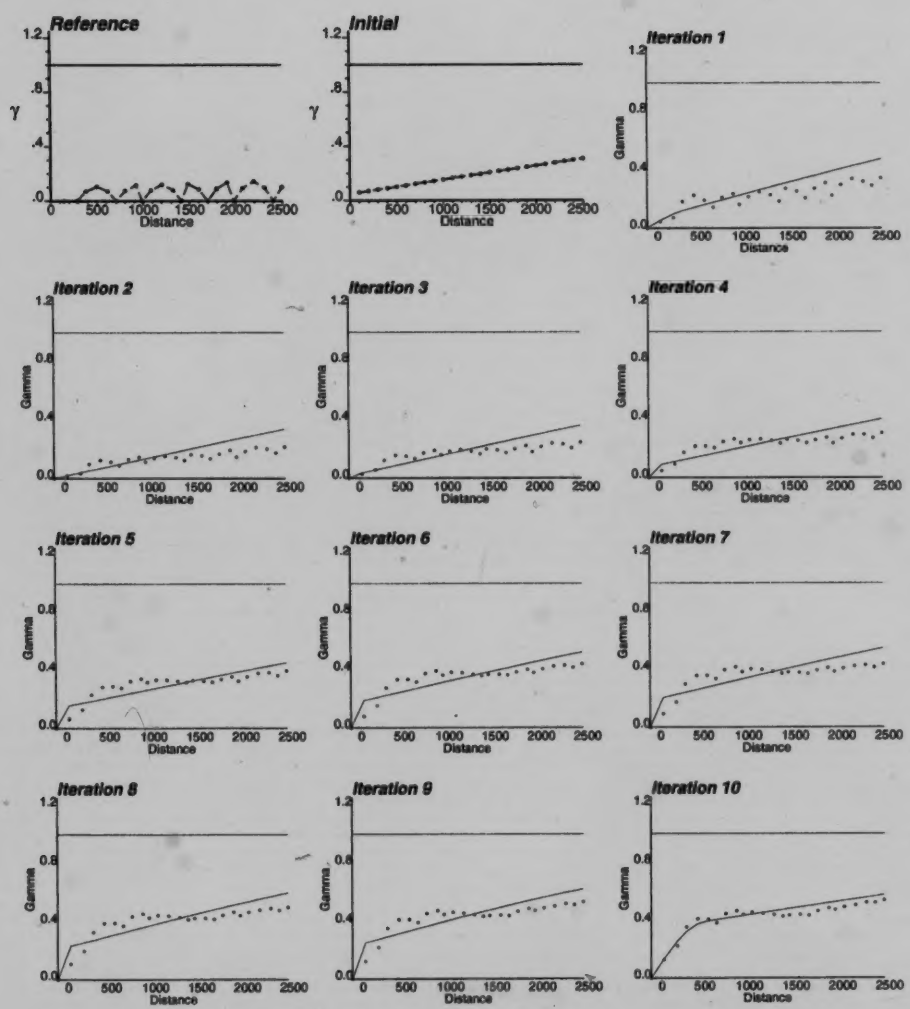


Figure 6.52: Reference, prior and updated variograms (experimental - dotted line, model - solid line) for $\phi$ at each outer iteration: 8 Well case. (Direction with azimuth 45)

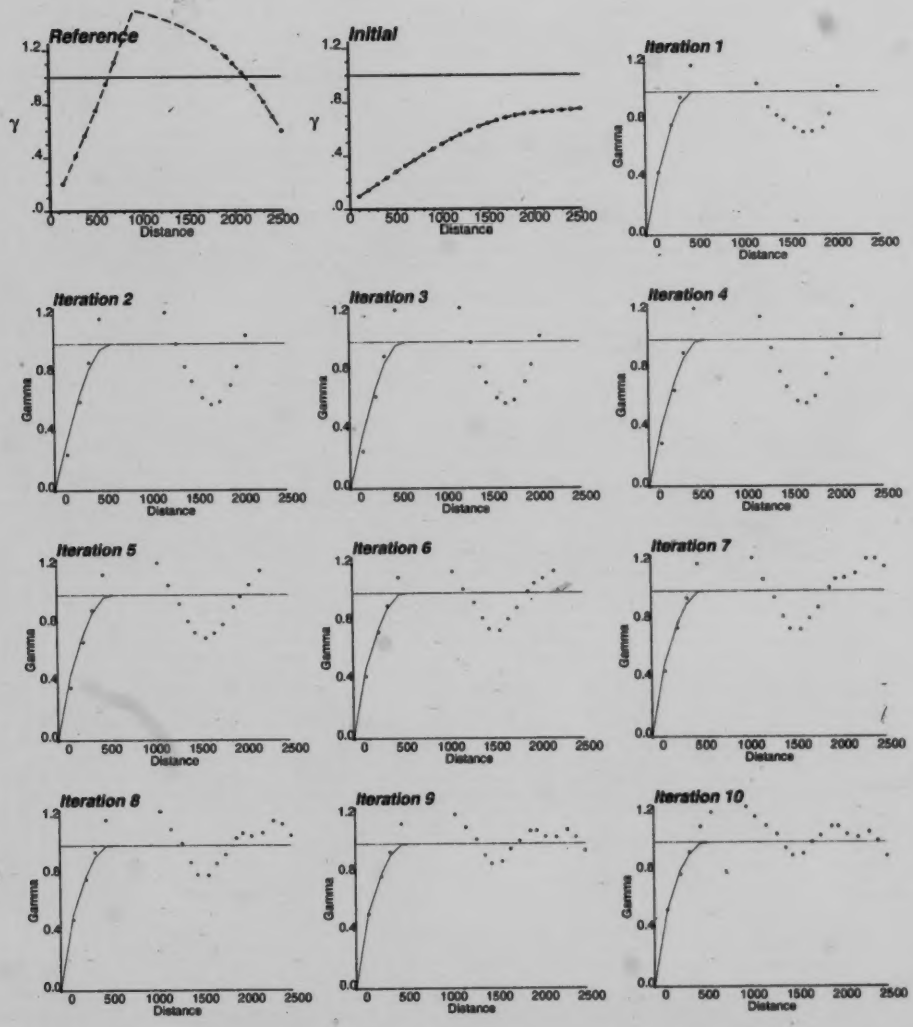


Figure 6.53: Reference, prior and updated variograms (experimental - dotted line, model - solid line) for $\phi$ at each outer iteration: 8 Well case. (Direction with azimuth 135)

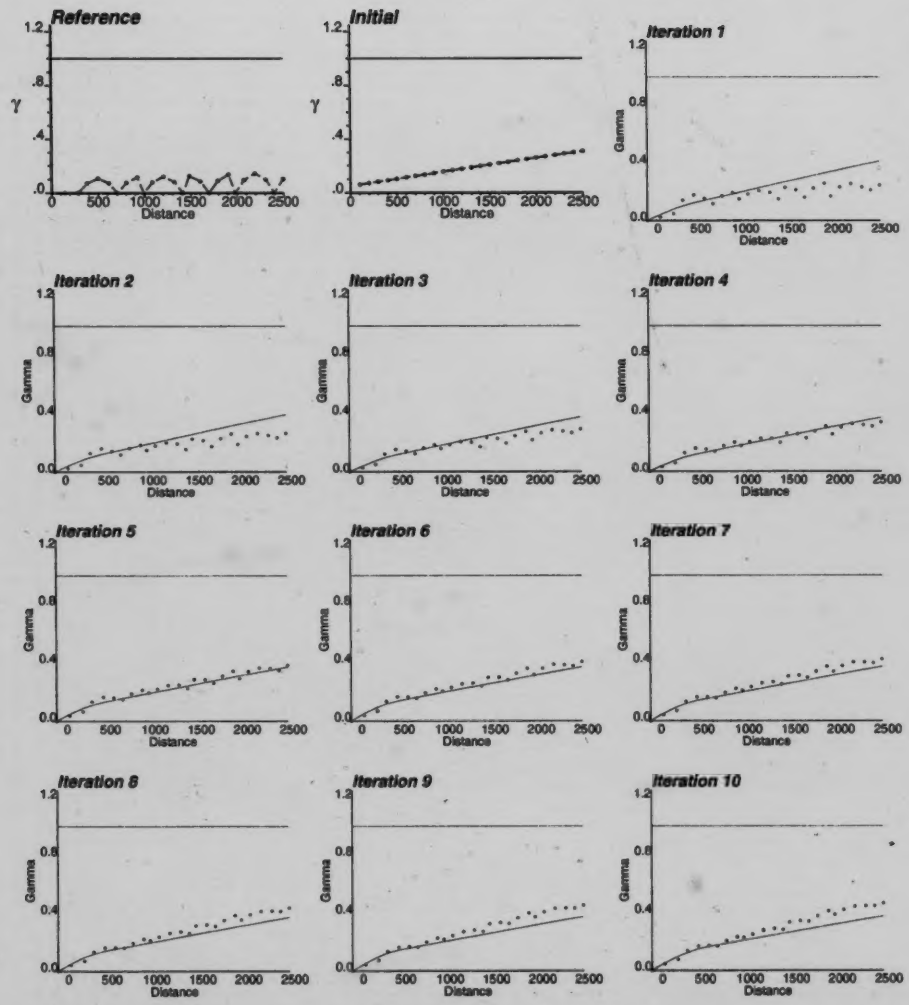


Figure 6.54: Reference, prior and updated variograms (experimental - dotted line, model - solid line) for $\ln(k)$ at each outer iteration: 8 Well case. (Direction with azimuth 45)

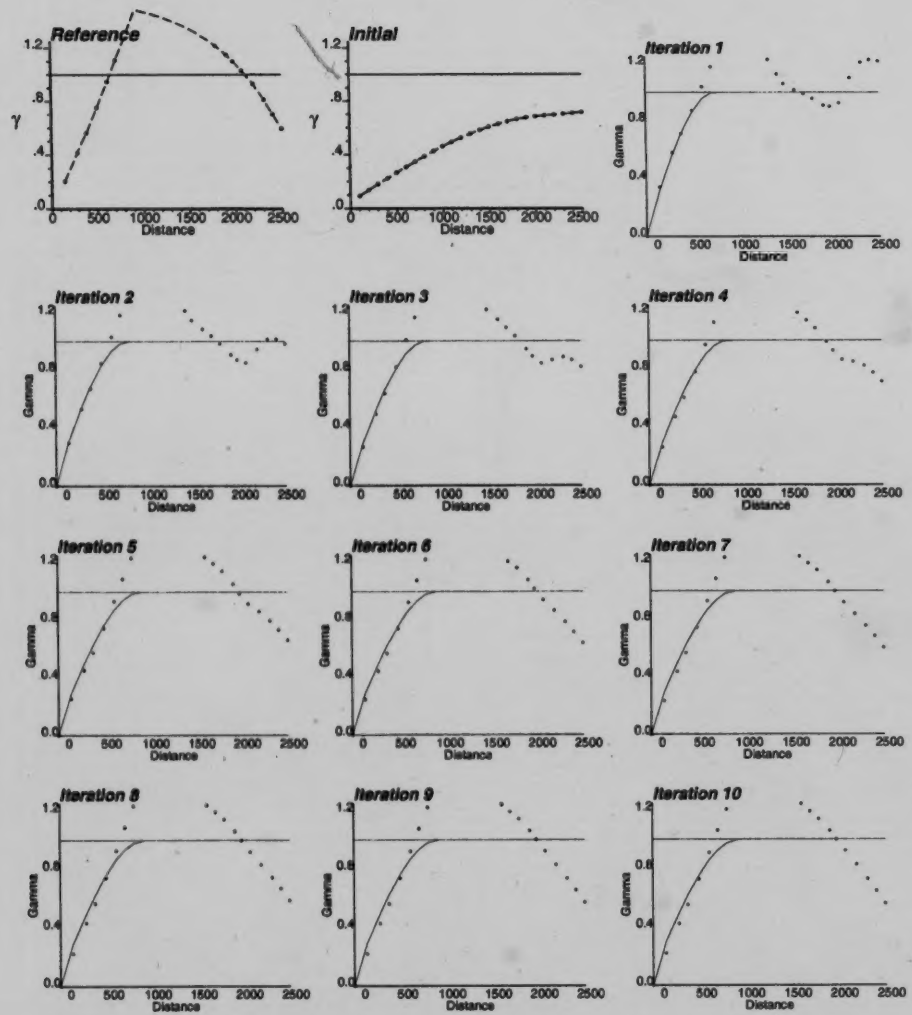


Figure 6.55: Reference, prior and updated variograms (experimental - dotted line, model - solid line) for $\ln(k)$ at each outer iteration: 8 Well case. (Direction with azimuth 135)

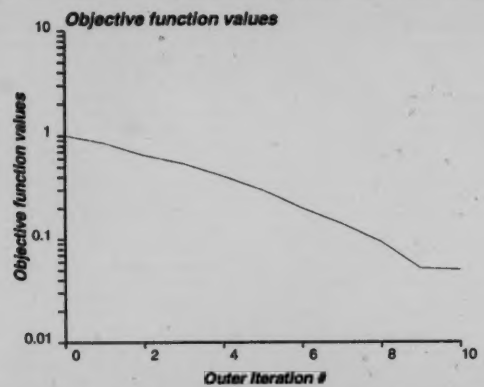


Figure 6.56: Mismatch norm of data integration at each outer iteration: 8 Well case.

# Chapter 7

# Fault Property Inversion Using Production Data

Reservoir heterogeneity has a large effect on performance of a reservoir. Faults may act as barriers creating compartmentalized reservoirs or as high conductivity conduits in an otherwise tight reservoir system. Often, the location of such faults or fault zones are identified with seismic data; however, the conductive characteristics of the fault zones cannot be resolved with seismics. Faults may affect the dynamic flow responses of the reservoir system. We develop an inversion algorithm for fault zone permeability characterization using multiple well flow response data.

## 7.1 Algorithm Description

An algorithm for simultaneous inversion of porosity and permeability was developed using a modified SSC method, see Chapter 4. Here, we extend the algorithm for fault zone permeability characterization.

The basic approach of sensitivity computation remains the same. Some master points are assigned for fault zone cells. The properties (porosity and permeability) in these cells are optimized in the same inner optimization loop with the other master points for unfaulted zones. The optimal corrections for regular grid cells are propagated as before; however, the fault zone properties are taken as averages for each fault and kept constant for every cell representing the fault.

Thus, a methodology has been developed for simultaneous inversion of porosity and permeability. The steps involved in this extended algorithm follow.

1. Select regular master points and fault zone master points.
2. Perform Steps (2) to (9) involved in simultaneous inversion algorithm discussed in Chapter 4.
3. Determine and assign the weighted averaged optimal corrections to fault blocks.
4. Update initial $\phi$ and $y$ fields.
5. Repeat Steps (1) to (4) till convergence is achieved.

The salient idea of this algorithm is to isolate the domains - the faulted ones and the unfaulted reservoir domain. Separate collection of master points and the constraint sets are set up for the respective domains. Propagation of optimal master point corrections are performed within the faulted domains by some averaging scheme, whereas for the unfaulted reservoir domain through kriging weights.

In the following sections, we demonstrate the ability of the code to retrieve fault zone properties with some synthetic examples. First, we discuss a sealing fault example with only two wells. We investigate the dependence of the well locations with respect to the fault. In one case, the wells are in the opposite side of the fault, while in the other they are in the same side of the faults. Then, we perform the inversion of a faulted reservoir with high permeability fault with similar two-well cases. Finally, some sensitivity studies on the inversion process are performed.

## 7.2 Sealing Fault Example

A synthetic realistic example is demonstrated here to evaluate the ability of the algorithm to characterize fault zone permeabilities from multiple well production data. Faulted reference porosity and permeability fields are constructed first. Dynamic pressure responses at a number of wells are obtained by flow simulation.

### Case A: 2 Wells on the Opposite Side of the Fault

A 2D 4000-ft square domain is discretized into 40 × 40 grid cells of 100 × 100 ft. Porosity and permeability fields are shown in Figure 7.1. There are 2 wells: Well W1 at the center of the cell (28,5), and Well W2 is at (30,34) (shown in Figure 7.1). The boundaries on all four sides are no-flow boundaries. Reservoir thickness is 100 ft, viscosity is 0.2 cp, formation compressibility $10^{-6}$ $\text{psi}^{-1}$, and well radius 0.3 ft. Figure 7.2 shows the imposed production rates and the corresponding numerically simulated pressure responses at the two wells. The histogram and the scatter-plot between $\phi$ and $\ln(k)$ are shown in Figures 7.3 and 7.4, respectively. Mean and standard deviation of reference distributions are 0.071 and 0.019 for $\phi$, and 1.293 and 1.277 for $\ln(k)$. The low average porosity confirms the low storativity of the reservoir. The correlation coefficient between porosity and permeability is 0.541. A fault extends across the reservoir dividing the reservoir in two separate compartments with one having relatively higher porosity and permeability. The fault is acting as a flow barrier with poor fault zone petrophysical properties. The reference fault zone porosity and $\ln(k)$ are 0.03 and -5.0. Despite the simplicity of this example, inversion of these fault zone properties can be extremely difficult using multiple well production data. The reason for difficulty is the fact that subsurface flow is diffusive in nature. The effect of fault zones or narrow streak of abnormal properties may be masked by an effective ensemble properties in the region. In other words, both the scenarios of the effective homogenized properties and the fault zones may give rise to similar pressure profile for given flow rates.

Static well data are shown in Figure 7.5. Inversion was performed using 5 × 5 (=25) master points for reservoir models and 8 master points for fault properties. The prior variogram models used in this run for $\phi$ and $\ln(k)$ are given in Equations 7.1 and 7.2:

$$\gamma_\phi(h) = 0.0 + 0.4Sph(h)\,{}_{\substack{a_x = 1000 \\ a_y = 3000}} + 0.6Sph(h)\,{}_{\substack{a_x = 9000 \\ a_y = 4000}} \tag{7.1}$$

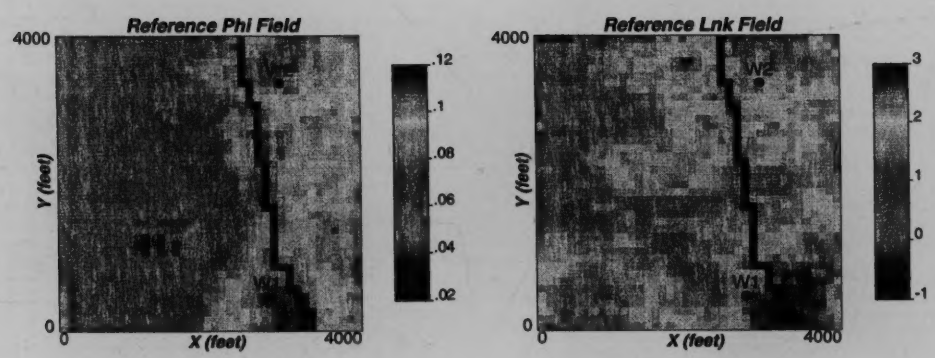


Figure 7.1: Reference faulted $\phi$ and $\ln(k)$ fields: Sealing Fault Example (Case A).

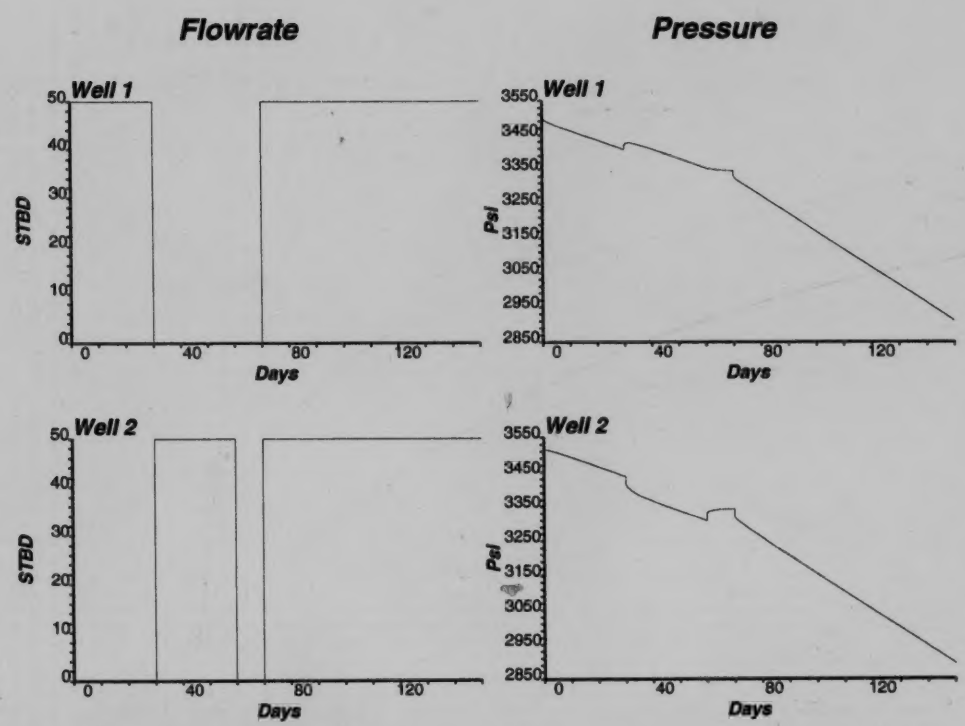


Figure 7.2: Production data (pressure and flow rates) obtained for 2 wells from the reference field: Sealing Fault Example (Case A).

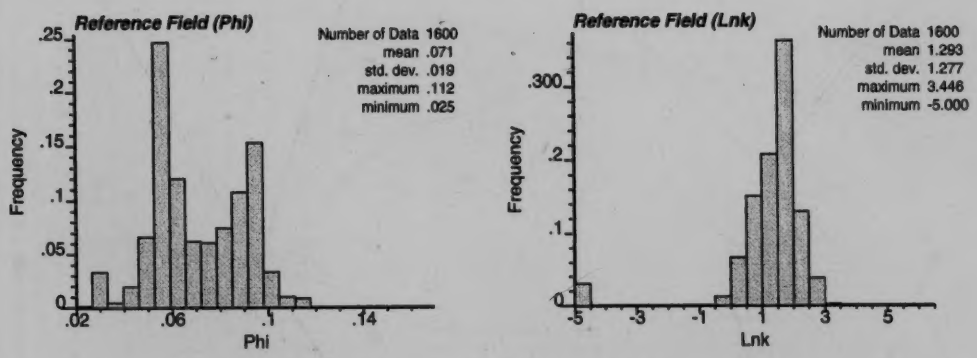


Figure 7.3: Histograms of reference $\phi$ and $\ln(k)$ fields: Sealing Fault Example (Case A).

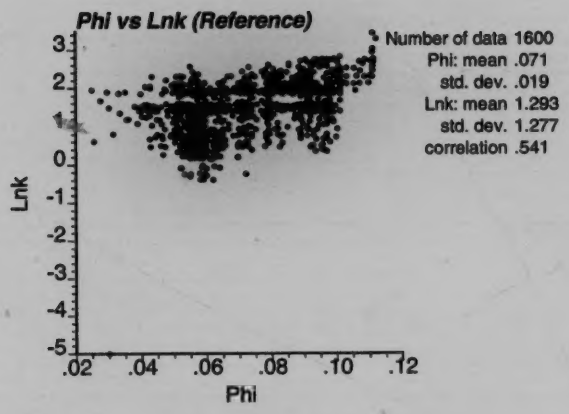


Figure 7.4: Scatterplot of reference $\phi$ and $\ln(k)$ distributions: Sealing Fault Example (Case A).

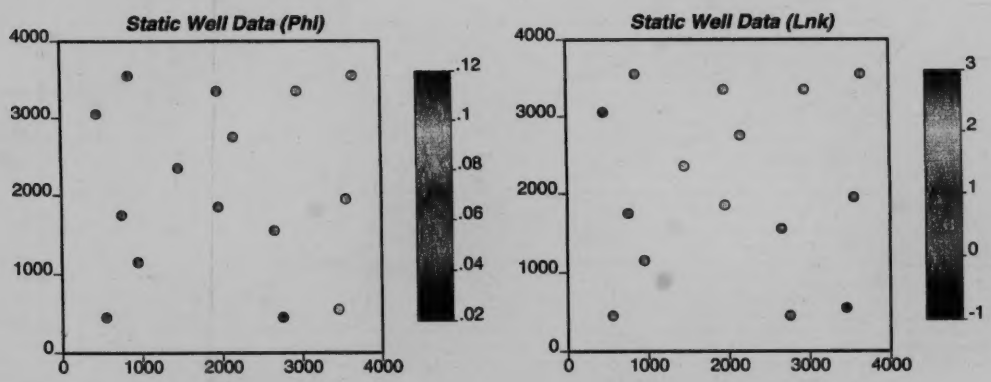


Figure 7.5: Static well data for $\phi$ and $\ln(k)$: Fault Property Inversion.

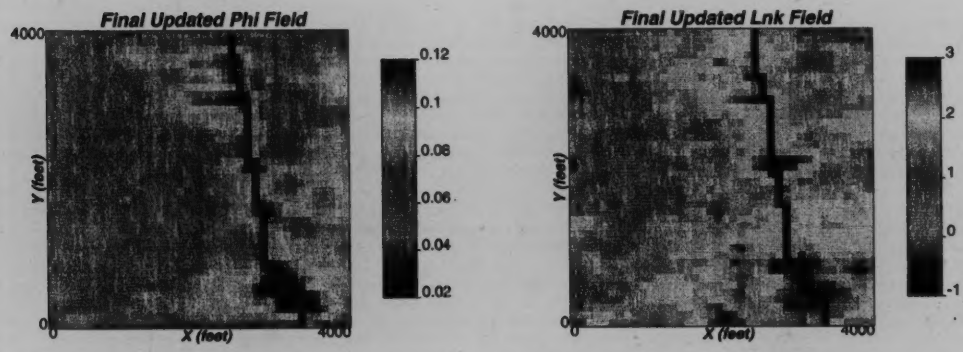


Figure 7.6: Updated $\phi$ and $\ln(k)$ fields: Sealing Fault Example (Case A).

and

$$\gamma_y(h) = 0.0 + 0.35Sph(h)\,{}_{\substack{a_x = 1000 \\ a_y = 3000}} + 0.65Sph(h)\,{}_{\substack{a_x = 8000 \\ a_y = 4500}} \cdot \tag{7.2}$$

The inverted models are obtained after 70 outer iterations (18.5 minutes in a 1.8 GHz processor personal computer). The pressure responses in the updated porosity and permeability fields converge to the reference pressure data. These inverted models are shown in Figure 7.6. Figure 7.7 shows the pressure values at the ten wells computed from the true (from reference), initial and final updated porosity and permeability fields. Final pressure match is remarkable. Final average pressure mismatch (in $L^2$ norm sense) was only 2.527 psi. The objective function values of the inversion process are shown in Figure 7.8. The fault zone properties at all outer iterations are shown in Figures 7.9 and 7.10 for porosity and permeability values. Updated porosity and permeability fields at some outer iterations of the inversion method are shown in Figures 7.11 and 7.12.

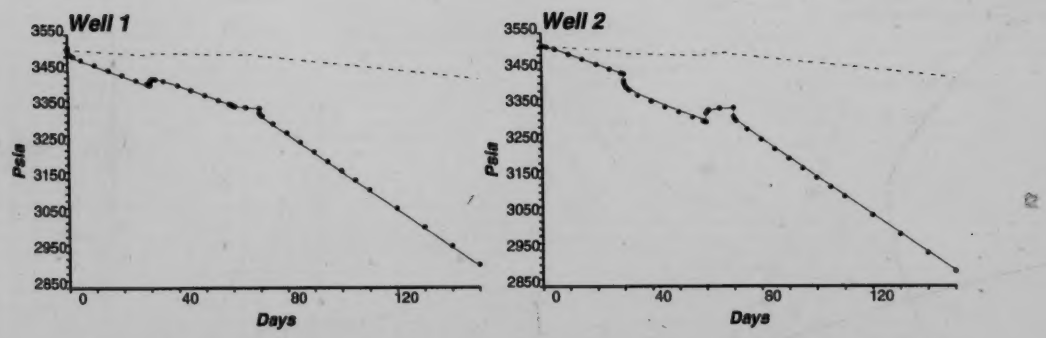


Figure 7.7: Pressure responses computed from initial (dashed lines) and updated (bullets) $\phi$ and $\ln(k)$ fields with the true data (solid lines): Sealing Fault Example (Case A).

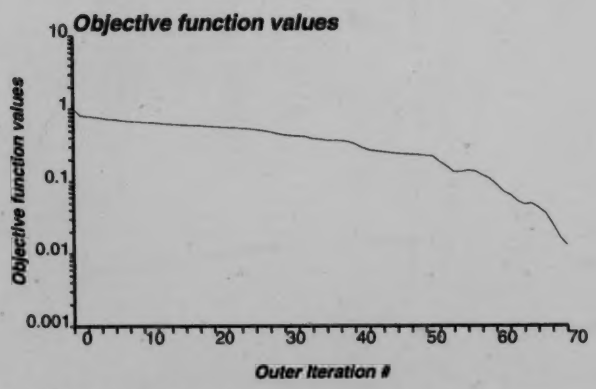


Figure 7.8: Objective function values of the inversion process: Sealing Fault Example (Case A).

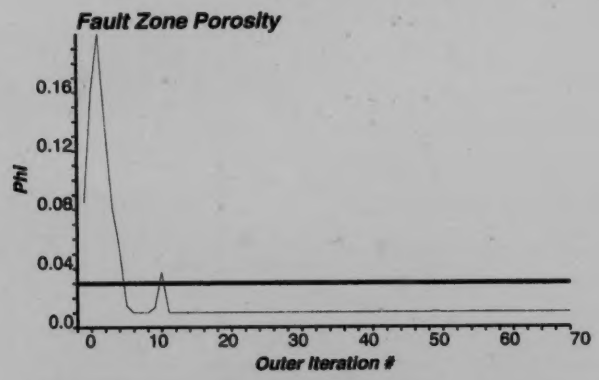


Figure 7.9: Fault zone $\phi$ values at each outer iteration: Sealing Fault Example (Case A). (Reference value: thicker horizontal line)

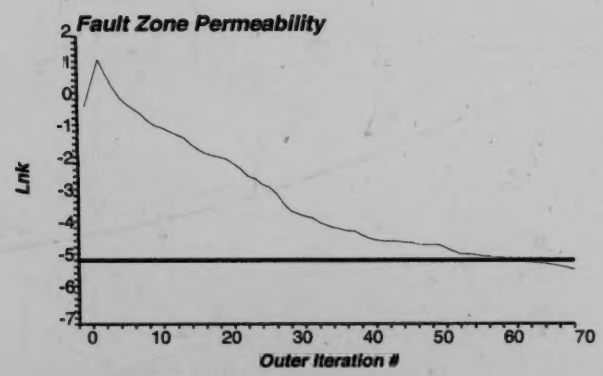


Figure 7.10: Fault zone $\ln(k)$ values at each outer iteration: Sealing Fault Example (Case A). (Reference value: thicker horizontal line)

## Case B: 2 Wells in the Same Side of the Fault

The 2 wells are now on the same side of the faults: Well W1 at the center of the cell (28,5), and Well W2 is at (20,34). The wells are shown in Figure 7.13. Other information and parameters are kept unchanged. Figure 7.14 shows the imposed production rates and the corresponding numerically simulated pressure responses at the two wells.

The inverted models are obtained after 216 outer iterations (59.5 minutes in a 1.8 GHz processor personal computer). The pressure responses in the updated porosity and permeability fields converge to the reference pressure data. These inverted models, shown in Figure 7.15, have a similar heterogeneity distribution to the reference truth. Figure 7.16 shows the pressure values at the two wells computed from the true (from reference), initial and final updated porosity and permeability fields. The objective function values of the inversion process is shown in Figure 7.17. Final average pressure mismatch (in $L^2$ norm sense) was 4.091 psi. The fault zone properties at all outer iterations are shown in Figures 7.18 and 7.19 for porosity and permeability values. Updated porosity and permeability fields after each outer iteration of the inversion method are shown in Figures 7.20 and 7.21.

## Some Conclusions

Comparison of the two cases reveal that it is more likely that one can capture heterogeneity information from production data when the wells are in the opposite sides of the fault and there exists interference information in the production data. Inversion in Case B takes a significantly higher number of iterations to achieve the same order of pressure match and consequently higher CPU time than that in Case A. In fact, fault permeability values (see Figure 7.19) are much higher than the reference values. One can attribute the reason for poor resolution to the fact that there is less interference information available in the production data in Case B. Another observation is that fault permeability values are better resolved with the production data than the porosity values.

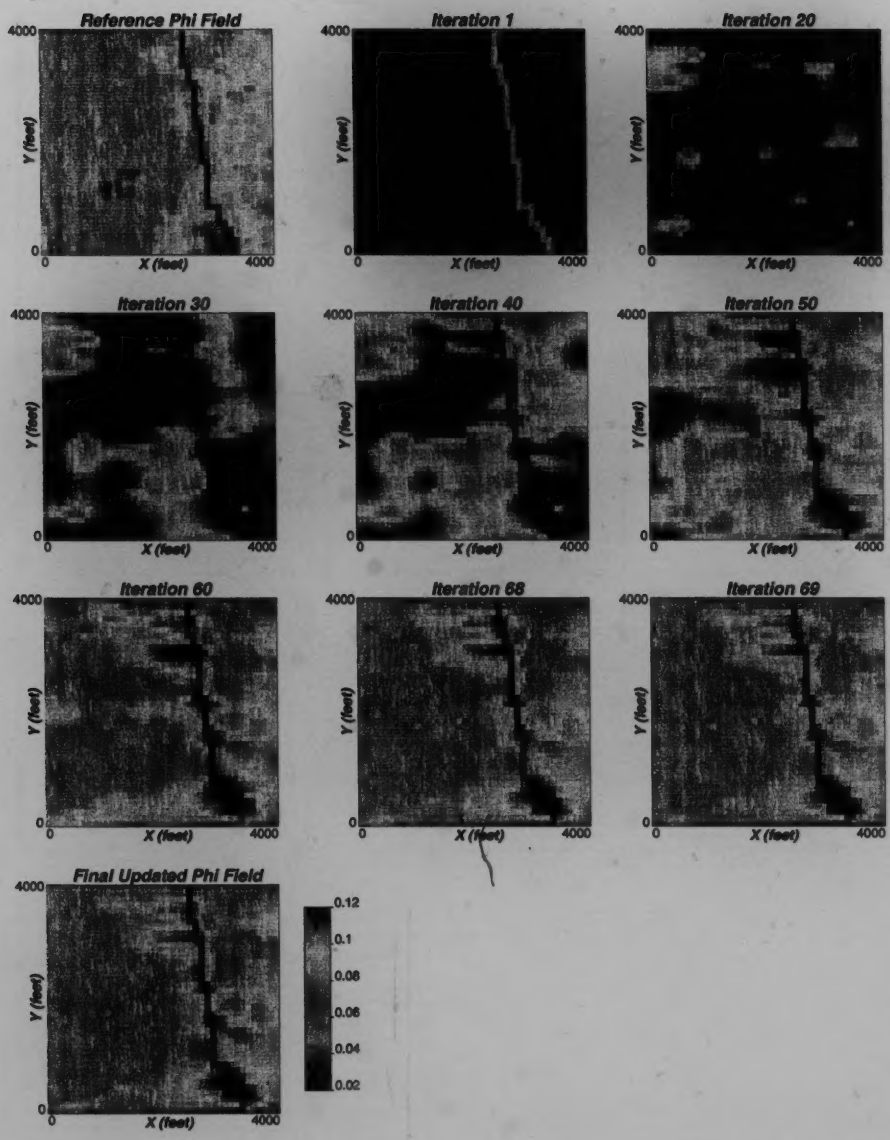


Figure 7.11: Updated $\phi$ fields at some iterations of the inversion process: Sealing Fault Example (Case A).

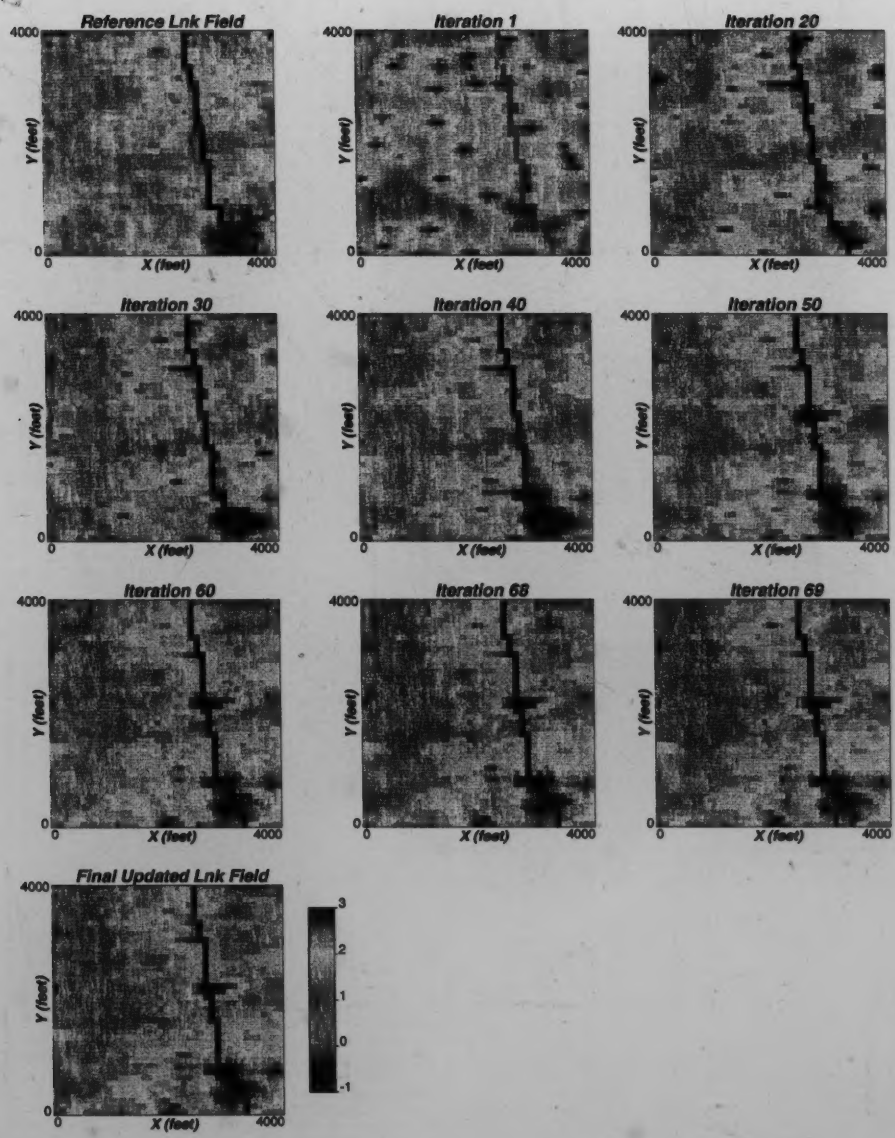


Figure 7.12: Updated $\ln(k)$ fields at some iterations of the inversion process: Sealing Fault Example (Case A).

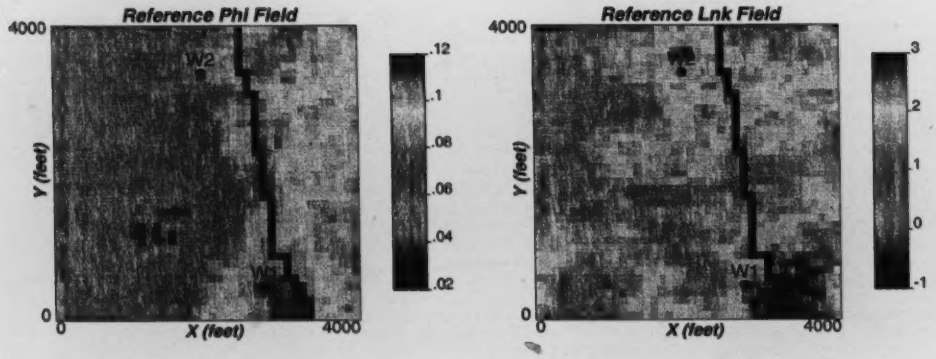


Figure 7.13: Reference faulted $\phi$ and $\ln(k)$ fields: Sealing Fault Example (Case B).

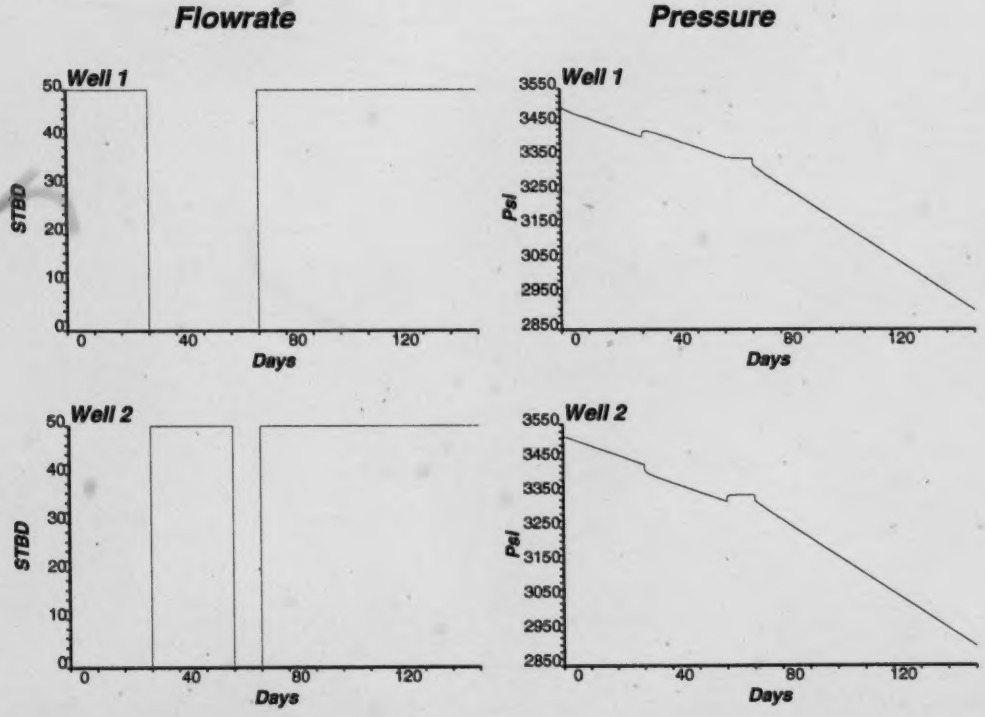


Figure 7.14: Production data (pressure and flow rates) obtained for 2 wells from the reference field: Sealing Fault Example (Case B).

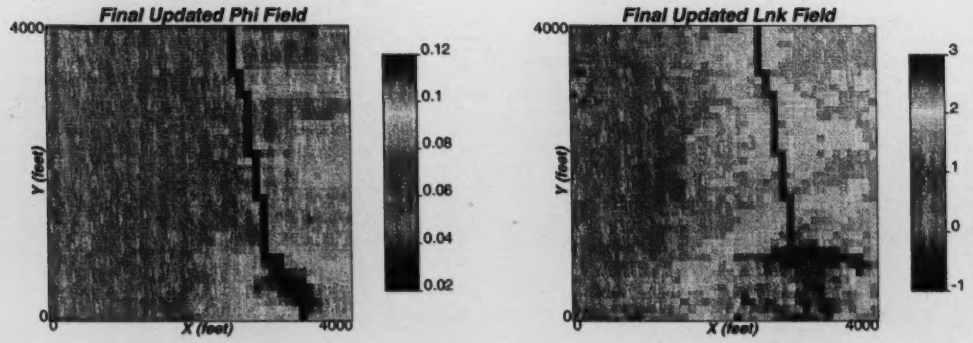


Figure 7.15: Updated $\phi$ and $\ln(k)$ fields: Sealing Fault Example (Case B).

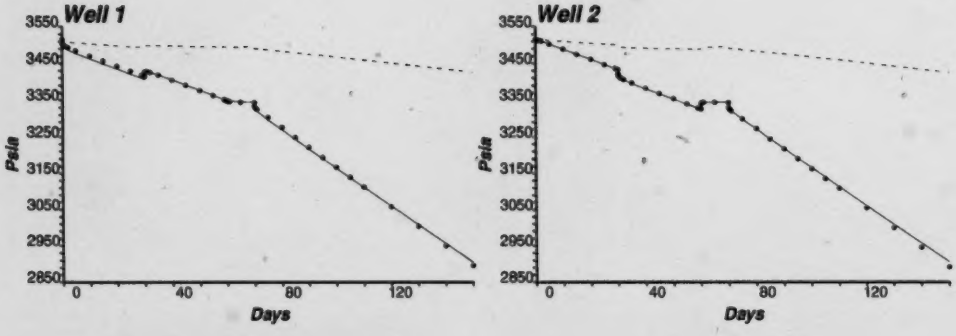


Figure 7.16: Pressure responses computed from initial (dashed lines) and updated (bullets) $\phi$ and $\ln(k)$ fields with the true data (solid lines): Sealing Fault Example (Case B).

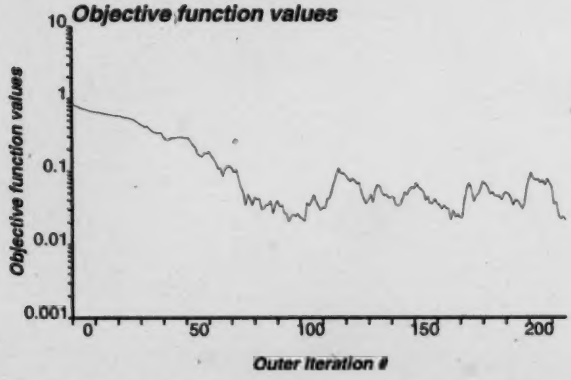


Figure 7.17: Objective function values of the inversion process: Sealing Fault Example (Case B).

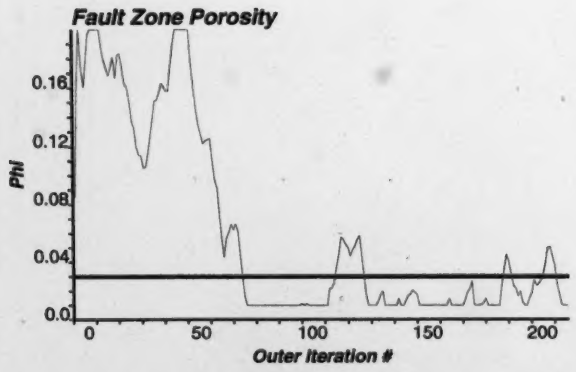


Figure 7.18: Fault zone $\phi$ values for each outer iteration: Sealing Fault Example (Case B). (Reference value: thicker horizontal line)

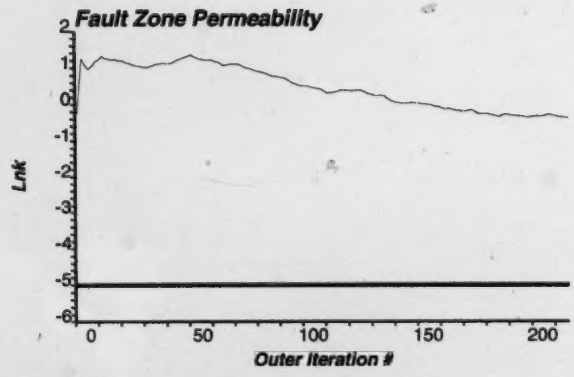


Figure 7.19: Fault zone $\ln(k)$ values for each outer iteration: Sealing Fault Example (Case B). (Reference value: thicker horizontal line)

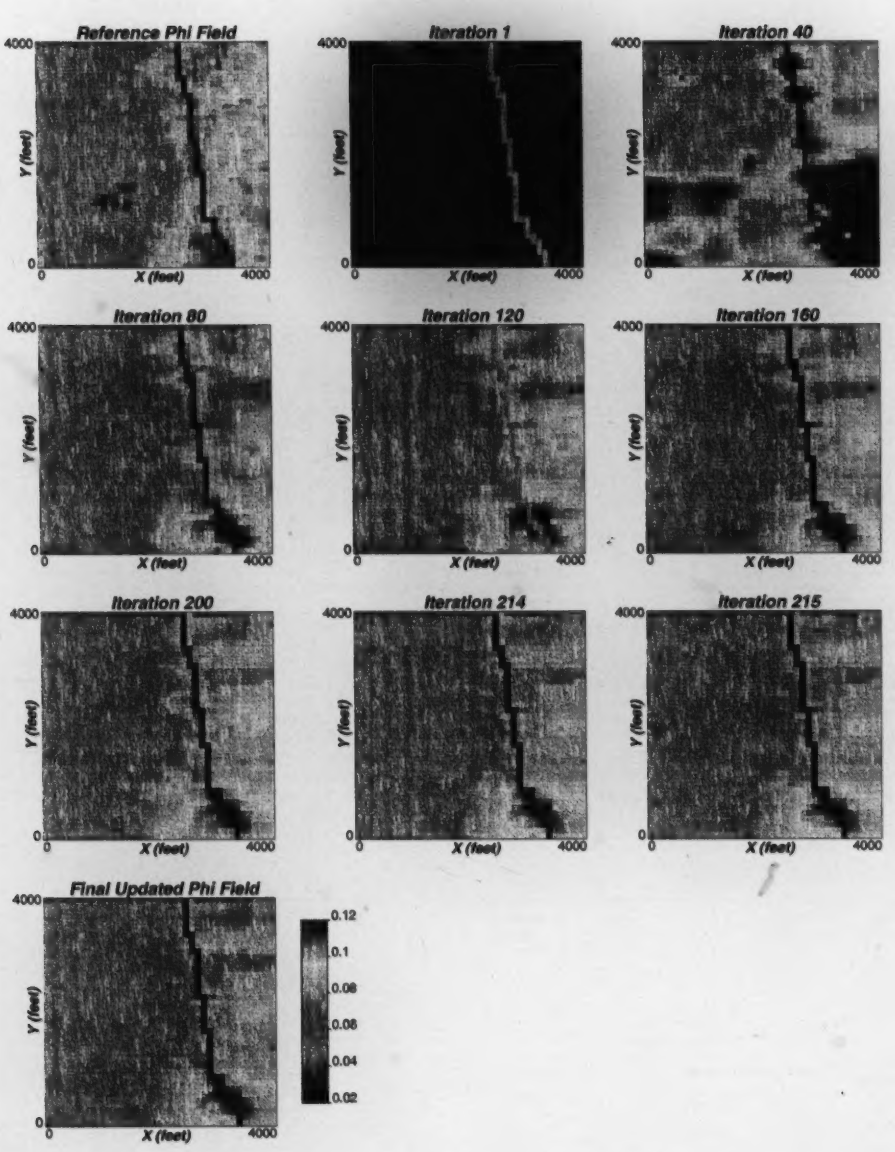


Figure 7.20: Updated $\phi$ fields at some iterations of the inversion process: Sealing Fault Example (Case B).

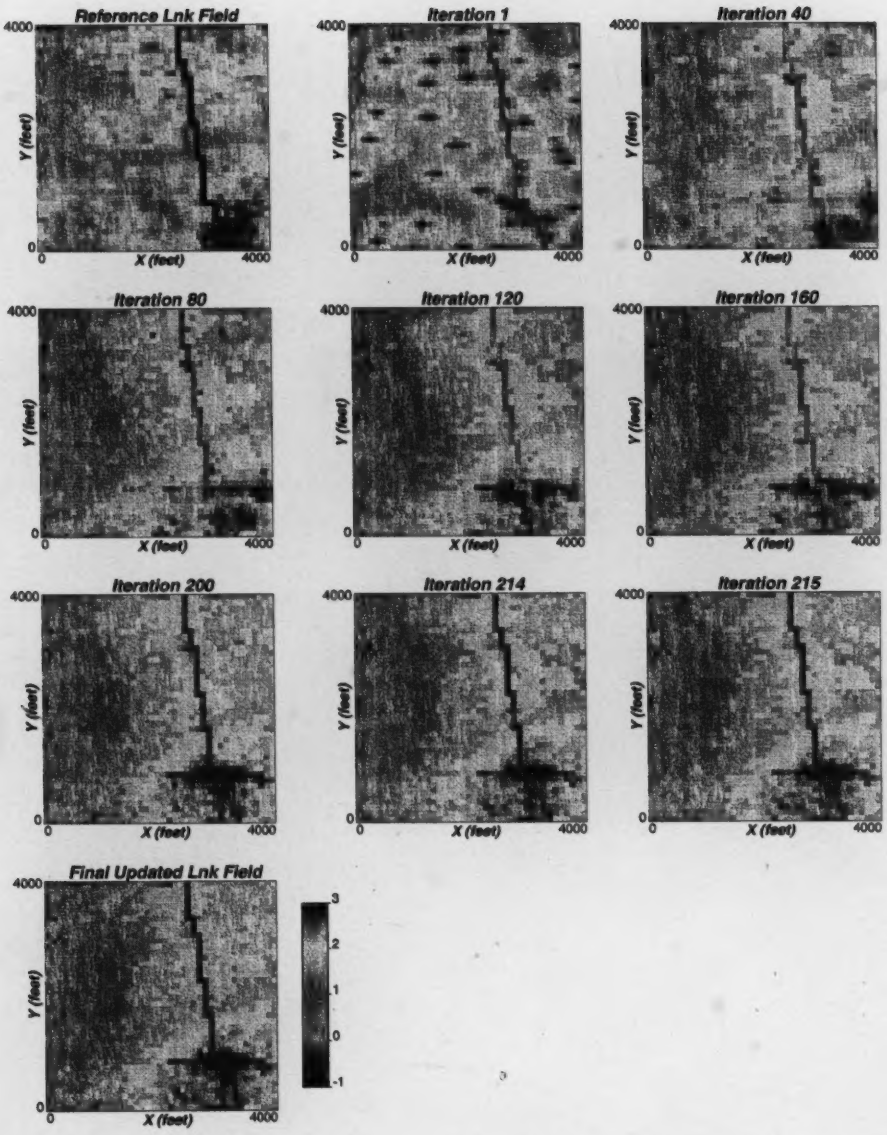


Figure 7.21: Updated $\ln(k)$ fields at some iterations of the inversion process: Sealing Fault Example (Case B).

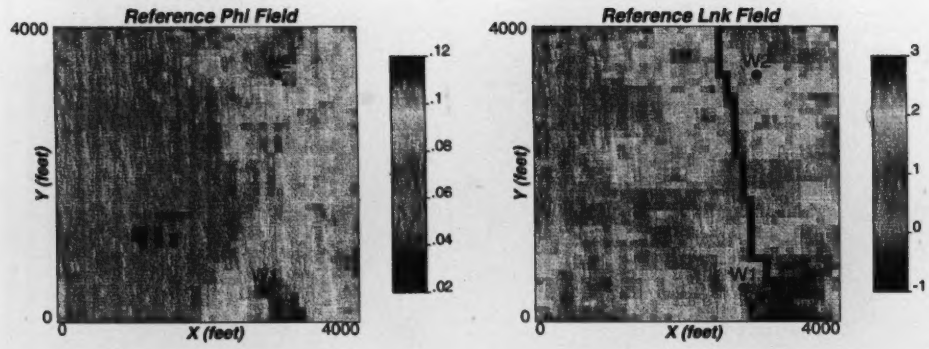


Figure 7.22: Reference faulted $\phi$ and $\ln(k)$ fields: High Permeability Fault Example (Case A).

## 7.3 High Permeability Fault Example

In this section, we discuss the inversion of the properties of a high permeability fault. Similar two-well cases are analyzed in this exercise. All the information are kept unchanged as in the previous section unless stated otherwise.

### Case A: 2 Wells on the Opposite Side of the Fault

The reference porosity and permeability fields are shown in Figure 7.22. Figure 7.23 shows the imposed production rates and the corresponding numerically simulated pressure responses at the two wells. The histogram and the scatter-plot between $\phi$ and $\ln(k)$ are shown in Figures 7.24 and 7.25, respectively. Mean and standard deviation of reference distributions are 0.073 and 0.018 for $\phi$, and 1.661 and 1.131 for $\ln(k)$. The low average porosity confirms the low storativity of the reservoir. The correlation coefficient between porosity and permeability is 0.462. The fault location is the same as in the previous section. The reference fault zone porosity and $\ln(k)$ are 0.1 and 7.0.

The inverted models are obtained after 95 outer iterations (23.2 minutes in a 1.8 GHz processor personal computer). The pressure responses in the updated porosity and permeability fields converge to the reference pressure data. These inverted models are shown in Figure 7.26. Figure 7.27 shows the pressure values at the ten wells computed from the true (from reference), initial and final updated porosity and permeability fields. Final pressure match is remarkable. Final average pressure mismatch (in $L^2$ norm sense) was only 5.55 psi. The objective function values of the inversion process are shown in Figure 7.28. The fault zone properties at all outer iterations are shown in Figures 7.29 and 7.30 for porosity and permeability values. Updated porosity and permeability fields at some outer iterations of the inversion method are shown in Figures 7.31 and 7.32.

### Case B: 2 Wells in the Same Side of the Fault

The wells are shown in Figure 7.33. Figure 7.34 shows the imposed production rates and the corresponding numerically simulated pressure responses at the two wells. The inverted models are obtained after 100 outer iterations (25.2 minutes in a 1.8 GHz processor personal computer). The pressure responses in the updated porosity and permeability fields converge

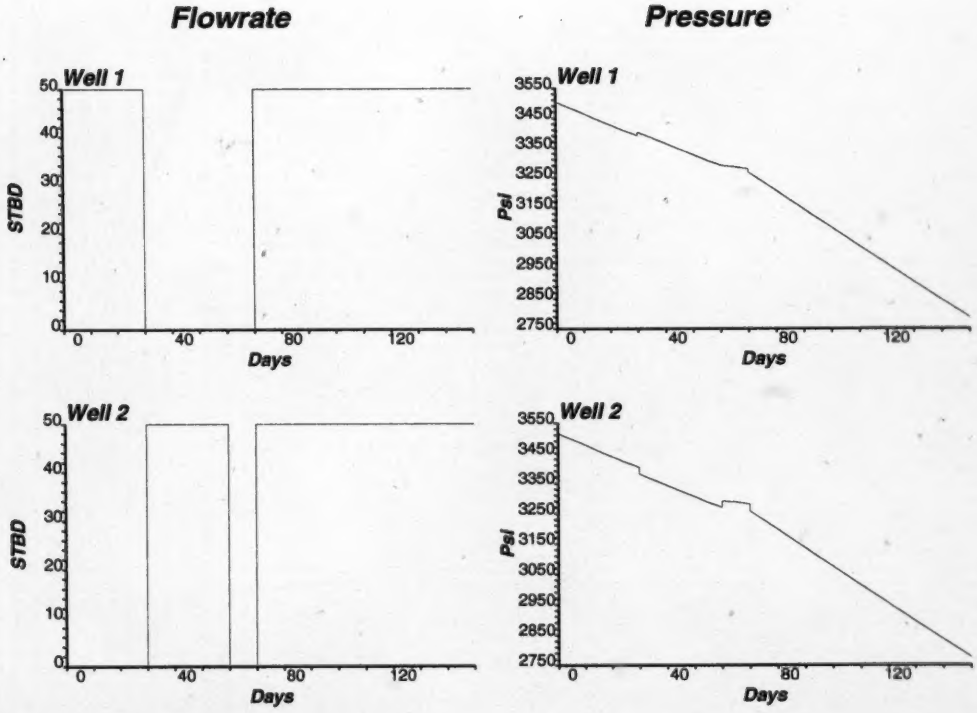


Figure 7.23: Production data (pressure and flow rates) obtained for 2 wells from the reference field: High Permeability Fault Example (Case A).

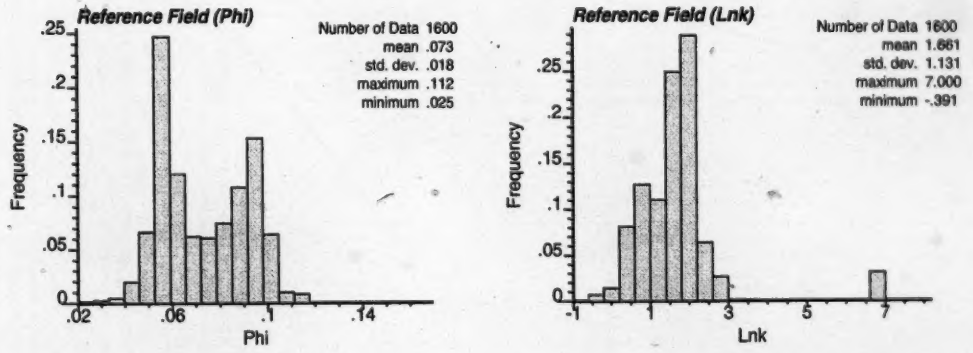


Figure 7.24: Histograms of reference $\phi$ and $\ln(k)$ fields: High Permeability Fault Example (Case A).

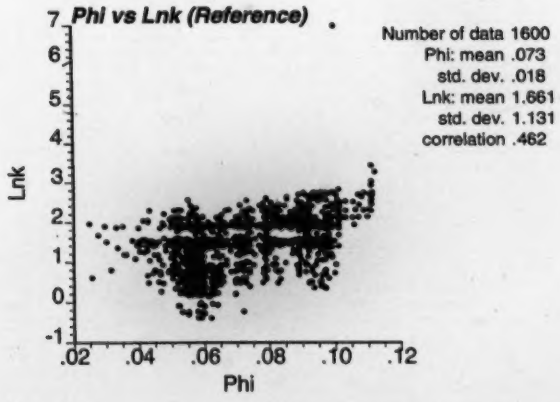


Figure 7.25: Scatterplot of reference $\phi$ and $\ln(k)$ distributions: High Permeability Fault Example (Case A).

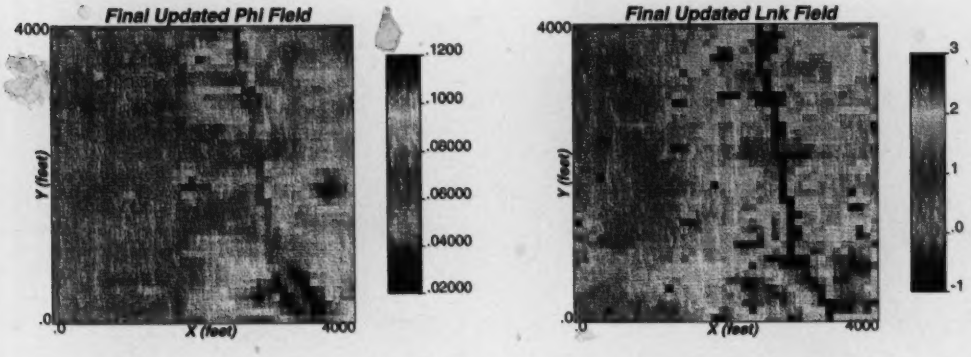


Figure 7.26: Updated $\phi$ and $\ln(k)$ fields: High Permeability Fault Example (Case A).

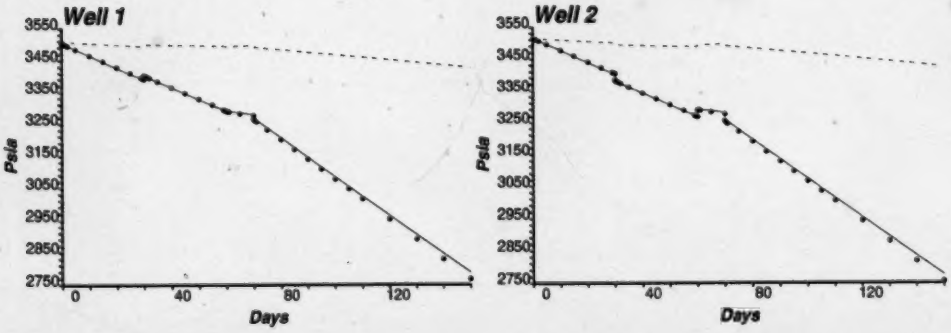


Figure 7.27: Pressure responses computed from initial (dashed lines) and updated (bullets) $\phi$ and $\ln(k)$ fields with the true data (solid lines): High Permeability Fault Example (Case A).

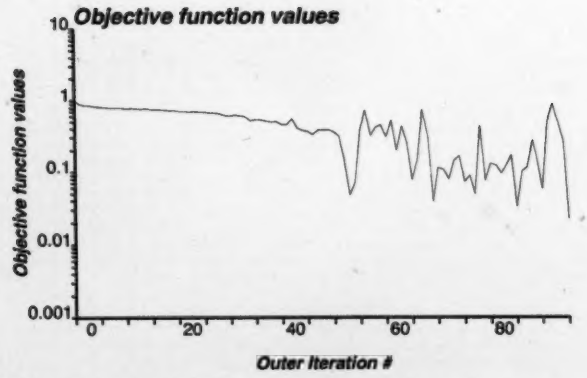


Figure 7.28: Objective function values of the inversion process: High Permeability Fault Example (Case A).

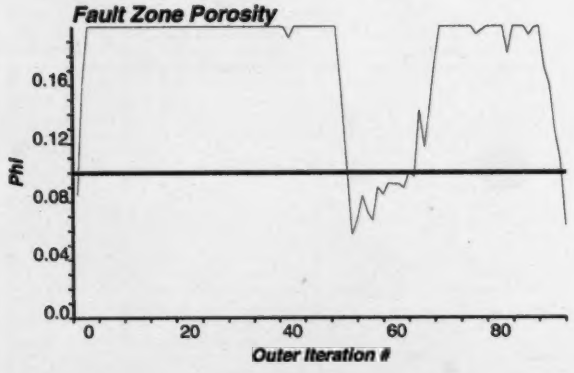


Figure 7.29: Fault zone $\phi$ values at each outer iteration: High Permeability Fault Example (Case A). (Reference value: thicker horizontal line)

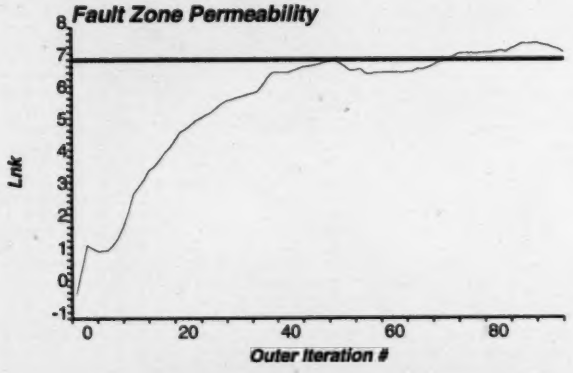


Figure 7.30: Fault zone $\ln(k)$ values at each outer iteration: High Permeability Fault Example (Case A). (Reference value: thicker horizontal line)

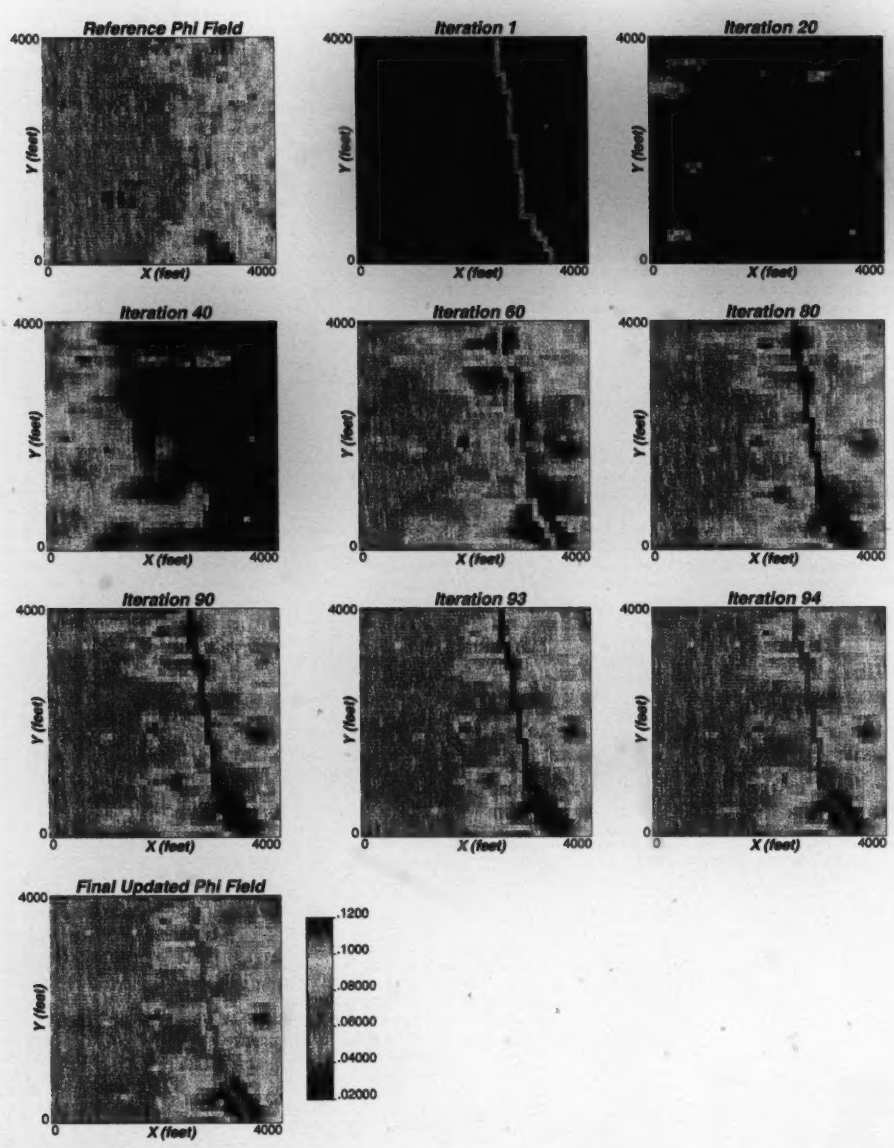


Figure 7.31: Updated $\phi$ fields at some iterations of the inversion process: High Permeability Fault Example (Case A).

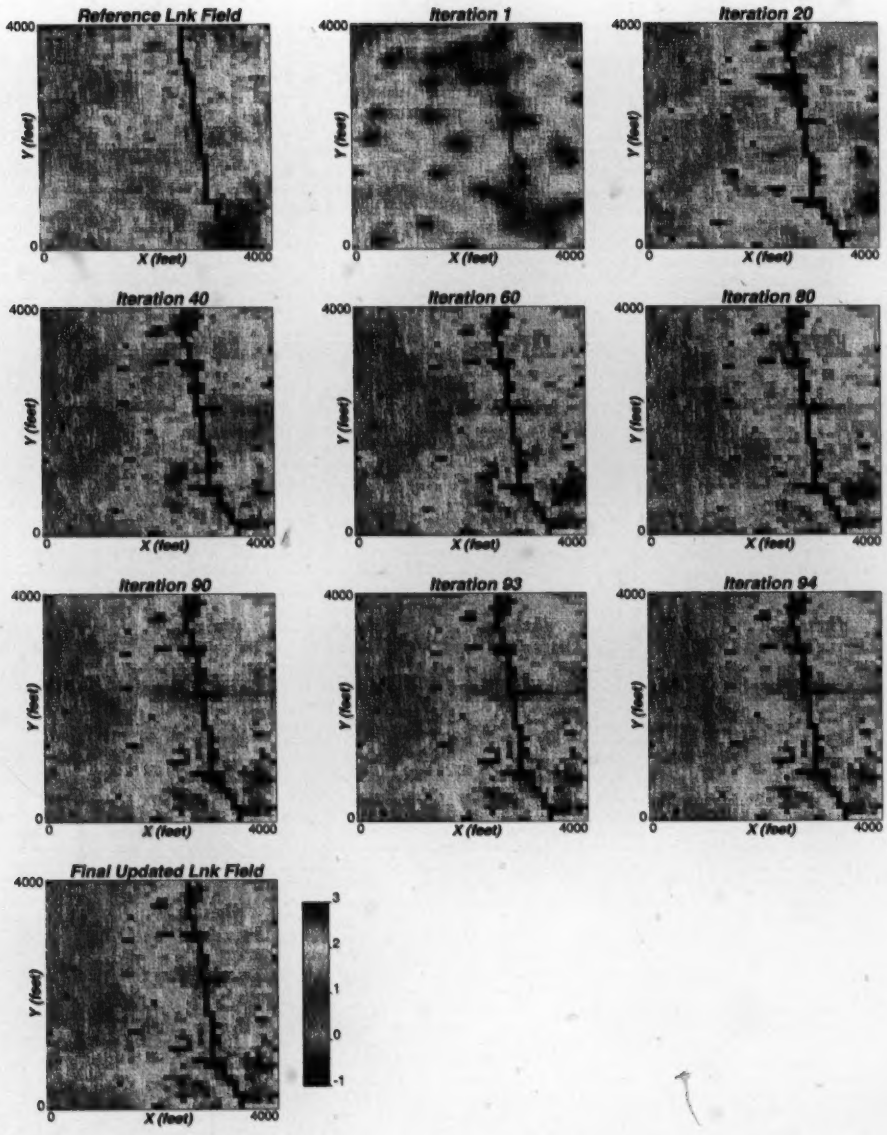


Figure 7.32: Updated $\ln(k)$ fields at some iterations of the inversion process: High Permeability Fault Example (Case A).

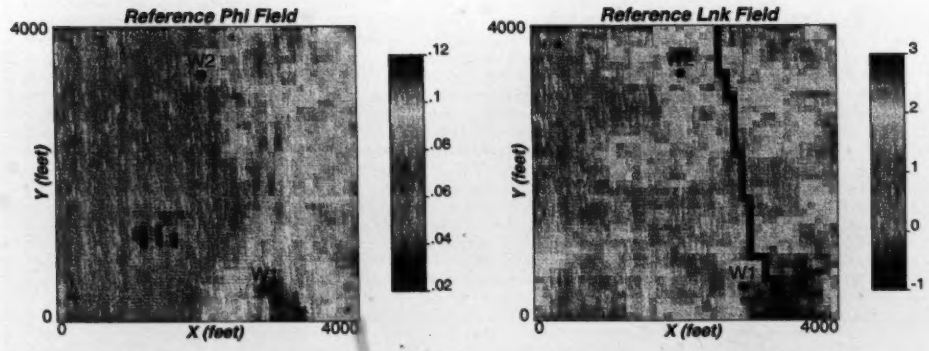


Figure 7.33: Reference faulted $\phi$ and $\ln(k)$ fields: High Permeability Fault Example (Case B).

to the reference pressure data. These inverted models, shown in Figure 7.35, have a similar heterogeneity distribution to the reference truth. Figure 7.36 shows the pressure values at the two wells computed from the true (from reference), initial and final updated porosity and permeability fields. The objective function values of the inversion process is shown in Figure 7.37. Final average pressure mismatch (in $L^2$ norm sense) was 3.002 psi. The fault zone properties at all outer iterations are shown in Figures 7.38 and 7.39 for porosity and permeability values. Updated porosity and permeability fields after each outer iteration of the inversion method are shown in Figures 7.40 and 7.41.

### Some Conclusions

For the high permeability fault, the inversion outcomes with both the cases changing the well locations show that reservoir heterogeneity is not captured well as in the situation with sealing faults. However, the objective values do converge faster in this case. Analyzing the objective function values (Figures 7.28 and 7.37), it is evident that jump in the values are drastic in this case. The reason for such jumps may be attributed to the erratic nature of the fault porosity values. There is clearly no convergence in the fault porosity values (Figures 7.29 and 7.38).

The other observation is that both the well location cases show similar nature of inverted outcomes. It is intuitively expected because with high permeability fault the well locations will not matter much. The wells will almost be in instantaneous communication with each other.

## 7.4 Sensitivity Studies

Sensitivity of the inversion solution to certain parameters in the inversion process was investigated. The sensitivity to prior fault zone $\ln(k)$ values and the number of fault zone master points are discussed below. Some general inversion related sensitivity studies were performed in Chapters 4 and 5.

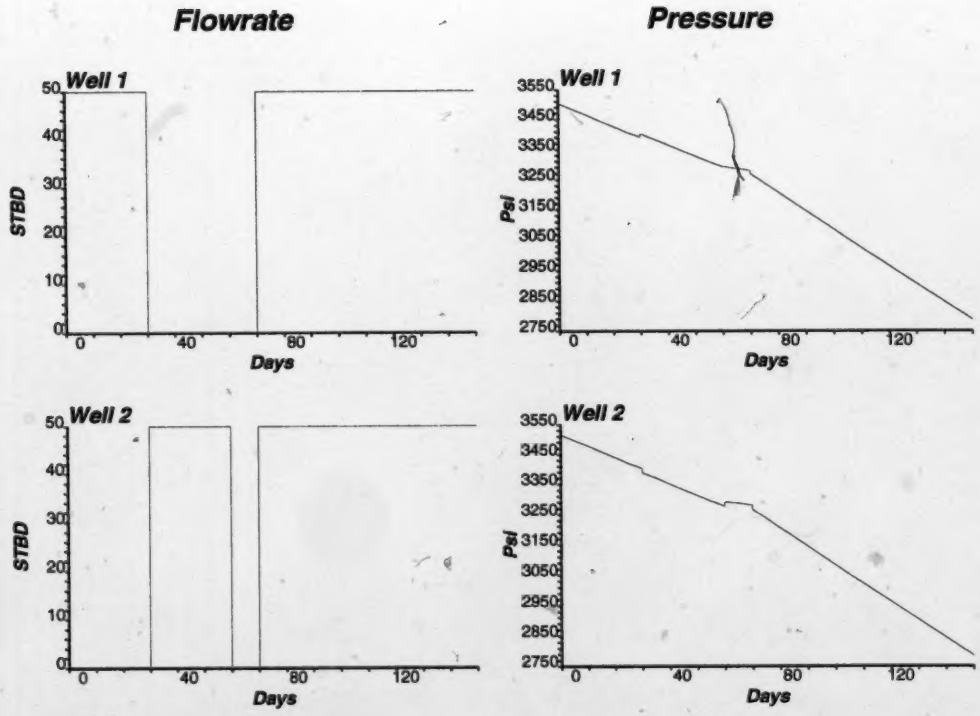


Figure 7.34: Production data (pressure and flow rates) obtained for 2 wells from the reference field: High Permeability Fault Example (Case B).

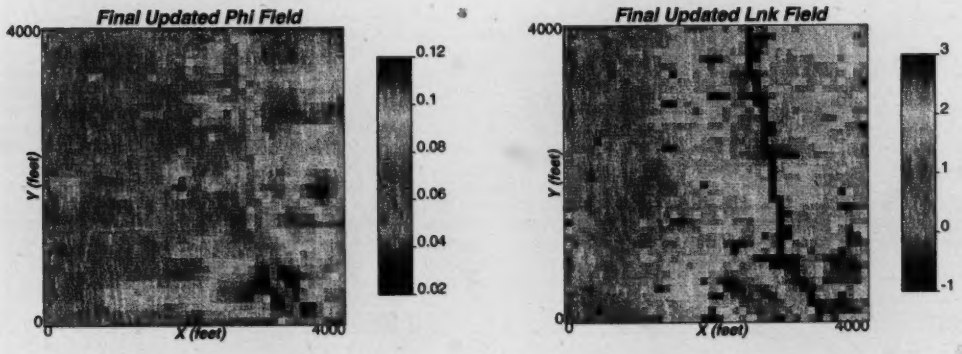


Figure 7.35: Updated $\phi$ and $\ln(k)$ fields: High Permeability Fault Example (Case B).

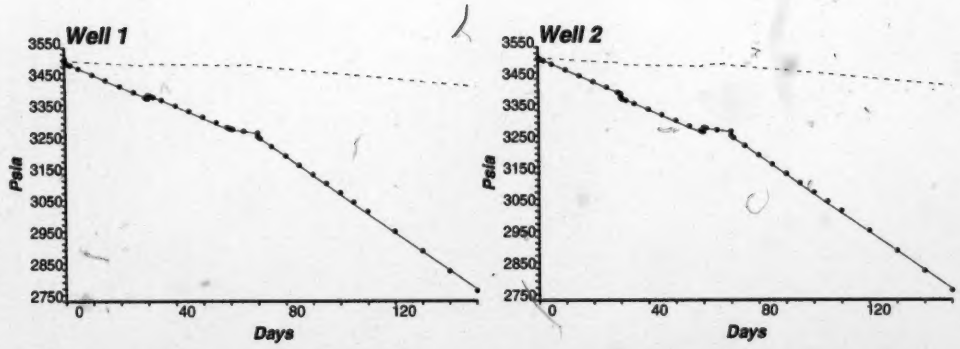


Figure 7.36: Pressure responses computed from initial (dashed lines) and updated (bullets) $\phi$ and $\ln(k)$ fields with the true data (solid lines): High Permeability Fault Example (Case B).

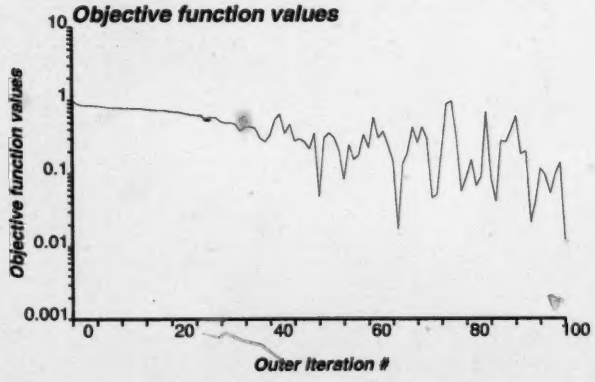


Figure 7.37: Objective function values of the inversion process: High Permeability Fault Example (Case B).

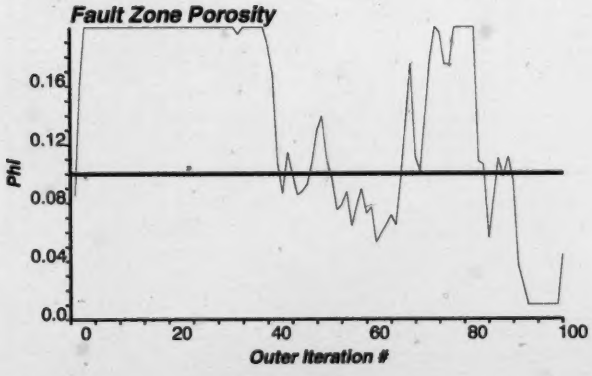


Figure 7.38: Fault zone $\phi$ values for each outer iteration: High Permeability Fault Example (Case B). (Reference value: thicker horizontal line)

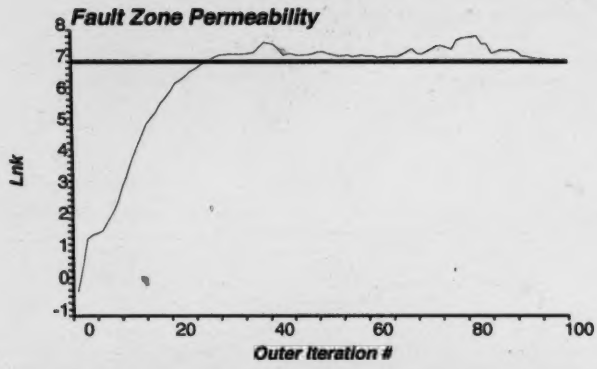


Figure 7.39: Fault zone $\ln(k)$ values for each outer iteration: High Permeability Fault Example (Case B). (Reference value: thicker horizontal line)

### Sensitivity to Prior Information

For the inversion of the fault properties, the code requires inputs of a priori fault zone $\ln(k)$ and $\phi$, which may affect on the inversion solution. For the base case, we have the result of sealing fault example Case A (that is, the wells are in the opposite side of the fault). For the base case, we used a priori fault zone $\ln(k)$ of -1.0 and $\phi$ of 0.01. In this sensitivity study, we employed in one run $\ln(k)$ value of 1.0 and $\phi$ of 0.01, while in another run these values were 1.0 and 0.1. Figures 7.42 and 7.43 show the updated porosity and permeability fields. These figures should be compared with Figure 7.6. Inverted fault zone $\ln(k)$ and $\phi$ values at each outer iteration of the inversion process are shown in Figures 7.45 and 7.46 for the three cases. The number of outer iterations for the convergence were 166, 124 and 70 for the three cases. Objective function values at each outer iteration are shown in Figure 7.44 for the cases. Corresponding final objective function $L^2$ norm values are 2.573, 2.843 and 2.527, respectively. It should be mentioned that the fault zone $\ln(k)$ and $\phi$ in the reference field are -5.0 and 0.03. Analyzing Figures 7.45 and 7.46 and the final objective function values that the inversion outcomes are more or less robust to prior information.

### Sensitivity to Number of Fault Zone Master Points

We performed a sensitivity study to number of fault zone master points. Most of the results shown in this work are done with 8 master points for the fault zone. We analyze the inversion solution with 6, 8 and 10 fault zone master points. For this sensitivity exercise, we again use the sealing fault exercise Case A (where we used 8 master points) as the base case.

Figures 7.47 and 7.48 show the updated porosity and permeability fields for the two cases with 6 and 10 master points. Inverted fault zone $\ln(k)$ values at each outer iteration of the inversion process are shown in Figure 7.50 for the three cases. Corresponding inverted fault zone $\phi$ values are shown in Figure 7.51. It is evident from this figure that fault zone porosity inversion is not very robust. The number of outer iterations for the convergence were 102, 128 and 70 for the three cases. Objective function values at each outer iteration are shown in Figure 7.49 for the cases. Corresponding final objective function $L^2$ norm values are 2.598, 2.087 and 2.527, respectively. It should be mentioned that the fault zone

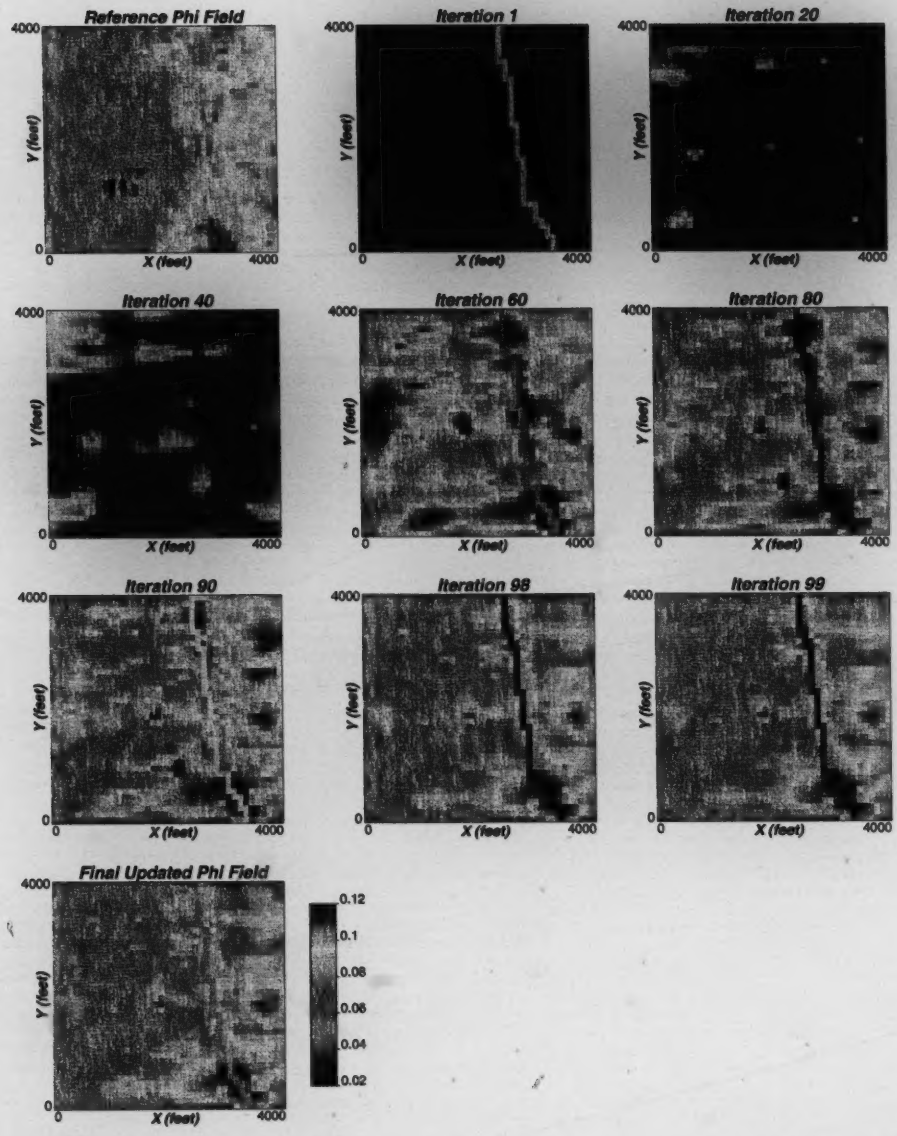


Figure 7.40: Updated $\phi$ fields at some iterations of the inversion process: High Permeability Fault Example (Case B).

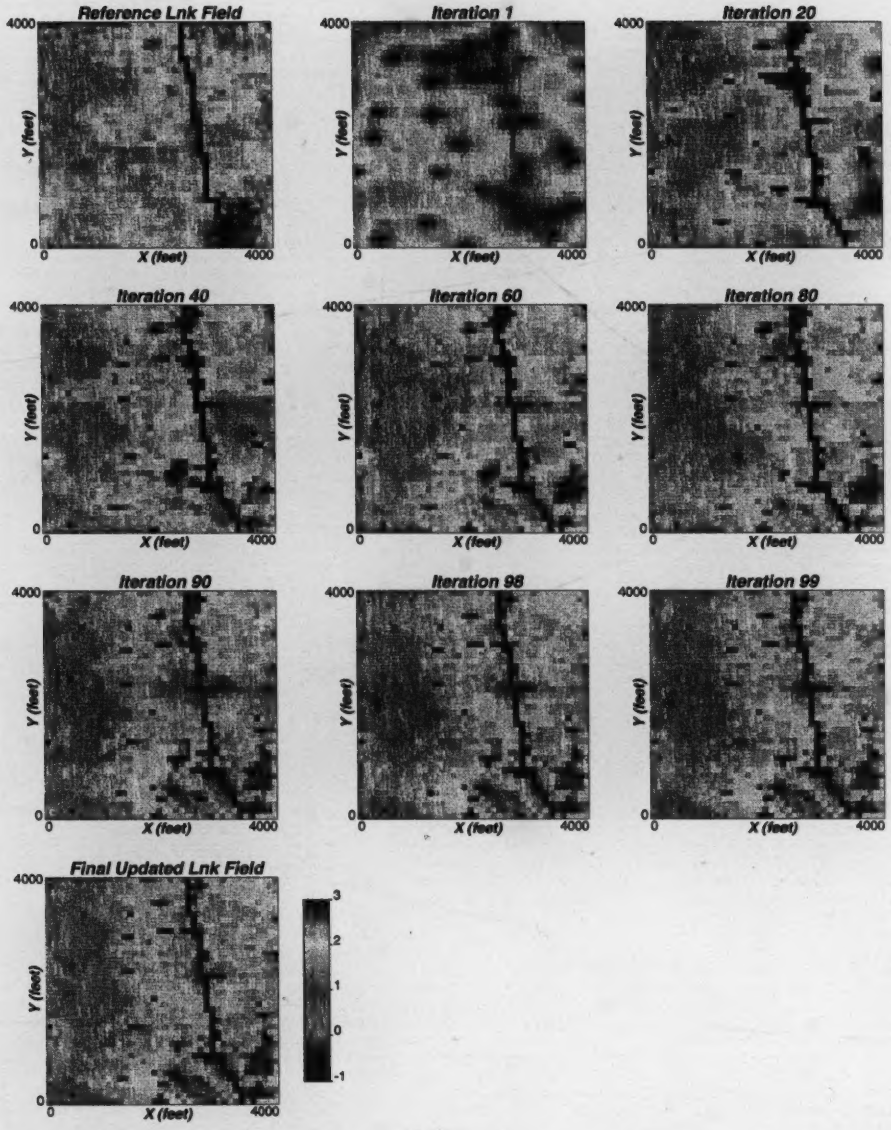


Figure 7.41: Updated $\ln(k)$ fields at some iterations of the inversion process: High Permeability Fault Example (Case B).

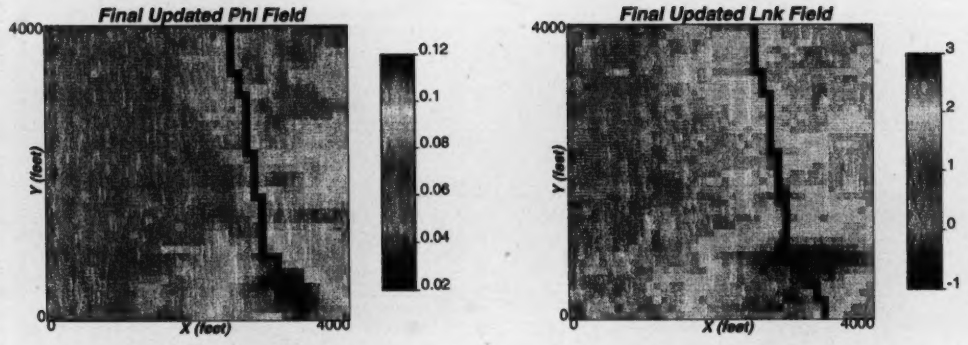


Figure 7.42: Updated $\phi$ and $\ln(k)$ fields: A Priori Fault Zone $\ln(k)$ of 1.0 and $\phi$ of 0.01.

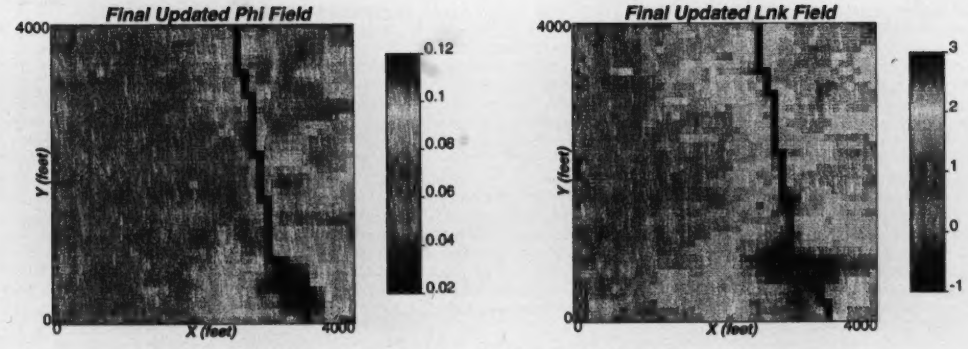


Figure 7.43: Updated $\phi$ and $\ln(k)$ fields: A Priori Fault Zone $\ln(k)$ of 1.0 and $\phi$ of 0.1.

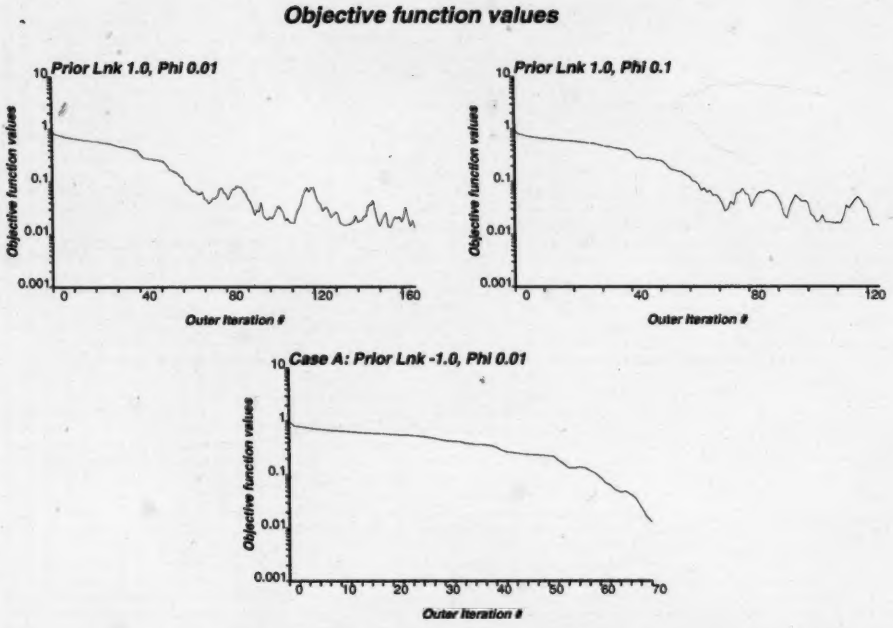
Objective function values
Prior Lnk 1.0, Phi 0.01
Prior Lnk 1.0, Phi 0.1
Case A: Prior Lnk -1.0, Phi 0.01
Objective function values
Outer Iteration #

Figure 7.44: Objective function values at each outer iteration for different a priori values.

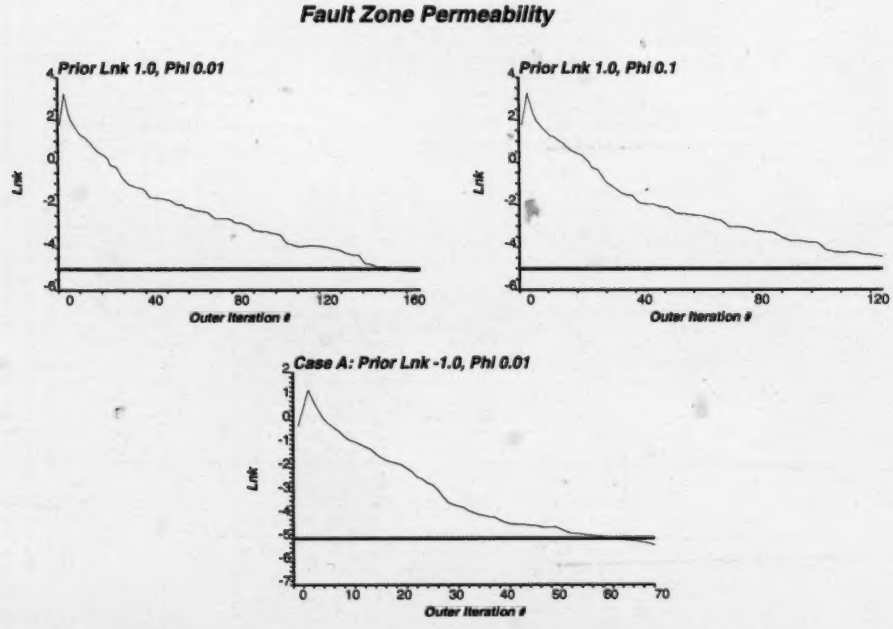


Figure 7.45: Fault zone $\ln(k)$ values at each outer iteration for different a priori values. (Reference value: thicker horizontal line)

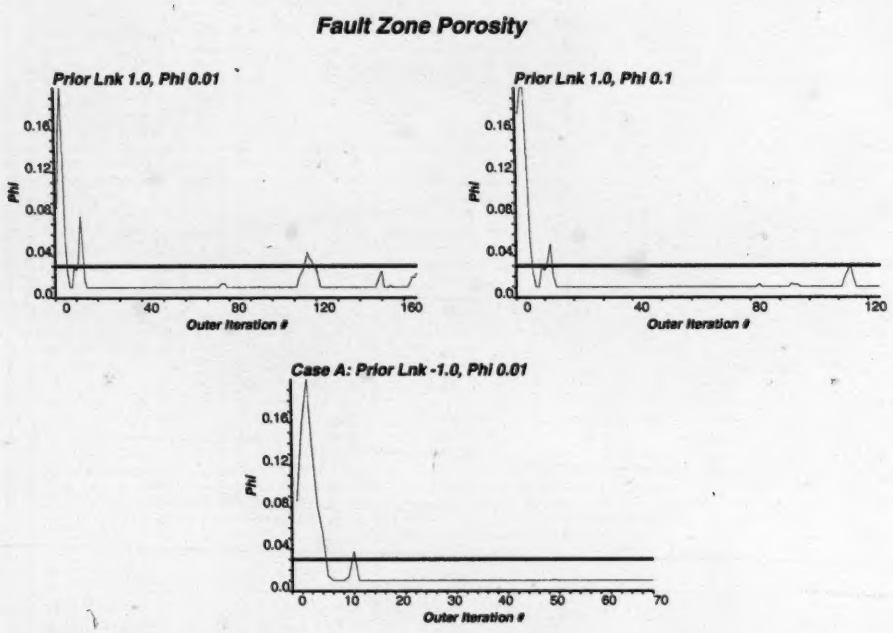


Figure 7.46: Fault zone $\phi$ values at each outer iteration for different a priori values. (Reference value: thicker horizontal line)

$\ln(k)$ and $\phi$ in the reference field are -5.0 and 0.03. Analyzing Figures 7.50 and 7.51 and the final objective function values that the inversion outcomes are more or less robust to number of master points.

## 7.5 Effect of Production Data

In this section, we investigate how production data affects the inversion of fault properties. We perform the inversion with production data from 3 and 4 wells. We employ similar parameters as in the sealing fault (Case A) exercise apart from the production data. The well locations for both the cases are shown in Figure 7.52.

### 3 Well Case

The 3 wells are: W1 at the center of the cell (28, 5), W2 at (30, 34), and W3 at (20, 34). Figure 7.53 shows the imposed production rates and the corresponding numerically simulated pressure responses at these wells. The inversion was run for 293 outer iterations. CPU time for the run was only 80.1 minutes in a 1.8 GHz Pentium 4 machine. The pressure responses in the updated porosity and permeability fields converge to the reference pressure data. These inverted models are shown in Figure 7.54. Figure 7.55 shows the pressure values at the three wells computed from the true (from reference), initial and final updated porosity and permeability fields. The objective function values of the inversion process is shown in Figure 7.56. Final average pressure mismatch in $L^2$ norm sense was 2.054 psi. The fault zone properties at all outer iterations are shown in Figures 7.57 and 7.58 for porosity

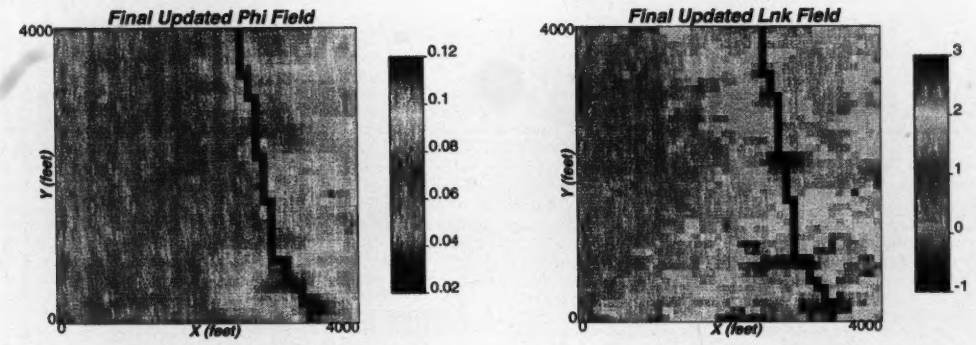


Figure 7.47: Updated $\phi$ and $\ln(k)$ fields honoring production data, local hard data, global distribution, prior variography information and prior fault zone $\ln(k)$ of -1.0 with 6 Master Point Case.

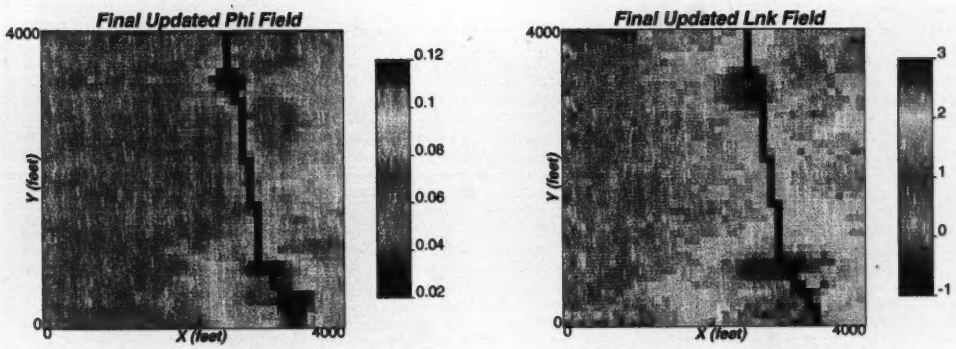


Figure 7.48: Updated $\phi$ and $\ln(k)$ fields: 10 Master Point Case.

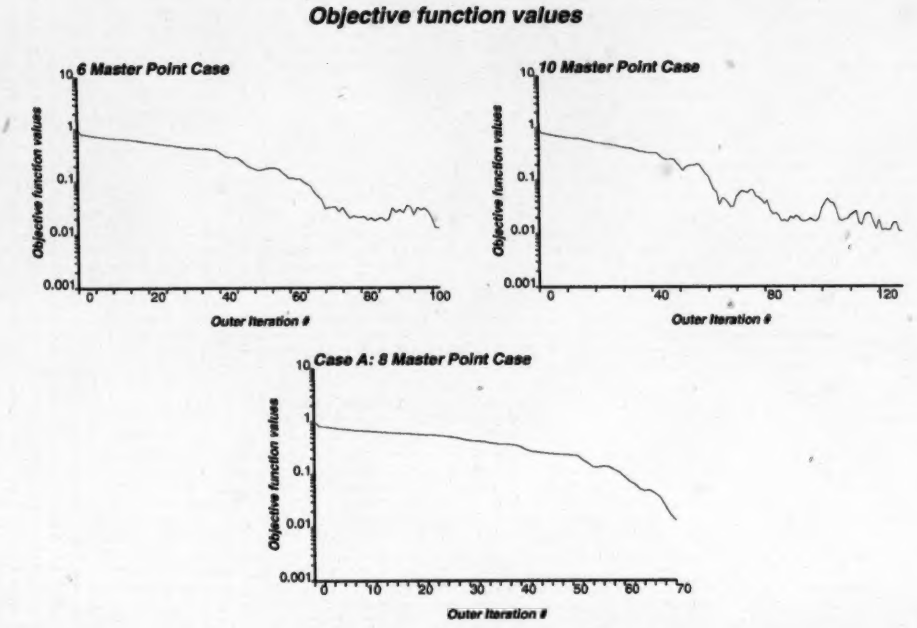


Figure 7.49: Objective function values at each outer iteration for varying number of master points.

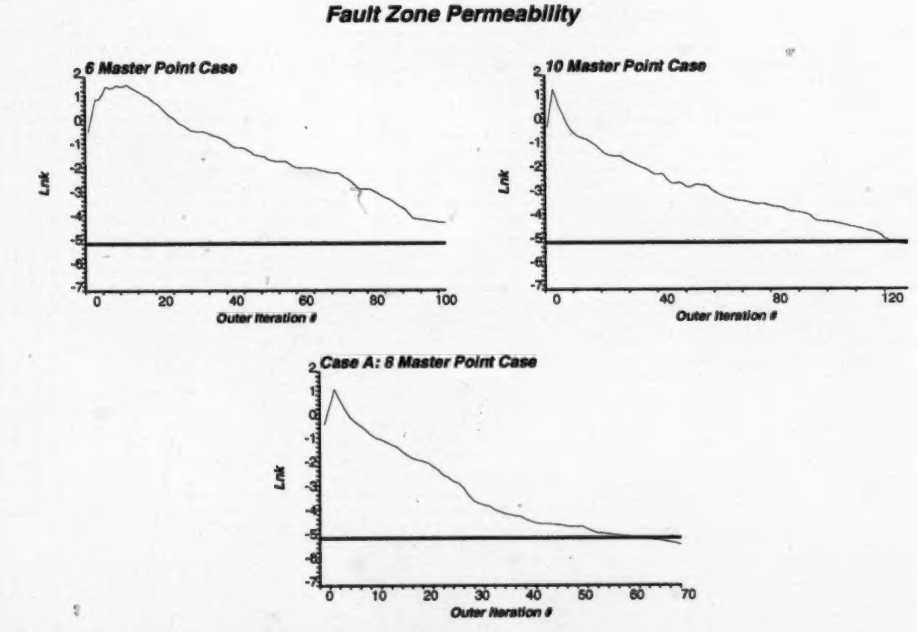


Figure 7.50: Fault zone $\ln(k)$ values at each outer iteration for varying number of master points. (Reference value: thicker horizontal line)

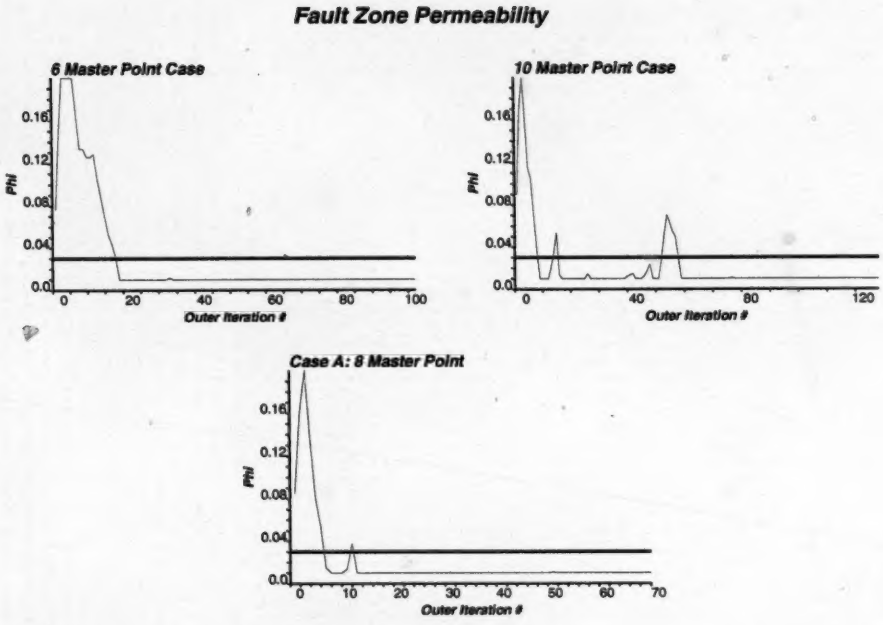


Figure 7.51: Fault zone $\phi$ values at each outer iteration for varying number of master points. (Reference value: thicker horizontal line)

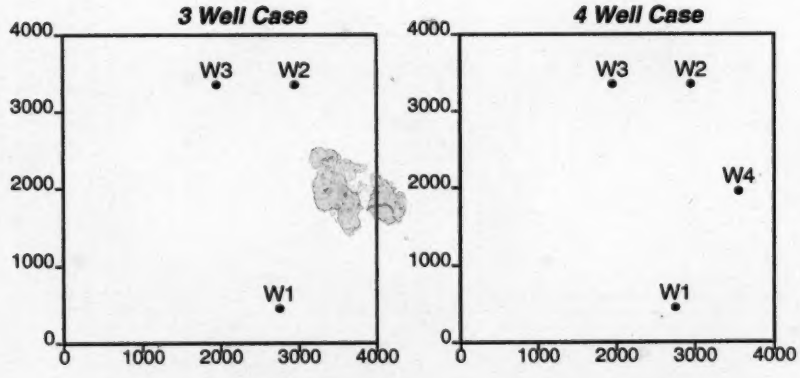


Figure 7.52: Well locations for 3 and 4 well cases.

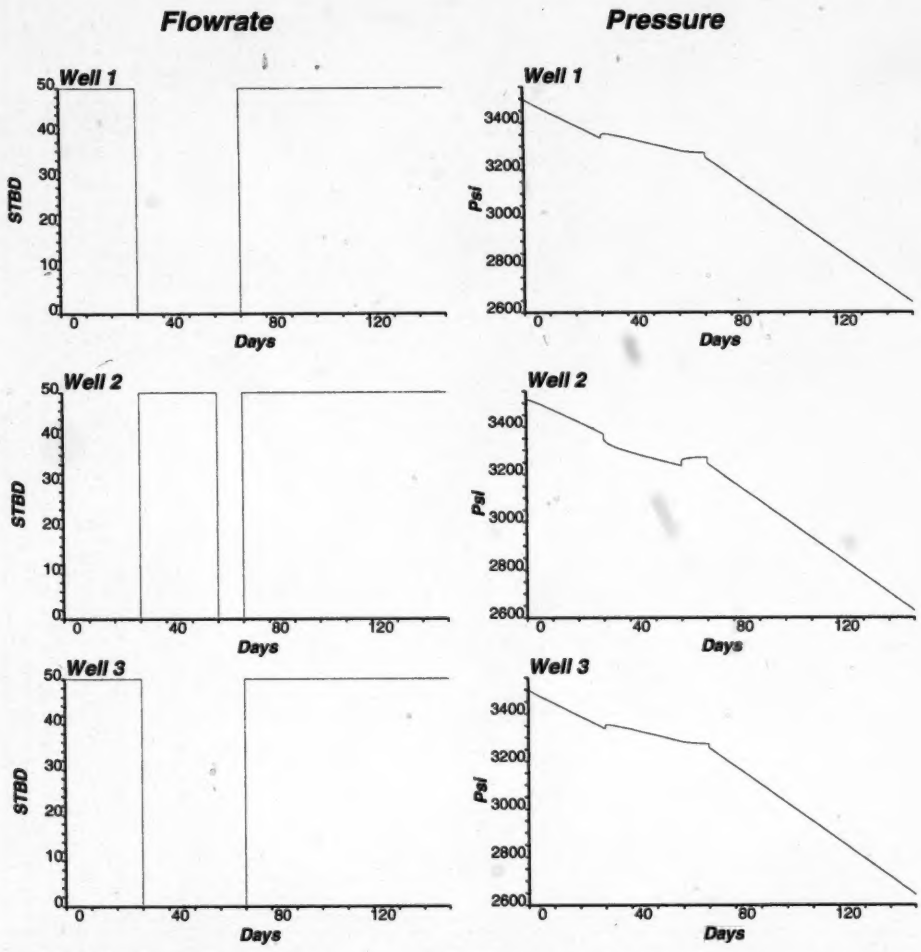


Figure 7.53: Production data (pressure and flow rates) obtained from the reference field: 3 Well Case.

and permeability values. Updated porosity and permeability fields at some outer iterations of the inversion method are shown in Figures 7.59 and 7.60.

## 4 Well Case

The 4 wells are: W1 at the center of the cell (28, 5), W2 at (30, 34), W3 at (20, 34), and W4 at (36, 20). Figure 7.61 shows the imposed production rates and the corresponding numerically simulated pressure responses at these wells. The inversion was run for 226 outer iterations. CPU time for the run was only 62.5 minutes in a 1.8 GHz Pentium 4 machine. The pressure responses in the updated porosity and permeability fields converge to the reference pressure data. These inverted models are shown in Figure 7.62. Figure 7.63 shows the pressure values at the four wells computed from the true (from reference), initial and final updated porosity and permeability fields. The objective function values of the inversion process is shown in Figure 7.64. Final average pressure mismatch in $L^2$ norm

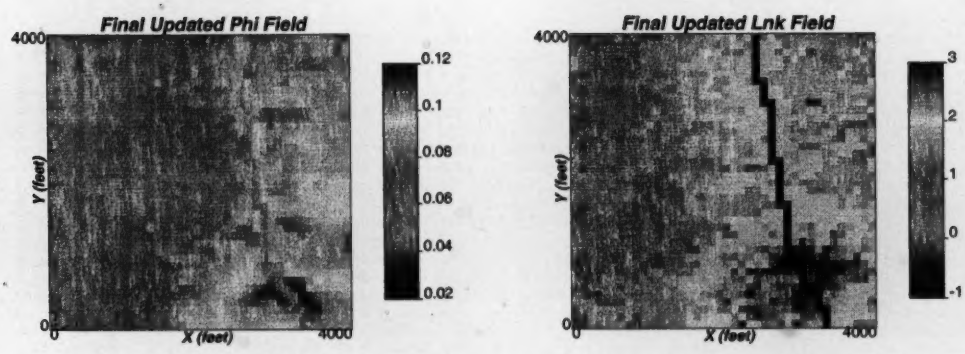


Figure 7.54: Updated $\phi$ and $\ln(k)$ fields: 3 Well Case.

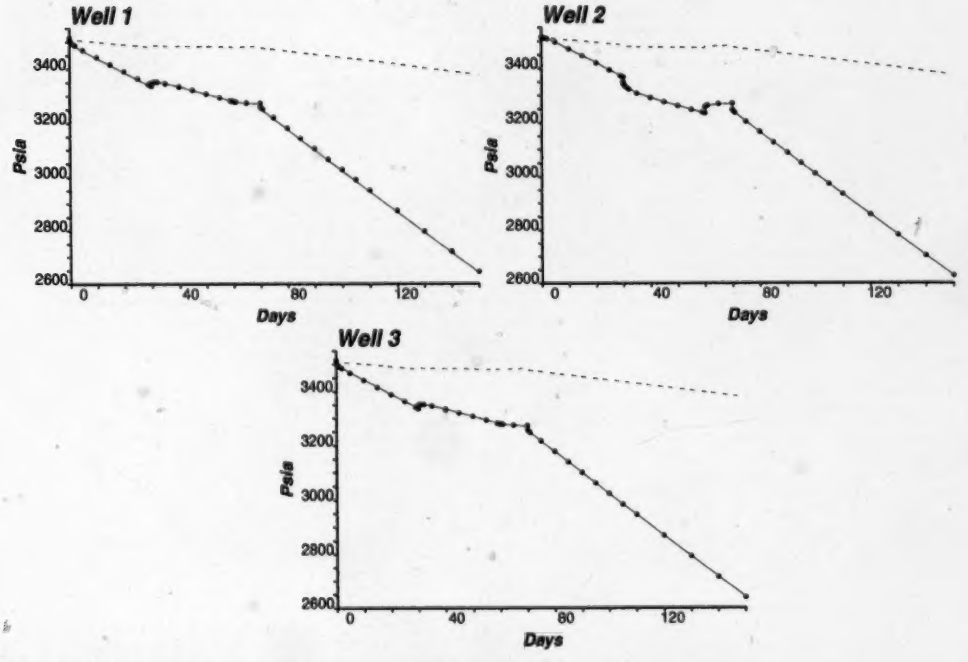


Figure 7.55: Pressure responses computed from initial (dashed lines) and updated (bullets) $\phi$ and $\ln(k)$ fields with the true data (solid lines): 3 Well Case.

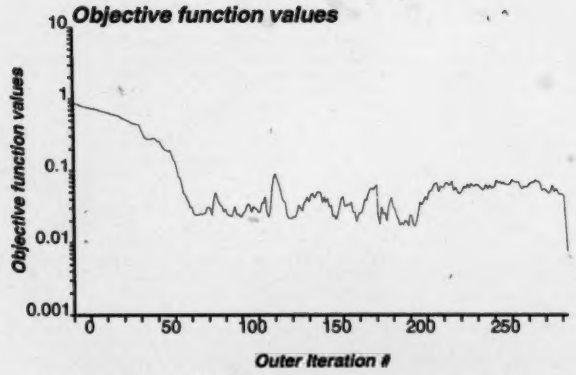


Figure 7.56: Objective function values of the inversion process: 3 Well Case.

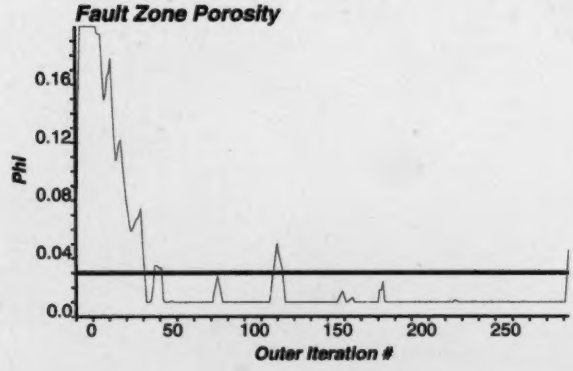


Figure 7.57: Fault zone $\phi$ values for each outer iteration: 3 Well Case. (Reference value: thicker horizontal line)

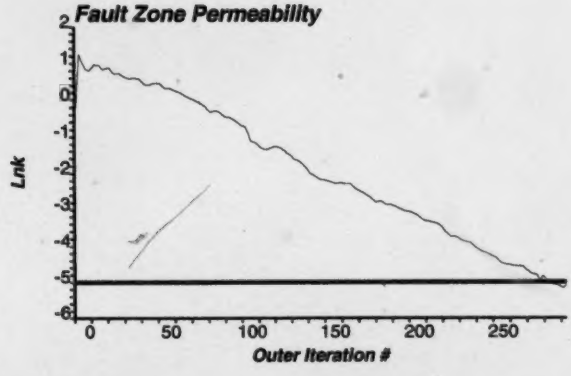


Figure 7.58: Fault zone $\ln(k)$ values for each outer iteration: 3 Well Case. (Reference value: thicker horizontal line)

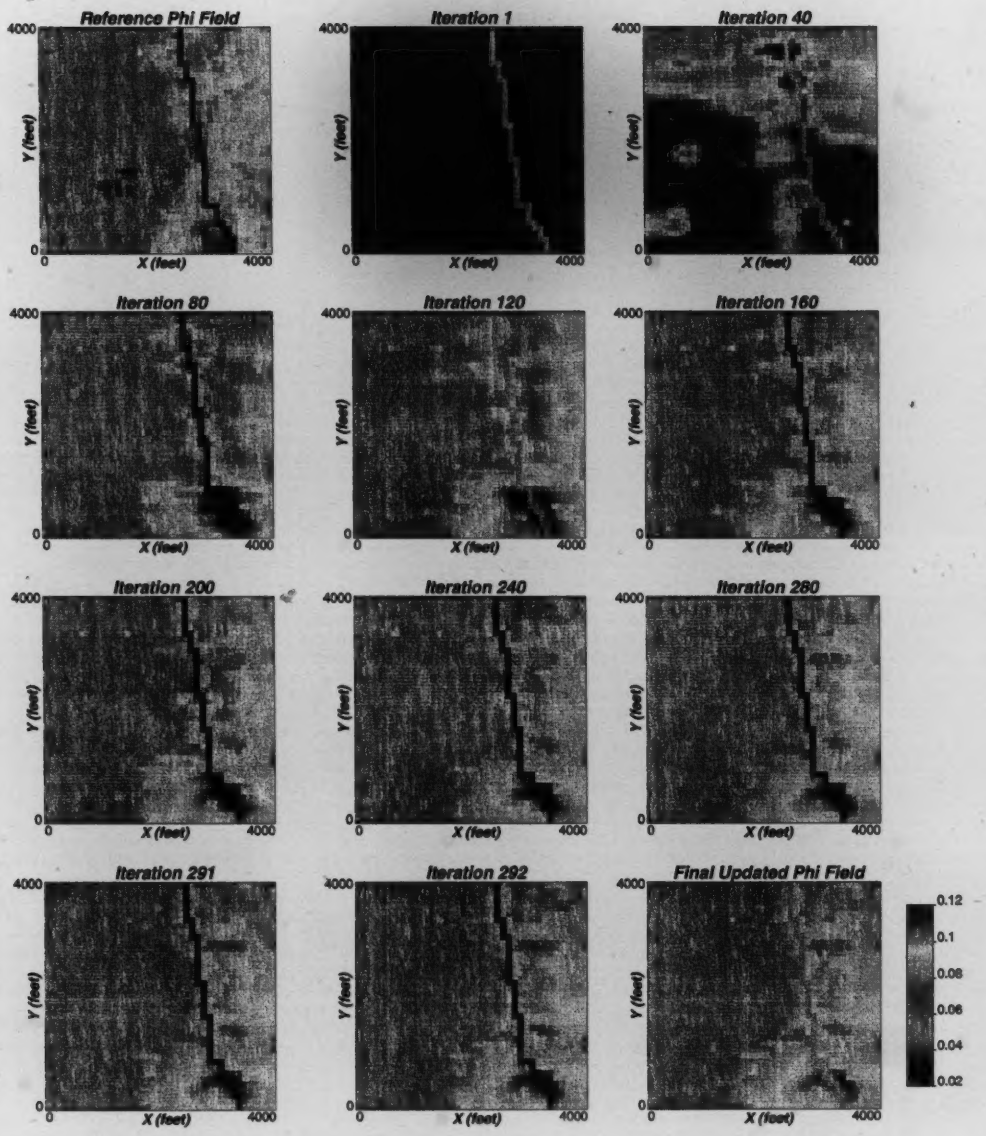


Figure 7.59: Updated $\phi$ fields at some outer iterations: 3 Well Case.

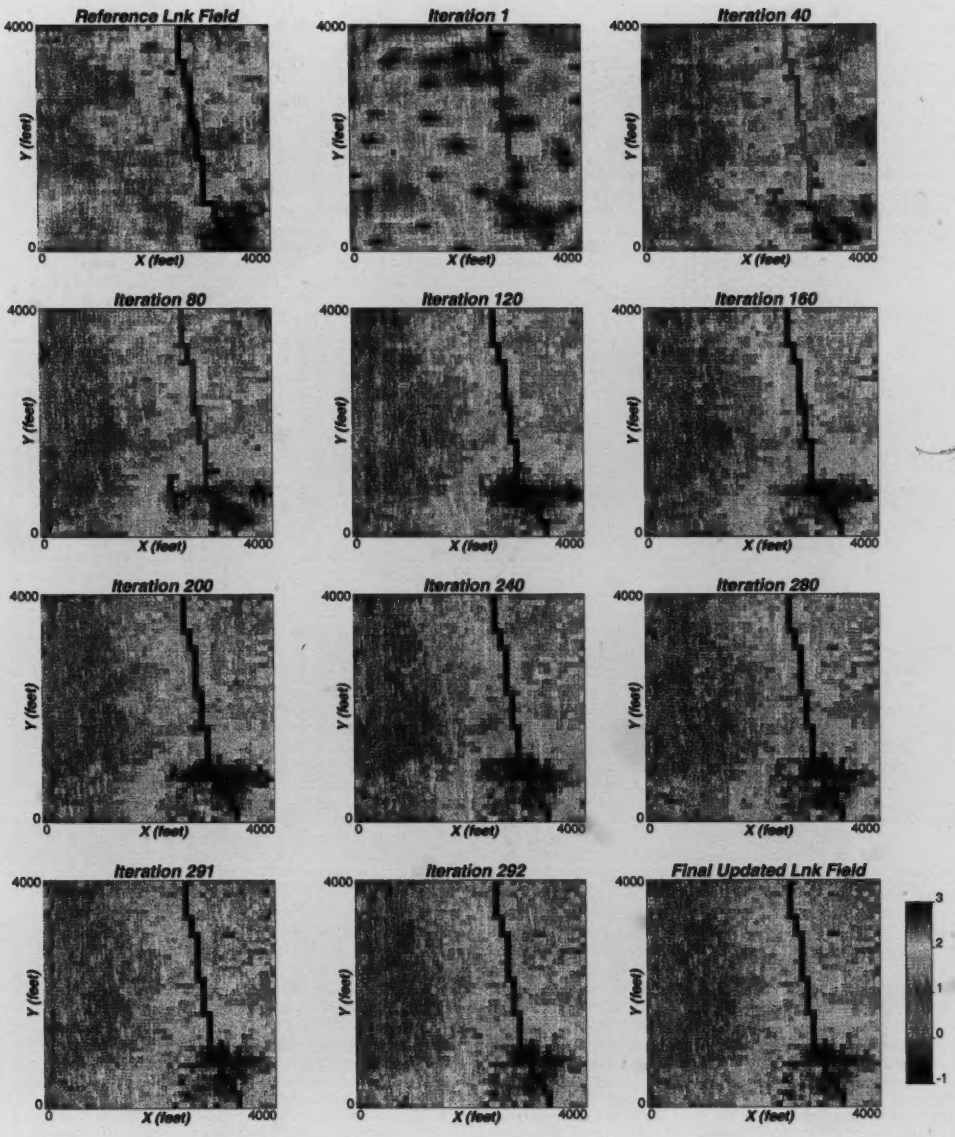


Figure 7.60: Updated $\ln(k)$ fields at some outer iterations: 3 Well Case.

sense was 3.217 psi. The fault zone properties at all outer iterations are shown in Figures 7.65 and 7.66 for porosity and permeability values. Updated porosity and permeability fields at some outer iterations of the inversion method are shown in Figures 7.67 and 7.68.

## Conclusion

In this chapter, we discussed our algorithm for fault property inversion and its capability to capture reservoir heterogeneity as well as fault properties. The inversion outcomes using different exercises discussed are remarkable. It appears that in the initial outer iterations reservoir heterogeneity is resolved. Information for fault properties are captured at the later outer iterations. This is evident from the objective function value curves for all the above exercises. Inversion of reservoir properties are better resolved for sealing fault when the production data have interference information as in Case A. Inversion outcomes are robust to number of master points or a priori fault zone information. Amount of production data may not affect the inversion results as long as the interference information is available.

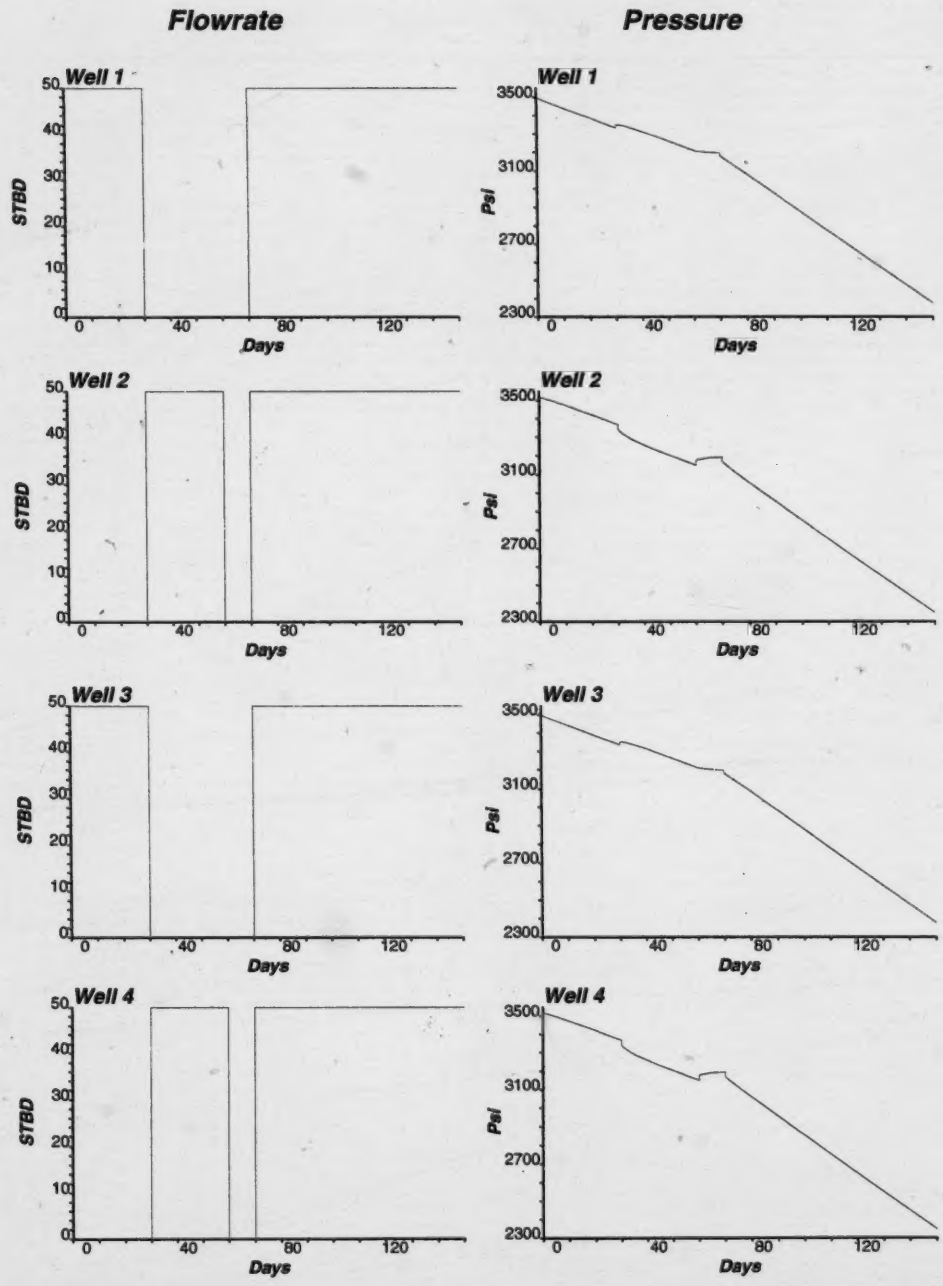


Figure 7.61: Production data (pressure and flow rates) obtained from the reference field: 4 Well Case.

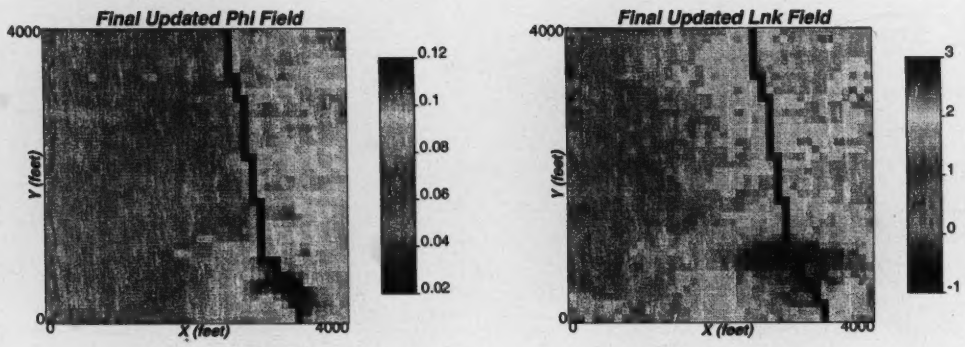


Figure 7.62: Updated $\phi$ and $\ln(k)$ fields: 4 Well Case.

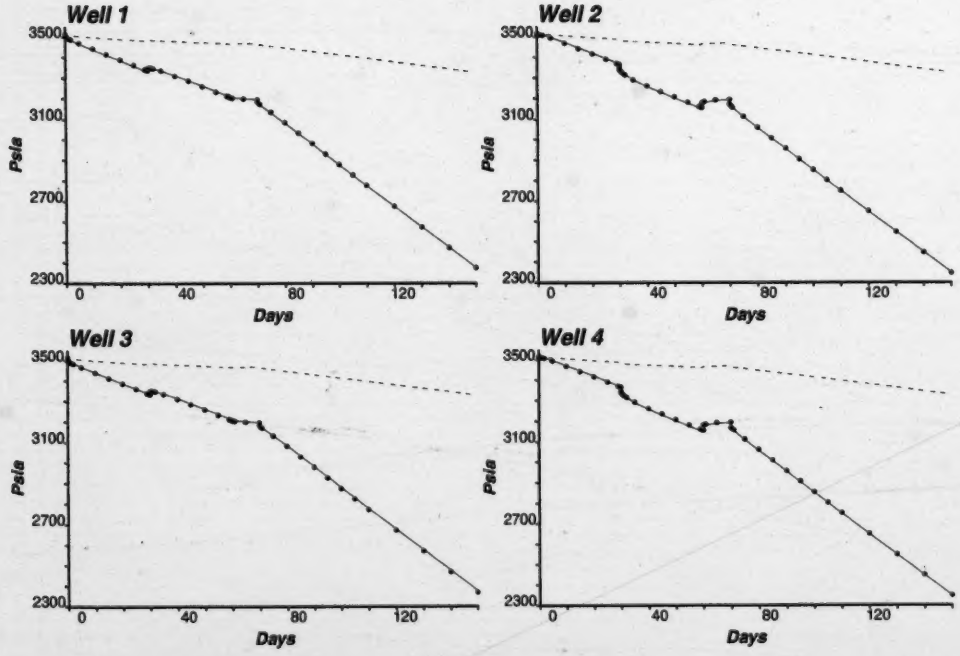


Figure 7.63: Pressure responses computed from initial (dashed lines) and updated (bullets) $\phi$ and $\ln(k)$ fields with the true data (solid lines): 4 Well Case.

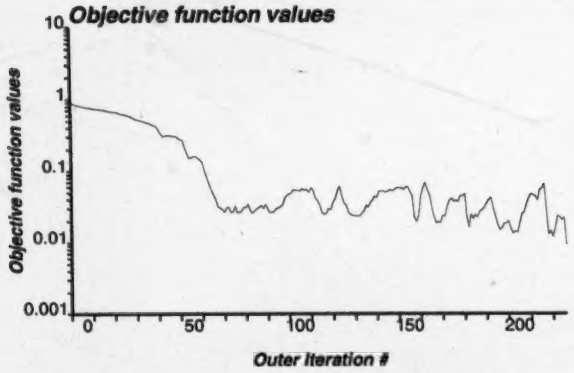


Figure 7.64: Objective function values of the inversion process: 4 Well Case.

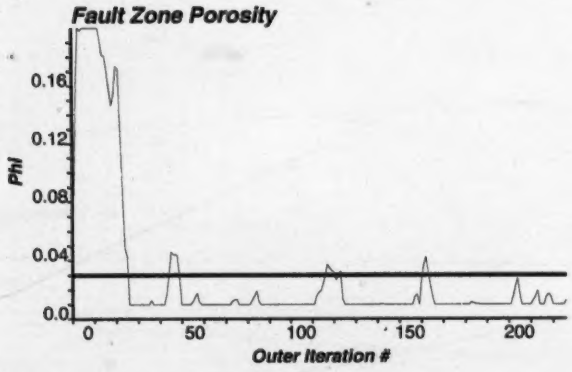


Figure 7.65: Fault zone $\phi$ values for each outer iteration: 4 Well Case. (Reference value: thicker horizontal line)

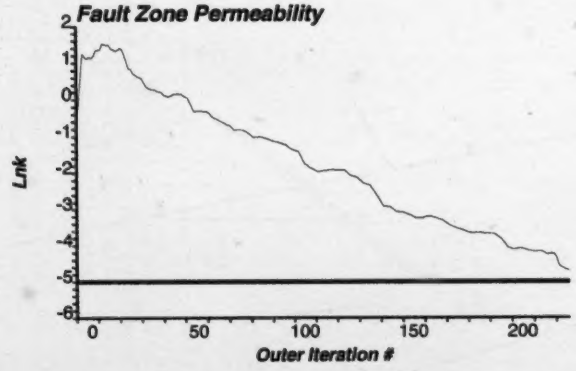


Figure 7.66: Fault zone $\ln(k)$ values for each outer iteration: 4 Well Case. (Reference value: thicker horizontal line)

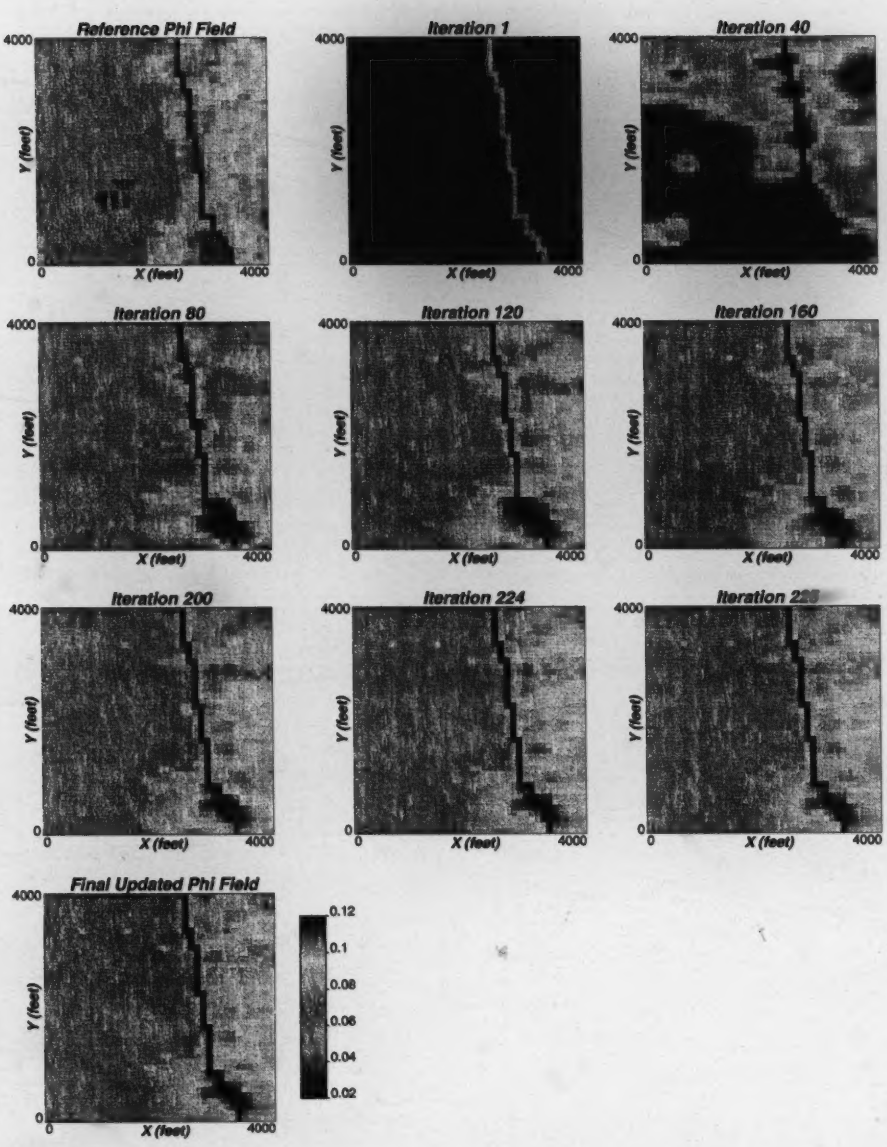


Figure 7.67: Updated $\phi$ fields at some outer iterations: 4 Well Case.

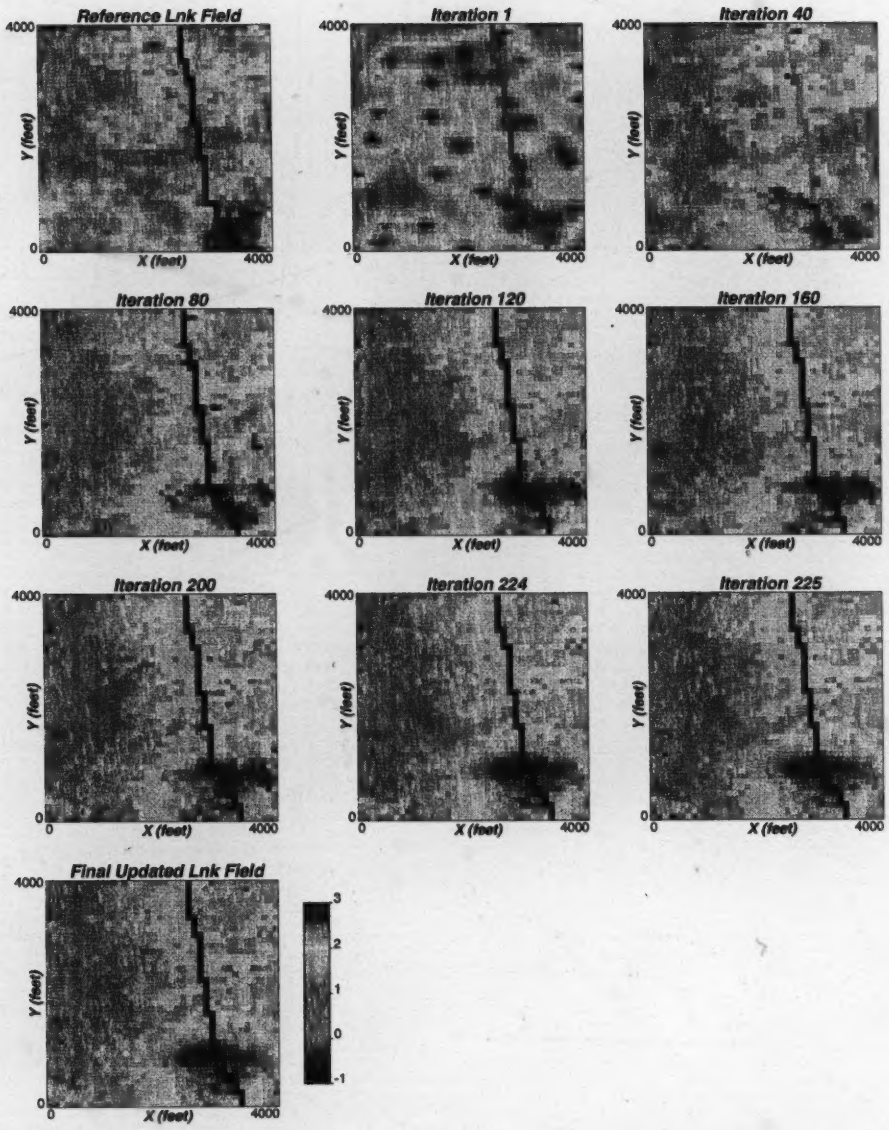


Figure 7.68: Updated $\ln(k)$ fields at some outer iterations: 4 Well Case.

# Chapter 8

# Discussion and Future Developments

Realistic reservoir description for the purpose of subsurface fluid flow simulation is a long-standing problem. Reality can only be attained with a correct fluid flow model and a reservoir description obtained through exhaustive measurement and sampling technique. This is prohibitive. Since the eighties, the industry has recognized the need for reservoir characterization with dynamic data. Dynamic data integration, in the name of history matching, has been applied since the beginning of the flow simulation. Of course, there are certain basic differences between the two. In dynamic data integration, the primary objective is to construct geologically realistic high resolution reservoir models. The uncertainty due to insufficient data should be reduced by a reasonable extent. There has been a tremendous amount of effort and research dollars spent on this problem. To date, none of the methods or techniques can claim to be suitable for any generalized reservoir scenario.

## 8.1 Discussion

This research involved the development of some methods for dynamic data integration in reservoir characterization. The developed algorithms appear to be quite promising with their efficiency and ability to integrate a variety of data. Uncertainty analysis by constructing equally likely multiple realizations has not been the focus of this work; however, this could be performed using the methods discussed here.

Chapter 4 describes an algorithm for simultaneous inversion of $\phi$ and $\ln(k)$. The algorithm extends the SSC technique [202]. The algorithm involves

- 2D, single phase flow simulation through finite differencing,
- inner optimization through gradient projection method,
- constraint determination using initial model, and a priori mean and variance, and
- optimal correction propagation of $\phi$ by simple kriging, and of $\ln(k)$ by collocated kriging

The spatial porosity and permeability variation can be identified with less uncertainty by integrating available static and dynamic information from different sources including production data. A number of sensitivity studies have been performed. Some controls in the

inversion process have been identified. Some of the findings from the illustrated examples and sensitivity analyses in Chapters 4 and 5 include:

- inversion with only production data and prior variography information may not be sufficient to capture heterogeneity features
- global distribution information is important in inversion performance
- minimum pressure mismatch criterion by itself may not lead to the best inverted model attainable
- unrealistic initial porosity and permeability fields may affect the inversion responses
- constraints are important for the overall inversion process
- number of master points affects the solution. Inversion with too few master points may lead to poor inversion; on the contrary, inversion with too many master points increases the execution time and at the same time may not guarantee better inversion solution
- increasing the frequency of master point location updating may reduce the possibility of getting stuck in local minima, but may not guarantee it
- prior variography information can be critical to inversion performance.

It was found that prior variogram information is critical in inversion performance. This is clearly a limitation because there are only well data to infer good prior variogram models. In order to eliminate this problem a variogram updating module is incorporated within the inversion algorithm. Chapter 6 extends the algorithm developed in Chapter 4 with a module facilitating variogram calculation and modeling. Better inversion outcomes were obtained using this code.

A spin-off of the modified algorithm is the ability to perform modeling and uncertainty analysis in variography using this algorithm. It is not possible to model reasonably good horizontal variograms in the common situation of a few wells. Expert modeler would use experience or analogue information to get around this very important aspect of reservoir modeling. This is a technique to address the problem by using information available from production history or well test data. Results proved encouraging.

Chapter 7 describes a developed algorithm for the inversion of fault property as well as the reservoir porosity and permeability. Equivalent petrophysical properties in the fault blocks were the focus of the algorithm. The inversion results were found to be interesting. It appears that during the initial outer iterations reservoir heterogeneity is resolved. Information for fault properties are captured at a later stage. Inversion of reservoir properties are better resolved for sealing fault when the production data have interference information. Amount of production data may not affect the inversion results as long as the interference information is available. Inversion outcomes are robust to number of master points or a priori fault zone information.

## 8.2 Limitations

Review of any work cannot be complete unless one upholds the limitations of the approaches employed. Certainly, there are number of limitations in the algorithms developed and the philosophy of the research. Some of these are discussed below.

- Working only with synthetic models cannot be a good way to evaluate the capability of the algorithms developed. One has to address the issues with 'real' data. In all the illustrated examples, the production data used for inversion runs are obtained using the similar forward simulator that is built into the inversion code. This naturally makes the problem well-posed to some extent.
- Good production data with interference information are rarely available. Also, in some of the examples quite a few blocks with hard data are considered. This may not happen in reality.
- Determination of the porosity gradients from the permeability gradients and the correlation coefficient leads to a more or less deterministic approach of obtaining the gradients. Although correlation coefficients are measures of scatter in the bi-variate distribution, their values are fixed. This cannot bring in the stochasticity in the estimation of the gradients. Some of the illustrations used in this research confirm this problem.
- Simultaneous optimization of parameters (here porosity and permeability) of different order of magnitudes can lead to artifacts in the inversion.
- Selection of master points is not implemented in a manner that will lead to efficient inversion.
- Variogram fitting module does not assign the number or the type of variogram structures. This is certainly a limitation of the algorithm.
- Within a fault system, the petrophysical properties are considered constant that may not be true. Also, fault locations are considered known. No uncertainty study was performed addressing this issue.
- Reservoir flow simulation approaches, gridding issues, scalings issues are not addressed in the research adequately.
- Uncertainty analysis for future reservoir performance prediction has not been performed. Although this is not a limitation of the implementation, but the content of the work.

## 8.3 Recommended Future Developments

Notwithstanding the progress made in this work, there is still a lot to achieve in this area of research. Complex reservoir scenarios with changing conditions are yet to be characterized properly or efficiently. Moreover, no practical case study is shown. Even the available techniques are devoid of the level of sophistication and versatility required for realistic application.

Envisaging the limitations and the range of applicability of the methods, the future course could consider the following avenues:

- A logical extension of the developed algorithms presented in this research would be to explore more rigorous ways to propagate the master point corrections to the entire domain. Multiple-point normal equations could be a viable option.

- Inversion with production data where few actual pressure measurements are available, or where only flow rate information is available should be investigated in greater detail.

- Object-based modeling, surface-based modeling techniques could be integrated into inversion algorithms using dynamic data.

- Incorporation of unstructured grids, local grid refinement in the inversion algorithms can be a logical extension in future research undertakings.

- Extensive 3D reservoir characterization with dynamic data has not yet found its place in practice. It is necessary for more practical use of this method to model separated-layer geology when production data such as production rate profiles along the bore holes are available.

- Extension of the techniques to true multiphase flow that can handle mobility changes during the course of production. Inversion using streamline methods are being developed. Finite-difference, finite-element or finite-volume formulation for the multiphase inversion could be a more rigorous approach. However, the balance between computational cost and realistic simulation features needs to be resolved.

- Incorporation of hydraulic anisotropy with $k_x$, $k_y$ and $k_z$ has not been properly implemented in the inversion algorithm. It must be remarked that incorporation of the diagonal permeability tensor will be sufficient in most cases.

- Provision for changing well conditions through time, e.g. new drilling, recompletions, workovers, infills, etc should be studied in a greater detail with more rigor. Inversion of production data from complex wells, e.g. deviated, horizontal, multiply completed, partially penetrated, gas-lift, etc. needs to be investigated.

- The inversion techniques should be able to handle process-specific reservoir situations and drive mechanisms, e.g. reservoirs with gravity segregation drive, bottom-water drive, edge-water drive, steam assisted gravity drainage mechanism, and waterflooding.

  With the decline of onshore petroleum reserves, exploitation of the off-shore reserves is increasing. It is typical, in these situations, to have sparse information about a large extent of the reservoirs. In the presence of such sparse data, the major issues are boundary delineations, aquifer influx, and major heterogeneities. Complex stratigraphy and structures including partially transmissible faults exist in many reservoir environment. Characterization of these reservoirs with dynamic data is challenging as the space of uncertainty is enormous. Future research in the field should address these issues.

- With a few exceptions, almost all the inversion techniques available to date suppress the time variation in the phase relative permeabilities and other fluid properties. A more realistic algorithm will account for such variations.
- Extension of the inversion to compositional production data is in the foreseeable future. The reason for this is that there exists a growing tendency in the industry to use compositional flow simulation in more and more practical cases. However, ideas are yet to be carved in a concrete manner.
- Techniques for proper quantification of the uncertainty space should be investigated with more rigor and application.
- Most importantly, extensive field application and testing is required, which will stimulate research into problems not yet investigated.

# Bibliography


[1] Y. Abacioglu, A. C. Reynolds, and D. S. Oliver. Estimating heterogeneous anisotropic permeability fields from multiwell interference tests: A field example. In *SPE Annual Technical Conference and Exhibition*, San Antonio, TX, October 1997. SPE Paper Number 38654.

[2] F. G. Alabert. Constraining description of randomly heterogeneous reservoirs to pressure test data: a Monte Carlo study. In *SPE Annual Conference and Exhibition*, pages 307–321, San Antonio, TX, October 1989. Society of Petroleum Engineers. SPE Paper Number 19600.

[3] F. G. Alabert and G. J. Massonnat. Heterogeneity in a complex turbiditic reservoir: Stochastic modelling of facies and petrophysical variability. In *65th Annual Technical Conference and Exhibition*, pages 775–790. Society of Petroleum Engineers, September 1990. SPE Paper Number 20604.

[4] F. G. Alabert and V. Modot. Stochastic models of reservoir heterogeneity: Impact on connectivity and average permeabilities. In *67th Annual Technical Conference and Exhibition*, pages 355–370. Society of Petroleum Engineers, October 1992. SPE Paper Number 24893.

[5] F. Anterion, R. Eymard, and B. Karcher. Use of parameter gradients for reservoir history matching. In *Tenth SPE Symposium on Reservoir Simulation*, pages 339–354, Houston, TX, February 1990. Society of Petroleum Engineers. SPE Paper Number 18433.

[6] H. Ates and M. G. Kelkar. Incorporation of two-phase production data into reservoir characterization. In *SPE Annual Technical Conference and Exhibition*, New Orleans, LA, September 1998. SPE Paper Number 48970.

[7] H. Ates and M. G. Kelkar. History matching with dual-loop techniques. In *SPE/DOE Improved Oil Recovery Symposium*, April 2000. SPE Paper Number 59371.

[8] D. Bandiziol and G. Massonnat. Horizontal permeability anisotropy characterization by pressure transient testing and geological data. In *1992 SPE Annual Technical Conference and Exhibition*, pages 39–52, Washington, DC, October 1992. Society of Petroleum Engineers. SPE Paper Number 24667.

[9] K. C. Bard, J. F. Arestad, A. Al-Bastaki, T. L. Davis, and R. D. Benson. Integrated reservoir characterization of a complex carbonate field. In *1995 SPE Annual Technical Conference and Exhibition*, pages 915–925, Dallas, TX, October 1995. Society of Petroleum Engineers. SPE Paper Number 30617.

[10] R. P. Batycky. *A Three-Dimensional Two-Phase Field Scale Streamline Simulator.* PhD thesis, Stanford University, Stanford, CA, 1997.

[11] R. P. Batycky, M. J. Blunt, and M. R. Thiele. A 3D field-scale streamline-based reservoir simulator. *SPE Reservoir Engineering*, pages 246–254, November 1997.

[12] R. A. Beier. Pressure transient model of a vertically fractured well in a fractal reservoir. In *SPE Annual Technical Conference and Exhibition*, pages 557–566, New Orleans, LA, September 1990. Society of Petroleum Engineers. SPE Paper Number 20582.

[13] J. P. Benkendorfer, C. V. Deutsch, P. D. LaCroix, L. H. Landis, Y. A. Al-Askar, A. A. Al-AbdulKarim, and J. Cole. Integrated reservoir modeling of a major Arabian carbonate reservoir. In *SPE Middle East Oil Show*, Bahrain, March 1995. Society of Petroleum Engineers. SPE Paper Number 29869.

[14] D. P. Bertsekas. *Constrained Optimization and Lagrange Multiplier Methods.* Academic Press, New York, 1982.

[15] D. P. Bertsekas. *Nonlinear Programming.* Athena Scientific, Belmont, MA, 1995.

[16] Z. Bi, D. S. Oliver, and A. C. Reynolds. Conditioning 3d stochastic channels to pressure data. *SPEJ*, 5(4):474–484, December 2000.

[17] R. C. Bissell, O. Dubrule, P. Lamy, P. Swaby, and O. Lepine. Combining geostatistical modelling with gradient information for history matching: the Pilot Point method. In *SPE Annual Technical Conference and Exhibition*, San Antonio, TX, October 1997. SPE Paper Number 38730.

[18] R. C. Bissell, J. E. Killough, and Y. Sharma. Reservoir history matching using the methods of gradients on a workstation. In *European Petroleum Computer Conference*, Stavanger, Norway, May 1992. Society of Petroleum Engineers. SPE Paper Number 24265.

[19] R. C. Bissell, Y. Sharma, and J. E. Killough. History matching using the method of gradients: Two case studies. In *SPE 69th Annual Conference and Exhibition*, pages 275–290, New Orleans, LA, September 1994. Society of Petroleum Engineers. SPE Paper Number 28590.

[20] G. Blanc, D. Huérillot, R. Rahon, and F. Roggero. Building geolostatistical models constrained by dynamic data - a posteriori constraints. In *SPE/NPF European Conference*, Stavanger, Norway, April 1995. Society of Petroleum Engineers. SPE Paper Number 35478.

[21] M. J. Blunt, K. Liu, and M. R. Thiele. A generalized streamline method to predict reservoir flow. In *8th European Symposium on Improved Oil Recovery*, pages 269–278, Vienna, Austria, May 1995.

[22] D. Bourdet, J. A. Ayoub, and Y. M. Pirard. Use of pressure derivative in well test interpretation. *SPEFE*, page 69, June 1989.

[23] P. R. Britto and A. S. Grader. The effects of size, shape, and orientation of an impermeable region on transient pressure testing. *Formation Evaluation*, pages 595–606, September 1988.

[24] G. F. Bunn, M. J. Wittmann, W. D. Morgan, and R. C. Curnutt. Distributed pressure measurements allow early quantification of reservoir dynamics in the jene field. *SPE Formation Evaluation*, pages 55–62, March 1991.

[25] J. E. Capilla, J. J. Gómez-Hernández, and A. Sahuquillo. Stochastic simulation of transmissivity fields conditioning to both transmissivity and piezometric data, 2. demonstration in a synthetic case. *Journal of Hydrology*, 302:175–188, 1998.

[26] J. Carrera, A. Medina, and X. S.-Vila. Geostatistical formulations of groundwater coupled inverse problems. In *Fourth International Geostatistics Congress*, pages 779–792, Troia, September 1992.

[27] J. Carrera and S. Neuman. Estimation of aquifer parameters under transient and steady state conditions: 1. maximum likelihood method incorporating prior information. *Water Resources Research*, 22(2):199–210, 1986.

[28] J. Carrera and S. Neuman. Estimation of aquifer parameters under transient and steady state conditions: 2. uniqueness, stability, and solution algorithms. *Water Resources Research*, 22(2):211–227, 1986.

[29] J. Carrera and S. P. Neuman. Estimation of aquifer parameters under transient and steady state conditions: Conditions: 3. application to synthetic and field data. *Water Resources Research*, 22(2):228–242, 1986.

[30] R. D. Carter, L. Kemp, A. Pierce, and D. Williams. Performance matching with constraints. *SPE Journal*, pages 187–196, April 1974.

[31] J. Chang and Y. C. Yortsos. Pressure transient analysis of fractal reservoirs. In *SPE Annual Conference and Exhibition*, Houston, TX, October 1988. Society of Petroleum Engineers. SPE Paper Number18170.

[32] M. M. Chang, M. Szpakiewicz, R. schatzinger, S. Jackson, B. Sharma, M. Tham, and F. H. Lim. Integration of a geological-engineering model with production performance: A case study at patrick draw field, wyoming. In *1993 SPE Annual Technical Conference and Exhibition*, pages 829–842, Houston, TX, October 1993. Society of Petroleum Engineers. SPE Paper Number 26499.

[33] G. Chavent, M. Dupuy, and P. Lemonnier. History matching by use of optimal theory. *SPE Journal*, pages 74–86, February 1975.

[34] W. H. Chen, G. Gavalas, J. Seinfeld, and M. L. Wasserman. A new algorithm for automatic history matching. *SPE Journal*, pages 593–608, December 1974.

[35] Y. M. Chen. Parallelism by hierarchy of GPST inversion algorithm for elastic wave equation. *Appl. Numer. Math.*, 4:83–95, 1988.

[36] Y. M. Chen and J. Q. Liu. A numerical algorithm for remote sensing of thermal conductivity. *J. Comput. Phys.*, 43:315–326, 1981.

[37] Y. M. Chen and J. Q. Liu. A numerical algorithm for solving inverse problems of two-dimensional wave equations. *J. Computational Physics*, 50:193–208, 1983.

[38] Y. M. Chen and J. Q. Liu. An iterative numerical algorithm for solving multiparameter inverse problems of evolutional partial differential equations. *J. Comput. Phys.*, 53:429–442, 1984.

[39] Y. M. Chen and J. Q. Liu. Efficiency improvement of GPST inversion algorithm. *J. Comput. Phys.*, 72:372–382, 1987.

[40] Y. M. Chen and F. G. Zhang. Hierarchical multigrid strategy for efficiency improvement of the GPST inversion algorithm. *Appl. Numer. Math.*, 6:431–446, 1989.

[41] L. Chu, M. Komara, and R. H. Schatzinger. Efficient technique for inversion of reservoir properties using iteration method. *SPEJ*, 5(1):71–81, March 2000.

[42] L. Chu, A. C. Reynolds, and D. S. Oliver. Computation of sensitivity coefficients for conditioning the permeability field to well-test pressure data. *In Situ*, 19(2):179–223, 1995.

[43] K. Cios, W. Pedrycz, and R. Swiniarski. *Data Mining Methods for Knowledge Discovery*. Kluwer Academic Publishers, 1998.

[44] P. M. Clifton and S. P. Neuman. Effects of kriging and inverse modeling on conditional simulation of the avra valley aquifer in southern arizona. *Water Resources Research*, 18(4):1215–1234, 1982.

[45] K. H. Coats, J. R. Dempsey, and J. H. Henderson. A new technique for determining reservoir description from field performance data. *SPE Journal*, pages 66–74, March 1968.

[46] R. L. Cooley. Incorporation of prior information on parameters into nonlinear regression groundwater flow models, 1. theory. *Water Resources Research*, 18(4):965–976, 1982.

[47] L. B. Cunha, D. S. Oliver, R. A. Redner, and A. C. Reynolds. A Hybrid Markov Chain Monte Carlo method for generating permeability fields conditioned to multiwell pressure data and prior information. In *SPE Annual Technical Conference and Exhibition*, Denver, CO, October 1996. Society of Petroleum Engineers. SPE Paper Number 36566.

[48] L. B. Cunha, D. S. Oliver, R. A. Redner, and A. C. Reynolds. A Hybrid Markov Chain Monte Carlo method for generating permeability fields conditioned to multiwell pressure data and prior information. *SPE Journal*, 3(3):261–271, September 1998.

[49] G. Dagan. Statistic modeling of groundwater flow by unconditional and conditional probabilities: The inverse problem. *Water Resources Research*, 21(1):65–72, 1985.

[50] E. Damsleth, C. B. Tjolsen, K. H. Omre, and H. H. Haldorsen. A two-stage stochastic model applied to a north sea reservoir. In *65th Annual Technical Conference and Exhibition*, pages 791–802, New Orleans, LA, September 1990. Society of Petroleum Engineers.

[51] A. Datta-Gupta and M. J. King. A semianalytic approach to tracer flow modeling in heterogeneous permeable media. *Adv. in Water Resources*, 18(1):9–24, 1995.

[52] A. Datta-Gupta, L. W. Lake, and G. A. Pope. Characterizing heterogeneous permeability media with spatial statistics and tracer data using sequential simulation annealing. *Math. Geology*, 27(6):763–787, 1995.

[53] A. Datta-Gupta, L. W. Lake, G. A. Pope, and M. J. King. A type-curve approach to analyzing two-well tracer tests. *SPE Formation Evaluation*, March 1995.

[54] A. Datta-Gupta, D. W. Vasco, J. C. S. Long, and S. Vomvoris. Stochastic modeling of spatial heterogeneities conditioned to hydraulic and tracer tests. In *Proc. 5th Annual International Conference on High Level Radioactive Waste Management*, volume 4, pages 2624–2632, 1994.

[55] G. de Marsily, G. Lavedau, M. Boucher, and G. Fasanino. Interpretation of interference test in a well field using geostatistical techniques to fit the permeability distribution in a reservoir model. In G. Verly, M. David, A. G. Journel, and A. Marechal, editors, *Geostatistics for Natural Resources Characterization, Proceedings of the NATO Advanced Study Institute*, pages 831–849. Dordrecht, Holland, 1984.

[56] J. P. Delhomme. Spatial variability and uncertainty in groundwater flow parameters: A geostatistical approach. *Water Resources Research*, 15(2):269–280, 1979.

[57] X. Deng. *Description of Heterogeneous Reservoirs Using Pressure and Tracer Data.* PhD thesis, Stanford University, Stanford, CA, 1996.

[58] X. Deng and R. Horne. Description of heterogeneous reservoir using tracer and pressure data simultaneously. In *1995 SPE Annual Technical Conference and Exhibition*, pages 639–652, Dallas, TX, October 1995. Society of Petroleum Engineers. SPE Paper Number 30590.

[59] C. V. Deutsch. *Annealing Techniques Applied to Reservoir Modeling and the Integration of Geological and Engineering (Well Test) Data.* PhD thesis, Stanford University, Stanford, CA, 1992.

[60] C. V. Deutsch. Conditioning reservoir models to well test information. In A. Soares, editor, *Geostatistics-Troia*, volume 1, pages 505–518. Kluwer, Dordrecht, Holland, 1993.

[61] C. V. Deutsch. Constrained modeling of histograms and cross plots with simulated annealing. *Technometrics*, 38(3):266–274, August 1996.

[62] C. V. Deutsch and P. W. Cockerham. Practical considerations in the application of simulated annealing to stochastic simulation. *Mathematical Geology*, 26(1):67–82, 1994.

[63] C. V. Deutsch and A. G. Journel. The application of simulated annealing to stochastic reservoir modeling. In *Report 4, Stanford Center for Reservoir Forecasting*, Stanford, CA, May 1991.

[64] C. V. Deutsch and A. G. Journel. Annealing techniques applied to the integration of geological and engineering data. In *Report 5, Stanford Center for Reservoir Forecasting*, Stanford, CA, May 1992.

[65] C. V. Deutsch and A. G. Journel. *GSLIB: Geostatistical Software Library and User's Guide*. Oxford University Press, New York, 1992.

[66] C. V. Deutsch and A. G. Journel. Integrating well test-derived absolute permeabilities. In J. M. Yarus and R. L. Chambers, editors, *Stochastic Modeling and Geostatistics: Principles, Methods, and Case Studies*, pages 131–142. AAPG Computer Applications in Geology, No. 3, 1995.

[67] C. V. Deutsch and A. G. Journel. *GSLIB: Geostatistical Software Library and User's Guide*. Oxford University Press, New York, 2nd edition, 1998.

[68] C. V. Deutsch and S. Srinivasan. Improved reservoir management through ranking stochastic reservoir models. In *SPE/DOE Tenth Symposium on Improved Oil Recovery, Tulsa, OK*, pages 105–113, Washington, DC, April 1996. Society of Petroleum Engineers. SPE Paper Number 35411.

[69] C. V. Deutsch, S. Srinivasan, and Y. Mo. Geostatistical reservoir modeling accounting for the scale and precision of seismic data. In *1996 SPE Annual Technical Conference and Exhibition*, pages 9–19, Denver, CO, October 1996. Society of Petroleum Engineers. SPE Paper Number 36497.

[70] R. C. Earlougher. *Advances in Well Test Analysis*. Society of Petroleum Engineers, New York, NY, 1977.

[71] Y. Emsellem and G. de Marsily. An automatic solution for the inverse problem. *Water Resources Research*, 7(5):1264–1283, 1971.

[72] R. Ewing and T. Lin. A class of parameter estimation techniques for fluid flow in porous media. *Adv. in Water Resources*, 14(2):89–97, 1991.

[73] G. Fasanino, J.-E. Molinard, G. de Marsily, and V. Pelcé. Inverse modeling in gas reservoirs. In *1986 SPE Annual Technical Conference and Exhibition*, New Orleans, LA, October 1986. Society of Petroleum Engineers. SPE Paper Number 15592.

[74] E. Feinerman, G. Dagan, and E. Bresler. Statistical inference of spatial random functions. *Water Resources Research*, 22(6):935–942, 1986.

[75] G. S. Feitosa, L. Chu, L. G. Thompson, and A. C. Reynolds. Determination of reservoir permeability distributions from pressure buildup data. In *1993 SPE Annual Technical Conference and Exhibition*, pages 417–429, Houston, TX, October 1993. Society of Petroleum Engineers. SPE Paper Number 26457.

[76] G. S. Feitosa, L. Chu, L. G. Thompson, and A. C. Reynolds. Determination of reservoir permeability distributions from well test pressure data. In *1993 SPE Western Regional Meeting*, pages 189–204, Anchorage, Alaska, May 1993. Society of Petroleum Engineers. SPE Paper Number 26047.

[77] R. Flether. *Practical Methods of Optimization.* John Wiley & Sons, New York, 1987.

[78] G. R. Gavalas, P. C. Shah, and J. H. Seinfeld. Reservoir history matching by Bayesian estimation. *SPE Journal*, pages 337–349, December 1976.

[79] D. E. Goldberg. *Genetic Algorithms in Search, Optimization and Machine Learning.* Addison-Wesley, 1989.

[80] S. Gomez, O. Gosselin, and J. W. Barker. Gradient-based history matching with a global optimization technique. In *SPE Annual Technical Conference and Exhibition*, Houston, Texas, October 1999. SPE Paper Number 56756.

[81] J. J. Gómez-Hernández, A. Sahuquillo, and J. E. Capilla. Stochastic simulation of transmissivity fields conditioning to both transmissivity and piezometric data, 1. the theory. *Journal of Hydrology*, 302:162–174, 1998.

[82] P. Grindrod and M. D. Impey. Fractal field simulations of tracer migration with in the WIPP culebra dolomite. Technical report, Intera Information Tech., U. K., December 1991.

[83] P. Grindrod, P. Robinson, and M. Williams. The art of noise: Self-affinity, flow and transport. Technical report, Intera Sciences, Henley-on-Thames, U. K., 1991.

[84] D. Guerillot and F. Roggero. Matching the future for the evaluation of extreme reservoir development scenarios. In *8th European Symposium on Improved Oil Recovery*, Vienna, Austria, May 1995.

[85] A. L. Gutjahr. Fast Fourier transforms for random fields. Technical Report No. 4-R58-2690R, Los Alamos, NM, 1989.

[86] A. L. Gutjahr and J. L. Wilson. Co-Kriging for stochastic models. *Transport in Porous Media*, 4(6):585–598, 1989.

[87] H. H. Haldorsen and E. Damsleth. Stochastic modeling. *Journal of Petroleum Technology*, pages 404–412, April 1990.

[88] C. Harvey and S. Gorelick. Mapping hydraulic conductivity: Sequential conditioning with measurements of solute arrival time, hydraulic head, and local conductivity. *Water Resources Research*, 31(7):1615–1626, 1995.

[89] R. P. Hatcher and Y. M. Chen. An iterative method for solving inverse problems of a nonlinear wave equation. *SIAM J. Sci. Stat. Comput.*, 4(2):149–163, 1983.

[90] G. W. Haws and N. F. Hurley. Applications of pressure-interference data in reservoir characterization studies, big jorn basin, wyoming. In *1992 SPE Annual Technical Conference and Exhibition*, pages 53–62, Washington, DC, October 1992. Society of Petroleum Engineers. SPE Paper Number 24668.

[91] N. He and K. T. Chambers. Calibrate flow simulation models with well-test data to improve history matching. In *SPE Annual Technical Conference and Exhibition*, Houston, TX, October 1999. SPE Paper Number 56681.

[92] N. He, D. S. Oliver, and A. C. Reynolds. Conditioning stochastic reservoir models to well-test data. In *SPE Annual Technical Conference and Exhibition*, San Antonio, October 1997. SPE Paper Number 38655.

[93] N. He, A. C. Reynolds, and D. S. Oliver. Three-dimensional reservoir description from multiwell pressure data and prior information. In *SPE Annual Technical Conference and Exhibition*, pages 151–166, Denver, CO, October 1996. SPE Paper Number 36509.

[94] E. L. Head, J. J. Pop, and F. E. Bettis. Reservoir anisotropy determination using multiple probe pressures. In *SPE Western Regional Meeting*, pages 205–219, Anchorage, Alaska, May 1993. Society of Petroleum Engineers. SPE Paper Number 26048.

[95] B. K. Hegstad and H. Omre. Uncertainty assessment in history matching and forecasting. In *Fifth International Geostatistics Congress*, Wollongong, September 1996.

[96] M. R. Hestenes and E. L. Stiefel. Methods of conjugate gradients for solving linear systems. *J. Res. Bureau National Standards*, 49:409–436, 1952.

[97] K. B. Hird and O. Dubrule. Quantification of reservoir connectivity for reservoir description applications. In *1995 SPE Annual Technical Conference and Exhibition*, pages 415–424, Dallas, TX, October 1995. Society of Petroleum Engineers. SPE Paper Number 30571.

[98] K. B. Hird and M. G. Kelkar. Conditional simulation method for reservoir description using spatial and well-performance constraints. *SPE Reservoir Engineering*, pages 145–152, May 1994.

[99] R. J. Hoeksema and P. K. Kitanidis. An application of the geostatistical approach to the inverse problem in two-dimensional groundwater modeling. *Water Resources Research*, 20(7):1003–1020, 1984.

[100] L. Holden, R. Madsen, K. A. Jakobsen, C. B. Tjølsen, and S. Vik. Use of well test data in stochastic reservoir modelling. In *1995 SPE Annual Technical Conference and Exhibition*, pages 653–661, Dallas, TX, October 1995. Society of Petroleum Engineers. SPE Paper Number 30591.

[101] R. N. Horne. *Modern Well Test Analysis. A Computer-Aided Approach.* Petroway Inc, 926 Bautista Court, Palo Alto, CA, 94303, 1995. Second Edition.

[102] L. Y. Hu, G. Blanc, and B. Noetinger. Estimation of lithofacies proportions using well and well test data. In *SPE 71st Annual Technical Conference and Exhibition*, Denver, CO, October 1996. Society of Petroleum Engineers. SPE Paper Number 36571.

[103] X. Huang, A. Gajraj, and M. G. Kelkar. The impact of integrating static and dynamic data in quantifying uncertainties in the future prediction of multi-phase systems. In *SPE 71st Annual Technical Conference and Exhibition*, Denver, CO, October 1996. Society of Petroleum Engineers. SPE Paper Number 36570.

[104] X. Huang and M. G. Kelkar. Integration of dynamic data for reservoir characterization in the frequency domain. In *SPE 71st Annual Technical Conference and Exhibition*, Denver, CO, October 1996. Society of Petroleum Engineers. SPE Paper Number 36513.

[105] X. Huang and M. G. Kelkar. Reservoir characterization by integration of seismic and dynamic data. In *SPE/DOE Tenth Symposium on Improved Oil Recovery*, Tulsa, OK, April 1996. Society of Petroleum Engineers. SPE Paper Number 35415.

[106] X. Huang, L. Meister, and R. Workman. Reservoir characterization by integration of time-lapse and production data. In *SPE Annual Technical Conference and Exhibition*, San Antonio, TX, October 1997. SPE Paper Number 38695.

[107] X. Huang, L. Meister, and R. Workman. Improvement and sensitivity of reservoir characterization derived from time-lapse seismic data. In *SPE Annual Technical Conference and Exhibition*, New Orleans, LA, September 1998. SPE Paper Number 49146.

[108] P. Jacquard and C. Jain. Permeability distribution from field pressure data. *SPE Journal*, pages 281–294, December 1965.

[109] H. O. Jahns. A rapid method for obtaining a two-dimensional reservoir description from well pressure response data. *SPE Journal*, pages 315–327, December 1966.

[110] F. E. Jansen and M. G. Kelkar. Applications of wavelets to production data in describing inter-well relationships. In *Parmian Basin Oil and Gas Recovery Conference*, Midland, TX, March 1996. SPE Paper Number 35184.

[111] F. E. Jansen and M. G. Kelkar. Applications of wavelets to production data in describing inter-well relationships. In *SPE Annual Technical Conference and Exhibition*, San Antonio, TX, October 1997. SPE Paper Number 38876.

[112] F. E. Jansen and M. G. Kelkar. Non-stationary estimation of reservoir properties using production data. In *SPE Annual Technical Conference and Exhibition*, San Antonio, TX, October 1997. SPE Paper Number 38729.

[113] A. G. Journel. Geostatistics for conditional simulation of orebodies. *Economic Geology*, 69:673–680, 1974.

[114] A. G. Journel and C. J. Huijbregts. *Mining Geostatistics*. Academic Press, New York, 1978.

[115] S. Kirkpatrick, C. D. Gelatt, Jr., and M. P. Vecchi. Optimization by simulated annealing. *Science*, 220(4598):671–680, May 1983.

[116] P. K. Kitanidis and E. G. Vomvoris. A geostatistical approach to the inverse problem in groundwater modeling (steady state) and one-dimensional simulations. *Water Resources Research*, 19(3):677–690, 1983.

[117] C. Kravaris and J. H. Seinfeld. Identification of parameters in distributed parameter systems by regularization. *SIAM J. Control and Optimization*, 23(2):217–241, 1985.

[118] C. Kravaris and J. H. Seinfeld. Identifiability of spatially-varying conductivity from point observation as an inverse sturm-liouville problem. *SIAM J. Control and Optimization*, 24(3):522–542, 1986.

[119] C. Kravaris and J. H. Seinfeld. Identification of spatially varying parameters in distributed parameter systems by discrete regularization. *J. Mathematical Analysis and Appl.*, 119:128–152, 1986.

[120] K. N. Kulkarni and A. Datta-Gupta. Estimating relative permeability from production data: A streamline approach. *SPEJ*, 5(4):402–411, December 2000.

[121] K. N. Kulkarni, A. Datta-Gupta, and D. W. Vasco. A streamline approach for integrating transient pressure data into high resolution reservoir models. In *SPE European Petroleum Conference*, Paris, France, October 2000. SPE Paper Number 65120.

[122] J. L. Landa and R. N. Horne. Procedure to integrate well test data, reservoir performance history and 4-d seismic information into a reservoir description. In *SPE Annual Technical Conference and Exhibition*, San Antonio, TX, October 1997. SPE Paper Number 38653.

[123] J. L. Landa, M. M. Kamal, C. D. Jenkins, and R. N. Horne. Reservoir characterization constrained to well test data: A field example. In *1996 SPE Annual Technical Conference and Exhibition*, pages 177–192, Denver, CO, October 1996. Society of Petroleum Engineers. SPE Paper Number 36511.

[124] A. M. LaVenue and J. F. Pickens. Application of a coupled adjoint sensitivity and kriging approach to calibrate a groundwater flow model. *Water Resources Research*, 28(6):1543–1569, 1992.

[125] A. M. LaVenue, B. S. RamaRao, G. de Marsily, and M. G. Marietta. Pilot Point methodology for automated calibration of an ensemble of conditionally simulated transmissivity fields, 2. application. *Water Resources Research*, 31(3):495–519, 1995.

[126] T. Lee, C. Kravaris, and J. H. Seinfeld. History matching by spline approximation and regrlarization in single-phase areal reservoirs. *SPE Reservoir Engineering*, 1:??, 1986.

[127] T. Lee and J. H. Seinfeld. Estimation of two-phase petroleum reservoir properties by regularization. *J. Computational Physics*, 69:397–419, 1987.

[128] P. M. Lemouzy, R. Eschard, and H. Beucher. An integrated approach EOR evaluation of production scenarios in the field delineation phase. In *66th SPE Annual Technical Conference and Exhibition*, pages 209–219, Dallas, TX, October 1991. Society of Petroleum Engineers. SPE Paper Number 22906.

[129] O. J. Lepine, R. C. Bissell, S. I. Aanonsen, I. Pallister, and J. W. Barker. Uncertainty analysis in predictive reservoir simulation using gradient information. *SPEJ*, 4(3):251–259, September 1999.

[130] R. Li, A. C. Reynolds, and D. S. Oliver. History matching of three-phase flow production data. In *SPE Reservoir Simulation Symposium*, Houston, Texas, February 2001. SPE Paper Number 66351.

[131] J. Q. Liu and Y. M. Chen. An iterative algorithm for solving inverse problems of two-dimensional diffusion equations. *SIAM J. Sci. Stat. Comput.*, 5(2):255–269, 1984.

[132] X. Y. Liu and Y. M. Chen. A generalized pulse-spectrum technique (gpst) for determining time-dependent coefficients of one-dimensional diffusion equations. *SIAM J. Sci. Stat. Comput.*, 8(3):436–445, 1987.

[133] X. Y. Liu and Y. M. Chen. Convergence of a generalized pulse-spectrum technique (gpst) for inverse problems of i-d diffusion equations in space-time domain. *Math. Comp.*, 51(184):477–489, 1988.

[134] M. E. Lord and R. E. Collins. Detecting compartmented gas reservoirs through production performance. In *1991 SPE Annual Technical Conference and Exhibition*, pages 575–581, Dallas, TX, October 1991. Society of Petroleum Engineers. SPE Paper Number 22941.

[135] E. M. Makhlouf, W. H. Chen, M. L. Wasserman, and J. H. Seinfeld. A general history matching algorithm for three-phase, three-dimensional petroleum reservoirs. *SPE Advanced Technology Series*, 1(2):83–92, 1993.

[136] S. Mantica, A. Cominelli, and G. Mantica. Combining global and local optimization techniques for automatic history matching production and seismic data. In *SPE Reservoir Simulation Symposium*, Houston, Texas, February 2001. SPE Paper Number 66355.

[137] V. Maroongroge, N. Saad, and G. A. Pope. Use of inverse modeling for conditioning geostatistical models to vertical tracer profiles. In *1995 SPE Annual Technical Conference and Exhibition*, pages 661–672, Dallas, TX, October 1995. Society of Petroleum Engineers. SPE Paper Number 30592.

[138] K. Masumoto. Pressure derivative matching method for two phase fluid flow in heterogeneous reservoir. In *SPE Asia Pacific Conference on Integrated Modelling for Asset Management*, Yokohama, Japan, April 2000. SPE Paper Number 59462.

[139] C. D. McElwee. Sensitivity analysis of groundwater models. In *Advances in Transport Phenomena in Porous Media*. NATO Advanced Science Institute, Series E, No. 82, 1984.

[140] W. Menke. *Inverse Problem Theory.* Elsevier, Amsterdam, The Netherlands, 1989.

[141] N. Metropolis, A. Rosenbluth, M. Rosenbluth, A. Teller, and E. Teller. Equation of state calculations by fast computing machines. *J. Chem. Phys.*, 21(6):1087–1092, June 1953.

[142] Z. Michalewski. *Genetic Algorithms + Data Structures = Evolution Programs.* Springer-Verlag, 1992.

[143] L. Nazareth. A conjugate direction algorithm without line searchers. *Journal of Optimization Theory and Applications*, pages 373–387, November 1977.

[144] J. A. Nelder and R. Mead. A simplex method for function minimization. *Comput. Journal*, 7:308–313, 1965.

[145] S. P. Neuman and S. Yakowitz. A stochastic approach to the inverse problem of aquifer hydrology, 1. theory. *Water Resources Research*, 15(4):845–860, 1979.

[146] D. S. Oliver. The averaging process in permeability estimation from well test data. *SPE Formation Evaluation*, pages 319–324, September 1990.

[147] D. S. Oliver. Estimation of radial permeability distribution from well test data. In *SPE Annual Technical Conference and Exhibition*, pages 243–250, New Orleans, LA, September 1990. Society of Petroleum Engineers. SPE Paper Number 20555.

[148] D. S. Oliver. Estimation of radial permeability distribution from well test pressure data. *SPE Formation Evaluation*, pages 290–296, December 1992.

[149] D. S. Oliver. Incorporation of transient pressure data into reservoir characterization. *In Situ*, 18(3):243–275, 1994.

[150] D. S. Oliver. A comparsion of the value of interference and well-test data for mapping permeability and porosity. *In Situ*, 20(1):41–59, 1996.

[151] D. S. Oliver, L. B. Cunha, and A. C. Reynolds. Markov Chain Monte Carlo methods for conditioning a permeability field to a pressure data. *Math. Geology*, 29(1):61–91, 1997.

[152] D. S. Oliver, N. He, and A. C. Reynolds. Conditioning permeability fields to pressure data. In *5th European Conference on the Mathematics of Oil Recovery*, Leoben, Austria, September 1996.

[153] M. Onur and M. Al-Saddique. Comparisons of derivative algorithms used in pressure transient analysis. *The Arabian Journal for Science and Engineering*, 24(1B):59, April 1999.

[154] M. Onur and A. C. Reynolds. Nonlinear regression: The information content of pressure and pressure derivative data. In *SPE Annual Technical Conference and Exhibition*, New Orleans, Lousiana, September 2001. SPE Paper Number 71579.

[155] A. Ouenes, S. Bhagavan, P. H. Bunge, and B. J. Travis. Application of simulated annealing and other global optimization methods to reservoir description: Myths and realities. In *SPE 69th Annual Conference and Exhibition*, pages 547–561, Washington, DC, September 1994. Society of Petroleum Engineers. SPE Paper Number 28415.

[156] A. Ouenes, G. Fasanino, and R. L. Lee. Simulated annealing for interpreting gas/water laboratory corefloods. In *1992 SPE Annual Technical Conference and Exhibition*, pages 43–55, Washington, DC, October 1992. Society of Petroleum Engineers. SPE Paper Number 24870.

[157] R. Parish, V. Calderbank, A. Watkins, A. Muggeridge, A. Goode, and P. Robinson. Effective history matching: The application of advanced software techniques to the history-matching process. *SPEJ*, pages 187–196, 1993.

[158] Petroleum Society of CIM / Society of Petroleum Engineers. *Pressure Transient Field Data Showing Fractal Reservoir Structure*, Calgary, AB, June 10-13 1990.

[159] V. Phan and R. N. Horne. Determining depth-dependent reservoir properties using integrated reservoir analysis. In *SPE Annual Technical Conference and Exhibition*, Houston, Texas, October 1999. SPE Paper Number 56423.

[160] E. Polak. *Optimization Algorithms and Consistent Approximations*. Springer-Verlag, New York, 1997.

[161] D. W. Pollock. Documentation of computer programs to compute and display pathline results from the us geological survey modular three-dimansional finite-difference ground-water flow model. Technical report, U.S. Geological Survey, 1989. Open File Report 89-381.

[162] N. V. Queipo, S. Pintos, N. Rincon, N. Contreras, and J. Colmenares. Surrogate modeling-based optimization for the integration of static and dynamic data into a reservoir description. In *SPE Annual Technical Conference and Exhibition*, Dallas, Texas, October 2000. SPE Paper Number 63065.

[163] R. Raghavan. *Well Test Analysis*. PTR Prentice-Hall, Inc., New Jersey, NJ, 1993.

[164] R. Raghavan, T. N. Dixon, S. W. Robinson, and V. Q. Phan. Integration of geology, geophysics and numerical simulation in the interpretation of a well test in a fluivial reservoir. In *SPE Annual Technical Conference and Exhibition*, Dallas, Texas, October 2000. SPE Paper Number 62983.

[165] D. Rahon, G. Blanc, and D. Guérillot. Gradients method constrained by geological bodies for history matching. In *SPE Annual Technical Conference and Exhibition*, pages 841–850, Denver, CO, October 1996. Society of Petroleum Engineers. SPE Paper Number 36568.

[166] D. Rahon, P. F. Edoa, and M. Masmoudi. Identification of geological shapes in reservoir engineering by history matching production data. In *SPE Annual Technical Conference and Exhibition*, New Orleans, LA, September 1998. SPE Paper Number 48969.

[167] D. Rahon and M. Masmoudi. Inversion of geological shapes in reservoir engineering using well-tests and history matching of production data. In *SPE Annual Technical Conference and Exhibition*, pages 141–153, San Antonio, TX, October 1997. SPE Paper Number 38656.

[168] B. S. RamaRao, A. M. LaVenue, G. de Marsily, and M. G. Marietta. Pilot Point methodology for automated calibration of an ensemble of conditionally simulated transmissivity fields, 1. theory and computational experiments. *Water Resources Research*, 31(3):475–493, 1995.

[169] L. C. Reis, L. Y. Hu, G. de Marsily, and R. Eschard. Prodcution data integration using a gradual deformation approach: Application to an oil field (offshore brazil). In *SPE Annual Technical Conference and Exhibition*, Dallas, TX, October 2000. SPE Paper Number 63064.

[170] A. C. Reynolds, N. He, L. Chu, and D. S. Oliver. Reparamerterization techniques for generating reservoir descriptions conditioned to variograms and well-test pressure. In *1995 SPE Annual Technical Conference and Exhibition*, pages 609–624, Dallas, TX, October 1995. Society of Petroleum Engineers. SPE Paper Number 30588.

[171] F. Roggero. Direct selection of stochastic model realizations constrained to historical data. In *SPE Annual Technical Conference and Exhibition*, San Antonio, TX, October 1997. SPE Paper Number 38731.

[172] F. Roggero and L. Hu. Gradual deformation of continuous geostatistical models for history matching. In *SPE Annual Technical Conference and Exhibition*, New Orleans, LA, September 1998. SPE Paper Number 49004.

[173] A. J. Rosa and R. N. Horne. Reservoir description by well test analysis using cyclic flow rate variation. In *1991 SPE Annual Technical Conference and Exhibition*, pages 433–448, Dallas, TX, October 1991. Society of Petroleum Engineers. SPE Paper Number 22698.

[174] A. J. Rosa and R. N. Horne. Pressure transient behavior in reservoirs with an internal circular discontinuity. In *1993 SPE Annual Technical Conference and Exhibition*, pages 389–401, Houston, TX, October 1993. Society of Petroleum Engineers. SPE Paper Number 26455.

[175] Y. Rubin and G. Dagan. Stochastic identification of transmissivity and effective recharge in steady groundwater flow, 1. theory. *Water Resources Research*, 23(7):1185–1192, 1987.

[176] Y. Rubin and G. Dagan. Stochastic identification of transmissivity and effective recharge in steady groundwater flow, 2. case study. *Water Resources Research*, 23(7):1193–1200, 1987.

[177] M. A. Sabet. *Well Test Analysis*, volume 8 of *Contributions in Petroleum Geology and Engineering*. Gulf Publishing Company, Houston, 1991.

[178] R. K. Sagar, B. G. Kelkar, and L. G. Thompson. Reservoir description by integration of well test data and spatial statistics. In *1993 SPE Annual Technical Conference and Exhibition*, pages 475–489, Houston, TX, October 1993. Society of Petroleum Engineers. SPE Paper Number 26462.

[179] A. Satter, J. E. Vernon, and M. T. Hoang. Reservoir management: Technical perspective. In *SPE International Meeting on Petroleum Engineering*, Beijing, China, March 1992. SPE Paper Number 22350.

[180] Schlumberger GeoQuest, UK. *ECLIPSE 100 Reference Manual*, 1997.

[181] P. C. Shah, G. R. Gavalas, and J. H. Seinfeld. Error analysis in history matching: The optimum level of parametrization. *SPE Journal*, pages 219–228, June 1978.

[182] S. Srinivasan and J. Caers. Conditioning reservoir models to dynamic data - a forward modeling perspective. In *SPE Annual Technical Conference and Exhibition*, Dallas, Texas, October 2000. SPE Paper Number 62941.

[183] S. Srinivasan and A. G. Journel. Simulation of permeability field conditioned to well test data. In *SPE Annual Technical Conference and Exhibition*, New Orleans, LA, September 1998. SPE Paper Number 49289.

[184] A. J. Sultan, A. Ouenes, and W. W. Weiss. Reservoir description by inverse modeling: Application to EVGSAU field. In *1993 SPE Annual Technical Conference and Exhibition*, pages 637–652, Houston, TX, October 1993. Society of Petroleum Engineers. SPE Paper Number 26478.

[185] J. E. Sykes, J. L. Wilson, and R. W. Andrews. Sensitivity analysis for steady-state groundwater flow using adjoint operators. *Water Resources Research*, 21(3):359–371, 1985.

[186] T. Tan and N. Kalogerakis. Improved reservoir characterization using automatic history matching procedures. *Journal of Canadian Petroleum Technology*, 32(6):26–33, May-June 1993.

[187] Y. N. Tang, Y. M. Chen, W. H. Chen, and M. L. Wasserman. Generalized pulse-spectrum technique for 2-d and 2-phase history matching. *Appl. Numer. Math.*, 5:529–539, 1989.

[188] A. Tarantola. *Inverse Problem Theory: Methods for Data Fitting and Model Parameter Estimation.* Elsevier, Amsterdam, The Netherlands, 1987.

[189] E. Tauzin. Integration of well test data into stochastic modeling. Master's thesis, Stanford University, Stanford, CA, 1995.

[190] M. R. Thiele. *Modeling Multiphase Flow in Heterogeneous Media Using Streamtubes.* PhD thesis, Stanford University, Stanford, CA, 1994.

[191] M. R. Thiele, M. J. Blunt, and F. M. Orr, Jr. Predicting multicomponent, multiphase flow in heterogeneous systems using streamtubes. In *4th European Conference on the Mathematics of Oil Recovery*, Roros, Norway, June 1994.

[192] M. R. Thiele, M. J. Blunt, and F. M. Orr, Jr. Simulating flow in heterogeneous systems using streamtubes. *SPE Reservoir Engineering*, pages 5–12, February 1996.

[193] H. Tjelmeland and H. Omre. A complex sand-shale facies model conditioned on observations from wells, seismics, and production. In *Fifth International Geostatistics Congress*, Wollongong, September 1996.

[194] D. S. Tsien and Y. M. Chen. Computational methods in nonlinear mechanics. In *Proc. Int. Conf. Comput. Meth. Nonlinear Methods*, pages 935–943, Austin, TX, 1974. The University of Texas, Austin.

[195] D. Vasco, S. Yoon, and A. Datta-Gupta. Integrating dynamic data into high-resolution reservoir models using streamline-based analytic sensitivity coefficients. *SPEJ*, 4(4):389–399, December 1999.

[196] D. W. Vasco, A. Datta-Gupta, and J. C. S. Long. Integrating field production history in stochastic reservoir characterization. In *SPE 71st Annual Technical Conference and Exhibition*, Denver, CO, October 1996. Society of Petroleum Engineers. SPE Paper Number 36567.

[197] N. Vashist, R. N. Dennis, A. K. Rajvanshi, H. R. Taneja, R. K. Walia, and P. K. Sharma. Reservoir facies and their distribution in a heterogeneous carbonate reservoir: An integrated approach. In *1993 SPE Annual Technical Conference and Exhibition*, pages 819–828, Houston, TX, October 1993. Society of Petroleum Engineers. SPE Paper Number 26498.

[198] Y. Wang and A. R. Kovscek. Streamline approach for history matching prodcution data. *SPEJ*, 5(4):353–362, December 2000.

[199] M. L. Wasserman, A. S. Emanuel, and J. Seinfeld. Practical applications of optimal-control theory to history-matching multiphase simulator models. *SPE Journal*, pages 347–355, August 1975.

[200] A. T. Watson, J. H. Seinfeld, G. R. Gavalas, and P. T. Woo. History matching in two-phase petroleum reservoirs. *SPE Journal*, pages 521–532, December 1980.

[201] X.-H. Wen. *Stochastic Simulation of Groundwater Flow and Mass Transport in Heterogeneous Aquifers: Conditioning and Problem of Scales.* PhD thesis, Polytechnic University of Valencia, Spain, Valencia, Spain, 1996.

[202] X.-H. Wen, C. V. Deutsch, and A. S. Cullick. Integrating pressure and fractional flow data in reservoir modeling with fast streamline-based inverse method. In *SPE Annual Technical Conference and Exhibition*, pages 161–175, New Orleans, LA, September 1998. SPE Paper Number 48971.

[203] X.-H. Wen and J. J. Gómez-Hernández. Upscaling of hydraulic conductivity in heterogeneous media: An overview. *Journal of Hydrology*, 183:ix–xxxii, 1996.

[204] X.-H. Wen, J. J. Gómez-Hernández, J. E. Capillo, and A. Sahuquillo. Significance of conditioning on piezometric head data for predictions of mass transport in groundwater modeling. *Math. Geology*, 28(7):951–968, 1996.

[205] X.-H. Wen, T. T. Tran, R. A. Behrens, and J. J. Gómez-Hernández. Prodcution data integration in sand/shale reservoirs using sequential self-calibration and geomorphing: A comparison. In *SPE Annual Technical Conference and Exhibition*, Dallas, TX, October 2000. SPE Paper Number 63063.

[206] Z. Wu. A newton-raphson iterative scheme for integrating multiphase production data into reservoir models. In *SPE/AAPG Western Regional Meeting*, Houston, TX, June 2000. SPE Paper Number 62846.

[207] Z. Wu and A. Datta-Gupta. Rapid history matching using a generalized travel time inversion method. In *SPE Reservoir Simulation Symposium*, Houston, TX, February 2001. SPE Paper Number 66352.

[208] Z. Wu, A. C. Reynolds, and D. S. Oliver. Conditioning geostatistical models to two-phase production data. In *SPE Annual Technical Conference and Exhibition*, New Orleans, LA, September 1998. SPE Paper Number 49003.

[209] Z. Wu, A. C. Reynolds, and D. S. Oliver. Conditioning geostatistical models to two-phase production data. *SPEJ*, 4(2):142–155, June 1999.

[210] W. Xu, T. T. Tran, R. M. Srivastava, and A. G. Journel. Integrating seismic data in reservoir modeling: the collocated cokriging alternative. In *67th Annual Technical Conference and Exhibition*, pages 833–842, Washington, DC, October 1992. Society of Petroleum Engineers. SPE Paper Number 24742.

[211] G. Xue and A. Datta-Gupta. A new approach to seismic data integration during reservoir characterization using optimal non-parametric transformations. In *SPE 71st Annual Technical Conference and Exhibition*, Denver, CO, October 1996. Society of Petroleum Engineers. SPE Paper Number 36500.

[212] S. K. Yadavalli, J. R. Jones, L. D. Krase, N.-S. Yeh, and R. D. Roadifer. Use of pressure transient data to estimate permeability variograms. In *1995 SPE Annual Technical Conference and Exhibition*, pages 597–608, Dallas, TX, October 1995. Society of Petroleum Engineers. SPE Paper Number 30587.

[213] S. K. Yadavalli, R. D. Roadifer, J. R. Jones, L. D. Krase, and N.-S. Yeh. Use of pressure transient data to obtain geostatistical parameters for reservoir characterization. In *1994 SPE Annual Technical Conference and Exhibition*, New Orleans, LA, September 1994. Society of Petroleum Engineers. SPE Paper Number 28432.

[214] S. Yakowitz and L. Duckstein. Instability in aquifer identification: Theory and case studies. *Water Resources Research*, 16(9):1045–1064, 1980.

[215] T.-C. J. Yeh, M. Jin, and S. Hanna. An iterative stochastic inverse method: Conditional effective transmissivity and hydraulic head fields. *Water Resources Research*, 32(1):85–92, 1996.

[216] W. W.-G. Yeh. Review of parameter identification procedures in groundwater hydrology: The inverse problem. *Water Resources Research*, 22(2):95–108, 1986.

[217] S. Yoon, A. H. Malallah, A. Datta-Gupta, D. W. Vasco, and R. A. Behrens. A multiscale approach to production data integration using streamline approach. In *SPE Annual Technical Conference and Exhibition*, Houston, TX, October 1999. SPE Paper Number 56653.

[218] F. Zhang, A. C. Reynolds, and D. S. Oliver. Evaluation of the reduction in uncertainty obtained by conditioning a stochastic channel to multiwell pressure data. *Math. Geology*, 34(6):715–742, August 2002.

[219] D. A. Zimmerman, C. L. Axness, G. de Marsily, M. G. Marietta, and C. A. Gotway. Some results from a comparison study of geostatistically-based inverse techniques. Sandia National Laboratories, Albuquerque, NM, 1995.

# Appendix A

# Parameter Files in Computer Codes

This appendix briefly explains the parameters required for all the programs developed. The programs are arranged in order of chapters in the thesis. All the codes developed are presently for multiple-well single-phase inversion. These codes are for simultaneous inversion of $\phi$ and $\ln(k)$: **ssckphi**; for simultaneous inversion with variogram updating: **ssckphiv**; and finally, for fault property inversion: **ssckphif**. The source code, and parameter files may be supplied by the author on request.

## A.1 Program: ssckphi

A FORTRAN program, **ssckphi**, implements the methodology for simultaneous inversion of $\phi$ and $\ln(k)$. This **ssckphi** code allows to generate porosity and permeability realizations that honor a specified spatial variation structure defined by histogram and variogram, yet match dynamic multiple well production data.

The reservoir model is assumed 2-D rectangular discretized into $N_x$ by $N_y$ square cells with the size of each cell being $d_x = d_y$. The grid cells are numbered as shown in Figure A.1. Parameters required for **ssckphi** are given below:

- **datafl:** the file with local well conditioning $\phi$ and $\ln(k)$ data.
- **ixl, iyl, ivrlph, ivrrlph, ivrlk, ivrrlk:** the column numbers for $x$, $y$ coordinates, $\phi$, error in $\phi$, $\ln(k)$ and error in $\ln(k)$.
- **ntmedph, ntmedk, nwell:** the number of $\phi$, $\ln(k)$ data and the number of wells with flow data.
- **itrans:** the index for identifying desired histogram.
- **transfl:** the file with $\ln(k)$ histogram. Should be of the same scale as the SSCKPHI model.
- **ihvph,ihwtph,ihvk,ihwtk:** the column numbers for $\phi$, weight of $\phi$, $\ln(k)$ and weight of $\ln(k)$ in the desired histogram.
- **parltph,parutph,parltk,parutk:** lower and upper tail parameters for $\phi$ and $\ln(k)$ used in histogram transformation.
- **tmsk0, vtmsk0:** the apriori mean and variance of $\ln(k)$.
- **tmsph0, vtmsph0:** the apriori mean and variance of $\phi$.
- **wellpmfl:** the data file with reservoir and well parameters.

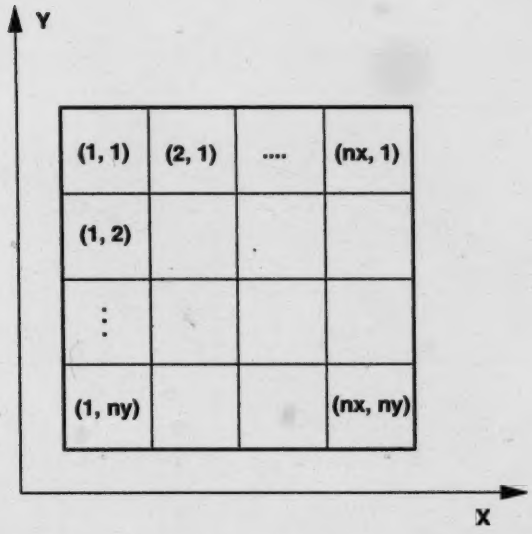


Figure A.1: Discretization and numbering of numerical reservoir model used in the **ssckphi** code.

- **flowrtfl:** the data file with input flow rate (STB/DAYS) and time step data.
- **wellprfl:** the data file with input pressure data (psia).
- **boundfl:** the data file boundary data.
- **initprfl:** the data file with initial pressure (psia) for the entire reservoir in GEOEAS format.
- **seedfl:** the data file with initial $\phi$ and $\ln(k)$ field in GEOEAS format.
- **icolph, icolk:** the column numbers for $\phi$ and $\ln(k)$ in **seedfl**.
- **nsim, nsim1, nsim2:** the number of total, start and end realizations.
- **tminph,tmaxph,tmink,tmaxk:** trimming limits for $\phi$ and $\ln(k)$.
- **idbg:** an integer debugging level between 0 and 3. The larger the debugging level, the more information written out.
- **dbgfl:** the file for the debugging output.
- **outfl:** the output file for $\ln(k)$ distribution in GEOEAS format.
- **objfl:** the output file for normalized objective function after each iteration . The first two records and the last records are total number iteration, initial normalized objective function, final objective function value.
- **prmtchfl:** the output file for pressure match responses. This gives the observed, the initial and the updated pressures at each time step in GEOEAS format.
- **nx, xmn, xsiz:** the definition of the grid system ($x$ axis).
- **ny, ymn, ysiz:** the definition of the grid system ($y$ axis).

- **iseed:** the random number seed.
- **nmpx, nmpy:** the number of master points in $x$ and $y$ directions.
- **it_gmp:** the number of iterations to update master points.
- **am_y:** the factor for defining the constraint interval for optimization.
- **nitera, relax, dconve:** the maximum number of outer iterations, dumping parameter and minimum tolerance.
- **it_min, eps3, eps4, eps5, ifobj:** the optimization parameters.
- **radius:** the search radius (ft) in kriging.
- **ndmin, ndmax:** the minimum and the maximum number of samples for kriging.
- **ktype:** the type of kriging. (**ktype=0** ordinary kriging, **ktype=1:** simple kriging).
- **colcorr:** corelation coefficient between $\phi$ and $\ln(k)$.
- **nstph** and **c0ph:** the number of variogram structures and the isotropic nugget effect for $\phi$.
- **itph(i), ccph(i), angph(i), aa1ph, aa2ph:** For each of the **nst** nested structures one must define the type of structure, the $c$ parameter, the angle defining the geometric anisotropy, the maximum horizontal range, the minimum horizontal range for $\phi$.
- **nstk** and **c0k:** the number of variogram structures and the isotropic nugget effect for $\ln(k)$.
- **itk(i), cck(i), angk(i), aa1k, aa2k:** For each of the **nst** nested structures one must define the type of structure, the $c$ parameter, the angle defining the geometric anisotropy, the maximum horizontal range, the minimum horizontal range for $\ln(k)$.

## A.2 Program: ssckphiv

A FORTRAN program, **ssckphiv**, implements the methodology for simultaneous inversion of $\phi$ and $\ln(k)$ with variogram updating. This **ssckphiv** code allows to generate porosity and permeability realizations that honor a specified spatial variation structure defined by histogram and variogram, yet match dynamic multiple well production data. This code also updates and model variograms.

The reservoir model is assumed 2-D rectangular discretized into $N_x$ by $N_y$ square cells with the size of each cell being $d_x = d_y$. The grid cells are numbered as shown in Figure A.1. Parameters required for **ssckphiv** are given below:

- **datafl:** the file with local well conditioning $\phi$ and $\ln(k)$ data.
- **ixl, iyl, ivrlph, ivrrlph, ivrlk, ivrrlk:** the column numbers for $x$, $y$ coordinates, $\phi$, error in $\phi$, $\ln(k)$ and error in $\ln(k)$.
- **ntmedph, ntmedk, nwell:** the number of $\phi$, $\ln(k)$ data and the number of wells with flow data.
- **itrans:** the index for identifying desired histogram.
- **transfl:** the file with $\ln(k)$ histogram. Should be of the same scale as the SSCKPHIV model.
- **ihvph,ihwtph,ihvk,ihwtk:** the column numbers for $\phi$, weight of $\phi$, $\ln(k)$ and weight of $\ln(k)$ in the desired histogram.

- **parltph,parutph,parltk,parutk:** lower and upper tail parameters for $\phi$ and $\ln(k)$ used in histogram transformation.
- **tmsk0, vtmsk0:** the apriori mean and variance of $\ln(k)$.
- **tmsph0, vtmsph0:** the apriori mean and variance of $\phi$.
- **apriorminph,apriormaxph:** the apriori minimum and maximum for $\phi$ values.
- **apriorminy,apriormaxy:** the apriori minimum and maximum for $\ln(k)$ values.
- **wellpmfl:** the data file with reservoir and well parameters.
- **flowrtfl:** the data file with input flow rate (STB/DAYS) and time step data.
- **wellprfl:** the data file with input pressure data (psia).
- **boundfl:** the data file boundary data.
- **initprfl:** the data file with initial pressure (psia) for the entire reservoir in GEOEAS format.
- **seedfl:** the data file with initial $\phi$ and $\ln(k)$ field in GEOEAS format.
- **icolph, icolk:** the column numbers for $\phi$ and $\ln(k)$ in **seedfl**.
- **nsim, nsim1, nsim2:** the number of total, start and end realizations.
- **tminph,tmaxph,tmink,tmaxk:** trimming limits for $\phi$ and $\ln(k)$.
- **idbg:** an integer debugging level between 0 and 3. The larger the debugging level, the more information written out.
- **dbgfl:** the file for the debugging output.
- **outfl:** the output file for $\ln(k)$ distribution in GEOEAS format.
- **objfl:** the output file for normalized objective function after each iteration . The first two records and the last records are total number iteration, initial normalized objective function, final objective function value.
- **prmtchfl:** the output file for pressure match responses. This gives the observed, the initial and the updated pressures at each time step in GEOEAS format.
- **nx, xmn, xsiz:** the definition of the grid system ($x$ axis).
- **ny, ymn, ysiz:** the definition of the grid system ($y$ axis).
- **iseed:** the random number seed.
- **nmpx, nmpy:** the number of master points in $x$ and $y$ directions.
- **it_gmp:** the number of iterations to update master points.
- **am_y:** the factor for defining the constraint interval for optimization.
- **nitera, relax, dconve:** the maximum number of outer iterations, dumping parameter and minimum tolerance.
- **it_min, eps3, eps4, eps5, ifobj:** the optimization parameters.
- **radius:** the search radius (ft) in kriging.
- **ndmin, ndmax:** the minimum and the maximum number of samples for kriging.

- **ktype:** the type of kriging. (**ktype=0** ordinary kriging, **ktype=1:** simple kriging).
- **colcorr:** corelation coefficient between $\phi$ and $\ln(k)$.
- **nstph** and **c0ph:** the number of variogram structures and the isotropic nugget effect for $\phi$.
- **itph(i), ccph(i), angph(i), aa1ph, aa2ph:** For each of the **nst** nested structures one must define the type of structure, the $c$ parameter, the angle defining the geometric anisotropy, the maximum horizontal range, the minimum horizontal range for $\phi$.
- **nstk** and **c0k:** the number of variogram structures and the isotropic nugget effect for $\ln(k)$.
- **itk(i), cck(i), angk(i), aa1k, aa2k:** For each of the **nst** nested structures one must define the type of structure, the $c$ parameter, the angle defining the geometric anisotropy, the maximum horizontal range, the minimum horizontal range for $\ln(k)$.
- **nlagph,nlagy:** the number of lags used in variogram calculation for $\phi$ and $\ln(k)$.
- **xlagph,xlagy:** lag separation distance used in variogram calculation for $\phi$ and $\ln(k)$.
- **xltolph,xltoly:** lag tolerance used in variogram calculation for $\phi$ and $\ln(k)$.
- **ndirph,ndiry:** the number of directions used in variogram calculation for $\phi$ and $\ln(k)$.
- **azmph(i), atolph(i), bandwhph(i):** For each of the **ndirph** directions one must define the azimuth angle, the the angle of azimuth tolerance, the bandwidth for $\phi$.
- **azmy(i), atoly(i), bandwhy(i):** For each of the **ndiry** directions one must define the azimuth angle, the the angle of azimuth tolerance, the bandwidth for $\ln(k)$.

## A.3 Program: ssckphif

A FORTRAN program, **ssckphif**, implements the methodology for inversion of fault property as well as $\phi$ and $\ln(k)$. This **ssckphif** code generates fault block permeability and porosity values and allows to generate porosity and permeability realizations that honor a specified spatial variation structure defined by histogram and variogram, yet match dynamic multiple well production data.

The reservoir model is assumed 2-D rectangular discretized into $N_x$ by $N_y$ square cells with the size of each cell being $d_x = d_y$. The grid cells are numbered as shown in Figure A.1. Parameters required for **ssckphif** are given below:

- **datafl:** the file with local well conditioning $\phi$ and $\ln(k)$ data.
- **ixl, iyl, ivrlph, ivrrlph, ivrlk, ivrrlk:** the column numbers for $x$, $y$ coordinates, $\phi$, error in $\phi$, $\ln(k)$ and error in $\ln(k)$.
- **ntmedph, ntmedk, nwell:** the number of $\phi$, $\ln(k)$ data and the number of wells with flow data.
- **itrans:** the index for identifying desired histogram.
- **transfl:** the file with $\ln(k)$ histogram. Should be of the same scale as the SSCKPHIV model.
- **ihvph,ihwtph,ihvk,ihwtk:** the column numbers for $\phi$, weight of $\phi$, $\ln(k)$ and weight of $\ln(k)$ in the desired histogram.

- **parltph,parutph,parltk,parutk:** lower and upper tail parameters for $\phi$ and $\ln(k)$ used in histogram transformation.
- **tmsk0, vtmsk0:** the apriori mean and variance of $\ln(k)$.
- **tmsph0, vtmsph0:** the apriori mean and variance of $\phi$.
- **apriorminph,apriormaxph:** the apriori minimum and maximum for $\phi$ values.
- **apriorminy,apriormaxy:** the apriori minimum and maximum for $\ln(k)$ values.
- **wellpmfl:** the data file with reservoir and well parameters.
- **flowrtfl:** the data file with input flow rate (STB/DAYS) and time step data.
- **wellprfl:** the data file with input pressure data (psia).
- **boundfl:** the data file boundary data.
- **initprfl:** the data file with initial pressure (psia) for the entire reservoir in GEOEAS format.
- **seedfl:** the data file with initial $\phi$ and $\ln(k)$ field in GEOEAS format.
- **icolph, icolk:** the column numbers for $\phi$ and $\ln(k)$ in **seedfl**.
- **nsim, nsim1, nsim2:** the number of total, start and end realizations.
- **tminph,tmaxph,tmink,tmaxk:** trimming limits for $\phi$ and $\ln(k)$.
- **idbg:** an integer debugging level between 0 and 3. The larger the debugging level, the more information written out.
- **dbgfl:** the file for the debugging output.
- **outfl:** the output file for $\ln(k)$ distribution in GEOEAS format.
- **objfl:** the output file for normalized objective function after each iteration . The first two records and the last records are total number iteration, initial normalized objective function, final objective function value.
- **prmtchfl:** the output file for pressure match responses. This gives the observed, the initial and the updated pressures at each time step in GEOEAS format.
- **nx, xmn, xsiz:** the definition of the grid system ($x$ axis).
- **ny, ymn, ysiz:** the definition of the grid system ($y$ axis).
- **iseed:** the random number seed.
- **nmpx, nmpy:** the number of master points in $x$ and $y$ directions.
- **it_gmp:** the number of iterations to update master points.
- **am_y:** the factor for defining the constraint interval for optimization.
- **nitera, relax, dconve:** the maximum number of outer iterations, dumping parameter and minimum tolerance.
- **it_min, eps3, eps4, eps5, ifobj:** the optimization parameters.
- **radius:** the search radius (ft) in kriging.
- **ndmin, ndmax:** the minimum and the maximum number of samples for kriging.

- **ktype:** the type of kriging. (**ktype=0** ordinary kriging, **ktype=1:** simple kriging).
- **colcorr:** corelation coefficient between $\phi$ and $\ln(k)$.
- **nstph** and **c0ph:** the number of variogram structures and the isotropic nugget effect for $\phi$.
- **itph(i), ccph(i), angph(i), aa1ph, aa2ph:** For each of the **nst** nested structures one must define the type of structure, the $c$ parameter, the angle defining the geometric anisotropy, the maximum horizontal range, the minimum horizontal range for $\phi$.
- **nstk** and **c0k:** the number of variogram structures and the isotropic nugget effect for $\ln(k)$.
- **itk(i), cck(i), angk(i), aa1k, aa2k:** For each of the **nst** nested structures one must define the type of structure, the $c$ parameter, the angle defining the geometric anisotropy, the maximum horizontal range, the minimum horizontal range for $\ln(k)$.
- **nfault:** the number of faults present.
- **ndatf(i),facmultph(i),facmultk(i),facmultphv(i),facmultkv(i):** For each of the **nfault** faults one must define the number of data specified, apriori $\phi$, $\phi$ variance, $\ln(k)$, $\ln(k)$ variance values.
- **faultdatfl:** the input file with fault specifications in GEOEAS format.
- **nmpfit:** the number of master point used for each fault.
- **faultmultfl:** the output file for fault multipliers.

# Appendix B

# Sensitivity Analysis and Derived Information

*This chapter describes an independent study on the sensitivity coefficients of the simulation responses with respect to reservoir parameters. However, it should be noted that no conclusive work or message is brought forth in this appendix. However, the appendix reveals some interesting informstion on the behavior of the sensitivity coefficients that may be exploited in some future work.*

## B.1 Introduction

An important constituent of a research on dynamic data integration is the computation and investigation of the sensitivities of reservoir parameters to the simulation responses. Understanding the behavior of these sensitivity coefficients is critical to dynamic data integration in reservoir characterization.

The reservoir simulator, `Eclipse`, is widely used [180]. It has been used, verified and validated for numerous reservoir scenarios, and many research and reservoir management studies have been based on the responses of this reservoir simulator. `Eclipse` has the feature of reporting certain sensitivity coefficients.

## B.2 Sensitivity Computation

The finite-difference formulation of the governing flow equations for 3D 3-phase reservoir simulation can be represented as:

$$F(U^{n+1}, U^n, \theta) = 0 \tag{B.1}$$

where $U^{n+1} = [P_o \ S_w \ S_g \ \ldots]^T$ at time step $(n+1)$, that is, the response variables to be simulated. Let $[\Theta] = [\theta_1 \ \theta_2 \ \cdots \theta_M] = [k \ \phi \ \ldots]^T$ be the set of reservoir simulation parameters, which may be the permeability vectors, porosity at all grid location. These algebraic equations are strongly coupled nonlinear ones. Gradient based iterative techniques used for the solution of the above equations involves:

$$\frac{\partial f}{\partial U^{n+1}}(U^{(k+1)} - U^{(k)}) = -f(U^{(k)}, U^n, \Theta) \tag{B.2}$$

where the superscript $k$ is the iteration index, while $n$ refers to the time step.

The sensitivity coefficients of the response variables with respect to any parameter, $\theta$, can be written as

$$\frac{\partial U^{n+1}}{\partial \theta}$$

| Variable | Variogram |
|---|---|
| Porosity | $\gamma_\phi(h) = 0.1 + 0.9Sph_{\substack{a_x=a_y=5000ft \\ a_z=15ft}}(h)$ |
| Permeability | $\gamma_k(h) = 0.3 + 0.7Sph_{\substack{a_x=a_y=5000ft \\ a_z=15ft}}(h)$ |

Table B.1: Porosity and permeability variograms for the 'base case' reservoir model.

which can be computed indirectly from Equation B.1 or B.2. Differentiation with respect to parameter $\theta$ of the flow equation (Equation B.1) leads to:

$$\frac{\partial f}{\partial U^{n+1}}\frac{\partial U^{n+1}}{\partial \theta} + \frac{\partial f}{\partial U^{n}}\frac{\partial U^{n}}{\partial \theta} + \frac{\partial f}{\partial \theta} = 0 \tag{B.3}$$

which can be rearranged to obtain

$$\frac{\partial U^{n+1}}{\partial \theta} = -\left[\frac{\partial f}{\partial U^{n+1}}\right]^{-1}\left(\frac{\partial f}{\partial U^{n}}\frac{\partial U^{n}}{\partial \theta} + \frac{\partial f}{\partial \theta}\right) \tag{B.4}$$

At each time step, discretized flow equations are solved once. In other words, the Jacobian of the flow equations, $\left[\frac{\partial f}{\partial U^{n+1}}\right]$, is inverted only once. The sensitivity coefficient with respect to any reservoir parameter $\theta$ is obtained using Equation B.4. This is an efficient approach as flow equations are solved only once regardless of the number of reservoir parameters. However, the computation time increases by a factor of (0.1-0.2) times the usual run for each sensitivity parameter depending on the complexity of the problem.

## B.3 Base Case Reservoir Description

In order to investigate the behavior of computed sensitivities, a 'base case' reservoir scenario is studied. A regular grid of 64×64×16 is considered with dimensions 500 ft × 500 ft × 7.5 ft for the reservoir overlying an aquifer (grid: 64×64×2; dimensions: 500 ft × 500 ft × 15 ft). A single structure variogram is used to generate a porosity model. Permeability is generated using collocated cokriging using the porosity model and correlation coefficient of 0.7. Variogram models used for porosity and permeability are shown in Table B.1. To simplify the problem, anisotropy is considered only for the vertical direction by a multiplier of 0.1. Porosity is considered to have truncated normal distribution with a mean of 10% and variance 25%, while permeability a log-normal distribution with a mean 100 mD and variance 1000 $mD^2$. Aquifer properties are homogeneous with a porosity of 0.1 and a permeability of 100 mD. The idea is to model a reservoir with a moderate bottom-water drive. This emulates a realistic reservoir fluid flow situation. Figure B.1 shows the isometric view of the porosity model.

A simplified two-phase oil-water system is employed for the simulation. The capillary pressure and the relative permeability curves for the "base case" are shown in Figure B.2. There is only one transition zone (layer 16) over the aquifer. Four producing wells are considered at (X,Y) grid locations (16, 17), (45, 15), (14, 40) and (39, 47). Top 12 grids of each are completed. For the limits of well controls, maximum oil production rate, maximum water production rate, maximum reservoir fluid volume flow rate and minimum bottom-hole pressure are set at 5000 STBD, 1500 STBD, 5000 RBD and 1000 PSI, respectively. It should be noted that no artificial well control change (e.g. well recompletions, plugging, etc.) has been activated for the base case simulation.

For the base case simulation run, the flow responses are obtained with ECLIPSE 100. Bottom-hole pressure, oil production rate and water-cut are shown here only for well 1 and well 2 in Figures B.3. The history of well control changes are shown in Table B.2.

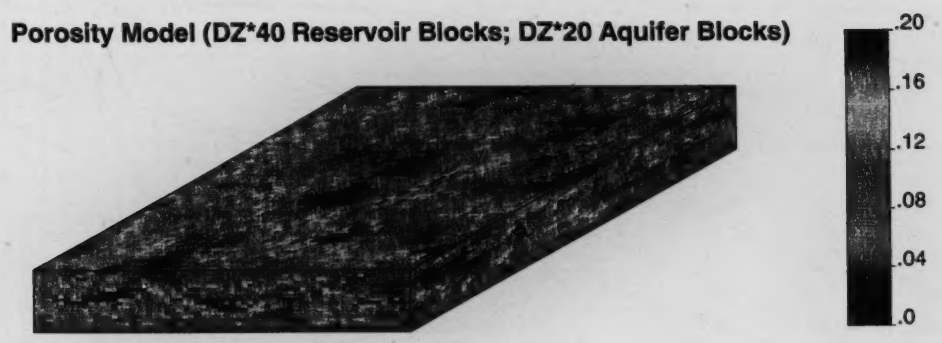


Figure B.1: Porosity model for the 'base case'.

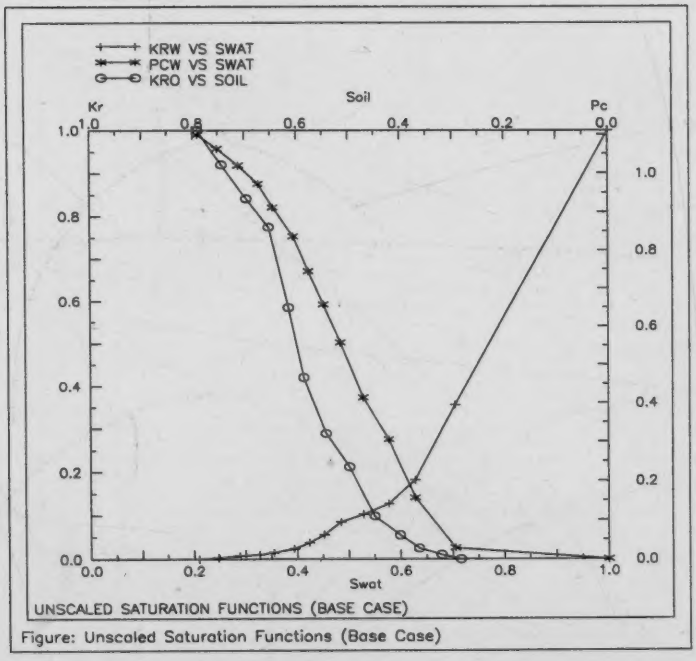


Figure B.2: Relative permeability and capillary pressure curves used for the 'base case'.

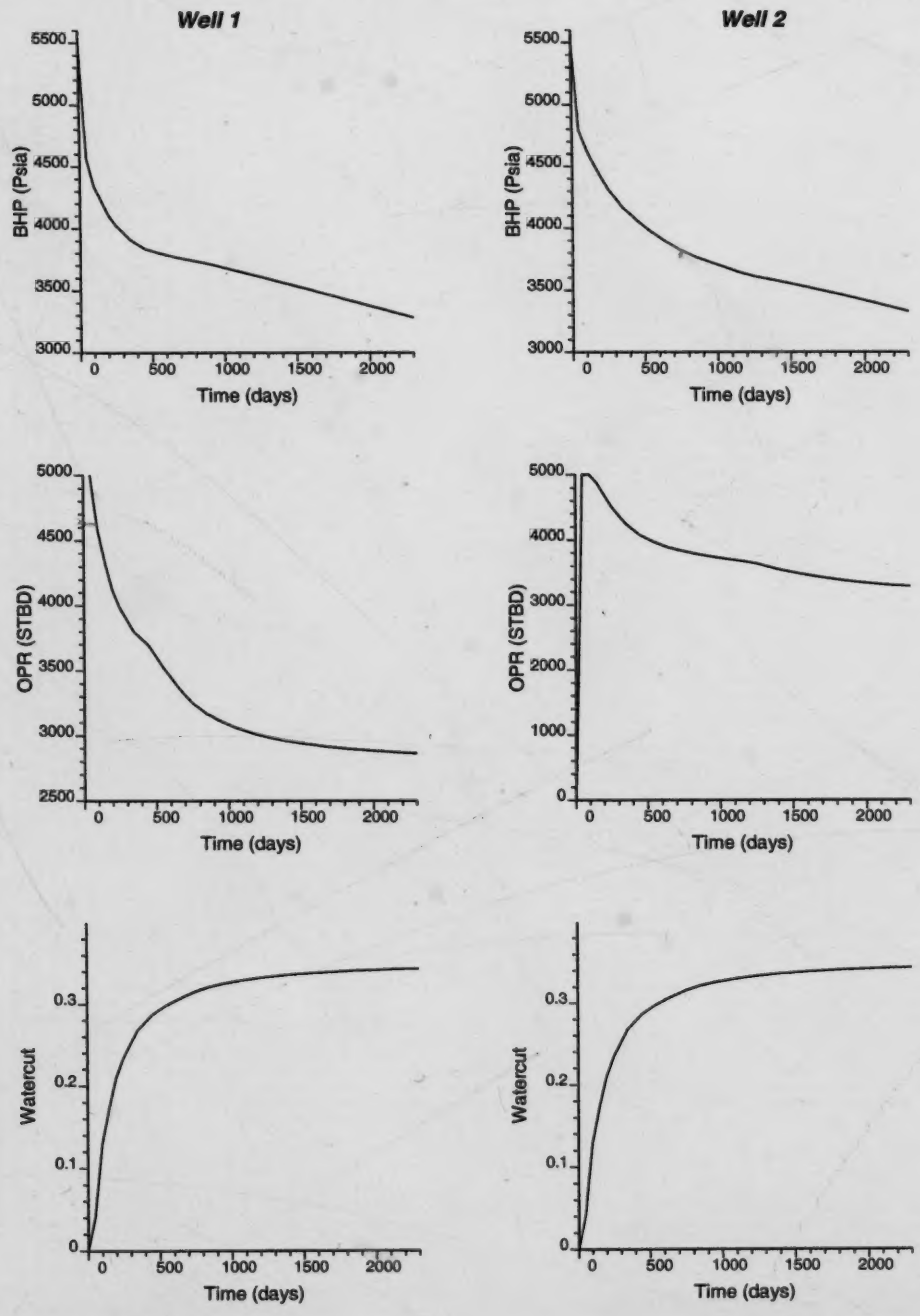


Figure B.3: Flow responses for the 'base case'. (BHP - Bottom-hole flowing pressure, OPR - Oil production rate

## B.4 Region Specification for Sensitivity Computation

In order to compute the sensitivities, reservoir parameters must be identified and their regions defined. The focus here is only on the permeabilities and porosities. Originally, the objective of the present study is to acquire as much information as possible from the computed gradients. Their pattern, behavioral changes in time, particularly due to some 'event' during the simulation period, may capture the influence of reservoir heterogeneity. Regions definition can be 'ad hoc', suitable to specific goals of the study. Regions can be chosen to be oriented along some geological features that are hypothesized to be present in the reservoir. Sensitivity of the response variables with respect to the parameters are computed for the defined regions and investigated. For the base case sensitivity calculation, five regions are defined for each parameter: transmissibility in the $x-$direction and pore volume. Figure B.4 shows the region definition for the gradient parameters.

## B.5 Typical Sensitivity Coefficient Behavior

For the 'base case' reservoir study, the sensitivity coefficients are computed. Parameters considered are transmissivity in $x-$direction and pore volume. Well variables for the sensitivities are analyzed are well bottom-hole pressure, well oil production rate, and well water-cut. The general behavior of the sensitivity coefficients can be quite complex depending on the flow and reservoir complexity. Signatures of various events are often present in the sensitivity coefficients. However, this depends on numerous factors and can be often masked by the interferences of different concurrent phenomena.

Figure B.5 shows the sensitivity coefficients computed for the 'base case' for Well 1 which is located at (16,17) in Region 1. These coefficients are for well bottom-hole pressure, well oil production rate, and well water cut with respect to $x-$direction transmissivity of Region 1. Events **A** after 50 days and **G** after 450 days have more pronounced effect on the trends as these events involve Well 1. There may be communication between the wells. The sensitivity coefficients here are reported only at the specified reporting intervals. A detailed investigation is required in order to fully understand these sensitivity curves.

### Results with Only One Well

A logical next approach is to decouple the problem by retaining only one well instead of four wells for the same reservoir description. Thus, there will be no well interference. With only Well 1 in Region 1 active, the sensitivity coefficients are computed. Figure B.6 shows the gradient for Well 1 bottom-hole pressure with respect to $x-$direction transmissivity of Region 1 at specified reporting intervals.

Comparing Figure B.6 with Figure B.5 (top one - for bottom-hole pressure), it can be seen that early time and late time trends are quite similar. However, there are significant dissimilarities between the two curves. This suggests that interwell communication affects

| Event ID | Days | Event |
|---|---|---|
| **A** | 50 | Well 1 and Well 4 change from oil rate control to reservoir fluid rate control |
| **B** | 74.5 | Well 3 changes to reservoir fluid rate control |
| **C** | 100 | Well 2 changes to reservoir fluid rate control |
| **D** | 450 | Well 1 changes to water rate control |
| **E** | 550 | Well 4 changes to water rate control |
| **F** | 600 | Well 3 changes to water rate control |
| **G** | 1150 | Well 2 changes to water rate control |

Table B.2: Well control history for the 'base case' simulation with four wells.

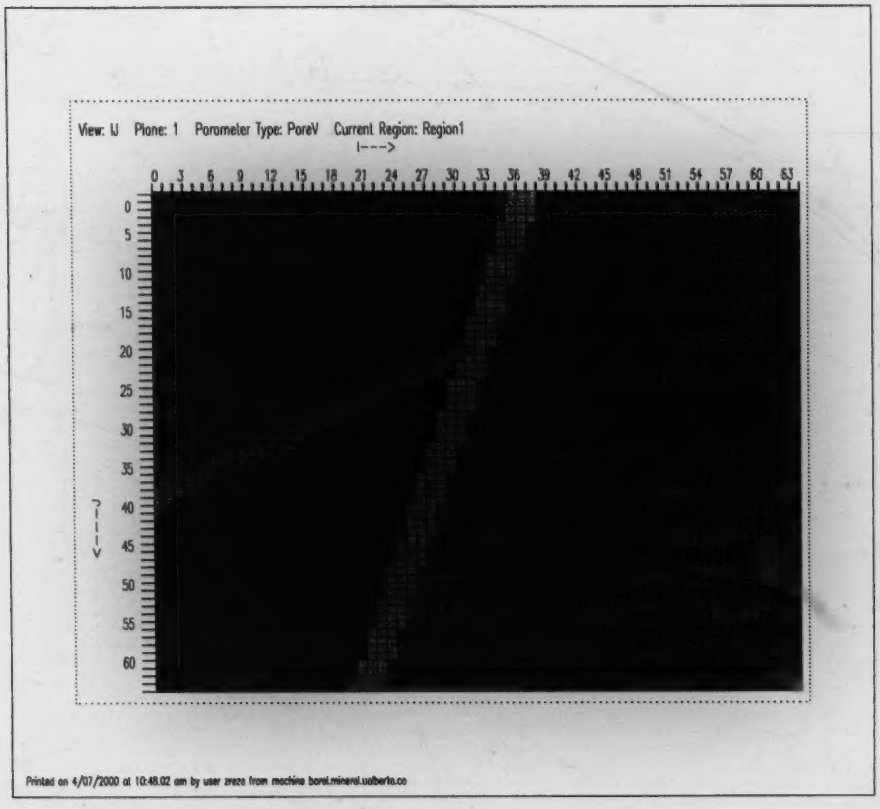
View: U Plane: 1 Porometer Type: PoreV Current Region: Region1
I--->
0 3 6 9 12 15 18 21 24 27 30 33 36 39 42 45 48 51 54 57 60 63
0 5 10 15 20 25 30 35 40 45 50 55 60
J
I
V
Printed on 4/07/2000 at 10:48.02 am by user zreza from machine borel.mineral.ualberta.ca

Figure B.4: Parameter regions definition for the 'base case'. (Region 1: red, Region 2: green, Region 3: blue, Region 4: light blue; Region 5: purple)

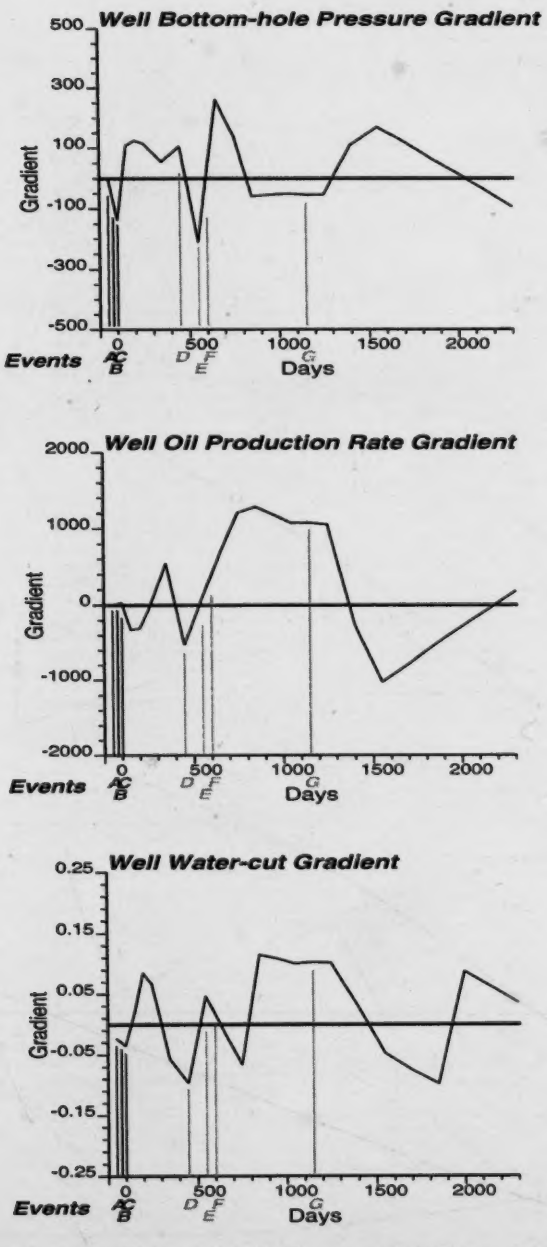


Figure B.5: Sensitivity coefficients for the 'base case' Well 1 bottom-hole pressure, oil production rate, and watercut with respect to Region 1 transmissibility. Events labeled (vertical lines) **A** to **G** are those in Table B.2.

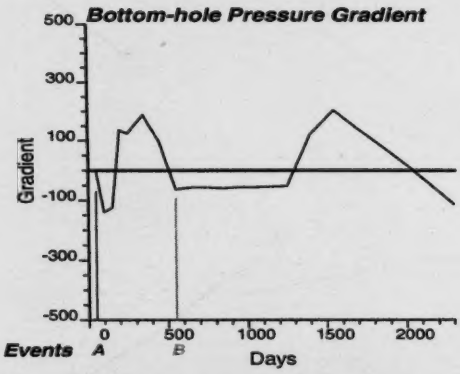


Figure B.6: Sensitivity coefficients for the 'base case' (1 Well Case) Well 1 bottom-hole pressure with respect to Region 1 transmissibility. Events labeled (vertical lines) are those in Table B.3.

| Event ID | Days | Event |
|---|---|---|
| A | 50 | Well 1 changes from oil rate control to reservoir fluid rate control |
| B | 450 | Well 1 changes to water rate control |

Table B.3: Well control history for the 'base case' simulation with only Well 1.

the sensitivity coefficient behavior as early as about 200 days. Well events have pronounced effect on the coefficients.

## Results for Different Regions

Not all wells are equally sensitive to all the regions. Sensitivity coefficients for regions in which wells are located are orders of magnitude higher than other regions. Figure B.7 shows the sensitivity coefficients of well bottom-hole pressure for Region 1, 2 and 5 for both cases: 'base case' with all four wells, and 'base case' with only Well 1. Well 1 is in Region 1. Thus, sensitivities with respect to parameters in Region 1 are quite large. Whereas, for the parameters in Region 2, which is the narrow strip of region along a presumed fault plane, well variables are almost totally insensitive. While, the variables are only slightly sensitive to parameters in region 5. A close look at the figure says that Well 1 bottom-hole pressure is slightly sensitive to Region 5 transmissivity when well interferences are active. It should be noted that these results apply to this case only.

## Effect of Reporting Specification

The sensitivity coefficients calculated above have been computed at the specified reporting interval only. For a better interpretation, the coefficients may be computed at all time steps (chopped and regular). It is observed that this can be a significant factor particularly when there are many events/phenomena happening in the subsurface flow process or there are some occurrences of non-convergence in the solution process. Figure B.8 illustrates this point. Gradients are computed with the same reservoir description but at all time steps. The figure reveals at early time when there are a few instances of chopped time steps due to some event or problem with solution process, the trends in the gradient curves are dissimilar. Gradients will be computed at all time steps for future investigation and analysis.

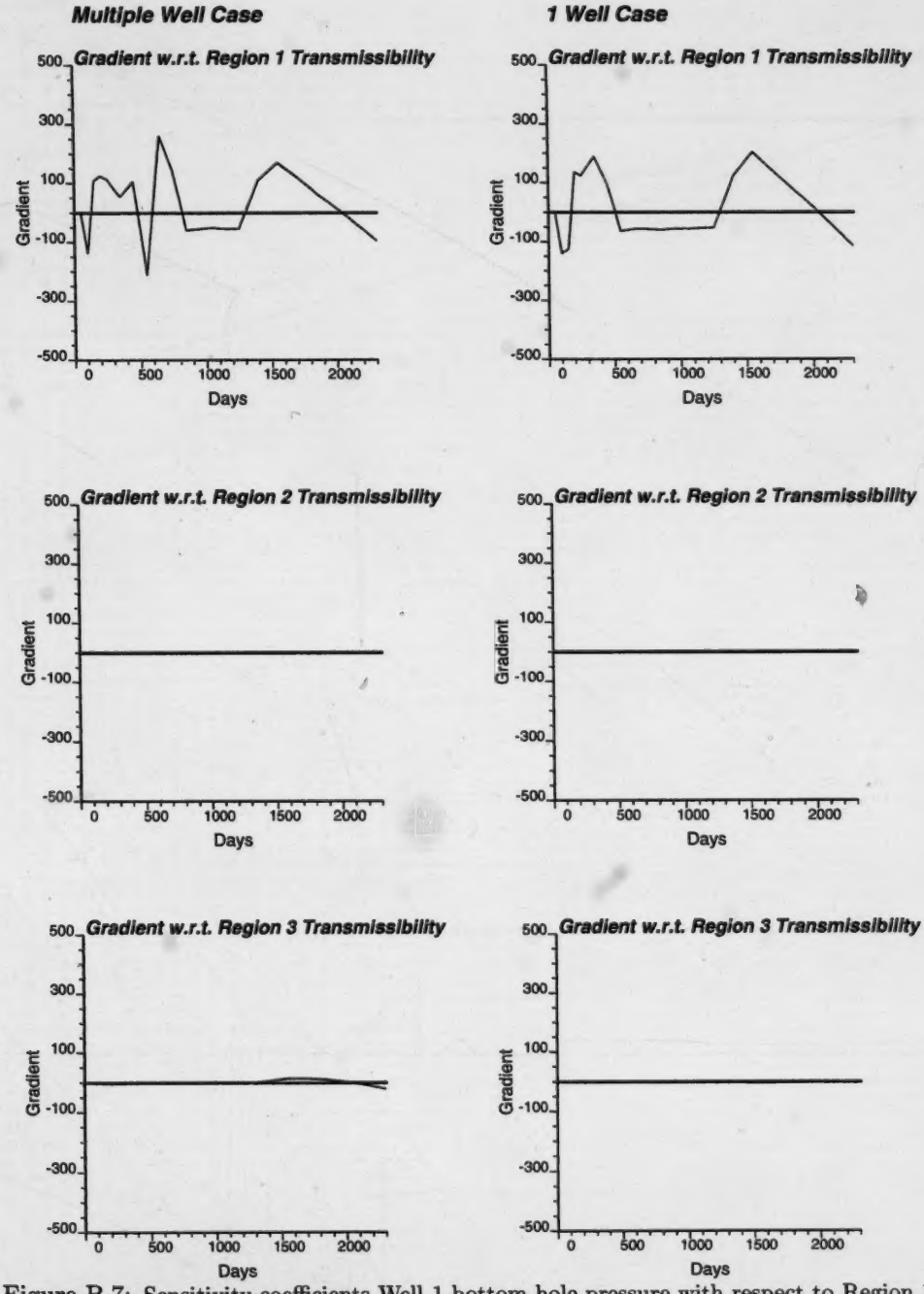


Figure B.7: Sensitivity coefficients Well 1 bottom-hole pressure with respect to Region 1, 2 and 5 transmissibility (Multiple Well Case and 1 Well Case).

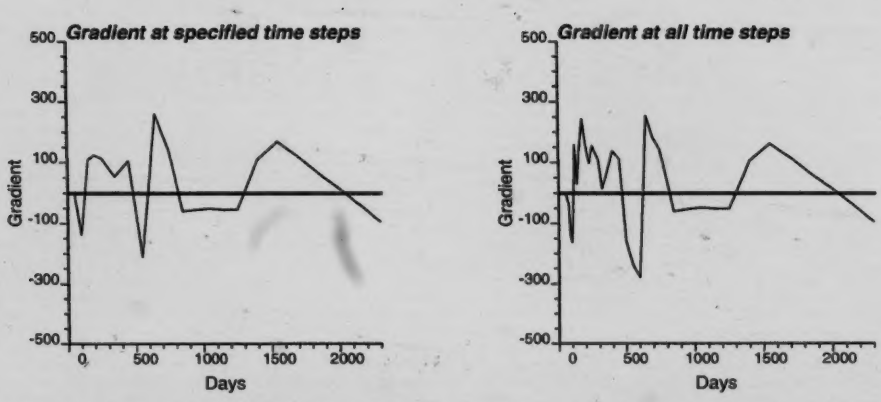


Figure B.8: Effect of reporting specification on bottomhole pressure sensitivity coefficients.

## B.6 Factors Affecting Sensitivity Coefficients

Several investigations were done to determine the changes in the sensitivity coefficient curves. How do these curves change when aquifer strength changes, or artificial well controls are activated? Does heterogeneity have a significant effect on the gradients? Are volumes or shapes of parameter regions important in this analysis? Does well location or grid configuration play a role?

### Strength of Aquifer

The flow process in a reservoir with a bottom-water drive can be quite complicated with water-coning and other flow phenomena. The volume of an aquifer can be considered as a measure of the strength of the underlying aquifer. To determine the effect of aquifer strength on the sensitivity coefficients, the aquifer thickness is changed.

To simplify the analysis, the reservoir description with only one well is investigated. The 'base case' has an aquifer thickness of 30 feet. Keeping the reservoir description same as in 'base case', the aquifer thickness is varied from 5 feet to 100 feet. Figure B.9 shows the sensitivity coefficients for Well 1 bottom-hole pressure with respect to $x-$direction transmissivity of Region 1 for these 3 cases. The figure reveals a significant change in the sensitivity coefficients as the aquifer strength changes.

In case of weak aquifer, well control changes only once (at 175 days) from oil rate control mode to reservoir fluid rate control mode. In fact, Well 1 does not attain water rate control during the simulation period. This makes a significant difference in the late time behavior from the other two cases. Strong aquifer case has similar trends as in the 'base case'. However, the well bottom-hole pressure is less sensitive to the region transmissibility (Region 1) when the aquifer is stronger. This is expected as pressure support will be higher for a reservoir with a stronger aquifer support or water-drive.

### Effect of Well Control

Due to numerous management decisions, well configurations or modes of operations are changed often within the life of a well. For example, a well connection may be artificially shut off at some depth when water coning occurs or is about to occur. These well control changes drastically affect the sensitivity coefficients.

To illustrate the effect of well controls, reservoir description with a strong underlying aquifer is chosen. The rationale for investigating the strong aquifer is that there are more occurrences of well control changes because of escalated water coning. Figure B.10 reveals significant differences in the sensitivity coefficients with and without artificial well controls. Event history for the case with artificial well control is tabulated in Table B.4. Figure B.10

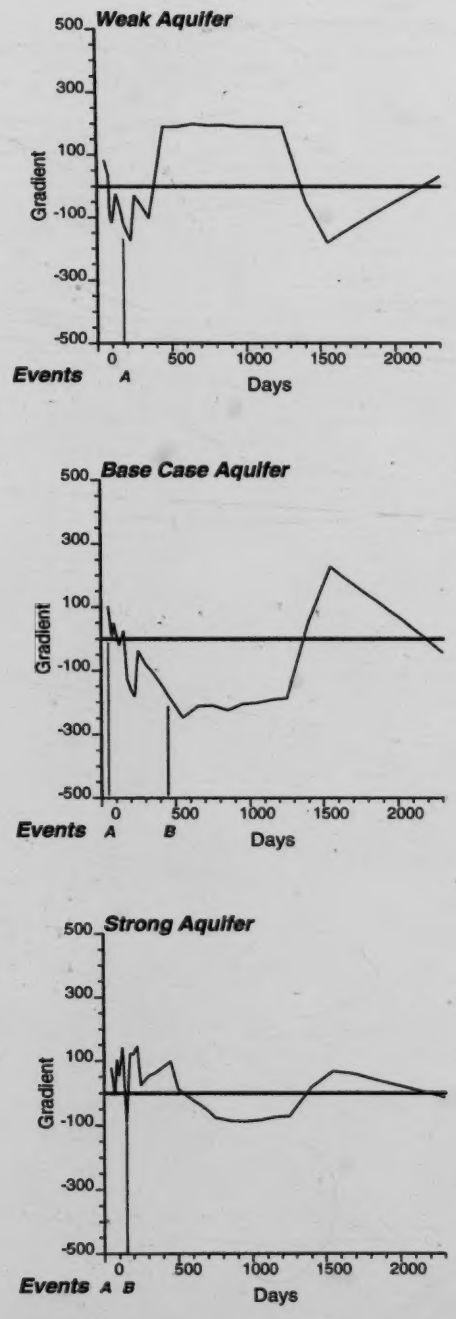


Figure B.9: Bottom-hole pressure sensitivity coefficients with respect to Region 1 transmissibility for cases: weak aquifer, 'base case' aquifer and strong aquifer. Events A (red): well control changes from oil rate control mode to reservoir fluid rate control mode; Events B (blue): well control changes to water rate control mode.

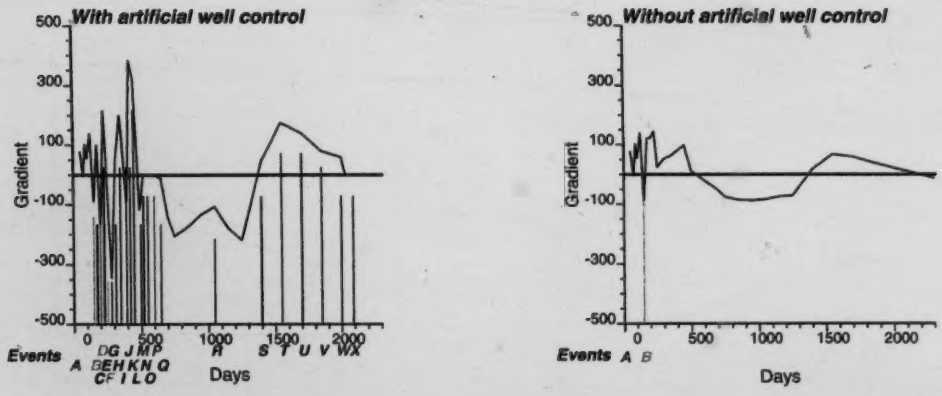


Figure B.10: Bottom-hole pressure sensitivity coefficients with respect to Region 1 transmissibility for cases: one with artificial well controls and the other without artificial well control. Events A to X are described in Table B.4.

reveals that before artificial well controls are activated (i.e. before 150 days) the trends are exactly same. Once a 'worst-offending connection' is shut off, subsequent gradient behavior changes significantly.

It is observed that the effect of any particular event, as water rate control mode, is not always the same. It depends on phase saturations, pressure level etc. An event like connection shut-off may cause higher oil production rate if oil phase in the vicinity has sufficient mobility and well bottom-hole pressure will decrease; however, when this is not the situation, flow of both oil and water is hindered and well bottom-hole pressure increases. The gradients show corresponding changes. Similarly, the effect of bottom-hole pressure control mode can be determined. In this case, there will not be any pressure sensitivity, but gradients of oil production rate or water-cut may change significantly.

## Effect of Temporal Discretization

A study was conducted whether temporal discretization in the flow simulation affects the sensitivity coefficients. Time steps are varied from 5 days to 200 days. In Figure B.11 sensitivity of time steps on the gradients (well bottom-hole pressure) are shown for variation of step sizes from 50 days to 200 days. Table B.5 gives the description of the color codes shown in Figure B.11. It is apparent from the figure that step increments have significant effect on the gradients. The events are shifted forward or backward in time as time steps are varied. One reason for this variation in the trend can be attributed to 'chain effect' that is a shift in any event may trigger different states of fluid saturation or pressure level for the subsequent duration of the flow.

It is also evident from the figure that coarser increments may mask some information. However, it is found that for the reservoir heterogeneity used in these models time steps of 50 days to 100 days will be ideal for future analysis. Less than 50 days step sizes show erratic behavior. In terms of computational efficiency, smaller steps will be quite expensive as opposed to larger time steps.

## Effect of heterogeneity

One objective of investigating the sensitivity coefficients is to determine a set of a priori constraints to be used in the optimization process. In an optimization loop, reservoir properties such as grid permeability and porosity values are modified, thus changing the heterogeneity of the reservoir. This optimization process is computationally intensive. To make the

| Event ID | Days | Event |
|---|---|---|
| A | 0 | Changes from oil rate control to reservoir fluid volume rate control mode (RFVRC) |
| B | 150 | Changes to water rate control mode (WRC) |
| C | 175 | Worst offending connection 12 shut-off (WOC 12) RFVRC |
| D | 200 | WRC |
| E | 225 | WOC 11 and RFVRC |
| F | 250 | WRC |
| G | 280.98 | WOC 10 |
| H | 314.75 | WOC 9 |
| I | 350 | WOC 8 |
| J | 392.45 | WOC 7 |
| K | 421.23 | WOC 6 |
| L | 450 | WOC 5 |
| M | 489.24 | WOC 4 and well changes to bottom-hole pressure control mode (WBHPC) |
| N | 519.62 | WOC 3 |
| O | 550 | WOC 2 |
| P | 600 | WOC 1; Well 1 completely shut-off; Well 1 immediately reopened; Secondary water cut limit (0.5) activated; WRC |
| Q | 650 | WOC 12; WOC 11; WOC 10 |
| R | 1050 | WOC 9 |
| S | 1400 | WOC 8 |
| T | 1550 | WOC 7 |
| U | 1700 | WOC 6 |
| V | 1850 | WOC 5 |
| W | 2000 | WOC 4; WBHPC; Non-linear equation convergence failure |
| X | 2090 | WOC 3 |

Table B.4: Well control and event history for simulations for aquifer strength study with artificial well control.

| Color Code | Event |
|---|---|
| Red | Change from oil rate control to reservoir fluid volume rate control mode |
| Light Blue | Change to water rate control mode |
| Black | Worst offending connection shut-off and change to reservoir fluid volume rate control mode |
| Blue | Worst offending connection shut-off |
| Green | Worst offending connection shut-off and change to well bottom-hole pressure control mode |

Table B.5: Event history in study of temporal discretization on sensitivity used in Figure B.11.

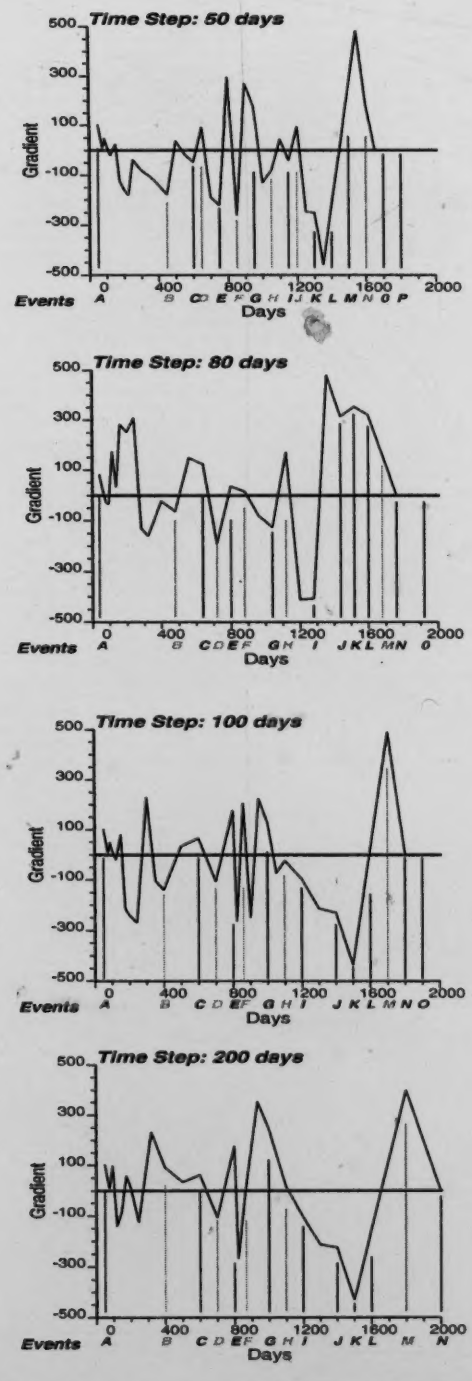


Figure B.11: Bottom-hole pressure sensitivity coefficients with respect to Region 1 transmissibility for cases with time steps of 50, 80, 100, and 200 days. Events color coded are described in Table B.5.

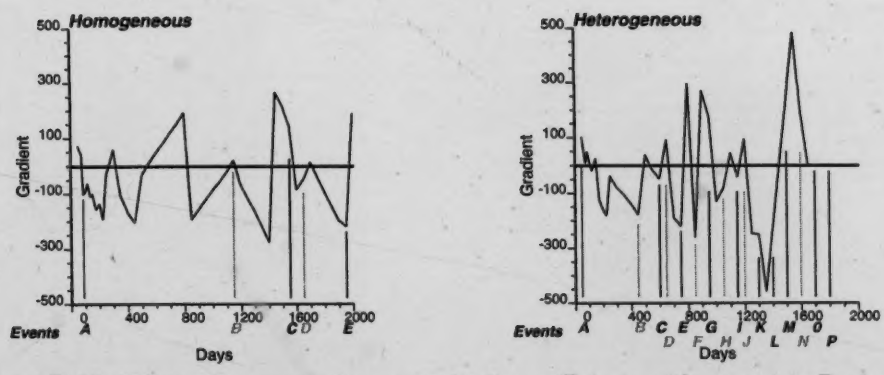


Figure B.12: Effect of heterogeneity on sensitivity coefficients with respect to Region 1 transmissibility: homogeneous and heterogeneous. Events are color coded in the same manner as in Table B.5.

algorithm efficient the gradients are frozen or kept unchanged for several iterations, which one could call an inner optimization loop. To ascertain the validity of such approximate technique one should investigate the effect of heterogeneity on the sensitivity coefficients of the flow responses with respect to relevant reservoir properties.

Figure B.12 shows the sensitivity coefficients of well bottom-hole pressure with respect to Region 1 transmissivity for a reservoir description with homogeneous properties and heterogeneous properties. It is apparent from the figure that heterogeneity plays a significant role in determining the gradient trends. Although not much can be explained about the effect of heterogeneity, Figure B.12 reveals homogeneous properties lead to less frequent changes in well control. However, this does not imply the variability in the gradients will be less for homogeneous reservoirs. Further investigation is needed to quantify the effect of heterogeneity on the sensitivity coefficients.

To quantify the effect of heterogeneity changes in reservoir property models in any optimization procedure, a random permeability ($x-$direction) model is generated with a mean of zero. This model multiplied with a scalar coefficient is added to a 'base case' permeability model. The sensitivity coefficients are computed for the new model. The random model can be considered as a gradient direction in a gradient based optimization technique, and the coefficient can be considered as the distance in this gradient direction. The coefficient is varied from 0.25 to 20. Figure B.13 illustrates the effect of such heterogeneity changes. It is evident from the figure that overall trend is quite similar with the exception of some local variation up to a coefficient as high as 10. This affirms the validity of keeping sensitivity coefficients frozen in an inner optimization loop.

## Effect of Region Volume, Well Location and Grid Configuration

Intuitively, a parameter region with a larger volume representation has greater effect than a smaller one. In order to investigate this a reservoir model similar to the 'base case' one is considered with only one well at the central location. Model has 64×64×16 reservoir grids with an underlying aquifer. Entire reservoir model is divided into two concentric regions. Volume of the region containing the central well is varied by including 1×1 to 33×33 grid blocks in $x-$ and $y-$direction. Figure B.14 shows the effect of region volume on sensitivity coefficients. There is a significant jump in the gradient absolute values when region volume increased from 1×1 to 3×3. However, any volume increase after that does not have any practical effect on the sensitivity coefficients.

In order to study the effect of the volume location relative to the well, 9 concentric parameter regions are specified around one central well. Regions are numbered in the

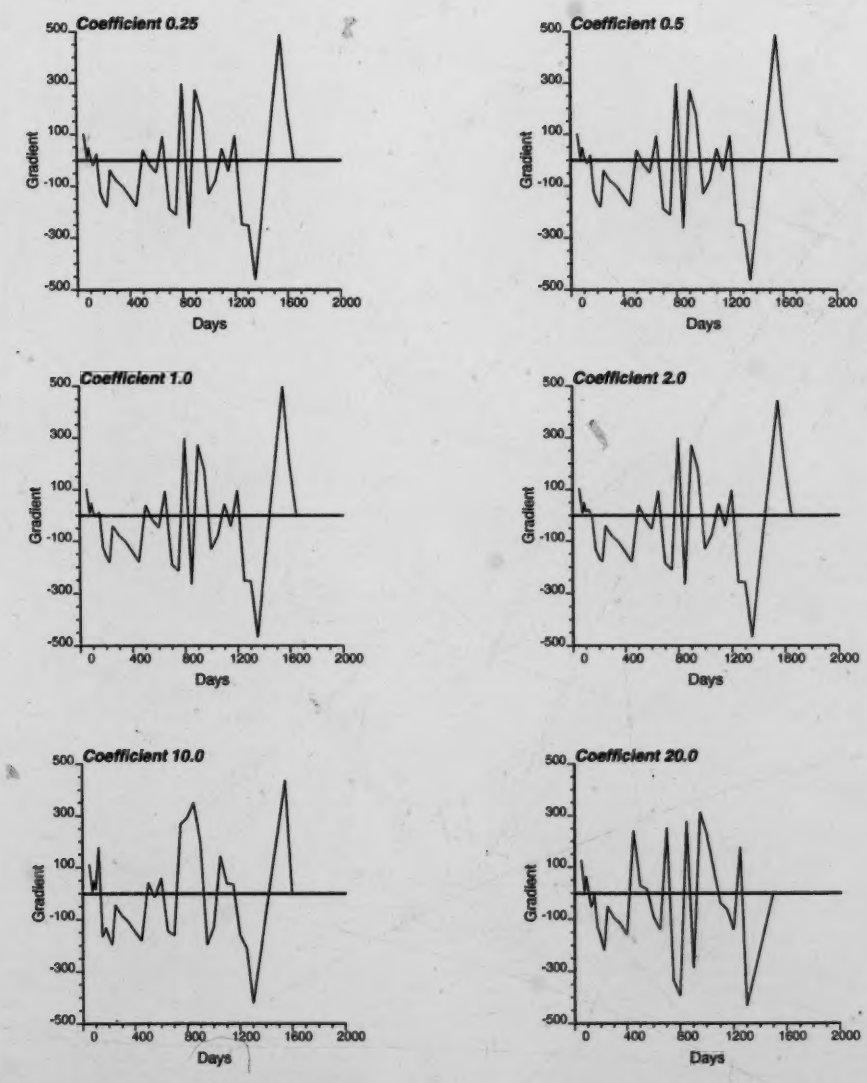


Figure B.13: Effect of degree of heterogeneity on sensitivity coefficients. Changes in permeability model obtained with a scalar coefficient multiplied random model added to a 'base case' model. The scalar coefficient is varied from 0.25 to 20.

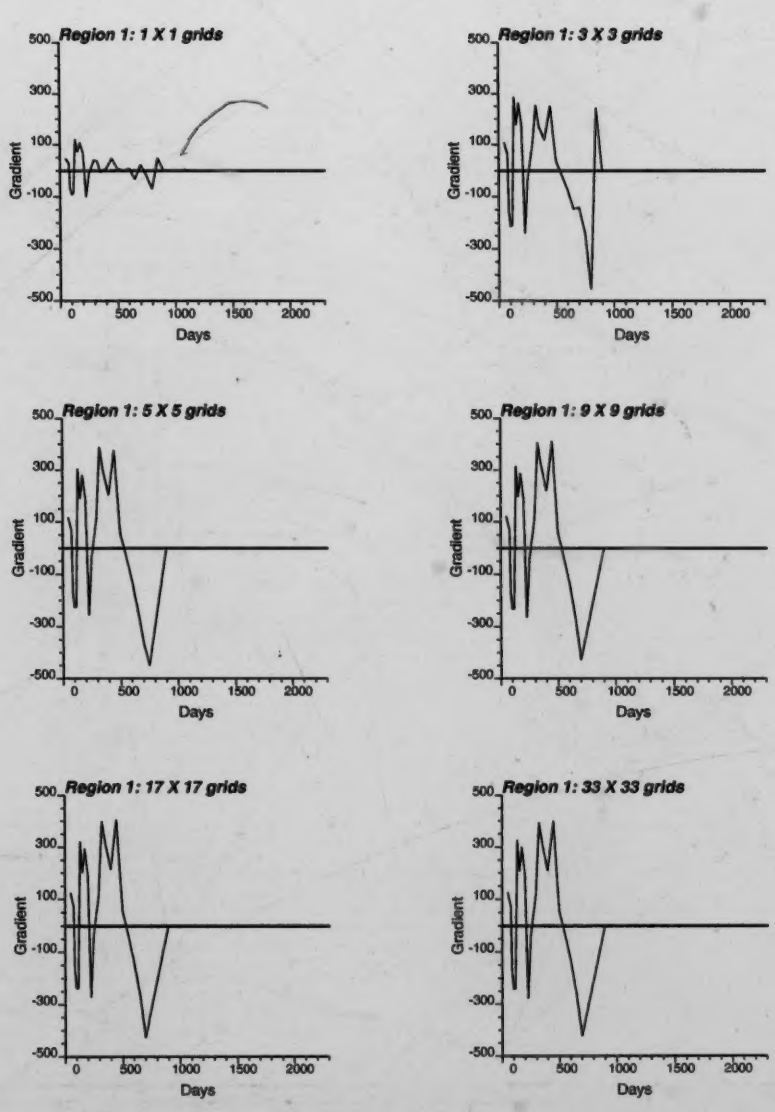


Figure B.14: Effect of region volume on the well borehole pressure sensitivity coefficients with respect to transmissibility of region containing the central well.

ascending order of proximity from the well. Figure B.15 shows the borehole pressure sensitivity coefficients for the concentric regions. It is evident from the figure that gradient absolute values diminish with the regions further away from the well.

Grid orientation affects the sensitivity coefficients. To mimic two different grid orientations, the same reservoir model is used but with two different parameter region orientations using square and triangular regions, respectively. There are four regions in each case. The parameter regions for the two cases are shown in Figure B.16. There are four regions in each case. The central well is located in Region 1 in both cases. Figure B.17 shows borehole pressure sensitivity with respect to transmissibilities of all four regions. Due to 7-point finite-differencing scheme of the flow equation, the sensitivity coefficients with respect to Region 4 transmissibility are insignificant in this case. For regions with no neighboring cell of well block, sensitivities to this region is insignificant compared to other regions.

### Sensitivity Coefficients for Regular Parameter Regions

Implementing a multilevel technique in case of regular parameter regions will be more systematic than for irregular regions. These techniques can be implemented at different levels of data integration with minor conforming at each level. It is worth investigating the sensitivity coefficients with regular regions.

Reservoir domain of grids 64×64×16 is subdivided by regular regions of size 8×8×8. Figure B.18 shows the sensitivity coefficients of Well 1 borehole pressure with respect to regular regions at different times (50, 74.5, 87.23, 100, 500, 1000, 1500 and 2000 days). Only the top regions are shown in the figure. A close inspection of Figure B.18 reveals the magnitudes of the sensitivity coefficients are much less than those observed earlier with only 5 regions. This reaffirms that region volumes have significant effect on the sensitivity coefficients.

### Effect of Grid Coarsening

Dynamic data integration is an inverse problem. By nature, any inverse problem suffers from ill-posedness. Forms of regularization are applied in solving these problems. Solution of the inverse problem in a fine grid setup is virtually impossible. One form of regularization is effected through an hierarchical multilevel strategy. Investigating the effect of grid coarsening on the sensitivity coefficients is important to implement this technique.

We started with a 'base case' reservoir description having 128×128×32 grids, resembling a numerical geological model of the reservoir. Dynamic data integration at this fine resolution model is prohibitive because of the extensive CPU requirement. Five levels of grid coarsening are applied with model sizes 64×64×16, 32×32×16, 32×32×8, 16×16×8 and 16×16×4. Porosity values for these different grids are arithmetically averaged from the finest resolution model. Power averaging with an index -1 (i.e. harmonic average) is applied to obtain the permeability models. Sensitivity coefficients are computed with respect to 5 regions as used in the earlier studies. Figure B.19 shows the sensitivity coefficients of Well 1 borehole pressure with respect to Region 1 transmissibility. It is evident from the figure that with very coarse grid models (as the last one, here) some information is lost. However, a close inspection reveals the overall trend remains same.

## B.7 Discussion

Although nothing conclusive can be said of the study related in this appendix, it shows some insights into the behavior of the sensitivity coefficients. This can be used be as a premise for future work on dynamic data integration. Better understanding of these coefficients will provide additional means of control in the parameter estimation problem in dynamic data integration. One might exploit and develop some stochastic gradient approximation technique for future inverse problem solution technique. Hierarchical data integration approach may possibly benefit from the this type of study.

Some of the derived informations from this study are discussed below.

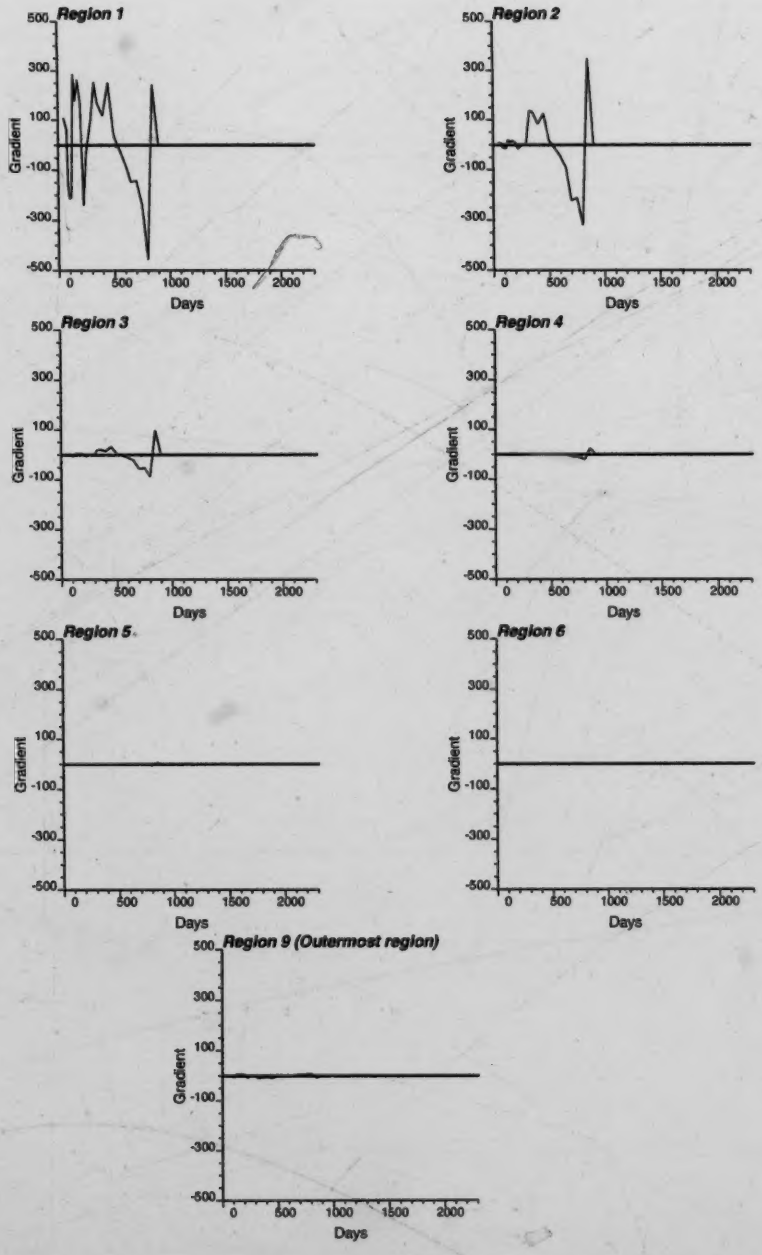


Figure B.15: Effect of region volume location relative to the the well on borehole pressure gradients with respect to transmissibility of concentric regions around a central well. Regions are numbered in the ascending order of proximity from the well.

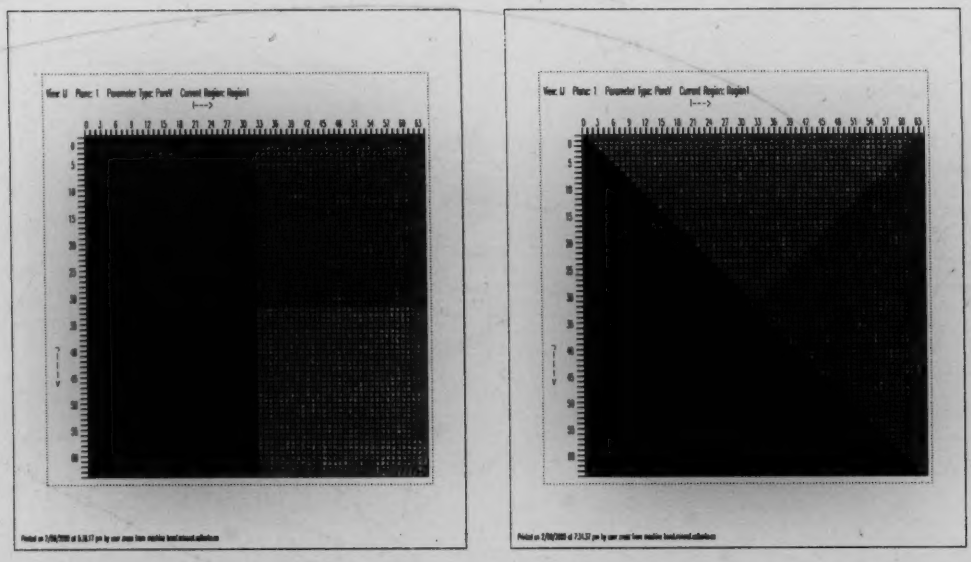

Figure B.16: Parameter regions specified to study the effect of grid orientation. Left: squares Right: triangles. Regions are color coded as: red - Region 1; green - Region 2; blue - Region 3; light blue - Region 4. Central Well in Region 1.

- Well bottomhole pressure, production rate are hardly influenced by the properties of another region.
- Well events have pronounced effect on the sensitivity coefficients. Interwell communication or well interference may affect these coefficients.
- Aquifer strength seriously affect the magnitude of the sensitivity coefficients.
- Temporal discretization has serious impact on the nature of the coefficients.
- Well controls can have serious impact on the gradients.
- Degree of spatial heterogeinty of petrophysical properties may not affect the gradients much. This gives rise to the possibility of using stochastic gradient scheme in the inversion process when spatial heterogeneity is varying.
- Sensitivity coefficients are mostly informed by the regions in the vicinity of the wellbore.
- Inversion of complex reservoirs will encounter significant level of difficulty because of the highly nonlinear and non-convex nature of the sensitivity coefficients.

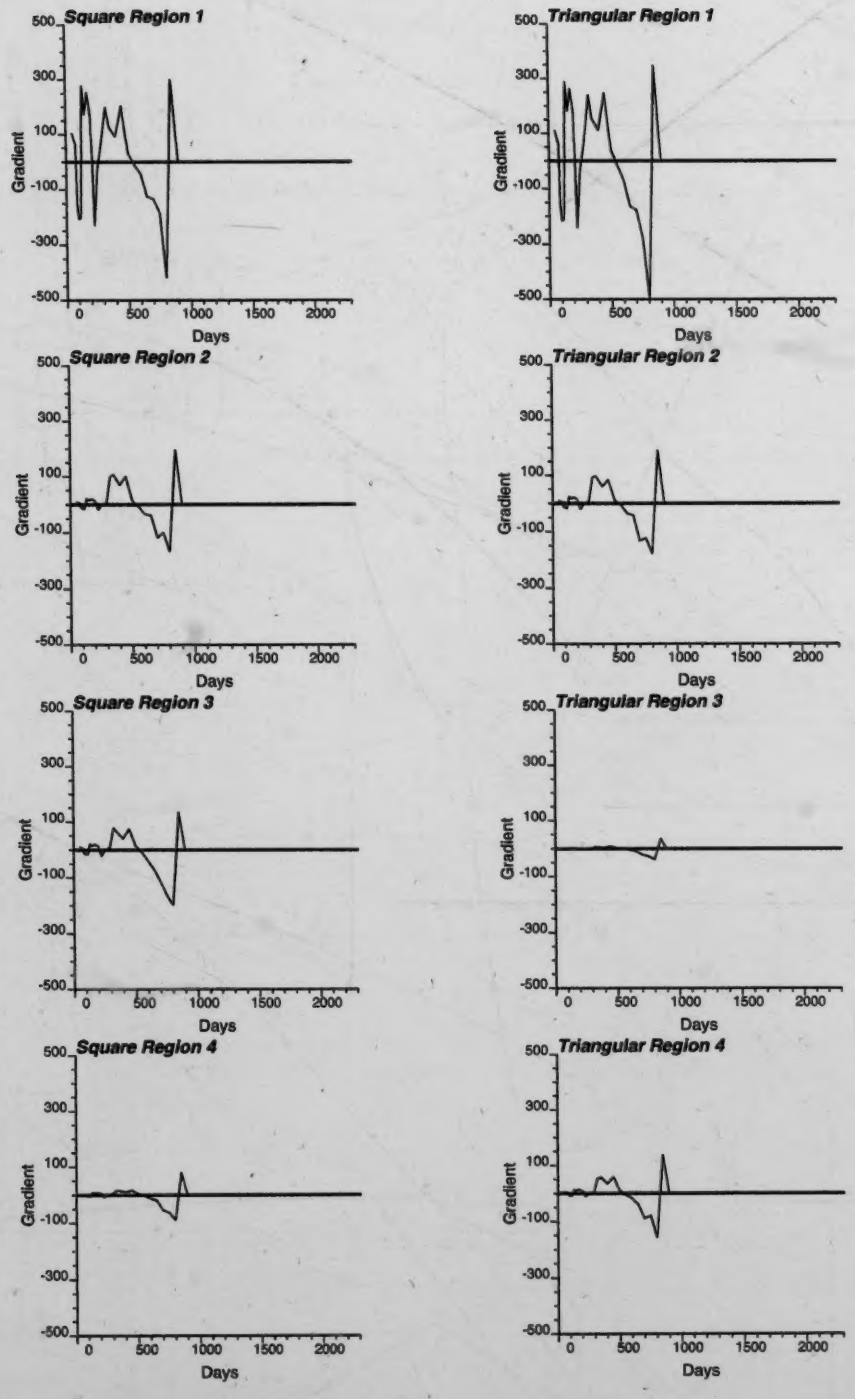


Figure B.17: Effect of grid orientation on pressure sensitivity coefficient with respect to transmissibility of Region 1. Region specifications are shown in Figure B.16

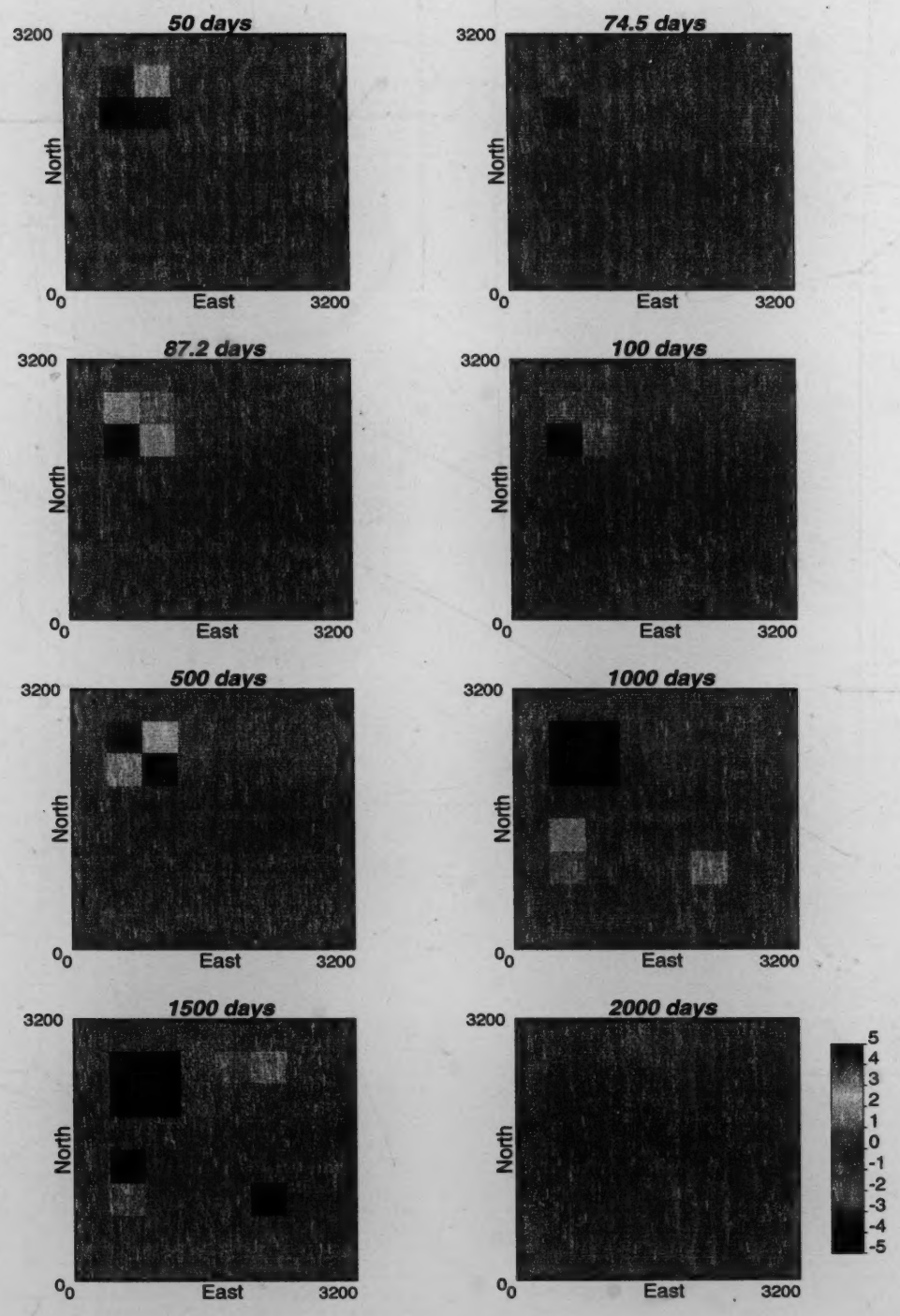


Figure B.18: Map of sensitivity coefficients of the Well 1 bottom-hole pressure with respect to transmissibility of regular regions at time steps of 50, 74.5, 87.23, 100, 500, 1000, 1500 and 2000 days. Top 8×8 regions of 8×8×2 are shown in the figure.

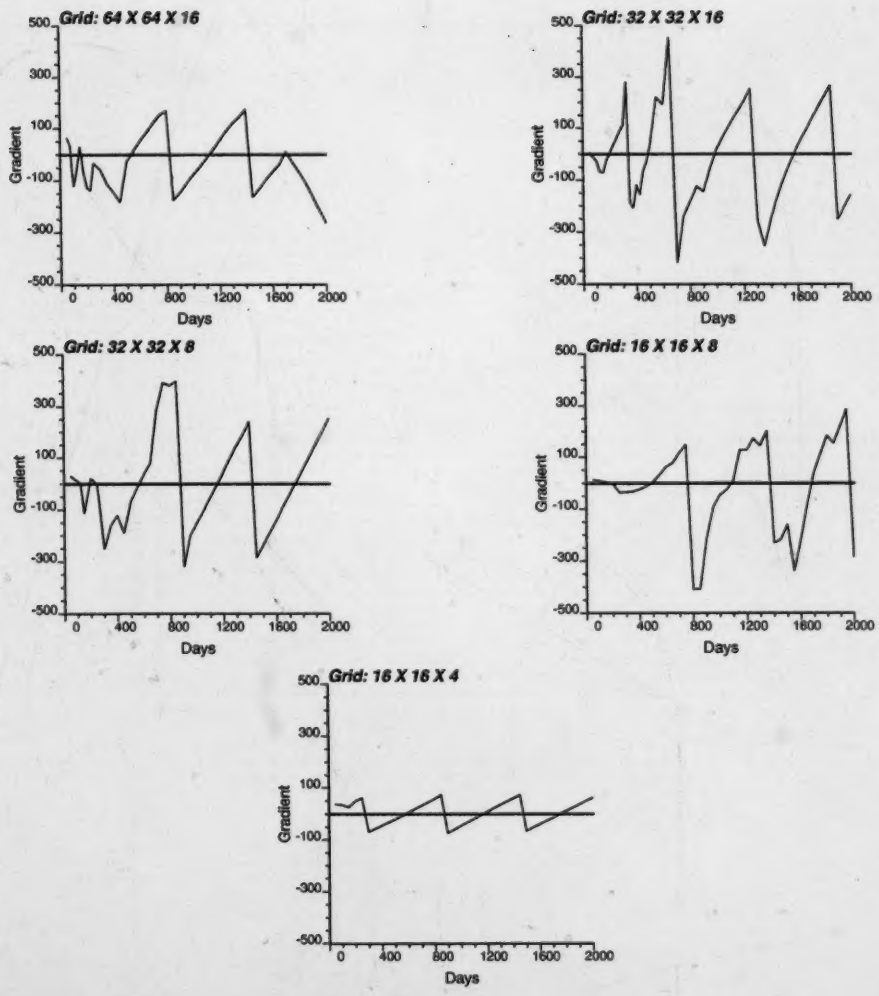


Figure B.19: Effect of grid coarsening on sensitivity coefficients of the Well 1 borehole pressure gradients with respect to transmissibility of Region 1.

# Appendix C

# Inversion with Pressure Derivative Mismatch

*This appendix offers the mathematics related to incorporating pressure derivative mismatch in the inversion algorithm. An implementation of inversion algorithm with backward difference technique for derivative computation was coded.*

## C.1 Mathematics of Inversion with Pressure Derivative Mismatch

In order to include the pressure derivative mismatch in the objective function for the minimization problem is given by:

$$O = \sum_i \sum_t W_p(i,t) \left[p_i^{obs}(t) - p_i^{cal}(t)\right]^2 + \sum_i \sum_t W_{p'}(i,t) \left[p_i'^{obs}(t) - p_i'^{cal}(t)\right]^2 \qquad \text{(C.1)}$$

where $p_i'^{obs}(t)$ and $p_i'^{cal}(t)$ are the observed and simulated pressure derivatives at well $i$ at time $t$. $W_{p'}(i,t)$ are weight assigned to pressure derivatives at different wells and at different time. Other notations remain the same as defined previously in the main text of the thesis.

Now, linearization of the objective function is attained by approximating the pressure data by retaining its first order Taylor expansion as shown in Equation 3.26. Using this linearization, the updating of the objective function (C.1) follows:

$$O(\{P^{cal}\}^1) = O(\{P^{cal}\}^0) + \sum_{t=1}^{n_t} \{D\}_t^T \{\Delta M\} + \sum_{t=1}^{n_t} \{\Delta M\}^T [C]_t \{\Delta M\}. \qquad \text{(C.2)}$$

which appears the same as that shown in Section 3.11. However, the matrices $\{D\}_t$ and $\{C\}_t$ are redefined as follows:

$$\{D\}_t = 2\left(\{P^{cal}\}_t - \{P^{obs}\}_t\right)^T [W]_t \{S\}_t + 2\left(\{P^{cal}\}_t - \{P^{cal}\}_{t-1} - \{P^{obs}\}_t + \{P^{obs}\}_{t-1}\right)^T [W]_{t'} \left(\{S\}_t - \{S\}_{t-1}\right)$$

$$\{C\}_t = \left(\{S\}_t\right)^T [W]_t \{S\}_t + \left(\{S\}_t - \{S\}_{t-1}\right)^T [W]_{t'} \left(\{S\}_t - \{S\}_{t-1}\right)$$

We employ the same definition of $\{S\}_t$ as given in Section 3.11. This implementation is based on the backward discretization method for derivative computation, that is,

$$p_i'(t) = \tau(t)\frac{p_i(t) - p_i(t-1)}{\tau(t) - \tau(t-1)}, \tag{C.3}$$

where $\tau(t)$ is time lapsed at interval $t$. The matrix $[W]_{t'}$ is computed from $[W]_t$ and the coefficients involved in the derivative computation.

Many different schemes for derivative computation [153] will give rise to different implementations of the gradients of the objective function. Another common scheme for derivative computation (Bourdet et al. [22]) is given by

$$p_i'(t) = a_i(t)p_i(t-1) + b_i(t)p_i(t) + c_i(t)p_i(t+1), \tag{C.4}$$

where

$$a_i(t) = -\frac{\ln\frac{\tau(t+1)}{\tau(t)}}{\ln\frac{\tau(t+1)}{\tau(t-1)}\ln\frac{\tau(t)}{\tau(t-1)}},$$

$$b_i(t) = \frac{\ln\frac{\tau(t+1)\tau(t-1)}{\tau(t)^2}}{\ln\frac{\tau(t+1)}{\tau(t)}\ln\frac{\tau(t)}{\tau(t-1)}},$$

and

$$c_i(t) = \frac{\ln\frac{\tau(t)}{\tau(t-1)}}{\ln\frac{\tau(t+1)}{\tau(t-1)}\ln\frac{\tau(t+1)}{\tau(t)}}.$$

This scheme leads to the pressure derivative vector given by the following relation

$$[P'] = [B][P],$$

where $[B]$ is a tridiagonal matrix with diagonals components comprising of terms $a_i(t)$, $b_i(t)$ and $c_i(t)$. For this scheme, the matrices $\{D\}_t$ and $\{C\}_t$ in Equation C.2 are defined as follows:

$$\{D\}_t = 2\left(\{P^{cal}\}_t - \{P^{obs}\}_t\right)^T [W]_t\{S\}_t$$
$$+ 2\left(\{P^{cal}\}_t - \{P^{obs}\}_t\right)^T [B]^T[W]_t[B]\{S\}_t$$

$$\{C\}_t = (\{S\}_t)^T [W]_t\{S\}_t + (\{S\}_t)^T [B]^T[W]_t[B]\{S\}_t.$$

Similar implementation of incorporating pressure derivative data is discussed by Onur and Reynolds [154].